Charm quark pair correlations with D^*-muon tag at HERA

Dissertation
zur Erlangung des Doktorgrades
des Fachbereichs Physik
der Universität Hamburg

vorgelegt von:

Dmitri Gladkov

aus Tschimken (Kasachstan)

Hamburg
2007

Gutachter der Dissertation:	Dr. A. Geiser Prof. Dr. P. Schleper
Gutachter der Disputation:	Dr. A. Geiser Prof. Dr. B. Naroska
Datum der Disputation:	15.06.07
Vorsitzende des Prüfungsausschusses:	Prof. Dr. C. Hagner
Vorsitzender des Promotionsausschusses:	Prof. Dr. G. Huber
Dekan der Fakultät für Mathematik, Informatik und Naturwissenschaften	Prof. Dr. A. Frühwald

To my Family.

Abstract

This thesis presents a measurement of double-tagged charm quark pair production via the process

$$ep \;\rightarrow\; e'\, c\bar{c}\, X \;\rightarrow\; e'\, D^*\mu\, X'$$

in lepton-proton collisions at HERA, using an integrated luminosity of 114 pb^{-1} gated by the ZEUS detector in the years 1996-2000.

Since the charm quark mass provides a large enough energy scale, the perturbative Quantum Chromo-Dynamics approach can be used to calculate the cross section for charm D^*-muon pairs. Using the D^*-muon pair to tag the charm quark pair, the measurement is sensitive not only to properties of the leading order hard scattering process but also to the hadronisation and the parton density in the proton as well as higher order effects. Employing the angular and charge correlations between the D^* meson and the muon, the fraction of charm events is extracted from the data. Cross sections for charm D^*-muon pair production in the visible range of the D^* transverse momentum $p_T^{D^*} > 1.5$ GeV, the D^* pseudorapidity $|\eta^{D^*}| < 1.5$, the muon transverse momentum $p_T^{\mu} > 1.0$ GeV and the muon pseudorapidity $|\eta^{\mu}| < 2.2$ are measured for the inclusive, photoproduction (inelasticity $0.05 < y < 0.8$ at $Q^2 < 1$ GeV^2) and deep inelastic scattering ($y < 0.65$ at $Q^2 > 2$ GeV^2) regimes. For the inclusive and photoproduction regimes differential cross sections in various kinematic variables of the D^*-muon pair are measured as well. The differential cross sections for the inclusive regime are compared to the leading order plus parton shower MC approach, while the differential cross sections for the photoproduction regime are compared to next-to leading order calculations. The momentum fraction carried by the gluon in the proton is also measured.

The possibility of extending the Global Track Trigger of the ZEUS DAQ/trigger system with a forward trigger algorithm is the technical task of this thesis. A forward trigger algorithm has been written which finds the event vertex position using STT and FMVD detector data.

Zusammenfassung

Diese Dissertation beschreibt eine Messung von doppelt identifizierter Charm-Quark-Paarproduktion aus dem Prozess

$$ep \;\rightarrow\; e'\; c\bar{c}\; X \;\rightarrow\; e'\; D^{*}\mu\; X'$$

in Lepton-Proton Kollisionen bei HERA. Es wurden Daten mit einer integrierten Luminosität von 114 pb^{-1} aufgezeichnet vom ZEUS Experiment in den Jahren 1996-2000, verwendet.

Da die Charm-Masse eine große Energie-Skala zur Verfügung stellt, kann die perturbative Quantenchromodynamik verwendet werden, um den Wirkungsquerschnitt für Charm D^{*}-Myon Paare zu berechnen. Durch die Verwendung von D^{*}-Myon Paaren zur Identifizierung von Charm-Paaren ist die Messung nicht nur auf Eigenschaften des harten Streuprozesses in führender Ordnung sensitiv, sondern auch auf die Hadronisierung und die Partondichten im Proton sowie Effekte höherer Ordnung. Der Anteil von Charm-Ereignissen wird aus den Winkel- und Ladungskorrelationen zwischen D^{*}-Meson und Myon aus den Daten gewonnen. Wirkungsquerschnitte für Charm D^{*}-Myon-Paarproduktion im sichtbaren Bereich des D^{*}-Transversalimpulses $p_T^{D^*} > 1.5$ GeV, der D^{*}-Pseudorapidität $|\eta^{D^*}| < 1.5$, des Myon-Transversalimpulses $p_T^{\mu} > 1.0$ GeV und der Myon-Pseudorapidität $|\eta^{\mu}| < 2.2$ wurden im inklusiven Regime, in Photoproduktion (Inelastizität $0.05 < y < 0.8$ bei $Q^2 < 1$ GeV^2) und in tief unelastischer Streuung ($y < 0.65$ bei $Q^2 > 2$ GeV^2) gemessen. Im inklusiven Regime und in Photoproduktion wurden zudem differentielle Wirkungsquerschnitte in verschiedenen kinematischen Variablen der D^{*}-Myon-Paare gemessen.Die differentiellen Wirkungsquerschnitte für das inklusive Regime wurden mit führender Ordnung plus Partonschauer MC verglichen, die differentiellen Wirkungsquerschnitte in Photoproduktion wurden mit Rechnungen in nächstführender Ordnung verglichen. Außerdem wird die Messung des Anteils am Protonimpuls, den das Gluon trägt, diskutiert.

Die Möglichkeit, den Globalen-Spur-Trigger des ZEUS DAQ/Trigger-Systems mit einem Vorwärts-Trigger-Algorithmus zu erweitern, ist der technische Teil dieser Arbeit. Ein Vorwärts-Trigger-Algorithmus, der in der Lage ist, die Position des Ereignisvertex aus STT und FMVD Detektor Daten zu bestimmen, wurde entwickelt.

Contents

Chapter 1

Introduction

The Standard Model (SM) is a theory which provides a successful description of the elementary structure of matter. In the SM, matter is made of 12 fundamental fermions: quarks and leptons. Interactions between these fermions are mediated by the exchange of the electromagnetic, weak and strong gauge bosons. The leptons are observed as free particles, whereas the quarks form bound states (hadrons) due to the confinement, which is an important property of Quantum Chromo-Dynamics (QCD) - the theory of the strong interaction.

The HERA collider can be considered as an electron microscope, where the electron or positron scatter off the constituents of the proton at high energies in order to investigate the internal structure of the proton. The lepton scatters off a parton of the proton via the exchange of the gauge bosons: photon, Z^0, $W^{\pm}$. This can lead the proton to break up into a proton remnant and hadrons produced in the hard scattering process. Measurements of the hadronic final state in electron-proton scattering processes provide a powerful testing ground for QCD. Moreover, due to the large center-of-mass energy available at HERA, the collider can be regarded as a charm factory, where charm hadrons are produced copiously. Charm production in lepton-proton scattering at HERA proceeds through two main processes: deep inelastic scattering, in which the virtuality Q^2 of the exchanged photon covers a region from few GeV^2 to the kinematic limit of 10^5 GeV^2, and photoproduction processes, where the exchanged photon is quasi-real with very low virtuality. The main charm production mechanism at HERA is boson gluon fusion.

At high energy scales (higher than 1 GeV), where the strong interaction becomes small, the perturbative approach of QCD can be applied. One of the most important aspects of perturbative QCD is the factorisation theorem. According to this theorem, the charm quark production cross section can be split into a calculable matrix element (ME) of the hard scattering and parton distribution functions (PDFs), in which the non-perturbative phenomena are hidden. To separate the hard scattering and soft phenomena, a hard scale (factorisation scale) is introduced. Such the factorisation scale can be the virtuality of the exchanged photon or transverse momentum or

the charm quark mass. Therefore, charm quark production provides ample opportunities to test perturbative QCD. The hadronisation of partons produced in the hard scattering process is also described by the non-perturbative fragmentation functions. Since predictions for the PDFs and the fragmentation functions in perturbative QCD cannot be made, they are determined using phenomenological approaches. Thus the description of the underlying parton dynamics of lepton-proton scattering is of great interest to test QCD.

Most previous analyses of charm production at HERA were based on the measurement of one charm quark (single tagging), where the D^* meson is commonly used for this tagging. In this analysis the double tagging technique, where both produced heavy quarks are tagged by the D^* meson and muon in the final state, is used. In principle, the charm quark pair can be also tagged by a D meson pair in the final state. But the net branching ratio of D meson pair production is small. The double tagging technique provides more information about the charm production mechanism than single tagging. Moreover, this technique is sensitive to higher order effects, hadronisation and initial state of partons participating in the hard scattering process. Apart from this the relatively low D^* background is one more fine feature of the technique. The advantage of double tagging is therefore obvious. On the other hand, disadvantages for the analysis are fake muon contamination and low statistics.

In the present thesis, the double tagging analysis is performed on data samples collected by the ZEUS detector in the years 1996-2000 with an integrated luminosity of 114 pb^{-1}. The data samples of the data taking in the years 2003-2007 are not yet used in this analysis due to the absence of the corresponding MC simulation. Using the angular and charge correlations between the D^* meson and the muon, the fraction of charm events is extracted from the data. The cross sections of charm D^*-muon pair production are measured for the inclusive, photoproduction and deep inelastic scattering regimes. For the inclusive and photoproduction regimes measurements of differential cross sections in various kinematic variables of the D^*-muon pair are also performed. The differential cross sections for the inclusive regime are compared with the leading order plus parton shower MC approach, while the differential cross sections for the photoproduction regime are compared with the next-to leading order calculations.

Since the boson gluon fusion process is dominant at HERA, the measurement of the momentum fraction carried by the gluon in the proton can be performed by means of kinematic information of the D^*-muon pair used as an approximation of the original charm quark pair system. To perform this measurement in this analysis, the corresponding technique is developed.

This thesis has the following structure.
In **Chapter 2** the theoretical and phenomenological methods used for the description of heavy quark production at the HERA collider are discussed. Special attention is devoted to D^*-muon pair production in the hard interaction. A short overview of

charm production at HERA is also given. In **Chapter 3** the HERA collider and the ZEUS detector are presented. The detector components used in this analysis and the trigger system are described in detail. **Chapter 4** is dedicated to the vertex finding algorithm developed for the ZEUS Forward Global Track Trigger, which is the technical task for this thesis. In **Chapter 5** the dataset and MC samples used in this analysis are summarised, the description of the event reconstruction and muon finding algorithms as well as the GMUON finder is given and the reconstructed variables are defined. Corrections applied to the reconstructed MC are summarised as well. **Chapter 6** covers the description of the event selection and the signal extraction procedure. A comparison of the data and MC as well as the obtained results are also discussed. In **Chapter 7** the measurements of the visible charm D^*-muon pair production cross section are presented for the inclusive, photoproduction and deep inelastic scattering regimes. The differential cross sections in bins of the kinematic D^*-muon pair variables are also measured and compared with leading order plus parton shower MC predictions and next-to leading order calculations. **Chapter 8** contains the description of the measurement of the gluon momentum fraction in the proton. **Chapter 9** concludes with the results of the present analysis.

Chapter 2

Heavy Quark Production Overview

In this section a summary of the theoretical and phenomenological techniques used for the description of heavy quark production at the HERA collider is discussed. First a brief introduction into the Standard Model of elementary particle physics is given. Afterwards, the kinematics of lepton-proton scattering at the collider is described. This is followed by the heavy quark production description along with sources of D^*-muon pairs produced in hard interactions. MC simulations of heavy quark production are discussed as well. A short overview of charm production at HERA is given.

2.1 Introduction to Standard Model

The Standard Model (SM) [1, 2] of elementary particle physics is a quantum field theory, which successfully describes the strong, weak and electromagnetic fundamental forces and the elementary particles from which matter is made up. The SM contains two kinds of particles: fermions and bosons. Fermions are spin-$\frac{1}{2}$ particles and obey the Pauli exclusion principle, which simultaneously forbids sharing of the same quantum state by two or more fermions. In contrast to fermions, bosons are integer spin particles and can share the same quantum state simultaneously. Fermions interact by the exchange of field quanta (virtual gauge bosons) which determine the properties of the interaction.

In the SM, matter is constructed from fermions which are split into two groups: leptons (and antileptons) and quarks (and antiquarks). Leptons as well as quarks are divided into three generations. The lepton and quark generations are represented in Table 2.1.

The SM describes the experimental results by using three fundamental interactions: electromagnetic, weak and strong. The electromagnetic interaction is described by *Quantum Electro-Dynamics* (QED). *Quantum Chromo-Dynamics* (QCD) is a theory of the strong interaction. All three interactions are summarised in Table 2.2.

	Generation			El. charge	Interaction		
	1	2	3		elec.magn.	weak	strong
Leptons	$\begin{pmatrix} \text{e} \\ \nu_e \end{pmatrix}$	$\begin{pmatrix} \mu \\ \nu_\mu \end{pmatrix}$	$\begin{pmatrix} \tau \\ \nu_\tau \end{pmatrix}$	-1 0	yes no	yes yes	no no
Quarks	$\begin{pmatrix} \text{up (u)} \\ \text{down (d)} \end{pmatrix}$	$\begin{pmatrix} \text{charm (c)} \\ \text{strange (s)} \end{pmatrix}$	$\begin{pmatrix} \text{top (t)} \\ \text{beauty (b)} \end{pmatrix}$	$+2/3$ $-1/3$	yes yes	yes yes	yes yes

Table 2.1: The fundamental particles in the SM and their charges and interactions.

Interaction	Boson	El.charge	Mass	Typical coupling	Related group
Electromagnetic	photon γ	0	0	10^{-2}	$SU(2)_L \times U(1)_Y$
Weak	$W^{\pm}/Z^0$	$\pm 1/0$	80.4/91.2 GeV	10^{-6}	$SU(2)_L \times U(1)_Y$
Strong	8 gluons g	0	0	1	$SU(3)_C$

Table 2.2: The fundamental forces in the SM and their properties. Couplings are given at energy scale of 1 GeV.

Gravitation is not incorporated into the SM theory. The exchanged bosons of the interactions are described by the group structure of the Standard Model:

$$SU(3)_C \times SU(2)_L \times U(1)_Y.$$

The weak and electromagnetic interactions are unified in the gauge group:

$$SU(2)_L \times U(1)_Y,$$

where $U(n)$ denotes the group of all unitary $n \times n$ matrices and $SU(n)$ is the group of all unitary matrices with determinant 1. The photon is massless, whereas the bosons of the weak interaction ($W^{\pm}/Z^0$) acquire masses through *spontaneous symmetry breaking*, where the masses of bosons and fermions are created by the interaction with the scalar *Higgs field*, mediated by the *Higgs* boson. The Higgs boson predicted by the SM has not been discovered yet, but it is expected to be observed soon after the start of the new pp collider LHC at CERN.

The strong interaction, which mediates forces between quarks and gluons, is an exact $SU(3)_C$ gauge symmetry. The octet of massless gluons carrying the colour charge is responsible for the interaction. Each quark can be assigned one of the three colours forming a $SU(3)_C$ triplet. Quarks cannot be observed as free particles as the strong force increases linearly with distance between quarks. This effect is called *confinement*. Therefore only bound states of quarks (hadrons) are observed. The quarks form colourless objects which can be either *mesons* (quark-antiquark pairs) or *baryons* (three quark state). Another important property of QCD is *asymptotic freedom*, which means that the strong interaction strength between two coloured objects decreases as the distance between them becomes shorter (or the energy of

the interaction becomes higher).

The prediction of the SM for particle interactions can be expressed as a power series expansion in the coupling constant α, if $\alpha \ll 1$. A graphical representation of this perturbative calculation approach is given by *Feynman diagrams*, where the interacting, intermediate and initial and final state particles are represented by lines, where each order of a coupling constant from the expansion is represented by a corresponding vertex [1].

2.2 Kinematics of ep Scattering

The kinematics of electron-proton (ep) scattering is described by two generic diagrams of the electron-proton interaction shown in Figure 2.1. The scattering process

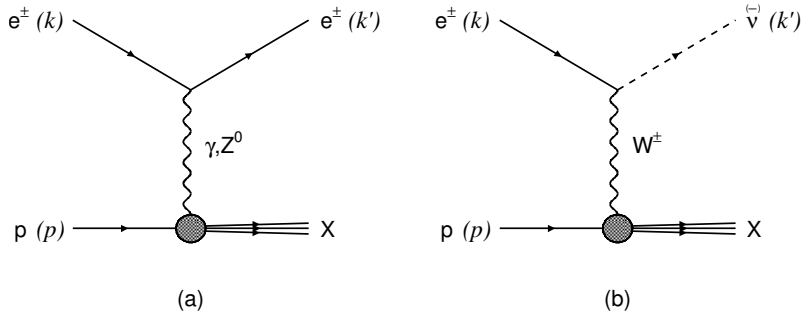

Figure 2.1: Schematic diagrams of the electron-proton scattering for the NC (left) and CC (right) processes.

of the incoming electron e and proton p goes via the exchange of a vector gauge boson. In case of the *charge current* interaction (CC) a $W^{\pm}$ boson is exchanged and the incoming electron is changed to a neutrino. In the *neutral current* interaction (NC) case, a photon or a neutral Z^0 mediates the interaction.

The four-vectors of the initial and final states can be defined as:

$$k = (E_e, \vec{k}), \quad P = (E_p, \vec{p}), \quad k' = (E'_e, \vec{k'}), \quad P' = (E_X, \vec{p'}), \tag{2.1}$$

where (E_e, $\vec{k}$) and (E_p, $\vec{p}$) are the energies and momenta of the incoming electron and proton respectively, and (E'_e, $\vec{k'}$) and (E_X and $\vec{p'}$) are the energies and momenta of the outgoing electron (or neutrino) and the hadronic system X respectively. The four-vector of the exchanged boson is given by $q = k - k'$. Since q is space-like, $q^2 < 0$, for convention one defines the negative value of the exchanged boson virtuality by:

$$q^2 = (k - k')^2 = -Q^2. \tag{2.2}$$

The center-of-mass energy $\sqrt{s}$ of the ep system is defined as :

$$s = (P + k)^2. \tag{2.3}$$

The inelasticity y, which describes the relative energy transfer from the electron to the hadronic system in the proton rest frame, is given by:

$$y = \frac{P \cdot q}{P \cdot k}, \quad 0 \ < \ y \ < \ 1. \tag{2.4}$$

The *Bjorken scaling variable* x is defined by:

$$x = \frac{Q^2}{2P \cdot q}, \quad 0 \ < \ x \ < \ 1. \tag{2.5}$$

In the naïve *Quark Parton Model* discussed in Section 2.3, x can be interpreted as the fraction of the proton momentum carried by the interacting parton. Assuming that the proton and electron masses (m_p and m_e respectively) are negligible in comparison to Q^2, the s, y and Q^2 kinematic variables can be simplified to:

$$\begin{aligned} s = (P + k)^2 &\approx 2P \cdot k, \\ y = \frac{P \cdot q}{P \cdot k} &\approx \frac{2P \cdot q}{s}, \\ Q^2 &\approx sxy. \end{aligned} \tag{2.6}$$

The center-of-mass of the boson-proton system W^2 is defined by:

$$W^2 = (P + q)^2 = P^2 + q^2 + 2P \cdot q \approx ys - Q^2. \tag{2.7}$$

With the incoming proton energy of 920 GeV and the electron energy of 27 GeV (see Section 3.1) the $\sqrt{s}$ at HERA is 318 GeV. The above variables are not independent. Therefore with given $\sqrt{s}$, it is enough to choose just two variables in order to describe the electron-proton scattering kinematics.

According to the Heisenberg uncertainty principle, the variable Q^2 defines also the transverse size in the proton $\lambda = \hbar c/\sqrt{Q^2}$ which can be resolved by the exchanged boson at HERA. For the maximum $Q^2 \approx s$, the resolution λ is about 10^{-18} m.

The phase space of the scattering process is split into two regions (regimes). The region with $Q^2 \to 0$ is called *photoproduction* (PHP). In this case the exchanged photon is *quasi-real*. The other region with Q^2 above a few GeV^2 and $W^2 \gg m_p^2$ is called *deep inelastic scattering* (DIS), where the exchanged boson is virtual. The present analysis covers mainly the low Q^2 region including the PHP and partially the DIS regions.

To describe the kinematics of final state particles, the following variables used in this analysis are introduced below.

θ^a Angle between the direction of particle a and the direction of the proton.

E^a Energy of the particle a.

p^a Momentum of the particle a

p_T^a Transverse momentum of the particle a.

η^a Pseudorapidity of the particle particle a, where $\eta^a = -\ln\left(\tan(\frac{\theta^a}{2})\right)$.

$p_T{}^{ab}_{v}$ Transverse momentum of particles a and b: $\vec{p}_T{}^{ab}_{v} = \vec{p}_T{}^{a} + \vec{p}_T{}^{b}$.

$\Delta\phi^{ab}$ Azimuthal angle difference between momenta of particles a and b.

2.3 Structure Functions and DIS Cross Section

In the DIS regime the electron-proton scattering can be described as an incoherent sum of elastic scattering processes of the electron off a set of (not self interacting) point-like partons. This simplest picture is called *Quark Parton Model* (QPM) [3, 4]. In this picture, as it was said before, the variable x can be referred to as the fraction of the proton momentum carried by the struck massless parton. The model describes the proton as a compound object which contains three *valence* quarks (uud) and *sea* quarks. The quarks are considered as quasi-free in the $infinite\ momentum\ frame$, where $Q^2 \to \infty$ but with finite x. In this frame the partons are considered to be massless, all transverse momenta are negligible and the interactions between the partons can be ignored due to the Lorentz time dilatation.

The general form of the electron-proton cross section can be written as:

$$\frac{d^2\sigma}{dxdy} \sim L_{\mu\nu}W^{\mu\nu}, \tag{2.8}$$

where $L_{\mu\nu}$ and $W^{\mu\nu}$ are leptonic and hadronic tensors [1] respectively. The lepton and hadron vertices are calculated separately due to the space-like nature of the scattering process. The leptonic vertex is evaluated by QED. The hadronic tensor includes the non-perturbative structure of the proton. In the QPM picture, this structure of the proton can be expressed in the mentioned limit of large Q^2 as $structure\ functions\ F_1(x)$ and $F_2(x)$, which do not depend on the Q^2 scale (*scaling invariance*). In the QPM, the structure functions are related to the *parton density functions* $f_q(x)$ (PDFs), which describe the probability of finding a parton q with the momentum fraction x in the proton. If the parton q ($\bar{q}$) is a quark (antiquark) with charge e_q, then the structure functions can be expressed as:

$$F_2(x) = 2xF_1(x) = \sum_q e_q^2 x(f_q(x) + f_{\bar{q}}(x)). \tag{2.9}$$

For unpolarised beams, the ep NC differential cross section in terms of these structure functions is given by:

$$\frac{d^2\sigma}{dxdQ^2} = \frac{4\pi\alpha_{em}^2}{xQ^4}\left[(1-y)F_2(x) + \frac{1}{2}y^2 2xF_1(x)\right], \tag{2.10}$$

where α_{em} is the fine structure constant. The dependence of the cross section on Q^2 can be clearly seen.

The structure functions cannot be calculated from first principles but have to be extracted from experimental measurements. Although the QPM states independence of the structure functions from the scale Q^2 and dependence of the functions on the scaling variable x, it was observed that the cross section deviates from the prediction of the model (*scaling violation*) with increasing Q^2. To explain the existing scaling violation, the interaction between quarks described by QCD should be taken into account and the dependence on the scale Q^2 has to be introduced. For the scattering via longitudinally polarised bosons it is convenient to include in the Equation 2.10 the *longitudinal structure function*, which is defined as:

$$F_L(x,Q^2) = F_2(x,Q^2) - 2xF_1(x,Q^2) \tag{2.11}$$

and is zero in the QPM. In the QCD picture, the longitudinal structure function is not zero because the inclusion of the interaction between quarks creates the possibility for gluons to split into quark-antiquark pairs with non-zero transverse momentum. Thus, gluons can couple to longitudinally polarised bosons.

Another structure function $F_3(x,Q^2)$ [4] is introduced to include the effect of parity violation in the exchange of an electroweak boson. Thus, the unpolarised NC DIS cross section in terms of the NC structure functions is given by:

$$\frac{d^2_{NC}(e^{\pm})}{dxdQ^2} = \frac{4\pi\alpha_{em}^2}{xQ^4}\cdot$$
$$\left[Y_+(y)F_2^{NC}(x,Q^2) - y^2F_L^{NC}(x,Q^2) \mp Y_-(y)xF_3^{NC}(x,Q^2)\right], \tag{2.12}$$

where $Y_\pm(y)$ is defined by:

$$Y_\pm(y) = 1 \pm (1-y)^2. \tag{2.13}$$

In case of the CC DIS scattering, the differential cross section can be written similarly to the NC differential cross section but in terms of the CC structure functions F_1^{CC},F_2^{CC} and F_3^{CC}:

$$\frac{d^2_{CC}(e^{\pm})}{dxdQ^2} = \frac{G_F^2}{4\pi x}\left(\frac{M_W^2}{Q^2+M_W^2}\right)^2\cdot$$
$$\left[Y_+(y)F_2^{CC}(x,Q^2) - y^2F_L^{CC}(x,Q^2) \mp Y_-(y)xF_3^{CC}(x,Q^2)\right], \tag{2.14}$$

where G_F is the Fermi constant. The NC structure functions are determined by the photon and Z^0 exchanges and by their interference, whereas the CC structure functions are the result of the $W^{\pm}$ exchange.

At low Q^2 the Z^0 exchange as well as $W^{\pm}$ exchange are suppressed with respect to the γ exchange due to the mass of the exchanged bosons M_{z^0} and $M_{W^{\pm}}$ respectively:

$$\frac{\sigma(Z^0, W^{\pm})}{\sigma(\gamma)} \sim \frac{Q^4}{(Q^2 + M^2_{Z^0,W^{\pm}})^2}.$$

In this Q^2 regime the photon exchange is dominant as it can be seen from the above ratio.

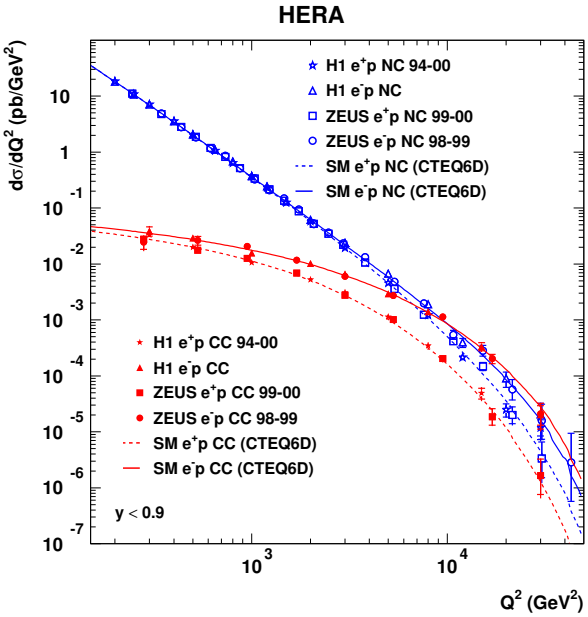

Figure 2.2: The NC and CC differential cross sections of electron (positron)-proton scattering measured by the ZEUS and H1 experiments.

The results of the NC and CC differential cross section measurements performed by the ZEUS and H1 experiments are shown in Figure 2.2. A good agreement between the measurements and SM predictions can clearly be seen. The CC cross section is suppressed with respect to the NC cross section until the scale of the interaction defined by Q^2 becomes comparable to the vector boson masses squared as expected from the SM. The difference observed in the CC cross section measurements for electrons and positrons can be explained by the smaller d quark than the u quark content in the proton, as in the CC interaction the positron interacts with d quarks, whereas the electron participates in the weak interaction with u quarks.

Since charm quark pair production is the subject of the present analysis, only the NC interaction is discussed further from now on.

2.4 QCD Framework

In QCD the strong interaction is mediated by gluons, which are coloured objects, as well as quarks. The non-Abelian nature of the strong interaction leads to the fact that gluons can couple also to each other. This is shown in Figure 2.3. Perturbative QCD provides a technique, which is able to perform calculations of cross sections as power series in the strong coupling constant α_s.

The *leading order* (LO) is the lowest order process which can be described by QCD. Higher orders imply quark loops (*virtual correction*) as well as gluon loops due to the gluon self interaction. This leads to different behaviour of the strong coupling with respect to QED, where only fermion loops are taken into account. The gluon self interaction results in quasi-free quarks for $Q^2 \to \infty$ and to confinement for $Q^2 \to 0$, where α_s becomes large and perturbative QCD cannot be applied.

Figure 2.3: One loop virtual correction to the gluon propagator. Gluon (left) and quark (right) loops.

To calculate cross sections, the integration over the full phase space of virtual and real quarks and gluons has to be performed. The integration over all particle momenta p introduces divergencies coming from the upper limit with $p \to \infty$, which leads to *ultraviolet divergencies*, and soft or almost collinear emission of massless gluons (gluon $p_T \to 0$) which causes *infrared divergencies*. However, in so-called *regularisation* and *renormalization* procedures, divergencies in the integral are replaced by finite expressions. This leads to introduction of a new scale μ, the *renormalization scale*. The scale μ is arbitrary. Thus, a measured physical observable quantity A has to be independent of μ.

In the case of ultraviolet divergencies, an effective strong coupling constant α_s absorbs these divergencies and becomes dependent on the renormalisation scale μ:

$$\mu^2 \frac{\partial \alpha_s(\mu)}{\partial \mu^2} = \beta(\alpha_s(\mu)), \tag{2.15}$$

where the β function is a power series in $\alpha_s(\mu)$ which describes the dependence of α_s on the renormalisation scale (running coupling). The LO solution is given by :

$$\alpha_s(\mu) = \frac{12\pi}{(33 - 2n_f) \cdot \ln(\mu^2/\Lambda^2_{QCD})}, \tag{2.16}$$

where n_f is a number of active quark flavours with quark mass lighter than scale μ and Λ^2_{QCD} is the scale of QCD, which depends on the number of active quark flavours. Λ^2_{QCD} represents the energy scale at which α_s becomes large and the perturbative approach is not applicable anymore.

In the case of infrared divergencies, a new so-called *factorisation scale* μ_f, which corresponds to non-perturbative QCD is introduced. The singularities are absorbed into the PDFs. This causes a running of the PDFs (renormalised PDFs). Thus, the factorisation scale splits the ep scattering process into two parts: hard and soft processes, where perturbative QCD is applicable for the hard process, whereas the scale of the soft process is below the factorisation scale and the soft process cannot be treated by the perturbative approach. The structure function F_2 can be therefore expressed as convolution of the perturbative part, the *coefficient functions* (C_2^a), which are perturbatively determined parton scattering cross sections, and the non-perturbative PDF ($f_a(\xi, \mu_f, \mu)$) for a given parton a:

$$F_2 = \sum_a \int_x^1 C_2^a\big(\frac{x}{\xi}, \frac{Q^2}{\mu^2}, \frac{\mu_f^2}{\mu^2}, \alpha_s(\mu)\big) f_a(\xi, \mu_f^2, \mu^2) d\xi. \tag{2.17}$$

This is called *factorisation* [5]. The evolution of the PDFs with the scale μ is described by the DGLAP equations [6], which can be expressed as:

$$\frac{\partial f_{q_i}(x, \mu_f^2)}{\partial \log \mu_f^2} = \frac{\alpha_s}{2\pi} \int_x^1 \frac{d\xi}{\xi} \Big[P_{qq}(\frac{x}{\xi}, \alpha_s) f_{q_i}(\xi, \mu_f^2) + P_{qg}(\frac{x}{\xi}, \alpha_s) f_g(\xi, \mu_f^2) \Big], \tag{2.18}$$

$$\frac{\partial f_g(x, \mu_f^2)}{\partial \log \mu_f^2} = \frac{\alpha_s}{2\pi} \int_x^1 \frac{d\xi}{\xi} \Big[\sum_i P_{gq}(\frac{x}{\xi}, \alpha_s) f_{q_i}(\xi, \mu_f^2) + P_{gg}(\frac{x}{\xi}, \alpha_s) f_g(\xi, \mu_f^2) \Big], \tag{2.19}$$

where $f_{q_i}(\xi, \mu_f^2)$ is the PDF for a given quark flavour i and $f_g(x, \mu_f^2)$ is the gluon density function. The DGLAP *splitting functions* $P_{ab}(\frac{x}{\xi})$ describe the probability of a parton a to radiate a parton b (a gluon or a quark) carrying a fraction $z = x/\xi$ of the momentum of parton a and can be expressed in LO by:

$$P_{qq}(z) = \frac{4}{3} \left[\frac{1 + z^2}{(1 - z)} \right],$$

$$P_{qg}(z) = \frac{1}{2} \left[z^2 + (1 - z)^2 \right],$$

$$P_{gq}(z) = \frac{4}{3} \left[\frac{1 + (1 - z)^2}{z} \right],$$

$$P_{gg}(z) = 6\left[\frac{z}{(1-z)} + \frac{1-z}{z} + z(1-z)\right]. \tag{2.20}$$

In order to calculate the PDFs at a scale μ, the measurement of the PDFs at a particular scale μ_0, which is used to derive values at the scale μ, is needed. As a consequence of the factorisation, the PDFs are process independent. Once the PDFs are measured, they can be exploited further in other measurements.

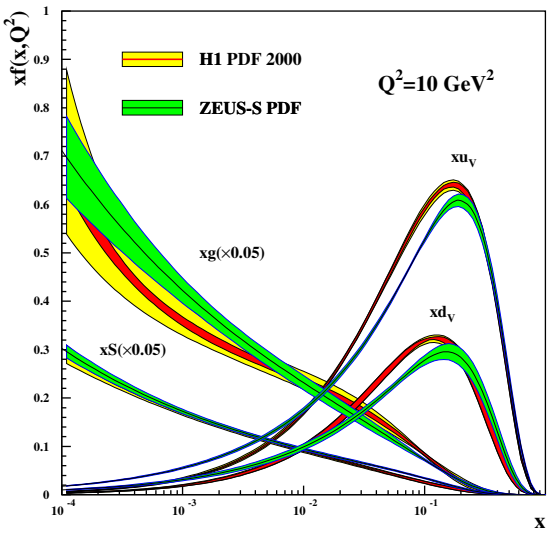

Figure 2.4: The proton density functions for u, d and s quarks and gluons extracted from NLO calculations by the H1 and ZEUS collaborations at $Q^2 = 10$ GeV^2.

The measurement of the PDFs has been performed at HERA [9]. The result of the measurement is given in Figure 2.4, where the parton density functions of valence and see quarks as well as gluons are shown. The dominance of the valence quarks at higher x is seen, whereas at low x the probability to find a gluon increases due to the soft gluon radiation from quarks before the interaction with the virtual photon.

2.5 Heavy Quark Production

The subject of the present thesis is a charm quark pair production study. Therefore in this section a description of the theoretical prediction of heavy flavour production is given. In the QPM heavy quark production cannot be easily explained. The mass of the incoming proton is lower than a mass of each heavy quark[1] ($m_c \approx 1.45$ GeV

[1]Only charm and beauty quarks are considered here. Top quark production is not possible at HERA due to its large mass

and $m_b \approx 4.45$ GeV) and the heavy quarks on their mass shell can thus not be constituents of the proton.

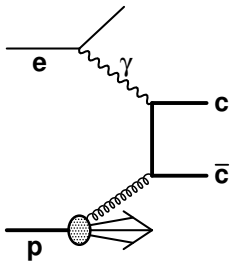

Figure 2.5: Feynman diagram of charm quark pair production in the BGF process.

The dominant contribution to ep heavy quark pair production at HERA comes from the boson-gluon fusion (BGF) process, which is shown in Figure 2.5. For low Q^2, where the BGF process is the lowest order heavy quark production process, the $\gamma^* g$ scattering can produce a quark pair $q\bar{q}$ (quark and antiquark), when the center-of-mass energy of the $\gamma^* g$ system is more than the squared mass of the $q\bar{q}$ pair. Thus, the heavy quark production measurement can be used to study the gluon density in the proton. In the region of $Q^2 \gg (2m_{c,b})^2$, the gluon splitting into a virtual quark pair is resolved by the exchanged photon and can be considered to occur inside the proton. The QPM can therefore be used for the heavy quark production description.

The heavy quark pair production cross section in BGF can be calculated as [11]:

$$\sigma_{BGF} = \frac{\pi e_q^2 \alpha_{em} \alpha_s}{\hat{s}} \Big((2 + 2\omega - \omega^2) \ln \frac{1+\xi}{1-\xi} - 2\xi(1+\xi) \Big), \tag{2.21}$$

where e_q is the electromagnetic charge of a heavy quark q produced in the hard process, $\hat{s}$ denotes the squared center-of-mass energy of the $\gamma^* g$ system and ω, ξ are defined by:

$$\omega = \frac{4m_q^2}{\hat{s}}, \quad \xi = \sqrt{1-\omega}. \tag{2.22}$$

From Equation 2.21 one can see that charm quark pair production is more favourable than beauty pair production due to the different charge and mass of c and b quarks.

2.5.1 Direct and Resolved Processes

In the LO picture used e.g. for MC predictions, the exchanged photon can fluctuate into a hadronic state with significant probability due to the long lifetime of the photon. Depending on the relative transverse momenta or mass of the produced quark pair, it can produce either a vector meson (bound quark pair state) or a perturbatively calculable state. To distinguish between the hard scattering processes,

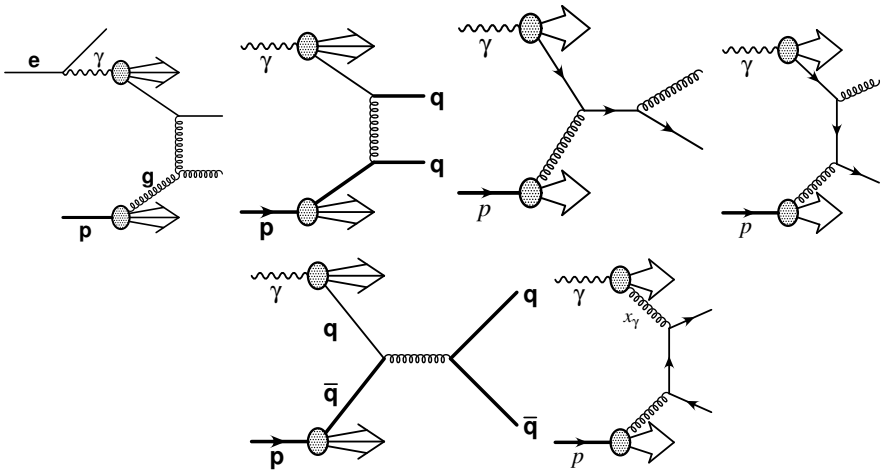

Figure 2.6: Feynman diagrams of LO resolved photon processes.

where the photon couples to a parton directly in BGF and other processes, where the photon shows its hadronic nature, the *direct photon* and *resolved photon* definitions are introduced respectively. In Figure 2.6 examples of resolved processes are given. The top diagrams in Figure 2.6 can be referred to as *excitation* processes, where heavy quarks are constituents of the resolved photon, whereas the bottom diagrams represent *hadron-like* processes, where heavy quarks are produced either in gluon-gluon fusion or light quark interactions. The interpretation and terminology of these processes are strongly connected with technical implementation and the perturbative order of the models and calculations. A strict separation of the direct and resolved photon processes is possible only at LO.

The description of the resolved photon in terms of the photon structure functions and the factorisation scale μ_γ is provided in a similar way as in case of the proton. As it can be seen the discussed resolved photon processes are sensitive to the parton density in both the proton and photon.

In case of the presence of both the resolved and direct components the heavy quark production cross section can be sectioned by the factorisation approach into the perturbative calculable part, which describes the hard parton cross section $\hat{\sigma}_{ij}(\hat{s}, m_q, \mu)$ of i and j quarks, two non-perturbative calculable PDFs of the photon ($f_{j/\gamma}(x_j, \mu^2)$) and proton ($f_{i/p}(x_i, \mu^2)$) and the photon flux $f_{\gamma/e}(y, \mu^2)$ obtained using the Williams Weizsäcker approximation (WWA) [10] and can be evaluated by:

$$\sigma_{PHP} = \sum_{partons} \int dy \int dx_j \int dx_i f_{\gamma/e}(y, \mu^2) f_{j/\gamma}(x_j, \mu^2) f_{i/p}(x_i, \mu^2) \hat{\sigma}_{ij}(\hat{s}, m_q, \mu). \tag{2.23}$$

2.5.2 Hadronisation of Heavy Quarks

Due to the confinement in QCD, the outgoing coloured partons produced in the hard interaction have to form colourless objects like mesons or baryons. This process is called *hadronisation*. Methods as applied in MC models or event generators (see Section 2.7), explicitly simulate the transition from partons to observable final states. The hadronisation process in these models consists of two parts: a perturbative and a non-perturbative component.

In the perturbative stage the radiation of additional partons before (initial state radiation) and after (final state radiation) the LO hard scattering is calculated in pQCD. In the final stage the outgoing parton with positive virtuality emits gluons (*parton cascade*). Due to such multi-parton emission it is complicated to perform the exact ME calculation of such high-order processes in perturbative QCD. Therefore, the *parton shower* approach (PS) is used. The concept of the approach is based on the use of an arbitrary number of branchings of one parton into two like $q \to qg$, $q \to q\gamma$ and $g \to q\bar{q}$ up to the cut-off scale Q_0^2 of 1 GeV^2 (DGLAP approach). A branching obeys the leading order splitting functions $P_{ab}(z)$ discussed in Section 2.4. In the DGLAP approach, the chain of partons emitted from the quark after the hard interaction is strongly ordered in the transverse momenta. Thus each emitted parton decreases the virtuality of the outgoing parton and the outgoing partons perform a transition to their mass shell.

In the initial stage, the radiation before the hard scattering process has to be also simulated. To do it, the PS approach is used in the *backward evolution* scheme starting from the scale Q_{max}^2. The backward evolution traces the showers backward in time decreasing negative virtuality down to the cut-off scale Q_0^2.

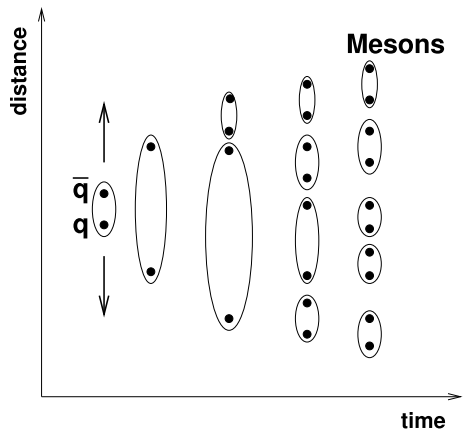

Figure 2.7: Schematic view of the string fragmentation model.

In the non-perturbative stage, the formation of hadrons after the parton cascade is described by using phenomenological fragmentation models. A model, which is

exploited in the MC simulation used in this analysis, is called *string fragmentation*. The principle of this model is given in Figure 2.7. Since quarks are coloured objects, the connection between the $q\bar{q}$ pair can represented by the calor field line (*string*). The potential stored in the string is motivated by QCD. If the stored potential of the string is large enough to produce new $q\bar{q}$ pairs the string is broken up into two. This process continues until the string energy is not sufficient to produce additional particles. To form heavy hadrons from a produced string fragment, the analogue of the PDFs, so-called *fragmentation functions*, are used. The fragmentation function ($D_q^h(z)$) gives a probability that hadron h is produced from parton q with the longitudinal momentum fraction z of the q. The *Peterson fragmentation function* [13] is widely used for heavy quark production:

$$D_q^h(z) \propto \frac{1/z}{(1 - 1/z - \epsilon_q/(1-z))^2}, \tag{2.24}$$

where ϵ_q is the free Peterson parameter, which is proportional to $1/m_q^2$ and needs to be measured in the experiment.

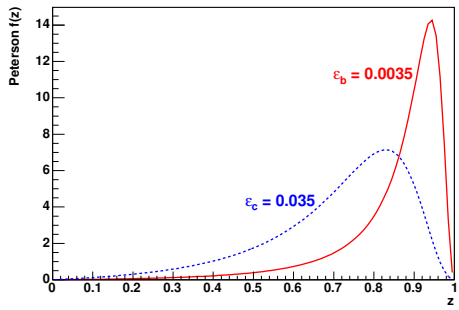

Figure 2.8: Shape comparison for the Peterson fragmentation function for charm and beauty values ϵ_q.

The charm quarks, which are the subject of the present analysis, are fragmented into hadrons according to the Peterson fragmentation function. The free Peterson parameter measured experimentally in e^+e^- collisions for charm production is $\epsilon_c = 0.035$ (D^* meson production at the ARGUS experiment, at $E = 10.6$ GeV) and for beauty production (B meson production at the ALEPH experiment, at $E = 91.2$ GeV) is $\epsilon_b = 0.0035$ (values obtained from [14]). To compare in an arbitrary scale the shape of the fragmentation function for the values mentioned above, Figure 2.8 is given. The fragmentation of beauty quarks to beauty hadrons shows a harder spectrum than the case of charm. This is due to the larger beauty mass.

2.5.3 Next-to-Leading Order Processes

Next-to-leading order (NLO) calculations of partonic cross sections have been performed in [12]. The NLO calculations reduce the sensitivity to the hard scale μ

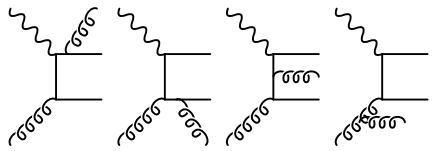

Figure 2.9: Examples of Feynman diagrams of real NLO QCD contributions to heavy quark production.

by taking into account the diagrams of order α_s^2. Examples of Feynman diagrams used in these calculations are shown in Figure 2.9 (real corrections) and Figure 2.10 (virtual corrections contributing to the interference term with LO) respectively. By comparing the NLO diagrams with the BGF LO diagram, it can be clearly seen that the main differences are additional hard gluon radiation and interference with virtual corrections.

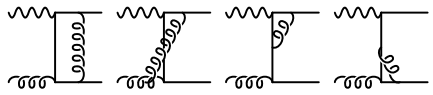

Figure 2.10: Examples of Feynman diagrams of virtual NLO QCD contributions to heavy quark production.

The hadron-like component (see Section 2.5.1), where the photon fluctuates into quarks and gluons before the hard scattering process, is also taken into account. Corresponding diagrams are shown in Figure 2.11. This component is expected to be small for charm production.

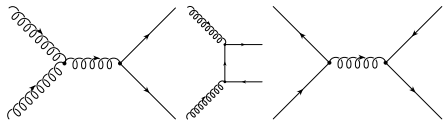

Figure 2.11: Feynman diagrams of NLO QCD contributions of the hadron-like component to heavy quark production.

When going from LO to NLO, one needs to keep in mind that a distinct assignment of a process to LO plus parton shower (LO+PS) or NLO is not always possible since the LO+PS model simulates higher order processes, e.g. NLO, in the parton showering.

In general, for heavy quark production at HERA two kinds of the calculation approaches can be used.

The massive approach:
Since BGF is the main LO process in α_s, the heavy quark pair is produced

dynamically in the hard scattering process. The heavy quarks can be treated as heavy objects which do not occur within the proton (massive approach or fixed-flavour number scheme). In this approach the number of active quark flavours is fixed (only u, d and s) and independent of Q^2. The heavy quark masses provide a hard scale, which allows application of the perturbative QCD approach for calculations of the hard process. This approach is reliably applicable, where the transverse momentum p_T of the heavy quark is less than or similar to its mass. This is particularly relevant for the low Q^2 region.

The massless approach:
At a large scale, where $p_T \gg m_c$ (or $Q^2 \gg m_c^2$), large terms proportional to $\ln(p_T^2/m_{c,b}^2)$ in the massive approach might spoil the convergence in the perturbative series. To solve this problem, the massless approach, which treats the heavy quarks as active flavours in the proton, can be employed. The approach interpretes $q\bar{q}$ pairs produced in gluon virtual splitting and resolved by the photon to occur within the proton (flavour excitation). Thus, heavy flavour structure functions can be measured by using the QPM description.

In principle, a combination of both approaches is available on the market. This scheme, referred to as the variable-flavour number scheme (VFNS), provides a smooth transition from the massive description to the massless behaviour. In this thesis the massive approach is exploited for the NLO calculations.

2.5.4 Decays of Charm and Beauty Hadrons

Since $D^{*\pm}$ mesons and muons are used in this analysis, corresponding charm and beauty hadron decay chains, which produce a D^* and a muon in the final state, need to be discussed here. The probability of the fragmentation process $f(c \to D^{*+})$ is 0.235 [18]. The corresponding fragmentation fraction of $f(b \to D^{*+})$ is 0.173 [22] and $f(\bar{b} \to \bar{c}W^+(c\bar{s}) \to D^{*+})$ is 0.026 [25]. The weak force can change the type of the neutral beauty meson. This is so-called $B^0 - \bar{B}^0$ oscillation, where the b quark oscillates to its antiquark. The time integrated probability ξ of the oscillation process for a mixture of all b-hadrons is measured to $\xi = 0.1259 \pm 0.0042$ [25].

In this analysis the $D^{*+} \to D^0(\to K^-\pi^+)\pi_s^+$ decay chain[2] is considered to reconstruct the D^* meson (see Section 5.12). The D^{*+} vector meson consists of c and $\bar{d}$ quarks. It decays to D^0 via the strong interaction. The $D^0 \to K^-\pi^+$ decay occurs through the weak interaction. Branching ratios of D^0 and D^* decays as well as a combined branching ratios [23] at charm and beauty quark levels are summarised below.

$$Br(D^0 \to K^-\pi^+) = (3.80 \pm 0.07)\%.$$

$$Br(D^{*+} \to D^0\pi_s^+) = (67.7 \pm 0.5)\%.$$

[2]The charge conjugate modes are also implied

$$Br(D^{*+} \to D^0(K^-\pi^+)\pi_s^+) = (2.57 \pm 0.06)\%.$$

$$Br(c \to D^{*+} \to D^0(K^-\pi^+)\pi_s^+) = 0.6\%.$$

$$Br(b \to D^{*+} \to D^0(K^-\pi^+)\pi_s^+) = 0.44\%.$$

$$Br(\bar{b} \to D^{*+} \to D^0(K^-\pi^+)\pi_s^+) = 0.07\%.$$

Semi-leptonic decays of hadrons containing heavy quarks occur through the weak interaction. The charm hadrons decay into hadrons which contain a strange quark with a probability of about 100%. The beauty hadrons decay into charm hadrons with a probability of about 100%. Weak decays of the heavy hadrons are governed by the Cabibbo-Kobayashi-Maskawa matrix (CKM matrix). Muons can be produced either directly in semi-leptonic decays of beauty hadrons and charm hadrons or indirectly via the cascade decay ($b \to c \to \mu$ or $b \to \tau \to \mu$). Branching ratios of direct and cascade muon production are given below.

$$Br(c \to \mu) = (9.8 \pm 0.5)\%.$$

$$Br(b \to \mu) = (10.95^{+0.29}_{-0.25})\%.$$

$$Br(b \to cascade \to \mu) = (10.03 \pm 0.64)\%:$$

$$Br(b \to c \to \mu) = (8.0 \pm 0.4)\%,$$
$$Br(b \to \bar{c} \to \mu) = (1.6^{+0.4}_{-0.5})\%,$$
$$Br(b \to \tau \to \mu) = (0.43 \pm 0.05)\%.$$

The probability of having a D^*-muon pair in the final state in charm or beauty events can be evaluated by the multiplication and combination of branching ratios corresponding to the charm or beauty decay chains respectively.

2.6 Charm Quark Tagging with D^*-Muon Pair

In this analysis to tag a charm quark pair produced in the electron-proton scattering a D^*-muon pair reconstructed in the final state is used. This is the so-called *double tagging* technique. The advantage of the double tagging technique in contrast to the single tagging, where only a D^* meson is used to identify the charm production event, is the almost complete reconstruction of the heavy quark pair final state. Thus the technique provides a clear signature of charm quark pair production. Kinematic parameters of the D^*-muon pair (like the azimuthal angle difference between D^* and muon momenta or the scalar sum of D^* and muon transverse momenta) are sensitive to the NLO contribution. Tests of the perturbative NLO QCD calculations can therefore be performed. Since the BGF process is governed by the gluon distribution function, a gluon density measurement can be also done by means of the D^*-muon pair kinematic information used as an approximation of the tagged charm

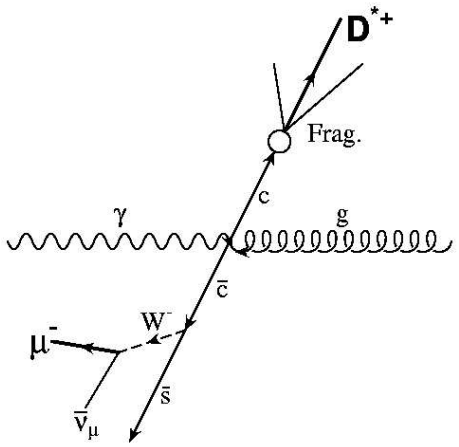

Figure 2.12: Principle of the charm double tagging technique. D^*-muon pair from $c\bar{c}$ with the unlike-sign configuration and back-to-back topology.

quark system.

The principle of the double tagging technique is given in Figure 2.12. The charm quark pair is mainly produced in the BGF process in the electron-proton interaction. The charge and angular correlations of the pair can be clearly seen. The charm quark pair has the *unlike-sign* configuration. Furthermore, in the PHP regime the transverse momenta of the quarks are opposite in the photon-gluon rest frame. The transverse momenta are also preserved in the photon-proton rest frame. The two frames are different only by a longitudinal boost in the Z direction due to the electron-proton beam energy asymmetry at HERA (see Section 3.1). Thus the azimuthal angular difference between the transverse momenta of the two quarks is 180^o (*back-to-back* topology) in both frames. The D^*-muon pair produced from the $c\bar{c}$ inherits the topology and charge sign configuration of the parent charm quark pair. Due to the fragmentation effects and the kinematics of the decays, the muon and D^* have approximately the same directions as the original quarks.

In the case of beauty production, which is considered as a background in this analysis, the D^*-muon pair can be in three combinations of the azimuthal angular and charge correlations. The first is a combination with the back-to-back topology and unlike-sign configuration as in the case of charm production. Here the muon of the pair is produced from b via the charm cascade decay or $B^0 - \bar{B}^0$ mixing. This is shown in Figure 2.13. The second combination appears, when the D^* and muon are produced from the same beauty quark and azimuthal angular difference between their transverse momenta is usually less than 90^o (*one-side* topology). The pair has unlike-sign configuration. The combination is shown in Figure 2.14.

In the case of the direct muon production from beauty hadrons, the last combi-

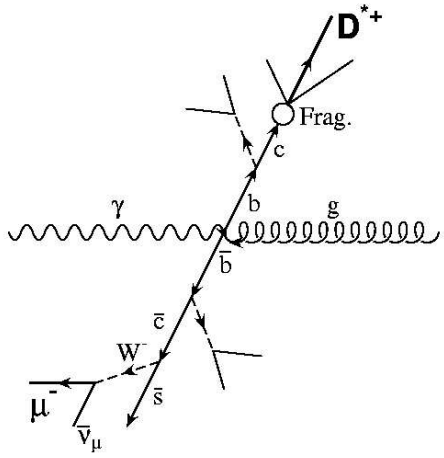

Figure 2.13: D^*-muon pair from different b with the unlike-sign configuration and back-to-back topology.

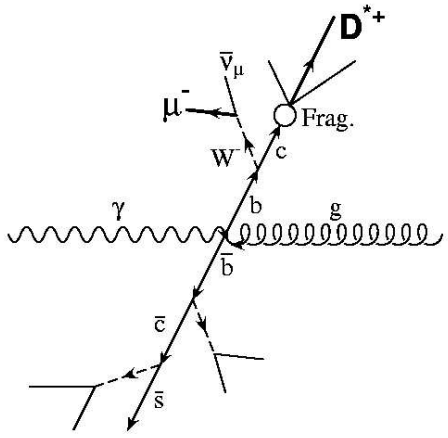

Figure 2.14: D^*-muon pair from the same b with the unlike-sign configuration and one-side topology.

nation needs to be considered. Here the D^*-muon pair inherits the back-to-back topology of the original $b\bar{b}$ and has the like-sign configuration. This is shown in Figure 2.15.

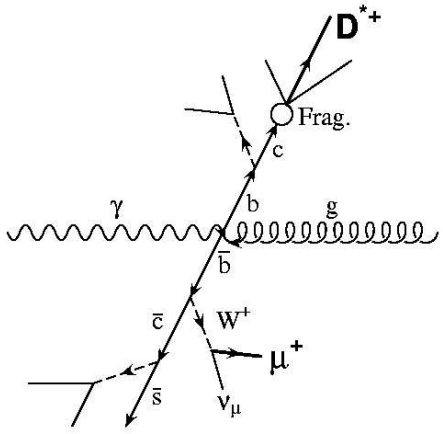

Figure 2.15: D^*-muon pair from the different b with the like-sign configuration and back-to-back topology.

Effects of the hadronisation, the NLO contribution, a possible non-zero initial intrinsic transverse momentum of heavy quarks smear the angular correlation between the D^* and muon. This should be taken into account in the event selection for the cross section to be measured.

2.7 MC Simulation of Heavy Quark Production

The Monte Carlo (MC) simulation technique is a key element of research in elementary particle physics. The existing models on the market provide descriptions of the ep scattering process. Events with the interesting physics can be generated by an event generator, and then passed through the detector simulation and stored for further comparison with the real data. Therefore, MC simulation is an important tool which can be used for many purposes like detector efficiency studies, unfolding the measured cross sections to the hadron level, trigger performance, track reconstruction efficiency and so on. In this analysis, the PYTHIA [15] and RAPGAP [24] MC generators both exploiting the LO+PS approach are used to describe the signal distributions. The techniques employed within these generators are discussed below.

The factorisation theorem [5] provides the possibility to perform a simulation of the ep interaction process, where each stage of the process can be calculated separately. In Figure 2.16 the schematic view of the sub-processes involved in a hard QCD interaction is shown.

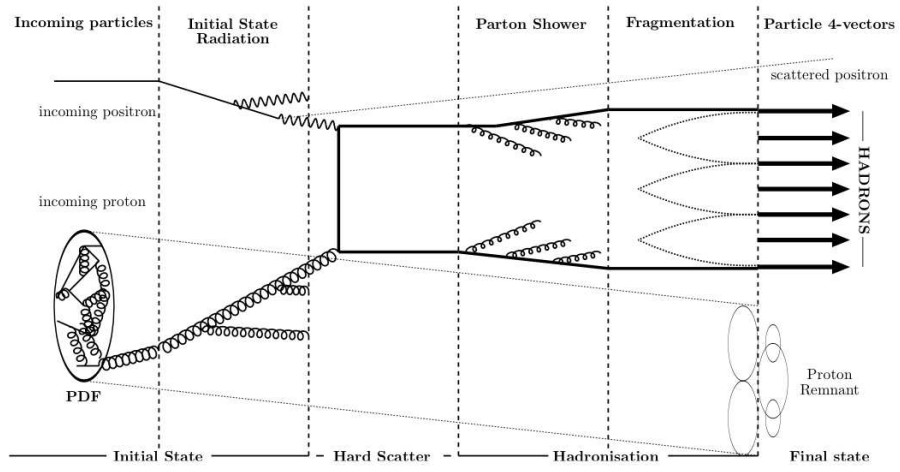

Figure 2.16: Schematic view of the processes involved in a hard QCD interaction.

The ep interaction process is factorised to the following stages:

- The hard interaction is the central part of the ep interaction process. The calculable matrix element (ME) describes the hard interaction of a parton from the proton with either the photon or a parton from the resolved photon. This part of the interaction is calculated in a fixed order perturbative expansion with some hard scale μ used to characterise the scattering process. The proton structure CTEQ5L [32] and photon structure function GRV-G LO [33] were used.

- The initial and final state radiations are processes, which describe the behaviour of a charged and/or coloured object before and after the hard interaction. The parton cascade produced by such an object can significantly change the topology and multiplicity of an event. The PS approach is used as an approximation scheme to describe the initial and final state radiation (see Section 2.5.2).

- The fragmentation is a process in which coloured and/or charged partons form colourless hadrons. This is a non-perturbative phenomenon which cannot be calculated and can be described only by phenomenological approaches like the Lund string model[3] [19]. The Lund string model was used in the production of the MC samples used in this analysis.

- The proton remnant is an almost undetectable hadron flow produced from the disruption of the proton after the hard interaction process. Since the initial state parton is a coloured object, the proton remnant is coloured also and is strongly connected to the fragmentation process. It participates in the formation of the fragmentation system of an event.

[3]This model is used in PYTHIA and RAPGAP

The resolved photon processes (hadron-like, excitation from the photon), the direct process as well as the process describing the excitation from the proton are included in the generators. To simulate the direct and hadron-like processes, the massive approach is exploited, whereas to generate the excitation in the photon or the proton, the heavy quarks are extracted in the massless approach by splitting a gluon from the partonic substructure into a heavy quark pair.

Short-lived hadronic final states generated by an event generator are decayed at the generator level, whereas long-lived particles should be further propagated and decayed in the detector simulation package.

In the ZEUS experiment, the detector simulation has been done by the MOZART package based on the GEANT 3.13 package [28]. The MOZART core contains the description of all the ZEUS components, their positions and the material they are made of. The responses of all the components of the detector have been simulated during the track propagation stage of GEANT and afterwards, stored in the same format as the real data. The trigger logic of the experiment is also simulated by the CZAR package [42]. The ZEPHYR package [42] is used to perform the event reconstruction and it is the final step of MC sample production. All the ZEUS data stored in ADAMO database tables [56] which are accessible in user analysis environments like EAZE.

2.8 NLO QCD Calculation

The NLO QCD expectations used in this analysis are calculated by means of the FMNR program [16] incorporated with the FMNR⊗PYTHIA interface [17]. Although FMNR provides a framework to fragment heavy quarks to hadrons and simulate the decay of these hadrons by interfacing them to appropriately chosen spectra, the implementation of complicated final states like a D^*-muon pair is needed. The FMNR⊗PYTHIA interface provides such capability by using the matching of the parton level information generated by FMNR and heavy hadron fragmentation and decay chain descriptions implemented in PYTHIA. The FMNR package is designed to give predictions for PHP. The FMNR prediction is based on the massive approach and NLO processes examples of which are shown in Section 2.5.3. To calculate the NLO prediction of the cross section to be measured in the analysis, the program used the WWA approximation.

The list of the parameters used by the FMNR program is given below.

Charm quark mass $m_c = 1.45$ GeV.

Proton PDFs: CTEQ5M [32].

Photon PDFs: GRV-H HO [33].

$Q^2 < 1$ GeV^2.

Charm production renormalisation scale $\mu = \sqrt{p_T^2 + m_c^2}$.

Charm production factorisation scale $\mu_f = \mu$.

Peterson parameter $\epsilon_c = 0.035$.

2.9 Charm Production Measurements at HERA

In this Section a brief overview of the charm production measurements performed at HERA is given. The HERA collider (see Section 3.1) can be regarded as a charm factory because charm hadrons are produced copiously. It opens ample opportunities to measure different aspects of the SM.

Since the present analysis uses the D^*-muon final state to tag the charm quark pair produced in the hard scattering, this overview is only focused on analyses used single D^* meson or the double tagging D^*-muon technique to measure charm production.

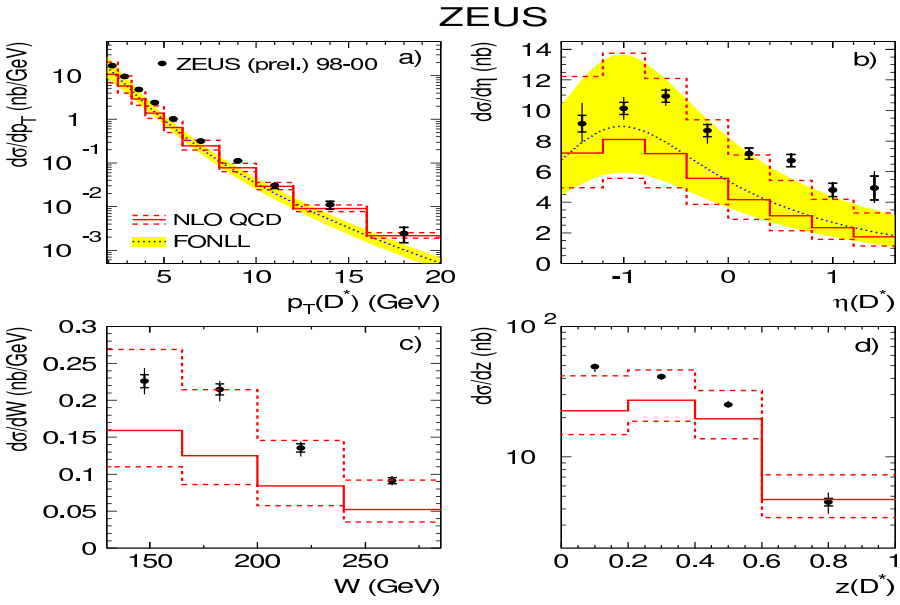

Figure 2.17: Inclusive D^* photoproduction as a function of $p_T^{D^*}$ (a), η^{D^*} (b), W (c) and z^{D^*} (d). The NLO predictions are given by the solid lines. The FONLL calculations are shown by the dotted curves.

Inclusive photoproduction of D^* mesons was measured [85] by the ZEUS detector in the kinematic region $Q^2 < 1$ GeV^2, $130 < W < 285$ GeV, $1.9 < p_T^{D^*} < 20$ GeV, $|\eta^{D^*}| < 1.6$ using an integrated luminosity of 79 pb^{-1}. The measured differential

cross section in bins of $p_T^{D^*}$, η^{D^*}, W and z^{D^*} (the fraction of the photon energy carried by D^* in the proton rest frame) were compared with the NLO (obtained by using the FMNR package) and FONLL (the VFNS NLO calculation [20]) QCD predictions (see Figure 2.17). The structure functions used in both calculations were CTEQ5M1 [32] for the proton and AFG [34] for the photon. The fraction of c quarks hadronising as D^* mesons was set to $f(c \to D^*) = 0.235$. The Peterson fragmentation function was used for the charm fragmentation in both calculations. For the NLO calculations, the Peterson parameter ϵ_c was set to the value 0.035 and for the FONLL calculations $\epsilon_c = 0.02$.

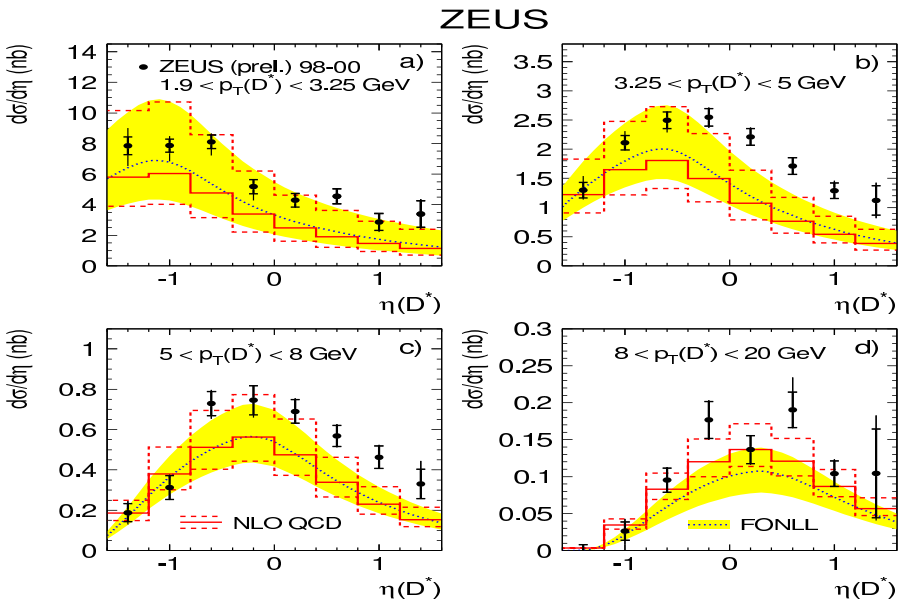

Figure 2.18: Differential cross sections in bins of η^{D^*} for different $p_T^{D^*}$ regions. The NLO predictions are given by the solid lines. The FONLL calculations are shown by the dotted curves.

The precision of the measurement is much better than the theoretical uncertainties. The theoretical uncertainties, which were obtained by simultaneously variation of the charm mass and the renormalisation scale for the FONLL and NLO calculations are large. The NLO prediction reproduces the shape of the $d\sigma/dW$ distribution and the general trend of the $d\sigma/dp_T^{D^*}$. However, the central value of the NLO prediction (as well as the FONLL) is below the measurement over almost the whole kinematic range. The largest differences are seen for low z^{D^*} values, medium $p_T^{D^*}$ and in the forward region ($\eta^{D^*} > 0$), which corresponds to the proton direction. This can be seen in Figure 2.18, where the differential cross sections in bins of η^{D^*} for different $p_T^{D^*}$ regions are given. The FONLL is close to NLO in the low $p_T^{D^*}$ due to inherited properties from NLO, but is below the NLO prediction at high $p_T^{D^*}$.

In the DIS region, the measurement of the charm contribution $F_2^{c\bar{c}}(x, Q^2)$ to the proton structure function $F_2(x, Q^2)$ is performed in the analysis [29] by the ZEUS

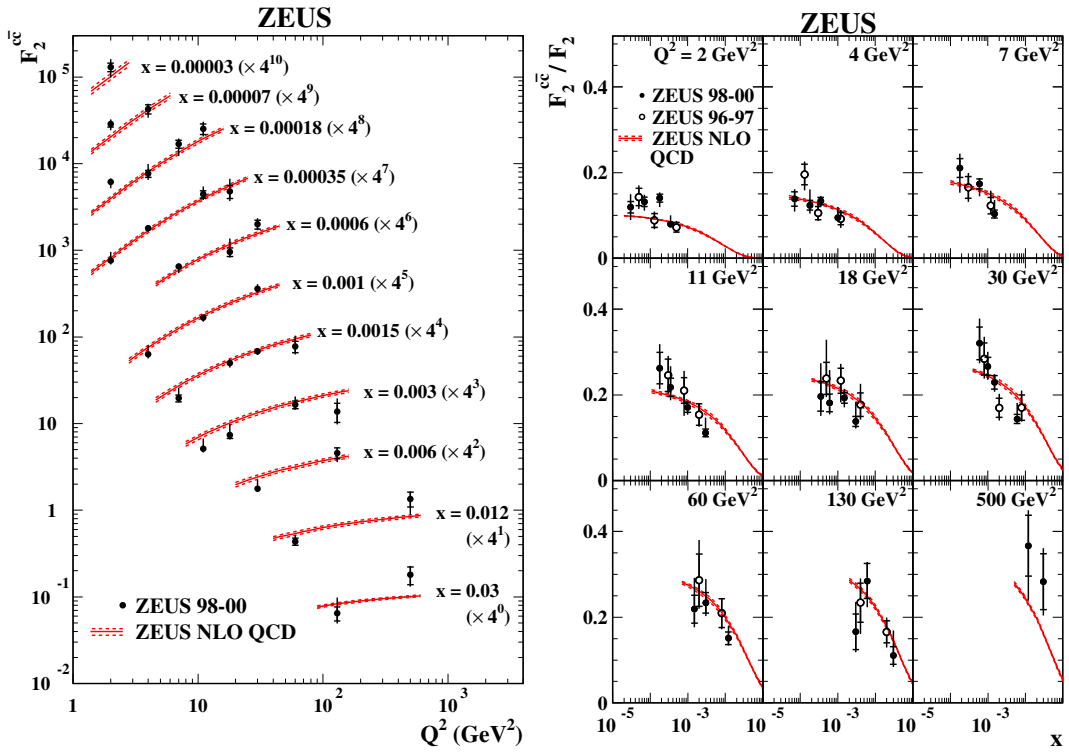

Figure 2.19: The measured $F_2^{c\bar{c}}(x, Q^2)$ (left) and the measured ratio $F_2^{c\bar{c}}(x, Q^2)/F_2(x, Q^2)$ (right) for different Q^2 as a function of x. The NLO predictions are indicated by the solid lines.

experiment. The production of D^* mesons was analysed in this measurement in the kinematic region $1.5 < Q^2 < 1000$ GeV^2, $0.02 < y < 0.7$, $1.5 < p_T^{D^*} < 15$ GeV and $|\eta^{D^*}| < 1.5$ using an integrated luminosity of 81.9 pb^{-1}. The NLO QCD calculations (obtained by using the HVQDIS package [21]) were found to be in reasonable agreement with the measured differential cross sections in bins of Q^2 and x. The extracted $F_2^{c\bar{c}}(x, Q^2)$ were compared with the NLO predictions. This is shown in Figure 2.19 (left). The measurements rise with increasing Q^2. The rise becomes steeper at low x. This is related to the gluon density in the proton because the scaling violation of $F_2(x, Q^2)$ is proportional to the gluon density. The measurements reveal the charm contribution $F_2^{c\bar{c}}(x, Q^2)$ to the proton structure function to be in a range from 10% to 30 % with increasing x (see Figure 2.19 right).

Another interesting measurement [30] was done by the ZEUS experiment in order to investigate the charm content of the photon in the LO picture. In the photoproduction region a significant fraction (40%) of events comes from the resolved photon process. This measurement requires the presence of two jets in the final state and a D^* meson associated with one of them. The differential cross section as a function of $cos\theta^*$ was measured, where θ^* is an angle between the jet-jet axis and the beam direction in the dijet rest frame. The variable x_γ, which is the fraction of the photon momentum contributing to the production of the two jets, is used to identify direct and resolved photon events.

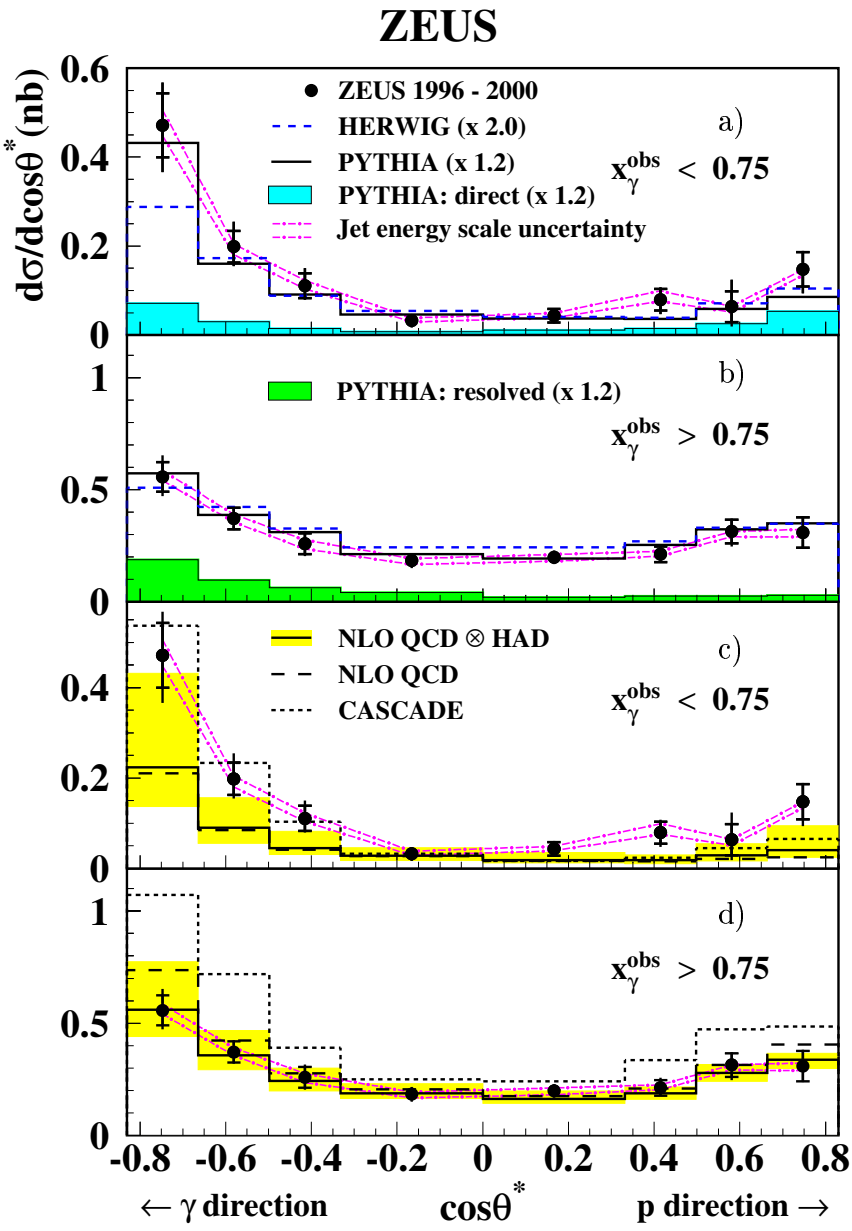

Figure 2.20: Differential cross sections $d\sigma/dcos\theta^*$ compared with MC simulations (a, b) and NLO calculations (c, d) for for resolved-enriched (a, c) and direct-enriched (b, d) samples. The model predictions are normalised to the data.

The differential cross sections were measured for resolved-enriched ($x_\gamma < 0.75$) and direct-enriched ($x_\gamma > 0.75$) samples in the kinematic range $Q^2 < 1$ GeV^2, $130 < W < 280$ GeV, $p_T^{D^*} > 3$ GeV, $|\eta^{D^*}| < 1.5$, $E_T^{jet} > 5$ GeV and $|\eta^{jet}| < 2.4$ using an integrated luminosity of 120 pb^{-1}. The cross sections are sensitive to the propagator of the hard scattering process (see Figure 2.6), where in the case of the gluon propagator the angular distribution is expected to follow $d\sigma/dcos\theta^* \sim (1-cos\theta^*)^{-2}$, whereas in the case of the quark propagator it depends on $d\sigma/dcos\theta^* \sim (1-cos\theta^*)^{-1}$.

In Figure 2.20 the cross section $d\sigma/dcos\theta^*$ is shown with predictions from LO+PS MC simulations for resolved-enriched (top) and direct-enriched (bottom) samples. As it is expected in region of large x_γ only small variation with $cos\theta^*$ is seen in the measurements. The distribution shows a small asymmetry mainly due to the influence of a small contribution of the resolved photon process. In the region of small x_γ, the measurement shows a strong backward asymmetry (the photon direction) due to the dominant process with the gluon propagator. Thus the charm content of the photon can be measured. The MC predictions show in principle good agreement with the data, although some differences in the low x_γ region for the resolved-enriched sample remains.

The NLO prediction (the PDF parameterisations used were CTEQ5M1 for the proton and AFG for the photon, the fraction of c quarks hadronising as D^* mesons was set to f($c \to D^*$) = 0.235, the Peterson fragmentation function was used for the charm fragmentation, the Peterson parameter ϵ_c was set to the value 0.035) obtained by the FMNR package yields a good description of the measurement in the case of large x_γ, but is below the measurement in the small x_γ distribution. The description provided by the NLO calculation might be improved by including even higher order contributions or the PS implementation.

A measurement of charm production very similar to the one in this thesis was performed in the H1 analysis [31], where to tag both charm quarks produced in the hard scattering process the D^* meson and muon in the final state (double tagging technique) are used. The measurement was performed in the kinematic region $Q^2 < 1$ GeV^2, $0.05 < y < 0.75$, $p_T^{D^*} > 1.5$ GeV, $|\eta^{D^*}| < 1.5$, $p^\mu > 2$ GeV and $|\eta^\mu| < 1.735$ using an integrated luminosity of 89 pb^{-1}. The same angular and charge sign correlations of the D^*-muon pair as described in Section 2.6 were used. This measurement does not depend on the reconstruction of jets and is thus capable of accessing a kinematic region of lower invariant mass of the charm quark pair. The visible cross section was compared to the theoretical predictions. These results given below show good agreement within the error.

Data: $\sigma = 250 \pm 57(stat.) \pm 40(syst.)$ pb.

PYTHIA total: $\sigma = 242$ pb.

PYTHIA direct only: $\sigma = 142$ pb.

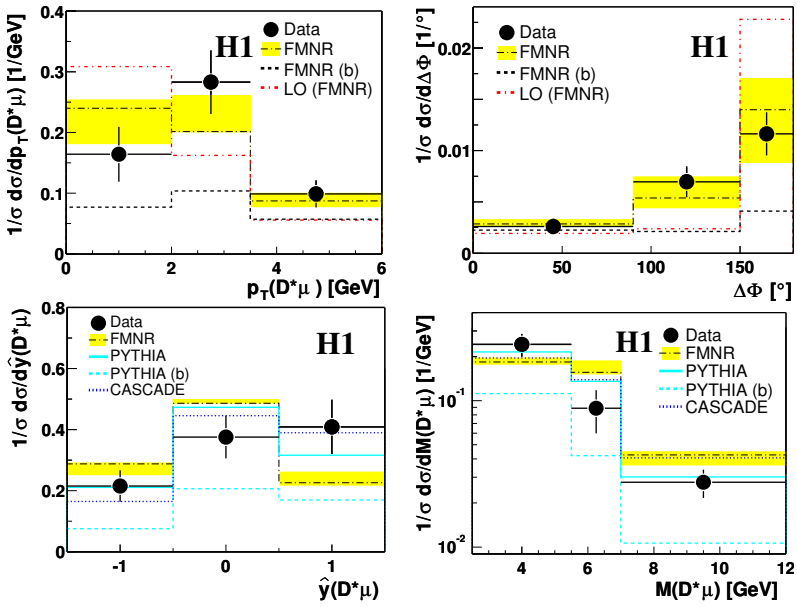

Figure 2.21: Differential cross sections of charm and beauty production in bins of $|p_{T\ v}^{D^*\mu}|$ (top left), $\Delta\phi^{D^*\mu}$ (top right), $\hat{y}^{D^*\mu}$ (bottom left) and $M^{D^*\mu}$ (bottom right) compared with LO MC simulations as well as the FMNR LO and NLO calculations.

$$\text{NLO: } \sigma = 286^{+159}_{-59} \text{ pb.}$$

The differential cross sections of charm and beauty production as a function of $p_{T\ v}^{D^*\mu}$, $\Delta\phi^{D^*\mu}$, the rapidity $\hat{y}^{D^*\mu}$ and the invariant mass $M^{D^*\mu}$ of the $D^*\mu$ pair were measured (see Figure 2.21). The NLO expectations (the PDF parameterisations used were CTEQ5M for the proton and GRV-G HO for the photon, the Peterson parameter ϵ_c was set to the value 0.035) exhibit good agreement with the measurements. The LO+PS MC simulations are also in well agreement with the measurements.

In charm production perturbative NLO QCD calculations provide predictions that are in reasonable agreement with the measurements, although differences between measurements and predictions are still visible, which could be due to additional higher order contributions missing in these calculations. The charm production mechanism still needs to be understood in order to have confidence in understanding all the underlying subprocesses contributing to charm.

The double tagging technique has been also used in the ZEUS analysis [82] to measure beauty production by means of the charge and azimuthal angular correlations (see Section 2.6). In contrast to [82], in this thesis the same technique is exploited to measure charm quark pair production, whereas the beauty contribution is treated as background. Using the unlike-sign configuration and back-to-back topology of D^*-muon pairs as well as the muon reconstruction redundancy, which is provided by the GMUON finder discussed in Section 5.10, charm quark pair production is measured with relatively low muon transverse momentum ($p_T^\mu > 1$ GeV) and wide

muon pseudorapidity range ($|\eta^{\mu}| < 2.2$). The double tagging technique also allows the measurement of the relative fraction of the direct and resolved photon components. The massive approach used in the NLO calculations and LO+PS MC method exploited in the MC event generators are expected to work well in this region and are also tested.

Chapter 3

Experimental setup

This chapter describes the Storage Ring HERA (*Hadron Elektron Ring Anlage*) and the ZEUS experiment at HERA. Details of the most relevant ZEUS detector components for this analysis are given.

3.1 HERA collider

The HERA collider [39] is the largest accelerator at the DESY (*Deutsches Elektronen Synchrotron*) in Hamburg.

Figure 3.1: An aerial view of DESY and HERA.

Figure 3.1 shows an aerial view of DESY with the HERA and PETRA (*Positronen-Elektronen Tandem Ring Anlage*) Storage Rings. The HERA machine is a unique facility built to study proton-electron[1] interactions at a center-of-mass energy of around 300 GeV. That is one order of magnitude larger than available in the previous fixed target experiments. As a consequence, it has been possible to study a new and wider kinematic region of $\{x, Q^2\}$ (see Section 2.2) at HERA (see Figure 3.2).

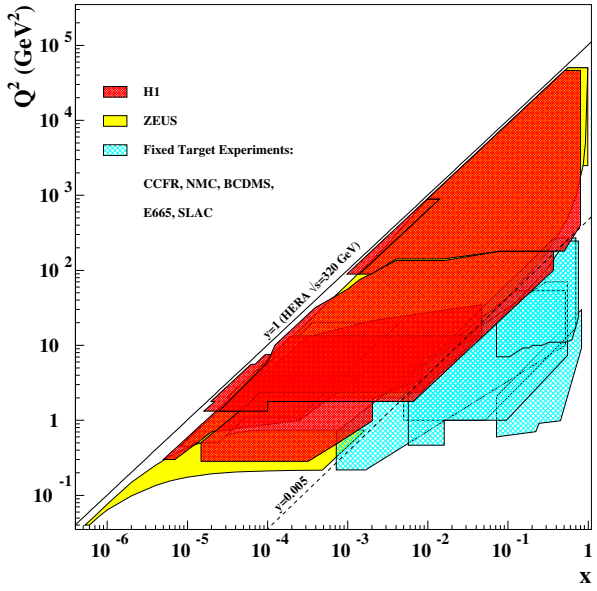

Figure 3.2: The kinematic range in the $\{x, Q^2\}$ plane accessible by fixed target and the HERA experiments ZEUS and H1.

The layout of the HERA machine and its pre-accelerator system and four experimental halls are presented in Figure 3.3. The machine consists of two separate storage rings, one for protons and one for electrons, which circulate in opposite directions. The rings operate at 27.5 GeV and at 920 GeV for electrons and protons respectively. Each storage ring is built up from four 90^o arcs connected by 360 m long straight line sections and is installed in a tunnel about 20 m under ground with 6.34 km circumference. The most important parameters of the HERA machine can be found in Table 3.1.

HERA collides electron and proton beams at the center of the ZEUS (South Hall) and H1 experiments (North Hall). The HERMES experiment (East Hall) uses only the electron beam to study the spin structure of the nucleon in a polarised gas target. The HERA-B experiment (West Hall) was designed to measure CP violation in the decay of B mesons. The experiment stopped operation in the year 2003.

[1]The term *electron* will be used to refer either to electron or positron since the machine can operate with either electrons or positrons

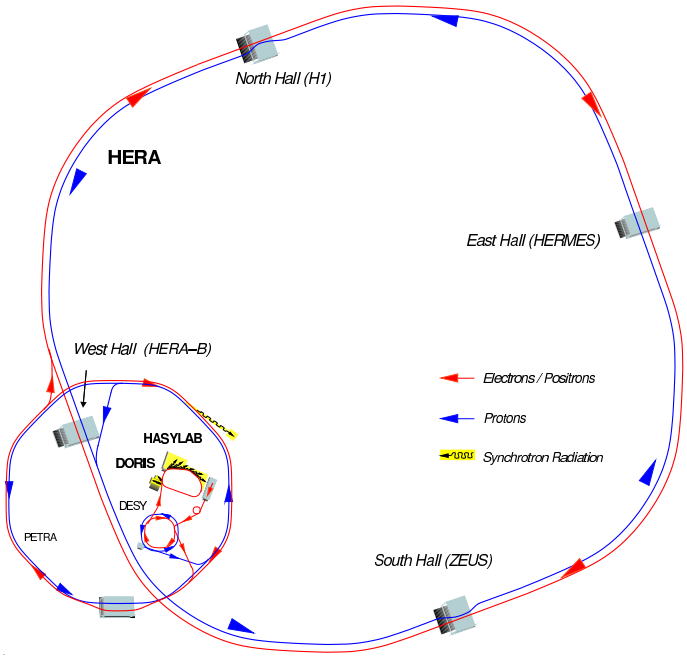

Figure 3.3: The HERA accelerator and its experiments:ZEUS, H1, HERMES and HERA-B.

HERA parameters	1998-2000	
	electrons	protons
Injection energy [GeV]	14	40
Energy [GeV]	27.52	920
Energy loss per turn [MeV]	127	1.4×10^{-10}
Typical beam currents [mA]	58	163
Number of bunches (paired + pilot)	210+10	210+10
Number of particles per bunch	3.65×10^{10}	10^{11}
Beam length at interaction point σ_z [mm]	0.85	19
Beam width at interaction point σ_x [mm]	0.286	0.28
Beam height at interaction point σ_y [mm]	0.06	0.058
Bunch distance	96 ns (28.8 m)	
Center-of-mass energy [GeV]	319	
Specific luminosity [$\mathrm{cm^{-2}s^{-1}mA^{-2}}$]	3.3×10^{29}	
Typical instantaneous luminosity [$\mathrm{cm^{-2}s^{-1}}$]	1.6×10^{31}	

Table 3.1: Typical HERA running parameters and performance during the 1998-2000 running period.

The proton acceleration in the machine starts with the acceleration of Hydrogen ions H^- up to 50 MeV in the linear accelerator (LINAC). The ions are produced by ionising Hydrogen at low temperature. Then the H^- ions are sent to a thin foil to strip off the electrons in order to get a proton beam. The proton beam is injected in 11 bunches to the DESY III storage ring at 96 ns spacing and accelerated up to 7.5 GeV. These bunches are then injected into the PETRA storage ring until 70 bunches are accumulated. In PETRA the bunches are accelerated up to an energy of 40 GeV and injected to HERA. The procedure described above is repeated until HERA is filled with 210 proton bunches. The protons are then accelerated to their final energy of 920 GeV.

The lepton acceleration follows the same scheme as the protons. The acceleration starts with the LINAC, where the leptons are accelerated up to an energy of 450 MeV. The lepton bunches formed are then transfered to DESY II, where they are accelerated to 7 GeV and then injected into the PETRA II storage ring until 70 bunches are accumulated. After accelerating the electrons to 14 GeV, they are finally injected to HERA until 210 bunches are filled.

In order to control the background conditions in HERA, some of these bunches have to be kept unpaired or empty. Unpaired bunches are called *pilot* bunches. They offer a good opportunity to study the beam related background that comes from interactions of the lepton or proton beam with the residual gas in the beam pipe. When either the lepton or proton bunch is empty (unpaired), the beam related background can be studied, whereas when both bunches are empty non-beam-related background could be estimated, such as the rates of cosmic rays. Figure 3.4 shows a schematic view of the bunch distributions.

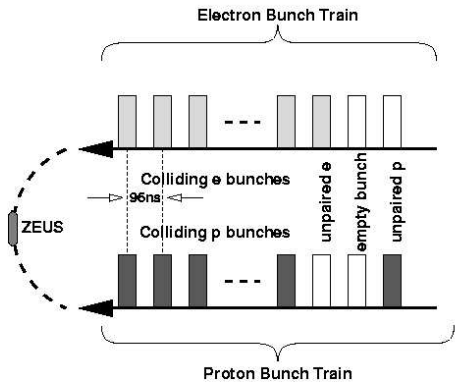

Figure 3.4: Bunch distribution for electrons and protons.

When the bunches interact in the interaction region, protons and electrons have to run in the same orbit in order to collide at zero angle. A total of 123 guiding magnets are used to deflect the proton trajectory from the proton orbit until it is in the same vacuum pipe as the electrons. After passing the interaction point the

proton trajectory is brought back to the level of the proton ring.

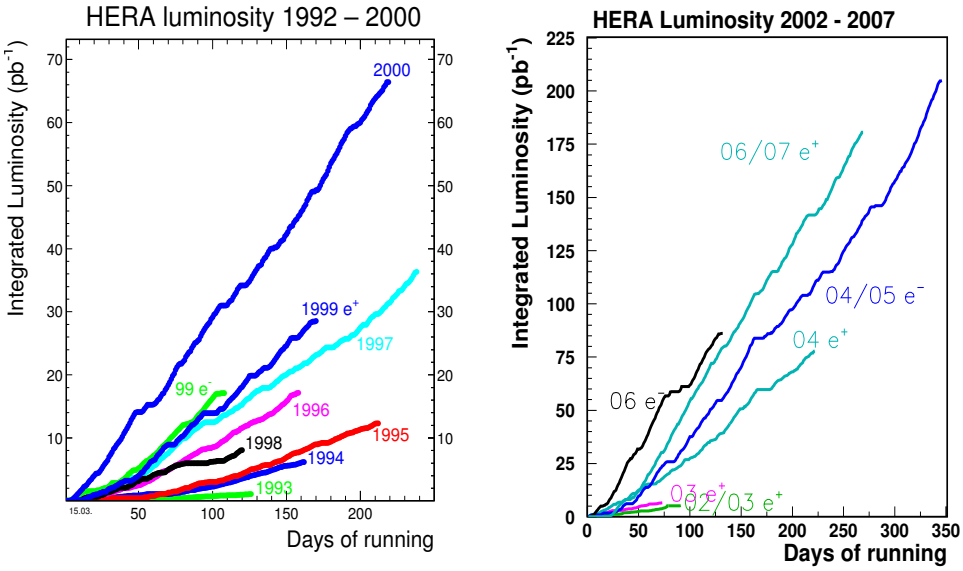

Figure 3.5: The integrated luminosity as delivered by HERA in each operating year as a function of running days.

In the years 1996-1997 the proton beam energy was 820 GeV. In 1998 the proton beam energy was changed from 820 GeV to 920 GeV. In the year 2000 HERA completed its first running period (HERA I). Starting from year 2001, important upgrade modifications were made [40]. Superconducting beam focusing magnets were installed near the interaction points at ZEUS and H1. These are designed to improve the instantaneous luminosity by a factor of five. In addition, the electron beam was polarised longitudinally. The detectors of ZEUS and H1 were upgraded with new detector components in order to make best use of the higher luminosity. In 2002, HERA started its last run period (HERA II), which, will end in summer 2007. The collected luminosity for both running periods is shown in Figure 3.5. In this thesis the dataset corresponding to the HERA I running period is used.

3.2 ZEUS detector

The ZEUS detector [41, 42] is a multi-purpose detector designed to study various aspects of lepton-nucleon scattering. It was built by the ZEUS collaboration in the late 1980s. In the beginning of the 1990s it was installed in the South hall of the HERA tunnel. The experiment started operation in 1992, when first interactions were recorded. The detector has a weight of about 3600 tons and its dimensions are 12 m×10 m×19 m. Figure 3.6 gives a 3D view of the ZEUS detector.

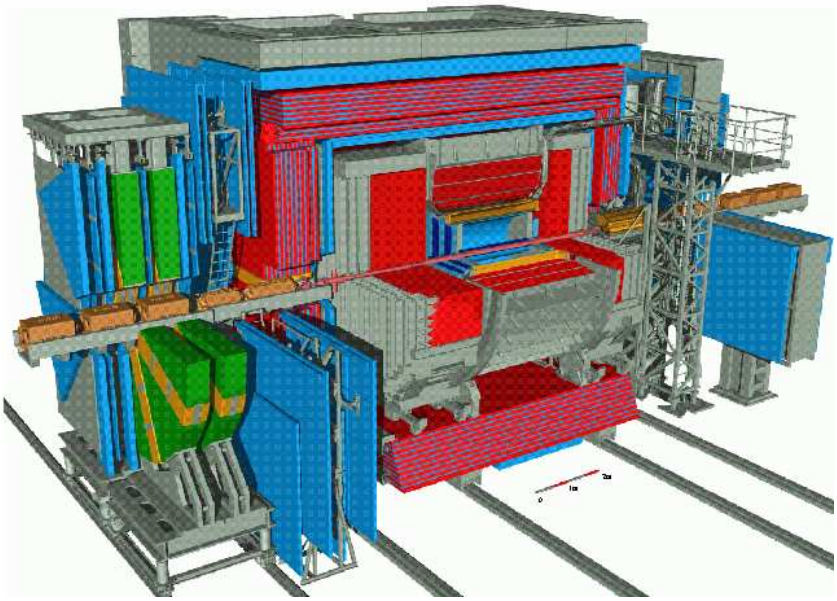

Figure 3.6: 3D view of the ZEUS experiment showing the main components.

In the ZEUS coordinate system (see Figure 3.7) the direction of the outgoing proton beam defines the direction of the Z axis with the origin at the nominal interaction point. The direction from the interaction point to the center of the HERA Storage Ring defines the positive X axis. The Y axis is then defined such as to complete a right-handed orthogonal coordinate system. In spherical polar coordinates, the polar angle θ is defined with respect to the Z axis, while the azimuthal angle ϕ and radius ρ are defined in the $X - Y$ plane with respect to the X axis.

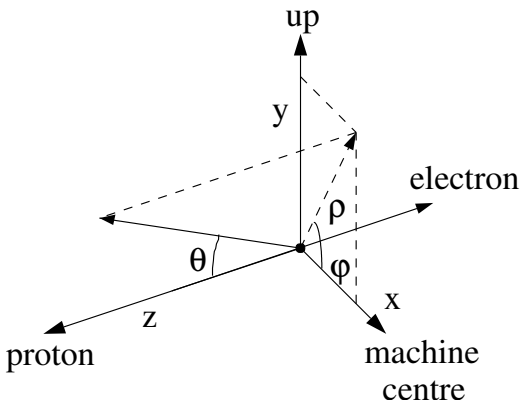

Figure 3.7: The ZEUS coordinate system.

The ZEUS detector covers most of the 4π solid angle with the exception of regions around the beam pipe. The layout of the detector is shown in the $\rho - \phi$ plane in Figure 3.8 and in Figure 3.9 in the $Z - Y$ plane. The asymmetric shape of the detector

layout is due to the huge energy difference of the electron and proton beams. As a consequence of this difference, the final state particles produced in electron-proton collisions are predominantly boosted to the forward direction.

The detector provides the capability to measure final state particles with momenta from tens of MeV to hundreds of GeV.

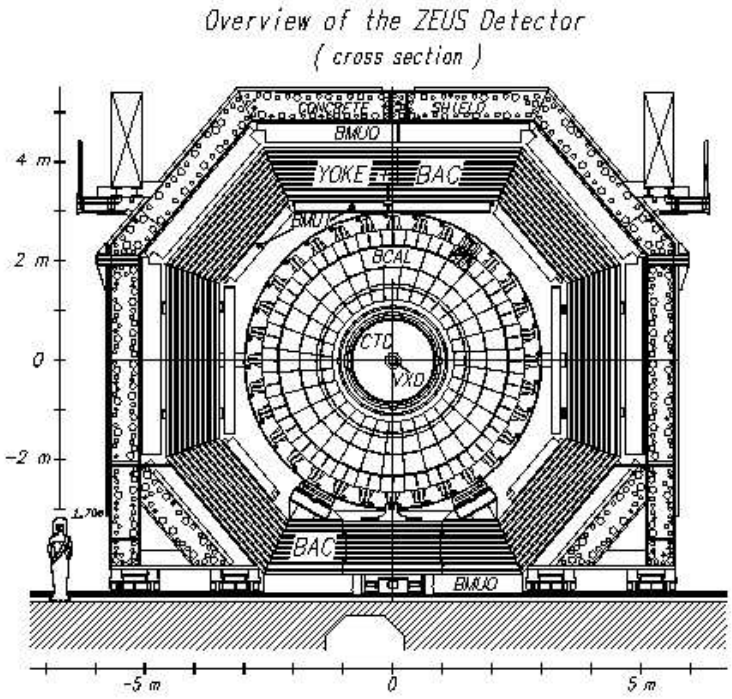

Figure 3.8: Cross Section of the ZEUS detector in the $\rho - \phi$ plane.

The innermost part of the ZEUS detector around the beam pipe is covered by a Silicon Strip Micro Vertex Detector (MVD) [43]. It was installed during the shutdown in 2000 at the same place (see on Figure 3.8 and Figure 3.9) as the earlier Vertex Detector (VXD), which was removed after 1995 due to high beam background. The central Tracking Detector (CTD) [45] is a gaseous drift chamber, which surrounds the interaction point, including the MVD. Those two components form the central tracking system, which is enclosed by a super-conducting solenoid producing a magnetic field of 1.43 T parallel to the beam pipe. The tracking system provides high precision tracking measurements and can measure momentum and charge of final state particles with high accuracy.

In the forward region, the tracking system is supplemented by three sets of planar drift chambers (FTD) with the transition radiation detector (TRD) in between. The TRD was replaced during the shutdown in 2000 by a Straw Tube Tracker (STT) [47].

Together with a Rear Tracking Chamber (RTD), these components provide extra tracking information and particle identification in the forward and rear directions. Since the dataset corresponding to the HERA I running period is used in this thesis, the MVD and STT information is not available.

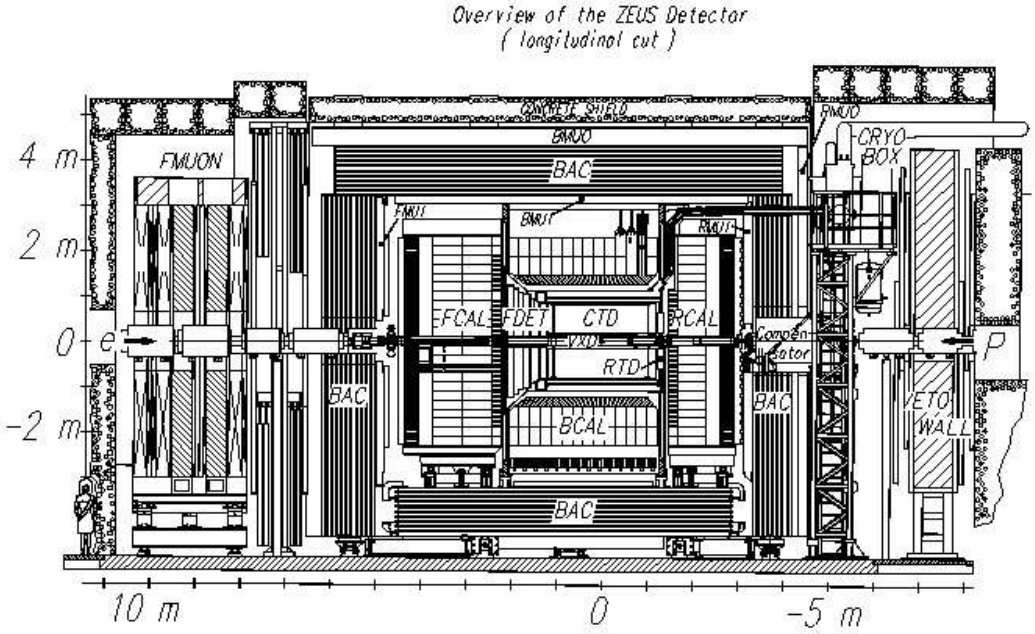

Figure 3.9: Cross Section of the ZEUS detector in the $Z - Y$ plane.

The tracking system is surrounded by a calorimeter, which is a compensating high-resolution uranium-scintillator calorimeter (CAL) [48]. The CAL is the main instrument to measure the energy of electrons and hadrons. It is separated into three sections: the FCAL in the forward region, the RCAL in the rear section and the BCAL, which is a barrel section in the central region. In front of the RCAL, BCAL and FCAL are presampler detectors RPRES, BPRES and FPRES [49].

A Small Angle Rear Tracking Detector (SRTD) [50] is installed in the front of the RCAL in an area of 68×68 cm^2 around the beam pipe for reconstruction of the electron kinematics with high accuracy, especially for the case, when the primary electron is scattered under a small angle.

The CAL is enclosed by an iron yoke, which provides the return path for the solenoid magnetic field flux. The yoke is magnetised to 1.6 T by copper coils and instrumented by proportional chambers (BAC) [51] in order to measure energy leakage out of the CAL. Muon identification chambers [42, 52] are installed behind and in front of the BAC in the forward (FMUO, FMUI), barrel (BMUO, BMUI) and rear (RMUO, RMUI) regions. Together with the muon chambers, the BAC is used for

better muon reconstruction.

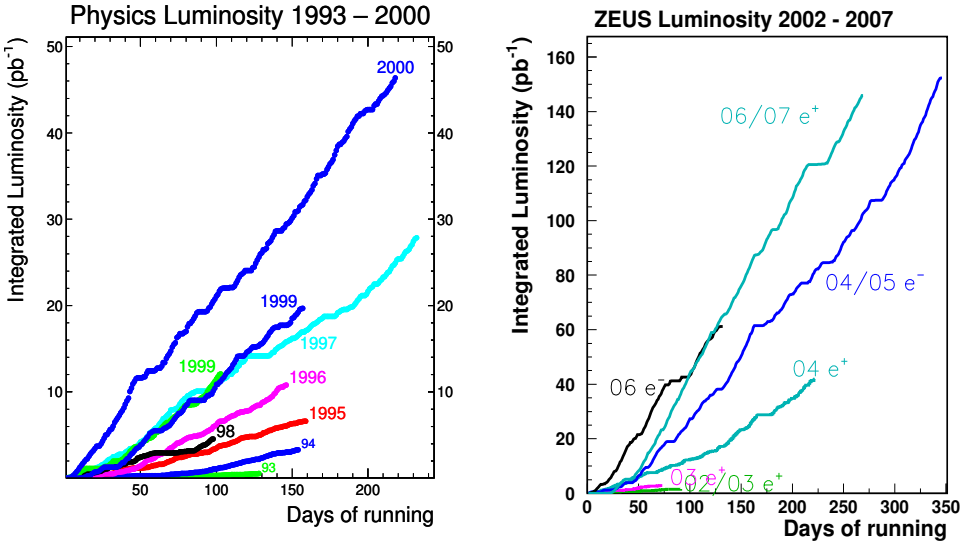

Figure 3.10: The integrated luminosity delivered by HERA and gated by the ZEUS experiment in each operating year as a function of running days.

In the rear direction, at $z = -7.5$ m, the VETOWALL detector [42] composed of iron and scintillator is used to reject beam-related background. A small lead/scintillator counter (C5) located around the beam-pipe at $z = -3.15$ m is used to monitor the beam conditions and to measure the timing and the longitudinal structure of the proton and electron bunches.

There are several detector components close to the beam line, which address various more specialised topics. The most important of those is the luminosity measurement system (LUMI), which consists of two small calorimeters at $z = -34$ m and $z = -107$ m. It measures photons and electrons from the bremsstrahlung process $ep \rightarrow ep\gamma$ for which the cross section is well known and is used to determine the luminosity. In Figure 3.10 the ZEUS integrated luminosity is shown for two running periods (HERA I and HERA II). In this analysis, the HERA I dataset is used.

3.2.1 Micro Vertex Detector (MVD)

The Silicon Strip Micro vertex Detector [43] was installed in ZEUS during the shutdown in 2001. The detector significantly improves the global precision of the ZEUS track reconstruction and the acceptance in the forward region. It allows efficient identification of long-lived ($c\tau \approx 100$ μm) heavy flavour particles by their impact parameter reconstruction. In this thesis the MVD hit information is only used in the Forward GTT vertex finding algorithm (technical task) described in Section 4.

The design of the MVD has been dictated by the physics requirements and restricted available space between the beam pipe and the CTD:

- radial size smaller than 32.4 cm (the CTD inner volume),
- polar angle coverage between 10^o and 150^o,
- hit resolution for normal incident tracks smaller than 20 μm,
- two track separation of 200 μm,
- three points per track in two projections each,
- hit efficiency better than 95%,
- noise occupancy better than 10^{-3}.

The MVD is divided into three parts: Barrel MVD (BMVD), Forward MVD (FMVD) and Rear MVD (RMVD) [44]. The RMVD is only used for cabling, monitoring and readout system. No sensitive detecting sensors are installed there.

The BMVD is 64 cm long and covers the extended interaction region, where the average longitudinal event vertex is located due to the proton bunch length (20 cm.). The polar angle acceptance of the BMVD is between 30^o and 150^o. The BMVD consists of three layers of double silicon strip sensors (barrel modules) mounted on *ladders* parallel to the beam pipe. Cross sections of the MVD along the beam pipe (left) and in the $X-Y$ plane (right) are shown in Figure 3.11. The three layers are arranged in concentric cylinders (Cylinder 0, 1 and 2) around the beam pipe. The internal layer is not complete due to the elliptic shape of the beam pipe which is not centered around the interaction point.

The BMVD single sided silicon sensors have a quadratic shape (64.2×64.2 cm^2) and 320 μm thickness. They are arranged in half modules with strips parallel and perpendicular to the beam pipe (see Figure 3.12). Two half modules are placed on top of each other to form a module (double silicon strip sensors) with 1024 readout channels. This configuration allows to reconstruct a track hitting the module in two projections. The ambiguity due to the strip readout connections can be solved by full track reconstruction later.

The FMVD covers the polar angle range between 10^o and 30^o. It consists of four wheels of back to back layers with silicon strip sensors. The sensors are mounted on layers perpendicular to the beam pipe (see Figure 3.13).

The FMVD single silicon sensors are of the same type as the barrel sensors but they have a trapezoidal shape with strips parallel to one tilted edge and contains 480 readout channels (see Figure 3.14). The two overlapping sensors of the wheel

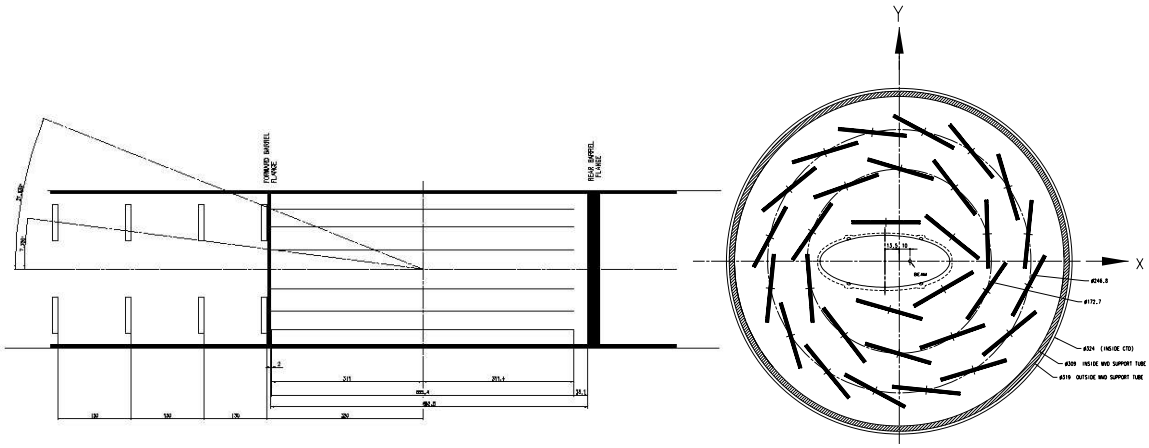

Figure 3.11: Cross sections of the MVD along the beam pipe (left) and in the $X - Y$ plane (right).

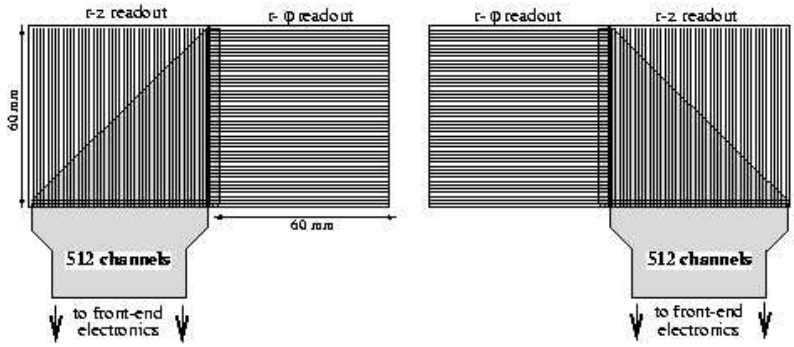

Figure 3.12: The two BMVD half modules with readout.

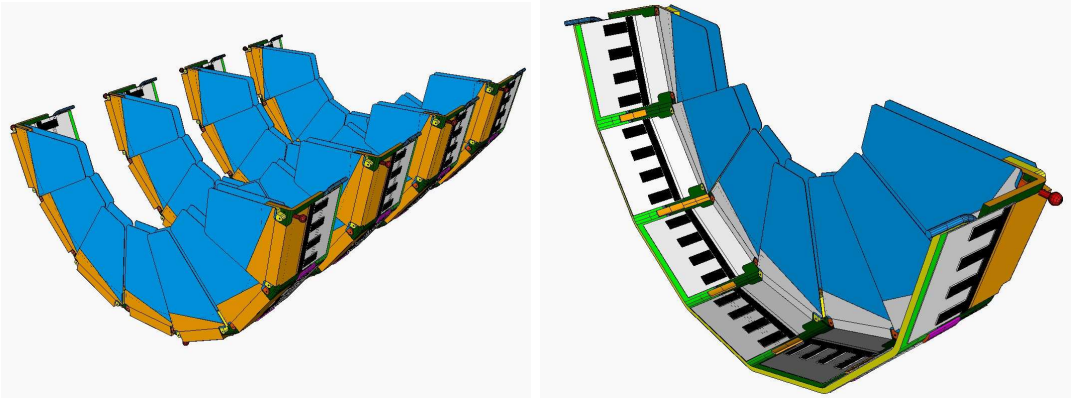

Figure 3.13: The FMVD (left) and the wheel (right) with support structure.

form a module (double silicon strip sensors) providing two coordinates of a particle track traversing the module.

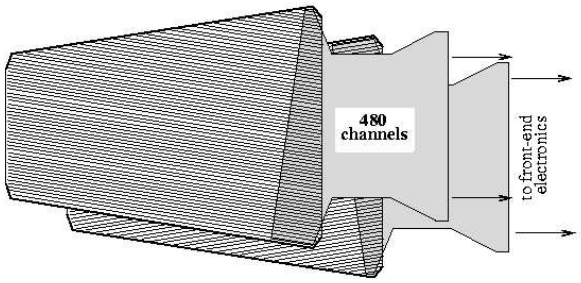

Figure 3.14: The FMVD module with readout.

3.2.2 Central Tracking Detector (CTD)

The CTD [45] is a key component of the ZEUS experiment. It is used to measure trajectories and transverse momenta of charged particles traversing its fiducial volume with a high precision. In addition, it provides information about energy loss (dE/dx) to identify particles.

The CTD is a cylindrical drift chamber with a length of 205 cm, an inner radius of 18.2 cm and outer radius of 79.4 cm, arranged around the nominal interaction point. It covers the polar angle range between 11.3^o and 168.2^o. It is composed of 72 radial layers of anode wires, grouped into 9 *superlayers*. Eight radial sense wires with the associated field wires are combined into a *cell*. The CTD is divided in the $X-Y$ plane into eight octants. Figure 3.15 shows the layout of a CTD octant. Layers with even numbers are inclined at angles around 5^o relative to the beam direction. These stereo layers provide a method of determining the Z coordinate of a track trajectory. Depending on the number of superlayers traversed, the resolution provided by the stereo layers in the Z-direction is approximately 2 mm. For trigger purposes, the so-called $z-by-timing$ information is used, in which superlayers with odd numbers determine the Z-vertex position from timing information with a resolution of $\sigma_z = 4{-}12$ cm, depending on the track multiplicity of the event. The CTD volume is filled with a gas mixture of argon (Ar), carbon dioxide (CO_2) and ethane (CO_2H_6) with a proportion of $85:5:1$.

When a charged particle traverses the CTD sensitive volume, it ionises the gas atoms and produces ion-electron pairs on its trajectory. To prevent recombination of the ion-electron pairs to chargeless atoms, a high voltage is applied. The electrons drift towards the sense wires (positive) with a velocity of approximately 50 μm/ns, whereas the positively charged ions drift towards negative field wires. In the field of the sense wires, at a distance about the wire radius, an avalanche process is started,

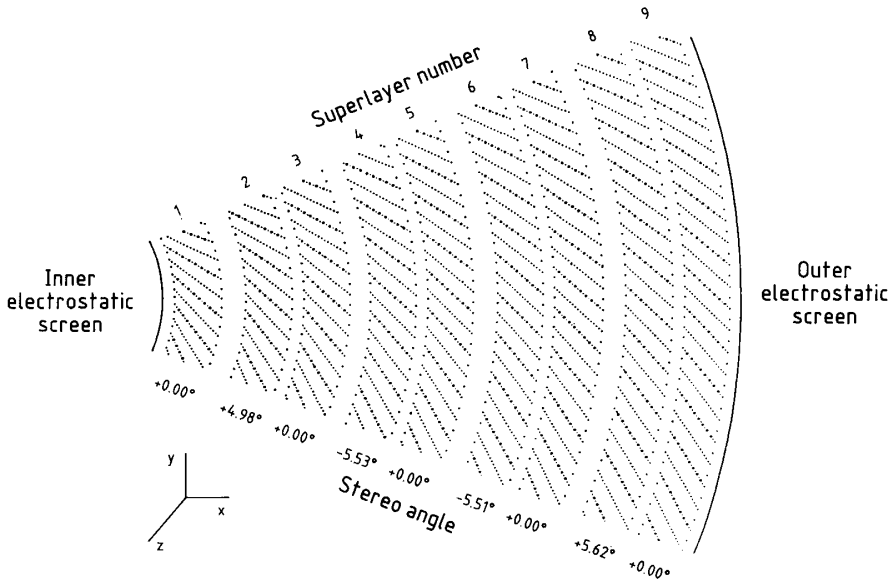

Figure 3.15: Layout of a CTD octant. The superlayers are numbered and the stereo angles of their sense wires are shown.

which produces a multiplication of electrons by a factor of 10^4.

The resolution in the $\rho - \phi$ plane is about 220−240 μm (depending on the polar angle θ). For tracks originating from the interaction vertex with transverse momentum $p_T > 150$ MeV, passing at least three CTD superlayers, the relative transverse momentum resolution [46] is:

$$\frac{\Delta p_T}{p_T} = 0.0058 \cdot p_T \oplus 0.0065 \oplus \frac{0.0014}{p_T}. \tag{3.1}$$

The sign $\oplus$ means the squared sum and p_T is measured in GeV. The first term is the hit position resolution, while the second and third terms depend on the multiple scattering inside and before the volume of the detector respectively. From the CTD alone, the interaction vertex is measured for events containing at least one CTD track with a typical resolution along (transverse) to the beam direction of 0.4(0.1) cm.

3.2.3 Calorimeter (CAL)

The ZEUS CAL [48] is a sandwich uranium-scintillator hermetic[2] calorimeter. It is divided into tree sections: the forward FCAL, barrel BCAL and rear RCAL calorimeters. The three parts of the calorimeter cover the pseudorapidity regions of:

- -3.49 to -0.72 for the RCAL,

[2]The CAL covers more than 99.6% of the total solid angle except regions around the beam pipe in the RCAL and FCAL.

- -0.74 to 1.10 for the BCAL,
- 1.01 to 3.95 for the FCAL.

Both the FCAL and BCAL have two hadronic calorimeter (HAC) layers: HAC1 and HAC2, and a third innermost layer forming the electromagnetic calorimeter (EMC). The RCAL contains only one HAC layer and one inner EMC layer. An overview of the calorimeter layout is shown in Figure 3.16. The asymmetry in the design of the CAL is due to the boosted system in the forward region.

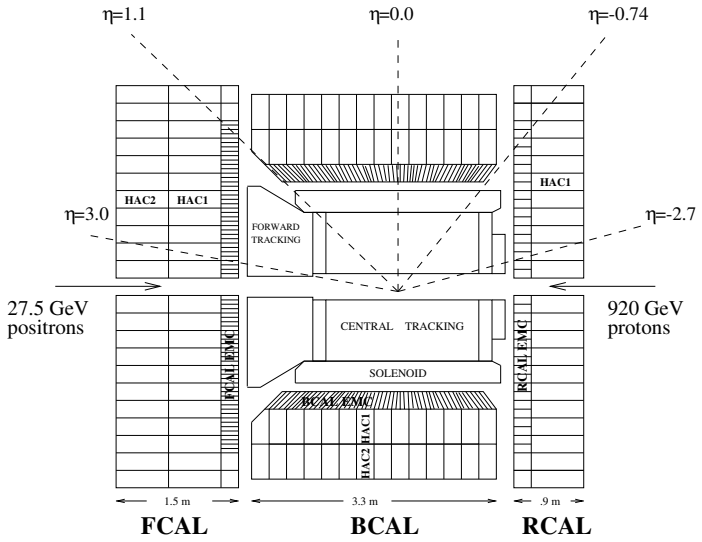

Figure 3.16: Cross section of the ZEUS CAL in the $Y - Z$ plane.

The CAL layers are composed of cells. In the FCAL and BCAL, the EMC and HAC cells have transverse dimensions of 5×20 cm^2 and 20×20 cm^2 respectively. In the RCAL, the cell size is 10×20 cm^2. In the FCAL and BCAL, a HAC1 cell together with a HAC2 cell and four EMC cells form a *tower*. In the RCAL, each HAC cell is combined with two EMC cells to form an RCAL tower. Linear groups of towers are then combined into *modules* (see Figure 3.17).

A cell is composed of layers of absorber[3], with a thickness of 3.3 mm, interleaved with 2.6 mm plates of plastic scintillator[4]. This combination of the thickness is chosen in order to achieve a compensating calorimeter, where the response to hadrons and electrons is equal ($e/h = 1$) over a wide range of energies. The scintillation light is guided to photomultiplier tubes (PMTS) by wavelength shifters. The cell is read out by two identical PMTS (see Figure 3.17).

[3]The absorber is made of 98.4% U^{238},1.4% Nb and less than 0.2% U^{235}.
[4]SCSN38.

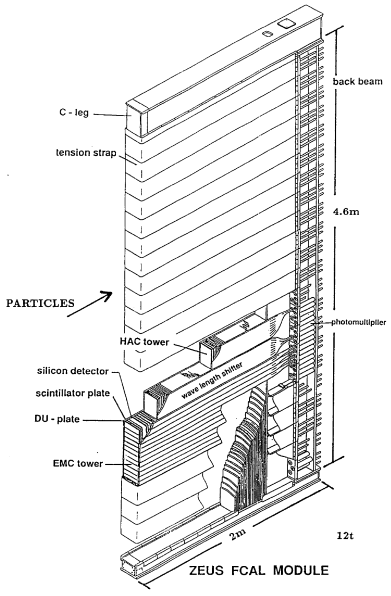

Figure 3.17: View of an FCAL module. The towers containing the EMC and HAC sections are shown.

The CAL energy resolution measured under test beam conditions is:

$$\frac{\sigma(E)}{E} = \frac{35\%}{\sqrt{E}} \oplus 2\% \tag{3.2}$$

for hadrons and

$$\frac{\sigma(E)}{E} = \frac{18\%}{\sqrt{E}} \oplus 1\% \tag{3.3}$$

for electrons with the energy E measured in GeV.

The EMC thickness corresponds to approximately 25 (21 in the BCAL) radiation lengths (X_0) for electromagnetic showers or approximately one interaction length (λ) for hadronic interactions. The total thickness of each calorimeter section varies (to reflect the lopsided event geometry) from 7.1λ in the FCAL, to 5.3λ in the BCAL and 4λ in the RCAL.

The CAL provides timing information for energy deposits at a resolution of approximately 1 ns for energy deposits over 4.5 GeV. This allows to efficiently reject beam gas and cosmic ray backgrounds.

3.2.4 Backing Calorimeter (BAC)

The backing calorimeter (BAC) [51] is a gaseous[5] detector composed of aluminium modules instrumented by 7 or 8 detecting cells of a cross section of 11×15 mm each

[5] $Ar - CO_2$ gas mixture used.

and a length of 1.8−7.3 m. Gold plated tungsten wires with diameter of 50 μm are stretched in the cell centers and supported every 50 cm in the longitudinal direction. Aluminium cathodes of length 50 cm are mounted on top of the modules. The modules are installed inside the return yoke used as an absorber (see Figure 3.9). The wires are read out on one side and provide both analog and digital signals. The pads have only an analog readout. Energy is measured by summing up the analog signals from the wires grouped in addition into towers of a width of 25−50 cm (2−4 modules) over the full depth of the BAC. The pads of 2−4 neighbouring modules are added to pad towers with an area of 50×50 cm^2 (4 modules) similar to the wire towers. They provide a measurement of the location of the energy deposit along the wires. The signals from the wires provide patterns of hit positions in the BAC to reconstruct muon trajectories.

The BAC can recognise events with showers leaking out of the CAL (e.g. high energy jets penetrating the CAL) to veto or to correct them later. It can distinguish between hadron and muon showers and provides muon identification and trigger capabilities in the bottom yoke and other areas poorly covered by the muon identification chambers. A summary of the BAC modules is given in Table 3.2.

	Barrel	Bottom	Forward	Rear
Area [m^2]	1902	296	460	322
Number of layers	9	9	10	7
Gas volume [m^3]	38.0	5.9	9.2	6.4
Number of 8-tube modules	2246	193	840	572
Number of 7-tube modules	658	120	280	112
Module length [m]	4.5 and 5.5	7.3	1.8 - 3.6	1.8 - 3.6
Number of wires	22574	2384	7980	5360
Wire towers	100	10	32	36
Pad towers	1100	150	222	230

Table 3.2: Summary of BAC modules.

The BAC spatial resolution perpendicular to the wires is about 1 mm. The longitudinal resolution defined mainly by the pad size is about $50/\sqrt{12}$ cm. The energy resolution determined by test beam measurements is given by the following formula:

$$\frac{\sigma(E)}{E} = \frac{1.1}{\sqrt{E}}, \tag{3.4}$$

where E is the particle energy in GeV

3.2.5 Straw Tube Tracker (STT)

During the upgrade after the year 2000, the Straw Tube Tracker (STT) [47] replaced the TRD formerly placed in between the planes of the FTD (see Figure 3.18 left). In

this thesis the STT hit information is only used in the Forward GTT vertex finding algorithm described in Section 4.

With its fine granularity, the STT is designed to significantly improve track reconstruction in the forward region. The tracker covers the polar angle range between 7^o and 25^o. It consists of two modules (STT1 and STT2) containing four *superlayers*, each perpendicular to the Z axis. Each superlayer is built of six sectors with trapezoidal shape. The four superlayers are rotated by 0^o, 30^o, $+15^o$ and -15^o in the $X-Y$ plane of the ZEUS coordinate system (see Figure 3.19). Each sector contains straws glued into a three layer structure providing mechanical stability for the tracker. The number of straws per sector varies between 196 and 280 depending on the Z position of a sector to match angular acceptance.

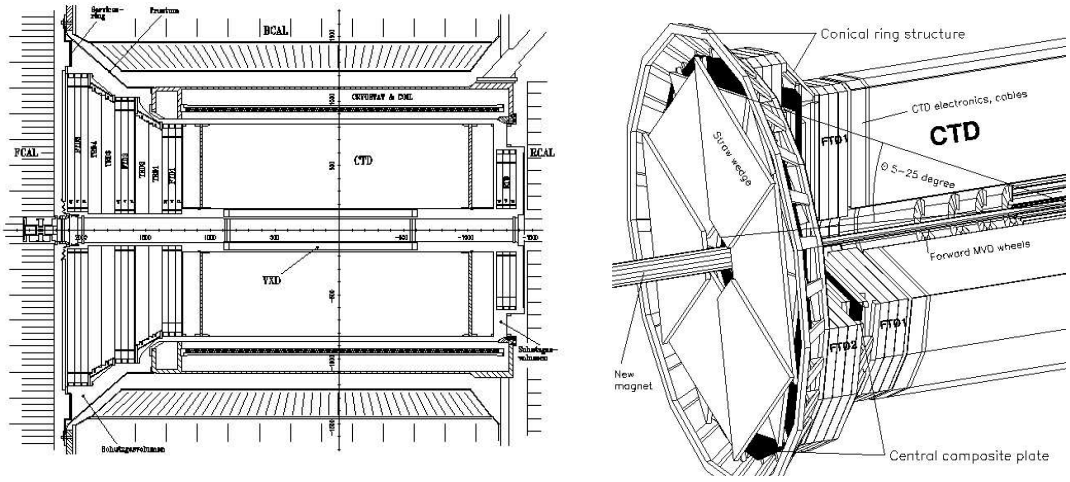

Figure 3.18: Cross Section (left) and 3D view (right) of the ZEUS tracking system.

The straw is a gaseous cylindrical proportional chamber made of two layers of 50 μm Kapton foil with a wire stretched in the center of the tube. It is filled by a gas mixture of 80% : 20% $Ar : CO_2$ in order to provide good efficiency (98%) and resolution ($\approx$ 200 μm) of the straw tube.

The most important features of the straw tube are:

- Good electrostatic stability,
- Constant drift velocity,
- The self-supporting property of the straw tube,
- The total radiation length of the STT is about 15%,
- Good radiation hardness ($>$ 2 C/cm),

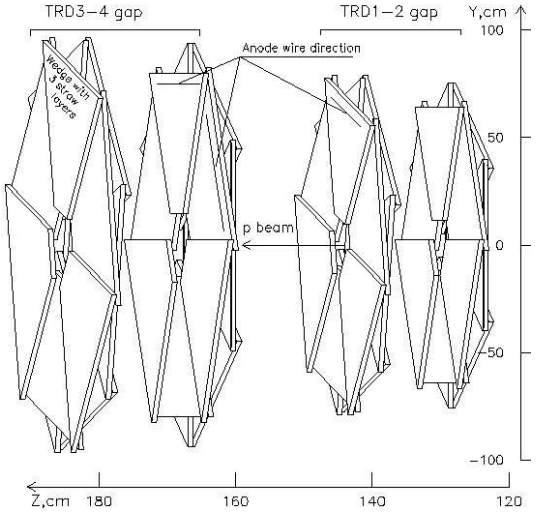

Figure 3.19: 3D view of the STT sectors.

- Low cost and simplicity of the straw production.

The STT is able to find tracks with high efficiency. A combination of this track information with information from the CTD and MVD provides high precision track reconstruction. Since the tracker can be used to reconstruct the event vertex position and tracks of charged particles, it is also used in the ZEUS trigger. This is particularly important for events in which no CTD track reconstruction information is available.

3.2.6 Muon System (MUON)

Muons are minimum ionising particles (MIP). They can penetrate large amounts of material without being absorbed. The muon identification system [42] uses the large amount of material provided by the CAL and the yoke as a muon filter. Therefore, the muon detectors are mounted in front of and behind the magnetised iron yoke. Such a design provides the capability to measure muon tracks produced at the nominal interaction point and reaching the muon detectors. Depending on the polar angle of the muons, the average muon momentum varies between a few GeV (the barrel and rear region) and 10 GeV (the forward region) due to the asymmetric nature of the electron-proton collisions at HERA. The muon detection system is split into two sub-detectors, the forward (FMUON), barrel (BMUON) and rear (RMUON) muon detectors.

3.2.6.1 Forward Muon Detector (FMUON)

The forward muon detector [42] is split into two modules. The inner module (FMUI) of the FMUON is located in the front of the iron yoke. The position of the outer part

(FMUO) is behind the yoke. Together with the BAC located inside the magnetised yoke the muon detectors form the muon identification system, which can reconstruct the muon tracks and measure the muon momentum (see Figure 3.20).

The FMUON is composed of:

- A system of four planes of limited streamer tube (LST) trigger planes (LST1 - LST4) with digital azimuthal ϕ and radial ρ readout,
- Two large angle planes of limited streamer tubes with digital (ρ, ϕ) and analog (ρ) readout in the large polar angle region (LW1,LW2),
- Four planes of drift chambers (DC1 - DC4),
- Two large toroidal iron magnets with a magnetic field of 1.7 T for the momentum separation and measurement in the polar angle region between 5^o and 16^o.

The first planes LST1 and DC1 form the FMUI detector. The rest is combined into the FMUO detector.

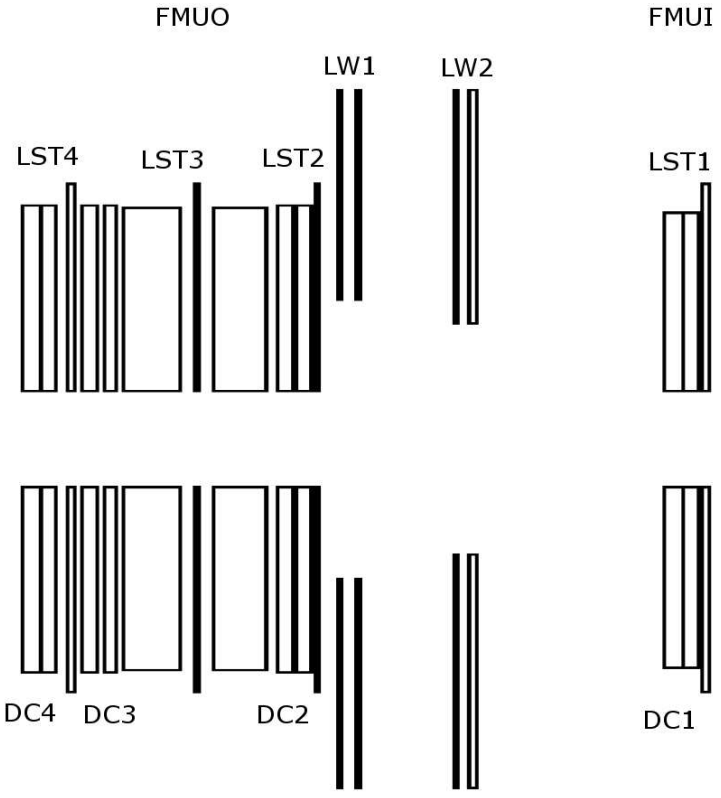

Figure 3.20: Schematics layout of the FMUON detector.

The goal of the LST planes is to trigger on a muon candidate and to reconstruct its position in terms of the azimuthal and radial coordinates of the track. A trigger plane is made of four LST chambers combined to two half planes. A quadrant contains two layers of LST positioned horizontally inside a plastic sheet. The tubes of the two planes are slightly displaced by 0.5 cm in order to achieve complete geometrical acceptance. Each quadrant is contained in an aluminium air tight box. On the outer side, copper strips are glued in polar geometry. The LSTs induce a signal in the copper strips when a particle crosses the plane. The number of radial strips is 132 while each strip is 1.9 cm wide. They are divided along the bisector of the quadrant so that the simplest unit of the trigger plane to be read out is an octant. The number of strips is 32 per octant. Each strip covers an interval of 1.4^o in the azimuthal angle.

The drift chambers are used in order to obtain a good momentum resolution. Each plane contains four chambers grouped two by two in two half planes fixed on a support panel. The basic element of the chamber is the *cell* made of four sense wires, and the layers needed to generate the appropriate electric field. The four sense wires measure the radial coordinate. The information gathered by the wires are sent to a TDC, which converts them into a time interval related to the drift distance by a known relation.

The two large angle coverage planes (LW) are used in order to achieve the desired geometrical acceptance also in the region left uncovered by the toroids ($16^o < \theta < 32^o$). Each plane contains eight air tight aluminium wrappings that contain a LST layer. The LST signal is induced on copper strips with radial geometry spaced of 0.7 cm in the coordinate and of 1.8 cm in the coordinate. The number of strips is 64 per octant while the strips are 192 per octant. The achieved resolution in the coordinate, using a center of gravity algorithm, is 1 mm.

3.2.6.2 Barrel (BMUON) and Rear (RMUON) Muon Detector

The barrel and rear muon detector [52] covers a very large area (2000 m^2) and is instrumented by LST chambers. The chambers covering the inner barrel part between the CAL and the iron yoke are called BMUI, while the chambers located outside the yoke are denoted as BMUO. The RMUON is divided into RMUI and RMUO chambers in a similar way (see Figure 3.21).

The chambers have different shapes and dimensions depending on their location, but with the same internal structure. The supporting structure of each chamber is an aluminium honeycomb frame 20 cm thick in the rear chambers and 40 cm in the barrel ones. Two planes of LST are placed on both sides of the honeycomb. The two layers on the same side of the chamber are displaced by 8.3 mm in order to minimise dead areas for particles traversing at 90^o with respect to the wire plane. Each LST is made of a plastic profile with eight cells. In each cell a copper-beryllium wire of 100 μm diameter is stretched. The distance between two sense wires is 1 cm. Each LST plane is equipped on one side by 13 mm wide readout strips with 15 mm

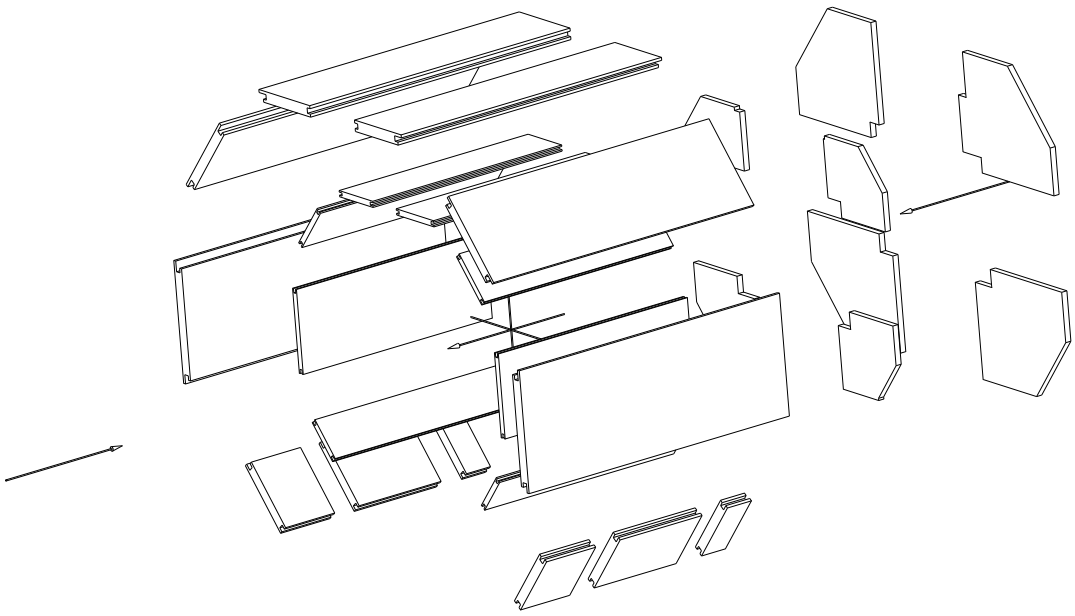

Figure 3.21: Layout of the BMUON and RMUON detectors.

pitch that run orthogonal to the wires. In the BMUI and BMUO chambers the LSTS are parallel to the beam direction, while in the rear chambers they are horizontal (parallel to the X axis). With the analog strip readout the achievable spatial resolution on the coordinate orthogonal to the wires is 200 μm, while it is 700 μm for the coordinate parallel to the wires.

3.2.7 Luminosity Measurement System (LUMI)

The cross section measurements calculated in this analysis are dependent on the knowledge of the total integrated luminosity gated by the ZEUS experiment in the HERA I running period. The luminosity is measured by means of hard bremsstrahlung photons from the *Bethe-Heitler* process: $ep \rightarrow e'p\gamma$. The cross section for this process is well known ($\sigma_{BH} \approx 20$ mb with accuracy 0.5%). For the experimental measurement of this process, the outgoing photons can be measured in the luminosity monitor (LUMI) [53] (see Fig. 3.22).

Within the experimental conditions this cross section agrees with QED calculations. The luminosity ($\mathcal{L}$) can be therefore extracted according to the following formula:

$$\mathcal{L} = \frac{N_{ev}}{\sigma_{ev}}, \tag{3.5}$$

where N_{ev} is the number of events produced in the bremsstrahlung process with cross section σ_{ev}.

The ZEUS luminosity monitor consists of a photon calorimeter and an electron

calorimeter installed along the beam axis upstream of the ZEUS experiment. The bremsstrahlung photons produced escape the ZEUS detector under small scattering angles $\theta_\gamma \leq 0.5$ mrad with respect to the beam axis. Photons continue down the proton beam pipe until they escape the beam pipe through the copper/beryllium exit window located at a distance of $z = -92.5$ m, and reach the photon detector (LUMIG) positioned at $z = -107$ m from the nominal interaction point. The LUMIG is a lead-scintillator sampling calorimeter with face dimensions $18{\times}18$ cm^2 and depth of 23 radiation lengths (X_0). Scintillator strips laid in the X and Y directions are set in the detector at a depth of $3X_0$ and provide information on the shower position with a resolution of approximately 3 mm. In front of the photon calorimeter, a carbon filter of thickness $2X_0$ is installed. It absorbs the large flux of synchrotron radiation from photons, which typically have an energy of the order of keV, whereas the bremsstrahlung photon's energy is above 1 GeV. A Cerenkov detector is located between the filter and the calorimeter in order to detect any possible photon conversions, such as e^+e^- pair production in the filter. The energy resolution of this calorimeter under test beam conditions is $18\%/\sqrt{E}$ (E in GeV). In practice it is a slightly worse $25\%/\sqrt{E}$ due to the filter. The acceptance for bremsstrahlung photons is about 98%, independent of energy.

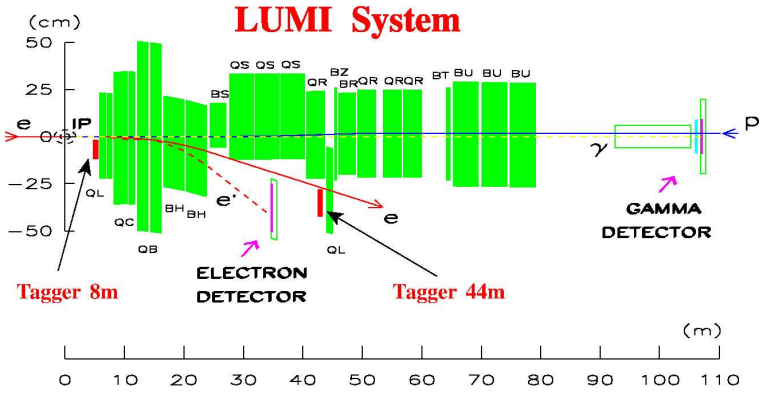

Figure 3.22: The ZEUS luminosity monitoring system with the photon LUMIG and electron LUMIE detectors is shown.

The electrons scattered at angles $\theta'_e \leq 6$ mrad and with an energy in the range $0.2E_e \leq E'_e \leq 0.9E_e$ are deflected by the beam magnets away from the nominal electron beam orbit. These electrons leave the beam pipe through the exit window located at $z = -27.5$ m and hit the electron detector (LUMIE) which is located at $z = -34.7$ m from the nominal interaction point. The LUMIE is a lead/scintillator sampling calorimeter ($23X_0$ deep) and it is able to measure the position of the tagged electron by means of scintillator fingers located at a depth of $7X_0$. The acceptance of LUMIE is measured to be above 70% and flat for scattered electrons with energies in the range $0.35\ E_e \leq E'_e \leq 0.65\ E_e$.

The most problematic contribution to the background is the beam-gas bremsstrahlung

process in which the electron interacts with a nucleus of residual beam gas ($eZ \rightarrow e'Z\gamma$). This process is impossible to distinguish from the desired process. The contribution of such background processes to the total counting rate of the LUMIG system is estimated by using the pilot electron bunches it is then subtracted from the total measured rate.

The measurement errors are dominated by systematic uncertainties. The statistics of the bremsstrahlung processes is large enough and the main contribution of uncertainty comes from background subtraction, pile-up effect[6], energy calibration, linearity as well as acceptance of the calorimeter. This all gives a systematic uncertainty between 1.5% and 2% for the 1996-2000 data taking period.

3.2.8 Trigger and Data Acquisition System (DAQ)

The HERA bunch crossing time of 96 ns means a very high beam crossing frequency of about 10 MHz. The interaction rate is dominated by background coming from the interaction of the proton beam with residual gas in the beam pipe or with the beam collimators before the interaction point. This rate is of the order of a few hundred kHz, while the rate of physics events written to tape is of the order of several Hz.

ZEUS has a three-level trigger system [54, 42] and a data acquisition system (DAQ) designed to reduce the initial interaction rate by suppressing background events and applying physics selection filters to accept interesting events, while inducing a minimum dead-time. In figure 3.23 a scheme of the ZEUS data acquisition system is shown.

At the *First Level Trigger* (FLT), a programmable hardware trigger has been designed to reduce the rate below 1 kHz. The FLT rejects a huge part of the background events. All ZEUS detector components store the data in a pipeline, while those participating to the trigger components make a decision, and send it to the *Global First Level Trigger* (GFLT). The GFLT combines all the sub-component information and decides whether to accept or reject the event. The FLT pipeline contains 46 crossings: 26 are needed by the detector components to produce a decision (2.5 μs), and 20 are used by the GFLT to collect all the information and produce a trigger decision (1.9 μs). The GFLT performs logical operations on the sub-component FLT information and can form the results in 64 different sub-triggers (*slots*). When the input rate to the GFLT exceeds the processing rate, the input events in excess are lost. The time, during which the trigger is unavailable while processing a previous trigger, is called *deadtime*. During normal operation, the GFLT dead time is smaller than 1%.

The *Second Level Trigger* (SLT) combines a set of algorithms running on a transputer network and has been designed for further reduction of the rate below 100 Hz.

[6]More then one photon per bunch crossing.

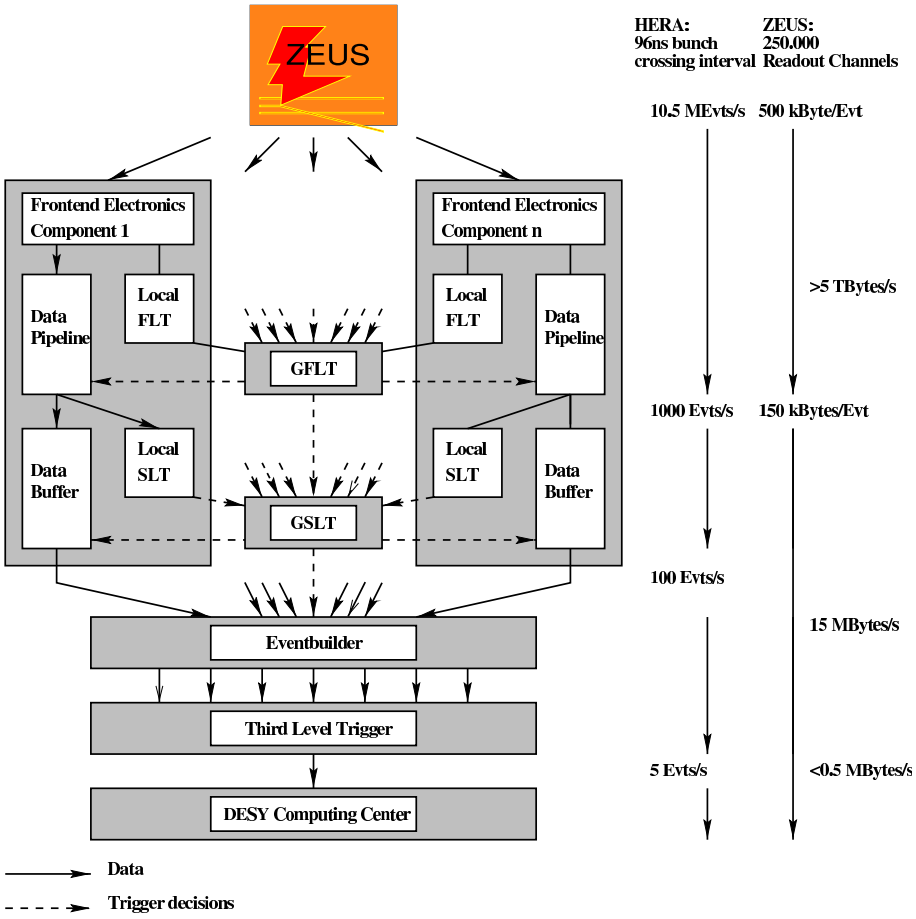

Figure 3.23: Diagram of the ZEUS trigger and data acquisition chain. The effects of trigger selection on lowering the rate (in events per second and in data size) is shown in the right had side for each decision diagram.

As for the FLT, several detector components have their own SLT and provide the local decision to the *Global Second Level Trigger* (GSLT). The GSLT releases the final decision whether to keep or reject the event. The time available to the GSLT is about order of 10 ms and depends on the input rate coming from the GSLT.

At the SLT stage more accurate information is available and more compound rejection algorithms are implemented. As mentioned in section 3.2.3, the ZEUS CAL provides timing information with a resolution of the order of 1 ns. This information is available at the SLT stage and used to reject residual beam gas background.

After the HERA upgrade, the ZEUS SLT was improved by adding the global tracking trigger (GTT) [35, 36], which performs track and vertex reconstruction using information of the tracking detectors: CTD, MVD and STT. It improves the physics triggering efficency. The development of the vertex finding algorithm for the Forward Global Tracking Trigger (FGTT) and its interface to the Global Tracking Trigger (GTT) was the technical task of the thesis. This will be discussed later in the Chapter 4.

After an event is accepted by the GSLT, all the components send their data to the *Event Builder*, which writes all the event information in a format similar to that used in the offline analyses[7] and sends it to the *Third Level Trigger* (TLT). The TLT is a computer farm and runs a simplified version of the offline reconstruction code. The TLT has been designed to reduce the rate to a few Hz. It applies a set of physics filters to the events and is able to further suppress background and classify events according to specific physics requirements. Events accepted by the TLT are stored on tape for further offline reconstruction and data analysis.

[7] One record in ADAMO database tables.

Chapter 4

Vertex Finding Algorithm for FGTT

The possibility of extending the Global Track Trigger (GTT) of the ZEUS DAQ/trigger system with a forward trigger algorithm, the development of which was the technical task in this thesis, is described in this chapter. The Forward GTT algorithm has been written which finds the event vertex position using STT and FMVD detector data. As will be seen in the conclusion the performance of the FGTT algorithm easily satisfies the time latency requirements and vertex finding efficiency and resolution, but its use online is prevented by the large data transfer latencies measured in the STT frontend readout.

4.1 Global Tracking Trigger (GTT)

The ZEUS Global Tracking Trigger (GTT) evolved from the requirement of using the greatly improved spatial resolution of MVD detector hits in the ZEUS second level trigger to improve the selection of physics events. The readout of the MVD is too slow to allow the use of its data within the first level trigger. The limited number of MVD hits per track, around 2-4 depending on the track flight direction, requires that additional tracking information from the CTD, in the barrel region, and, possibly, the STT, in the forward region, be used.

Figure 4.1 shows schematically how the GTT is implemented within the ZEUS trigger and readout system. Detector data from the MVD, CTD and STT is sent to the trigger algorithms running on computers of the GTT PC farm when an event is accepted by the GFLT. Two distinct types of data interfaces are used to forward event data to the GTT. An embedded MVD type, where data is read directly from the frontend ADC, and a parasitic CTD and STT type, where data is duplicated on-the-fly by a splitter transputer[1], specifically inserted into the detector's readout network, and sent to the interface via serial transputer links. The difference reflects

[1] INMOS Transputers were an advanced technological development in the early 90's when the ZEUS experiment was designed. Provided with a 32bit 25MHz processing unit, onboard memory, four 20 MHz serial input links for processor interconnection and a high level parallel programming

the fact that the GTT was designed as part of the MVD which does not use the now obsolete transputer in its readout. The use of the splitter transputer provides simple hardware access to the data with minimal software changes to the host transputer executable. The implementation of the interface types are similar allowing duplication of hardware and reuse of software. Each interface resides in a VME crate containing a single board computer (Motorola MVME2000 series PowerPC) responsible for reading out and sending the event data via FastEthernet.

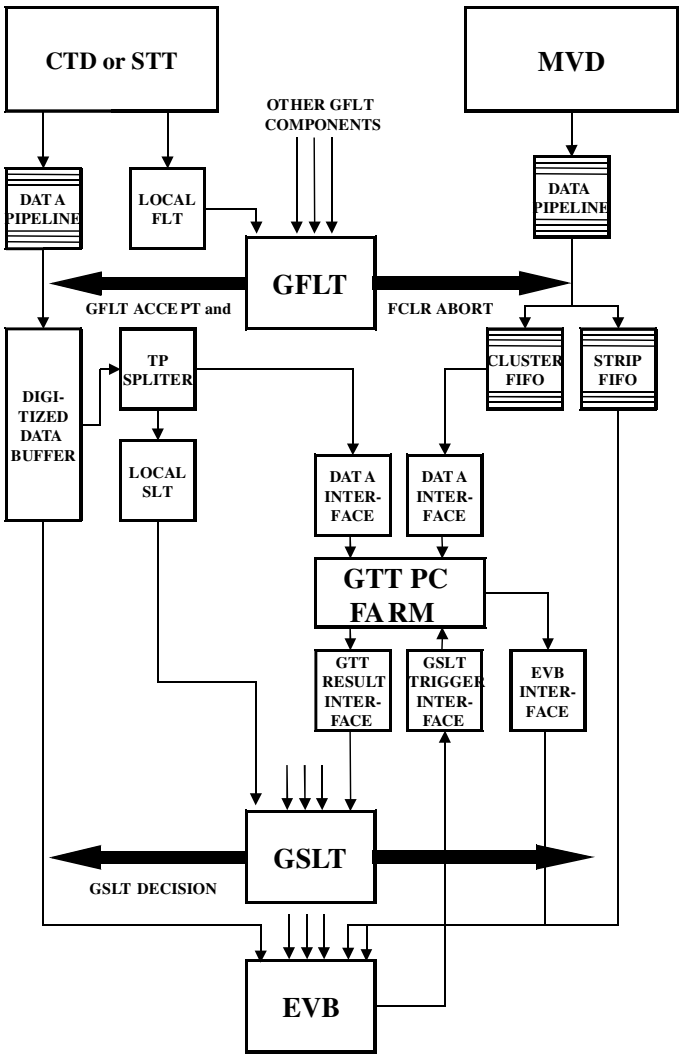

Figure 4.1: Schematic showing the GTT implementation within the ZEUS DAQ/trigger system.

The GTT's multi-threaded environment provides a framework within which trigger algorithms run. The results of the GTT algorithm (primary vertex, track multiplicities, vector meson masses, background flags, etc.) are sent to the GSLT, where

language (OCCAM), transputers were ideal for parallel processing and data transfer. Transputer development ceased in the mid 90's.

the second level trigger decision is evaluated. The GSLT evaluates the trigger information provided by the contributing components and generates an accept or reject decision. Component and trigger data from accepted events are sent to the Event Builder before being processed further by the TLT.

During pre HERA luminosity upgrade running, vertex and tracking information evaluated by the CTD second level trigger (CTD-SLT) was sent to the GSLT. This system was replaced by the GTT after the upgrade.

4.2 Forward Global Tracking Trigger (FGTT)

The time latency of trigger information arriving at the GSLT is crucial to the performance of the ZEUS trigger system. It is required that GTT results arrive at the GSLT with a latency not worse than that of the CTD-SLT in pre-upgrade running. Thus, the FGTT decision result is required to arrive at the GTT within 25 msec with an average value of 10 msec. The main aim of the FGTT algorithm implementation is therefore simplicity, fastness and maximum quality within the last two requirements.

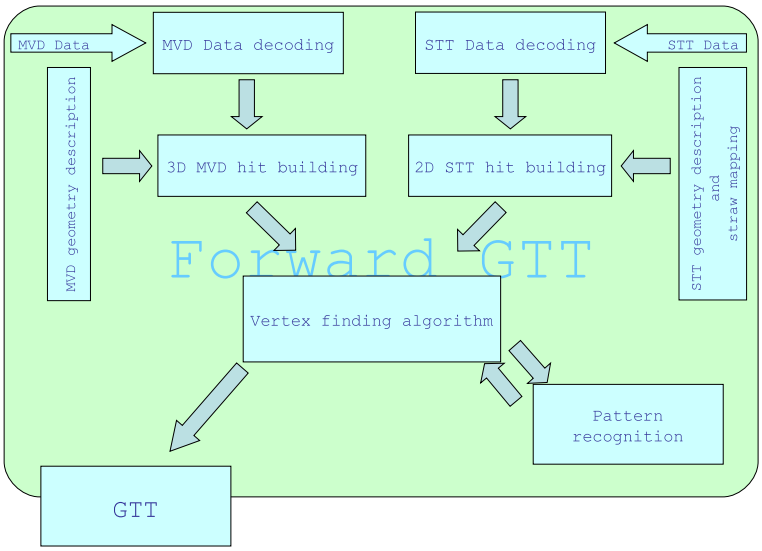

Figure 4.2: Block diagram of the FGTT algorithm structure.

In Figure 4.2 a block diagram of the FGTT algorithm structure is shown. The STT and FMVD data coming from the STT and FMVD data interfaces are first decoded. After the decoding stage STT and FMVD hit building is performed using the decoded information and the geometry description of both detectors. The STT decoding additionally exploits the straw mapping table which describes the connection between straws and electronics.

Hit information is then sent to the FGTT vertex finding algorithm, which performs the reconstruction of a vertex position of the event. Exploiting the found vertex position, the pattern recognition is started to reconstruct track seeds in two dimensions. In the case of positive results of the pattern recognition, the confirmed reconstructed vertex is sent to the GTT. The processing stages are described in the following sections.

4.2.1 Decoding of STT and MVD Raw Data

The FMVD data is decoded using the Barrel GTT software as both Barrel and Forward MVD data banks have the same format. The decoded data with FMVD cluster information is then used by the FGTT algorithm. The decoding of the STT data is performed by means of the same algorithm as in the STT offline code. To describe the algorithm, an example of the STT data bank is shown in the Table 4.1, the data bank contains 32 bit words readout and formatted by the STT frontend electronics. The data bank consists of eight sections which correspond to eight STT VME readout crates. A crate section in the data bank is extracted by using the word count of associated data words. A part of the data bank corresponding to a crate is sectioned by a number of slots which contain information about pins, where straws are connected. Each slot can be extracted by a number of 16 bit words corresponding to the slot.

Decoding begins from the first data bank word (see Table 4.1), which corresponds to a crate identifier, followed the word count of data words associated with the crate. The first of these data words, the third row, contains two 16 bit words of information. The first 16 bits contains the number of 16 bit slot words associated with the crate, the second 16 bit word is used for control purpose. The next 32 bit word contains the version number (the first 16 bits) of the STT DSP coding algorithm used to pack the STT data and coded address of a channel containing up to six straws (second 16 bits). The coded address of the channel contains information about the slot and pin number and the number of fired straws in the channel. Three 16 bit words follow the channel address correspond to time and signal amplitude information of a fired straw in the channel. The decoding algorithm counts the number of fired straws to read the corresponding amplitude and time information in the corresponding straw. After decoding the first channel, the decoder reads the next channel address and executes the same procedure described above. The procedure is continued until all 16 bit slot words have been decoded, after which the next slot is decoded, or no more slots remain. In this way all data words associated with a crate are processed. The entire procedure is then repeated until all crates have been processed.

Afterwards, when the STT dataflow decoding is complete, the STT straw information is ready for the vertex finding algorithm.

Raw word number	Raw 32 bit word content	Description
1	1	crate identifier
2	6b	crate data word count
3	000f0014 0014 000f	slot data word count (first 16 bits) control word (second 16 bits)
4	c2340000 0000 c234	DSP codec version (first 16 bits) channel address (second 16 bits)
5 6	966c0041 4796	time and amplitude information of the channel (one fired straw in the channel) (first 16 bits)
6	c83b	next channel address (second 16 bits)
7 8 9 10 11 12	966c0001 160696 1s969660 9654002a 563096 5c969678	time and amplitude information of the channel (four fired straws in the channel)
13	000f002c 002c 000f	next slot data word count(first 16 bits) control word (second 16 bits)
14	c6480000 0000 c648	DSP codec version (first 16 bits) channel address (second 16 bits)

Table 4.1: Example of the STT dataflow.

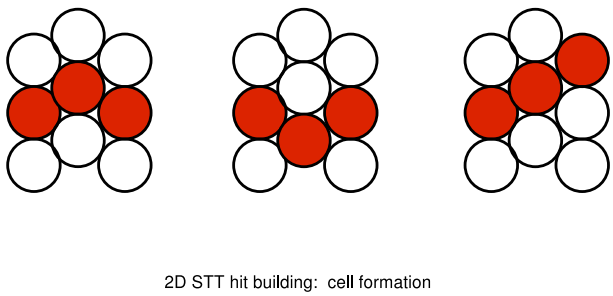

Figure 4.3: 2D STT cell formation. Three types of cell formation are possible. The cell window is shadowed.

4.2.2 FGTT Vertex Finding Algorithm

A charged particle track traversing the STT volume fires straws, which are packed in the three layer structure of a sector. The track induces a signal in the straw with a probability of around 98%. The probability to have three fired straws on the track in the sector is therefore around 94%. This is high enough to use combinations of three straws (cell) in the sector (see Figure 4.3) to identify candidate track elements. The straw's cell window provides the geometrical area within which the track lies. The size of the window (shadowed straws) is restricted by the centers and radii of the straws forming the cell. This can be seen in Figure 4.3, where three possible cell patterns in a sector are shown. The process of finding candidate track elements in one cell is called 2D STT hit building (see Figure 4.2).

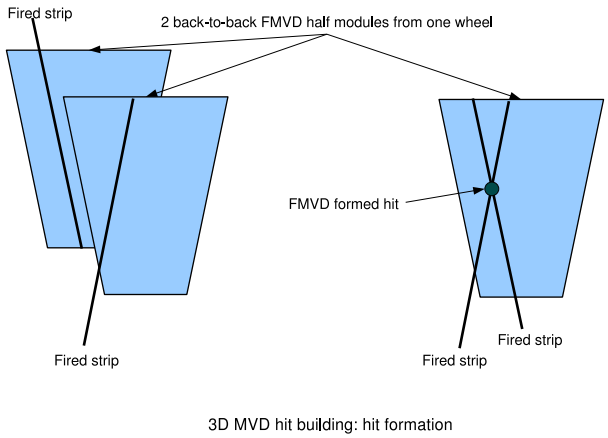

Figure 4.4: 3D FMVD hit formation. Leading strips from the two half modules are used in order to build the hit.

Charged particles traversing the silicon sensor half modules of the FMVD induce signals with an efficiency of almost 100%. Neighbouring fired strips are grouped into a single cluster by the firmware of the MVD frontend readout and this information is sent to the GTT framework. To build a 3D FMVD hit, the FMVD geometry description implemented in the FGTT algorithm is employed. The position of wheels, modules and strip coordinates are taken from [44]. After decoding of the FMVD cluster information, the cluster's central strip coordinates are calculated using the FMVD's geometry description. Using the fact that two half modules of a wheel are mounted back-to-back and tracks traversing the two half modules leave a cluster of fired strips in each half module, FMVD spatial hits are then calculated using the crossing point in the 3D space of the two central strips from both half modules (see Figure 4.4).

The STT geometry is azimuthally symmetric. The STT1 and STT2 contain pairs of sectors which are parallel in the $X-Y$ plane (see Figure 3.19). This feature of

the STT detector is exploited in the FGTT algorithm to provide enough hit information for vertex finding, the FMVD hit information is translated to match the STT azimuthal geometry. To do this, each FMVD hit is projected to azimuthal directions of the nearest STT sectors when an azimuthal angle difference between a FMVD hit and STT sector direction is less than 30^o. The translated FMVD information thus repeats the STT azimuthal symmetry.

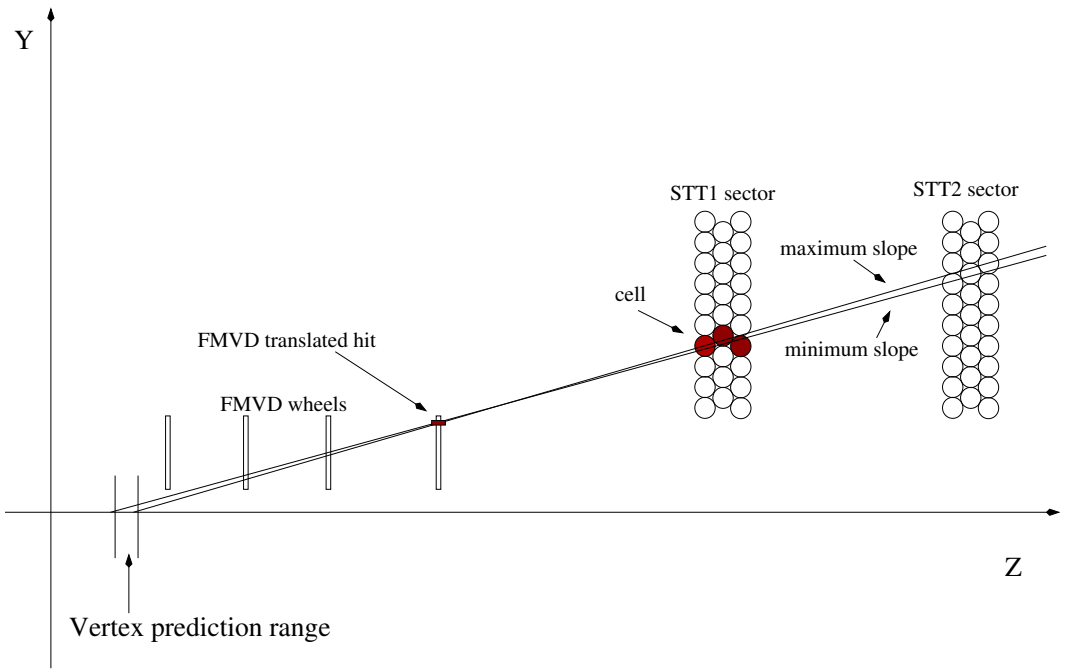

Figure 4.5: Schematic view of the vertex prediction range construction principle.

Charged particle tracks passing through STT1 (or STT2[2]) leave hits in at least four sectors. Four track projections are therefore available. Since the FMVD and STT hit geometry are matched a single track projection reconstruction can be performed by constructing straight lines passing through a STT1 cell window and a projected FMVD hit (see Figure 4.5). The size of the window is used to calculate minimum and maximum slopes of the straight lines. The extrapolation of both lines up to the beam line renders a vertex prediction range. An extrapolation of the lines to a parallel STT2 sector from the pair is also performed. If any cell from the STT2 sector does not fall into the open window produced by the minimum and maximum slope lines crossing, the reconstructed track projection is then discarded. The same procedure described above is performed for all STT1 FMVD hit pair for all STT projections. The resulting information is collected in a histogram, where reconstructed vertex ranges from all track projection passing the STT2 veto condition are summed.

[2]Due to the large amount of the background coming mainly from interactions of the proton remnant with the focusing magnet and beam pipe which contaminate STT2, the STT2 hit information is used only as a veto as the contamination is too high.

The maximum of the vertex range overlap is the predicted track vertex position.

Using the predicted vertex position, the FGTT algorithm goes into a final stage. Fired straws from STT1 are transformed into a 2D dimensional space by a Hough transformation [38]. The histogramming technique is exploited to collect information about all fired straws in the event. In addition to the straw information, FMVD hits are added. Peaks above a threshold on the 2D histogram correspond to track seeds. If the vertex position is reconstructed correctly, the track seed recognition should see at least one peak above threshold. If so, the found vertex position is then treated as correct and it is sent to GTT.

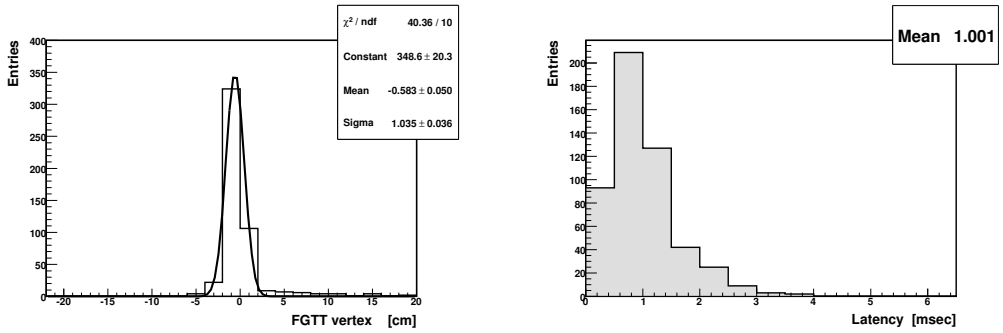

Figure 4.6: The vertex position (left) reconstructed by the FGTT and latency (right) of the FGTT algorithm tested on the MC sample.

The result of the FGTT algorithm performance test can be seen in Figure 4.6, where the reconstructed vertex position is shown. The test is performed on the Intel Pentium M processor with a frequency of 1600 MHz. The MC event sample used contains D^* mesons whose decay tracks traverse the forward region. The event production vertex was fixed to the nominal interaction point. The D^* MC sample is selected because it provides a track multiplicity, which is enough for the test, and contains background mainly dominated by interactions of the proton remnant with the beam pipe and focusing magnet. One can see from Figure 4.6, the resolution of the vertex reconstruction provided by the FGTT algorithm is about 1 cm along with the vertex finding efficiency of 90% and the algorithm latency is about 1 msec.

The FGTT algorithm performance has additionally been evaluated using event data samples corresponding to GFLT accepted events. The aim of the test is to make a comparison of the FGTT algorithm latency with that of the CTD-SLT reconstruction. This result is shown in Figure 4.7, where the reconstructed vertex position (right) and the total FGTT latency (left) (the decoding and vertex reconstruction) are shown.

The correlation with the CTD-SLT reconstruction is given in Figure 4.8 (left). It demonstrates a good agreement. The reconstructed vertex position corresponds to

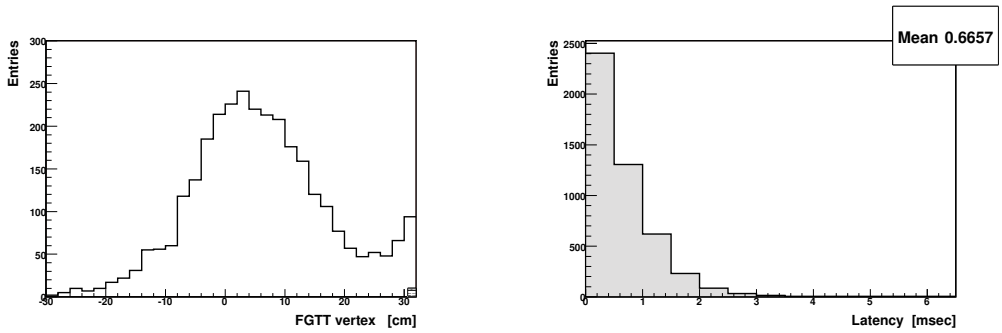

Figure 4.7: The vertex position (left) reconstructed by the FGTT and latency (right) of the FGTT algorithm tested on the real data.

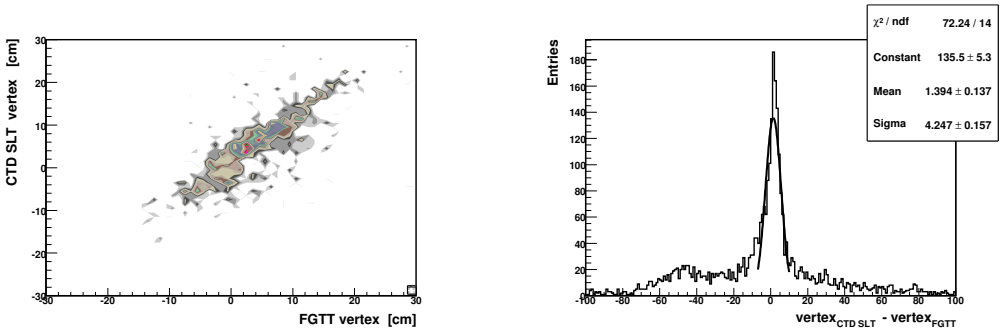

Figure 4.8: Correlation between the CTD-SLT and FGTT vertex reconstruction (left). Resolution of the FGTT vertex reconstruction versus CTD-SLT found vertex (right).

the expected vertex distribution from the real data (-20 cm : 20 cm). The bump around 30 cm comes from the interaction with the beam pipe and can be removed by a cut on the vertex position $|Z_{vertex}| < 20$ cm. One can conclude that a FGTT algorithm can be applied for triggering very forward events, which cannot otherwise be caught by the GSLT due to the CTD acceptance.

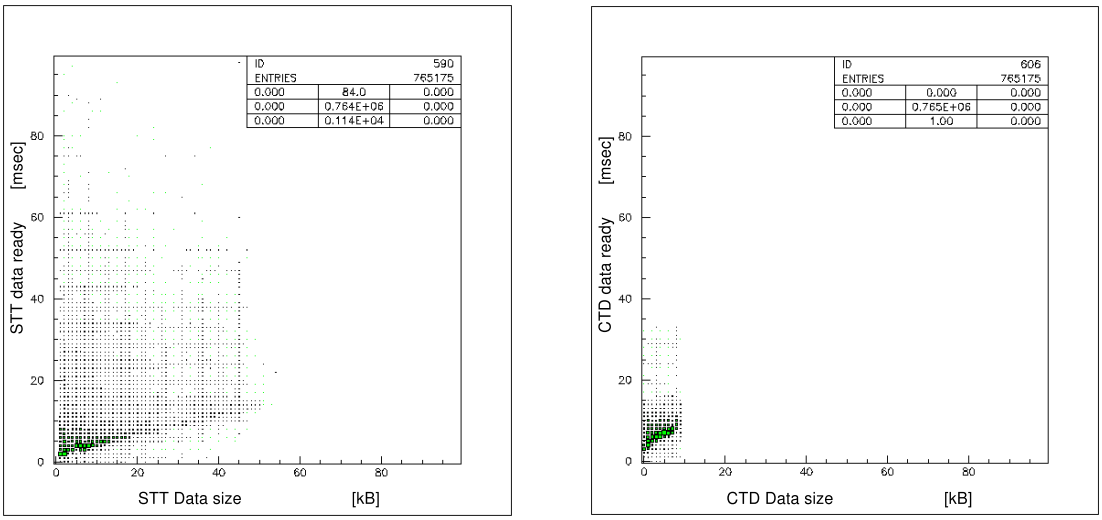

Figure 4.9: The STT (left) and CTD (right) data ready latency versus data size.

The FGTT algorithm computation latency is shown in Figure 4.7 and is easily contained within the CTD-SLT trigger (data ready at the GTT plus computation latency) latency at the GSLT. Unfortunately, online measurements of the arrival time of STT data at the GTT showed that the data transfer latency is high and had a large tail. Both effects are driven by the large data size produced by the STT readout, which could not be reduced significantly without substantial modification to the frontend readout system. A comparison of the data ready (the latency of all data from the frontend being available at the GTT framework) versus data size for the CTD and STT are shown in Figure 4.9. The CTD distribution is well behaved, in terms of trigger usage, the data size is always below 10 kB and, consequently, the transfer times are small. The STT readout is capable of producing very large data sizes with correspondingly large data ready delays. Note that the data ready delay should scale linearly with the data size at a rate corresponding to the transputer serial link speed, or a multiple of it.

As it is not possible to reduce the data size whilst keeping useful trigger hits it is unfortunately not possible to run the FGTT online due to the increased latency which would result in trigger dead-time.

Chapter 5

Dataset and Event Reconstruction

In this chapter the dataset taken for the 1996-2000 running period and the corresponding MC samples employed in the analysis are summarised. The post upgrade data of the HERA II running period are not yet used in this analysis due to the absence of a corresponding MC.

In order to reconstruct charm event candidates for the process:

$$ep \;\rightarrow\; e'\; c\bar{c}\; X \;\rightarrow\; e'\;\; D^{*}\mu\;\; X'$$

a number of techniques exploited in the analysis is also described. All the important corrections applied to the reconstructed event quantities are discussed as well. To describe the kinematics of the D^{*}-muon pair, the set of kinematic variables used in the analysis framework is introduced.

The ZEUS event reconstruction is performed by the ZEPHYR package [42]. The ZEUS reconstruction information is then stored in ADAMO tables [56], which can be easily linked to the user analysis environment. The event reconstruction involves track reconstruction information of the CTD, energy depositions and energy cluster positions in the CAL as well as information from the MUON and BAC detectors. To achieve high muon detection efficiency, the outputs of the different ZEUS muon reconstruction algorithms are combined into the ZEUS muon finder GMUON [59].

5.1 Data Samples

The dataset used in the analysis was taken during the HERA I running period, which corresponds to the data taking in the years 1996-2000, where the response of the ZEUS detector components is well understood, especially the performance of the muon identification system, the trigger, CAL and CTD. For this period ZEUS collected 121 pb^{-1} satisfying the requirements for good data quality (EVTAKE [55]) of the central components of the experiment: LUMI, CTD and CAL. The runs in the

year 2000 with shifted vertex position (0.815 pb^{-1}) are excluded from the analysis.

In addition to this general data quality, a run-by-run selection based on the data quality monitor of the BMUON and the RMUON (MBTAKE) is used. The requirement of EVTAKE and MBTAKE in the dataset corresponds to 114 pb^{-1}.

The dataset was preselected with the requirement of the presence of at least a muon and at least a D^* ($D^* \to K\pi\pi_s$) meson candidate. This significantly reduces the size of the dataset used in the analysis. The D^* preselection was:

- $p_T^{D^*} > 1.3$ GeV,
- $|\eta^{D^*}| < 1.5$.

The muon preselection was:

- $p_T^{\mu} > 0.5$ GeV.

Additional requirements to the muon preselection were:

- Either the number of muons > 1
- Or the number of muons $= 1$ and (muon quality ≥ 4 or $p_T^{\mu} > 5$ GeV).

5.2 Monte Carlo Samples

The PYTHIA [15] and RAPGAP [24] MC event generators have been used to generate events with charm and beauty production. In this analysis, the charm production process is regarded as the signal, whereas beauty production is treated as background. These MC samples contain several basic hard processes of heavy quark production: direct and non-direct consisting of the hadron-like resolved photon process, excitation in the incoming photon and excitation in the incoming proton. These processes are discussed in Section 2.5. The PYTHIA MC sample is employed only for PHP with $Q^2 < 1$ GeV^2, whereas the RAPGAP MC sample is used for DIS with $Q^2 \geq 1$ GeV^2.

In order to calculate the cross section for the charm D^*-muon pair production, the statistics of the MC samples should be larger than in the dataset. This reduces the influence of the MC statistical uncertainty. The MC sample luminosities are therefore a factor of 5 larger than the data luminosity. This is indicated in Table 5.1. Due to the fact that the proton beam energy was changed in 1998 from 820 GeV to 920 GeV, the different MC samples were generated for the various years of data taking proportionally to the corresponding luminosities. Light flavour samples were not generated because the D^* background discussed in Section 5.12 is determined

Process	Generator	PDF p/γ	Parameters	Luminosity [pb^{-1}]
$ep \to c\bar{c}X$	PYTHIA 6.156	CTEQ5L/GRV-G LO	$p_{T\ excit}^{min} = 1.5$ GeV $m_{charm} = 1.5$ GeV	515
$ep \to bbX$	PYTHIA 6.156	CTEQ5L/GRV-G LO	$p_{T\ excit}^{min} = 4.5$ GeV $m_{beauty} = 4.75$ GeV	515
$ep \to c\bar{c}X$	RAPGAP 2.08/18	CTEQ5L/GRV-G LO	$Q^2 > 0.6$ GeV^2 $m_{charm} = 1.5$ GeV	619
$ep \to bbX$	RAPGAP 2.08/18	CTEQ5L/GRV-G LO	$Q^2 > 0.6$ GeV^2 $m_{beauty} = 4.75$ GeV	619

Table 5.1: The MC samples used and their most relevant parameters.

Decay mode	p_T cut
$D^{*+} \to (D^0 \to K^-\pi^+)\pi_s^+$	$p_T^{D^{*+}} > 1.25$ GeV
$D^{*+} \to (K_s^0\pi^+\pi^-)\pi_s^+$	$p_T^{D^{*+}} > 1.35$ GeV
$D^{*+} \to (D^0 \to K^-\pi^+\pi^-\pi^+)\pi_s^+$	$p_T^{D^{*+}} > 2.3$ GeV
$D^0 \to K^-\pi^+$	$p_T^{D^0} > 2.6$ GeV
$D_s^+ \to (\phi \to K^+K^-)\pi^+$	$p_T^{D_s^+} > 1.7$ GeV
$D^+ \to (\phi \to K^+K^-)\pi^+$	$p_T^{D^+} > 1.7$ GeV
$D^+ \to K\pi\pi$	$p_T^{D^+} > 2.8$ GeV
$\Lambda_c^+ \to Kp\pi$	$p_T^{\Lambda_c^+} > 2.8$ GeV

Table 5.2: The D meson decay modes with their transverse momentum cuts p_T used in the MC samples.

from the data.

The MC samples used in this analysis have been generated with a transverse momentum preselection applied to the set of charm hadrons as given in Table 5.2, where the charm hadron decay modes generated are also indicated. All relevant masses, widths, branching ratios and life times have been set to the measured values [26]. The events have been generated with no requirement on the presence of muons.

As in case of the dataset preselection, the MC samples were also preselected with the requirement of the presence of at least a D^* ($D^* \to K\pi\pi_s$) meson candidate and at least a muon candidate in the final state. The same cuts as in case of the dataset preselection were used for the reconstructed MC samples. Events with non-reconstructed true D^* mesons or muons were also kept with the following cuts on generator level:

- $p_T^{D^*} > 1.3$ GeV,
- $|\eta^{D^*}| < 1.5$,
- $p_T^{\mu} > 0.5$ GeV.

5.3 CTD Track Reconstruction

The CTD is the main tracking device in the ZEUS experiment. Charged particles passing through the CTD sensitive volume induce charge on the CTD wires, which are used as hit information in the track reconstruction. The CTD track reconstruction [58] is performed in three stages.

The first stage, *pattern recognition*, consists of two fits. The track reconstruction starts from the outermost CTD superlayer. In the first circle fit, a track candidate is constructed in the $X-Y$ plane from track segments which can contain up to eight wire hits of a CTD cell. The second fit in the $X-Z$ plane is a linear function fit along the length s of circle trajectory of the track reconstructed in the $X-Y$ plane. Left-right position ambiguities induced by the measurement principle of the drift chamber are removed at this stage.

The second stage is a three dimensional fit of the track reconstructed by the pattern recognition. The fit takes into account the errors on the hit measurements, the dead material distribution and corresponding multiple scattering effect, energy losses and the non-uniform magnetic field.

In the third stage, a vertex fit is performed for the reconstructed tracks. The event vertex as well as secondary vertices can be reconstructed and used further to refit all tracks associated to the vertex.

For matching CAL energy cluster positions to the CTD track information, the reconstructed tracks and error matrices are extrapolated to the innermost CAL surface.

5.4 CAL Energy Reconstruction

The CAL energy measurement needs to be corrected for several detector effects. *Hot* cells corresponding to a malfunction of the CAL electronics or the PMT itself have been excluded. Noisy channels are suppressed by setting energy threshold for cells and using redundant information of both PMTs of a CAL cell. Initially, a cell energy cut of 60 (110) MeV is applied to suppress noise in the EMC (HAC) sections. This threshold is set higher, to 100 (150) MeV for isolated cells in the EMC (HAC). These thresholds were determined to correspond to approximately four standard deviations of the noise distributions. Occasionally, a PMT in the CAL fires, resulting in a *spark* which induces a large signal. Fortunately, each cell of the CAL is monitored by two PMTs, so sparks can generally be rejected by analysing the imbalance in the two readings.

A comparison of the calorimeter measurements [60] in the data and the MC has yielded a list of correction factors which should be applied to the CAL energy mea-

CAL region	cell type	energy corr. 1996-1997	energy corr. 1998-2000
FCAL	EMC	+4.0%	+2.4%
	HAC	-5.0%	-5.9%
BCAL	EMC	+4.0%	+5.3%
	HAC	+8.2%	+9.6%
RCAL	EMC	+2.2%	+2.2%
	HAC	+2.2%	+2.2%

Table 5.3: Energy correction factors for EMC and HAC sections of the CAL.

surements in the data. The list is summarised in Table 5.3 for the EMC and HAC sections of the CAL for the HERA I running period.

5.5 CAL Island and Energy Flow Object Reconstruction

In the event reconstruction, it is advantageous to combine individual calorimeter cells in order to produce objects, which resemble as closely as possible the final state particles or jets. Cells in the EMC, HAC1 and HAC2 layers are grouped separately in each layer in order to construct *islands*. This is done by grouping cells above the noise threshold starting from the cell with the highest energy deposition. The cell islands in different layers are then combined into three dimensional *cone islands*. The matching of cone islands starts in the outermost layer of the calorimeter HAC2 and proceeds inwards to the interaction point, combining HAC2 islands with HAC1 and EMC islands and finally HAC1 islands with EMC islands. The angular separation to neighbouring islands is calculated in azimuthal and polar angles. The single pion MC simulation is used to evaluate the matching probability [61]. The spacial center of the CAL cone island is calculated as the logarithmically weighted center of gravity.

The technique described above has low energy resolution for low energy charged particles. This is shown in Figure 5.1. The energy resolution of CAL cone islands is presented in full circles. One can see that the CAL energy resolution degrades at low energy. Fortunately, it is possible to compensate the low resolution at low momentum by the formation of an energy flow object (ZUFO) containing both the CAL energy measurement and the CTD track momentum reconstruction, which gives better resolution for low momentum particles. In Figure 5.1 one can see the momentum resolution provided by the track reconstruction in the CTD (open circles). It is clearly seen that the best reconstruction can be achieved by using a combination of CTD measurements, mainly for particle energies below 10 GeV, and CAL energy measurements for particles with higher energies.

To form a ZUFO, charged particle tracks reconstructed in the CTD are extrapolated

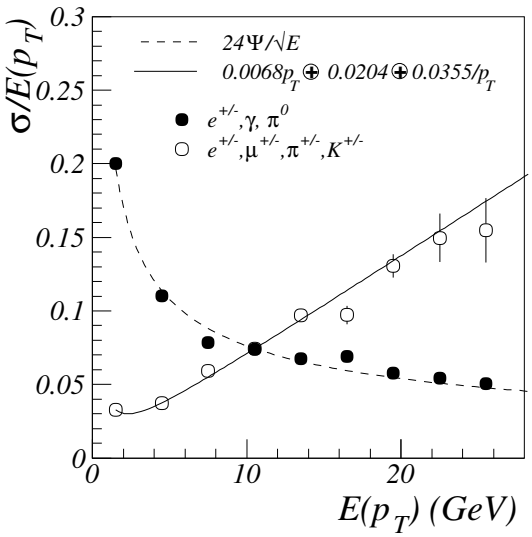

Figure 5.1: The CTD (open circles) tracking and CAL (full circles) energy resolution as a function of the energy or transverse momentum.

to the innermost surface of the CAL and matched to cone islands (see Figure 5.2). The matching is successful if the following quality requirements are met:

- The track has to be vertex fitted,
- Either the track has to traverse at least 4 CTD superlayers with the transverse momentum in the range $0.1 < p_T < 20$ GeV or the track has to pass through 7 CTD superlayers with the transverse momentum in the range $0.1 < p_T < 25$ GeV,
- Either the distance-of-closest-approach (DCA) of a track to a cone island is smaller than 20 cm or the track lies inside the area of the island.

Depending on the energy measurement resolution and track associations to cone islands, the four-vector of the ZUFO contains either the CAL energy measurement or the CTD tracking momentum. In the case of ZUFOs using the momentum measurement in the CTD, the calculation of the ZUFO four-vector assumes the ZUFO to be a pion ($m_{Zufo} = m_\pi$). If the four-vector of the ZUFO is determined from the CAL information, the ZUFO mass is set to zero. Different cases can be distinguished here (see Figure 5.2).

- A track without matching to a cone island is treated as a charged particle and the ZUFO energy is determined from the CTD tracking momentum with the assumption that the particle is a pion.
- A cone island without matching to a track is treated as a neutral particle and the CAL energy measurement is used to determine the four-vector of the ZUFO.

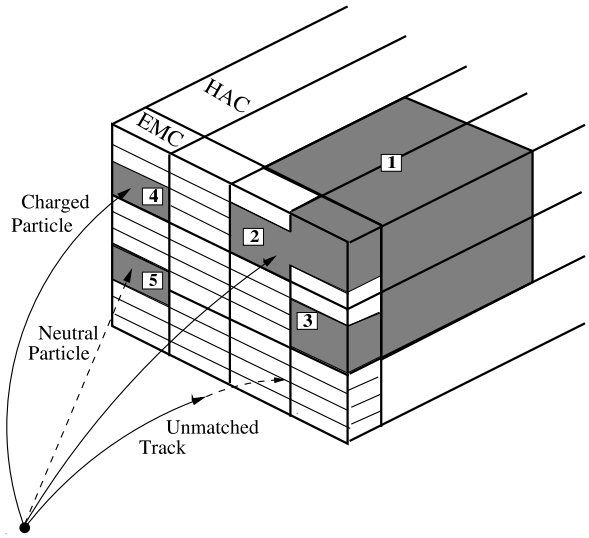

Figure 5.2: Schematic view of track-island matching. Four EMC cell islands and one HAC cell island are shown. EMC cell islands 2 and 3 are grouped with the HAC cell island 1 to a cone island.

- The association of one track to two or three islands or two tracks to one or two island: the sum of the island energies or track momentum is used.
- More than three tracks associated to one island are treated as a jet and the calorimeter information is used for the ZUFO.

A special treatment has to be applied for the muon case. As discussed in section 3.2.6, muons are MIPs and the measured energy of muons in the CAL is not proportional to their momentum. ZUFOs identified as muon are therefore treated differently and the tracking information is always favoured over the energy measurement (see Section 5.6).

5.6 Cone Island and ZUFO Corrections

Energy corrections were applied to the cone islands [62] and the ZUFOs. In case of the cone islands the contribution of the beam pipe, CTD and solenoid to the energy loss should be taken into account in the data and MC. Therefore the energy loss correction is applied to both the data and MC as a function of the energy and position of the island. The dead material map between the nominal interaction point and CAL is shown in Figure 5.3, where the radiation length is shown as a function of azimuthal and polar angles.

Muons are MIPs as discussed in Section 3.2.6, and their energy losses while traversing the CAL are dominated by ionisation. The measured energy is therefore not proportional to and usually less than the muon momentum. In case of the ZUFO formation, they need to be treated in a special way. Isolated muons have a separated

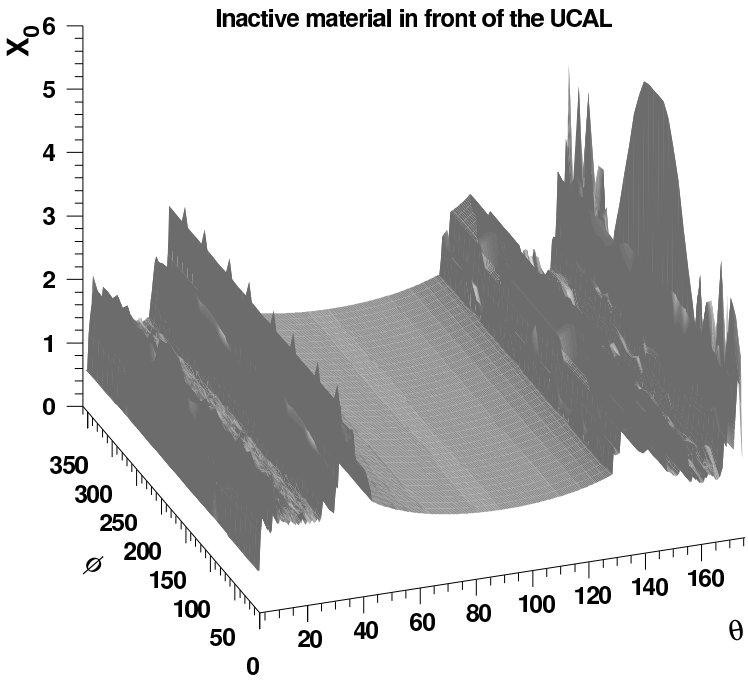

Figure 5.3: Map of dead material in units of the radiation length X_0 between the nominal interaction point and CAL as function of azimuthal and polar angles.

CAL MIP island and a CTD track. Non-isolated muons are usually inside a ZUFO containing also hadron activity. For isolated muons, the energy correction is applied by using the CTD track momentum. For non-isolated muons, first, the typical muon energy loss is subtracted from the ZUFO. In Figure 5.4, the typical muon energy loss is given as a function of the polar angle. In the Figure one can see the energy loss contribution in the EMC (crosses), HAC (open squares) as well as both sections (full circles) of the CAL. Secondly, a new ZUFO is created and the actual muon momentum measured in the CTD is used in this new ZUFO.

5.7 Electron Reconstruction

In the measurement of DIS events the identification of the scattered electron is critical. Most ep scatterings involve small momentum transfer due to the $1/Q^4$ dependence of the electron-proton cross section. In this case, the electron is scattered at small angles. In this analysis, the electron candidates are identified using a neural network package (SINISTRA) [63]. This package takes the transverse and longitudinal energy profiles of energy clusters from the entire calorimeter as input and calculates the probability that each electromagnetic cluster resulted from a real scattered electron. The program is trained on neutral current DIS MC, and yields $\sim$ 80% efficiency for finding electrons when the energy deposition in the EMC is larger than 10 GeV and the probability given by SINISTRA is larger than 0.9.

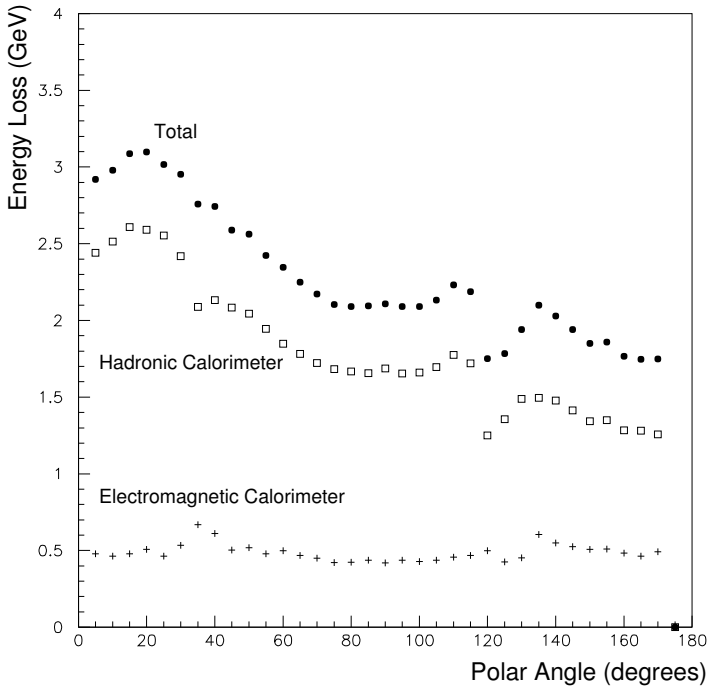

Figure 5.4: Muon energy loss in the CAL as function of the polar angle.

When the electron candidates are identified in the CAL, the scattering angle θ_e can be measured combining the impact position at the calorimeter with the event vertex. The calorimeter cells associated to the electron candidate are used together with the CTD and SRTD detectors, whenever the respective acceptance region permits, to measure the impact position.

5.8 Reconstruction of Kinematic Variables of ep Scattering

The present analysis covers three kinematic regions: the inclusive, where no separation between the PHP and DIS regimes is applied, PHP with $Q^2 < 1$ GeV^2 and DIS with $Q^2 > 2$ GeV^2. In this section two methods used for the estimation of the ep scattering kinematic quantities, are described. These estimated quantities are employed in the analysis framework to make a separation between the PHP and DIS regimes.

Since the incoming proton and incoming electron momenta are known, the kinematics of the DIS events is fully described by two independent variables $\{x, Q^2\}$ as discussed in Section 2.2. In the experiment, energy and polar angle of the scattered electron or/and the four-momenta of the particles belonging to the hadronic final

states can be measured. The kinematic variables $\{x, Q^2\}$ should be thus evaluated from these experimental measurements.

5.8.1 Electron Method

In this method [64] only the scattered electron needs to be measured. This method is therefore applicable only for DIS events. The kinematic variables can be calculated from the energy and the polar angle of the scattered electron:

$$Q^2_{el} = 2E_e E_e{}' (1 + \cos\theta_e), \tag{5.1}$$

$$y_{el} = 1 - \frac{E_e{}'}{2E_e} (1 - \cos\theta_e), \tag{5.2}$$

$$x_{el} = \frac{Q^2_{el}}{s y_{el}}, \tag{5.3}$$

where E_e is energy of the incoming electron, $E_e{}'$ and θ_e are energy and polar angle of the scattered electron respectively, s is the center of mass energy.

5.8.2 Jacquet-Blondel Method

An other possibility to measure the kinematic variables is provided by the Jacquet-Blondel method [65]. This method uses the reconstruction of the hadronic final state and is mainly applied when the scattered electron variables cannot be reconstructed as it happens in the PHP regime or in CC events, where the scattered lepton is an undetectable neutrino. In the DIS regime this technique can be also used.

The kinematic variables can be expressed in the following way:

$$y_{JB} = \frac{1}{2E_e} \ (E - p_z), \tag{5.4}$$

$$Q^2_{JB} = \frac{1}{1 - y_{JB}} \Big[\Big(\sum_i^{\text{ZUFO}} p_{x\ i} \Big)^2 + \Big(\sum_i^{\text{ZUFO}} p_{y\ i} \Big)^2 \Big], \tag{5.5}$$

$$x_{JB} = \frac{Q^2_{JB}}{s y_{JB}}, \tag{5.6}$$

where kinematic variable $(E - p_z)$ is the sum runs over all reconstructed ZUFOs in the detector, that is, it is equal to $\sum_i^{\text{ZUFO}} (E_i - p_{z\ i})$, excluding the detected DIS electron, if any. The method gives a better resolution for low y than the electron method. In case of the PHP regime only the y_{JB} calculation is used in this method.

5.9 Muon Reconstruction

In this section muon reconstruction algorithms are briefly discussed. Special attention is payed to the GMUON finder [59], which combines the muon reconstruction

algorithms in order to gain muon reconstruction redundancy. Afterwards, corrections applied for muon reconstruction are described as well.

In this analysis, muons are used to tag the charm production process and, in combination with the D^* mesons, to study charm quark pair correlations. As it is discussed in Section 3.2.6, the muon is a minimum ionising particle and, hence, a particle with a high penetration power. The energy loss of muons in uranium is $dE/dx = 1.082$ MeV cm^2/g [25]. The corresponding energy loss of muons in iron is about 1 GeV/m. This fact means that high energy muons can reach the muon identification chambers, whereas all other particles, like kaons and pions, are absorbed in the CAL, which yields the measurement of the total amount of their deposited energy. The other fact, which can help to identify muons coming from the charm decay (prompt muons), is an association with the event vertex because these muons are produced very close to the reconstructed interaction point. Thus, for the reconstruction of prompt muons, the BAC, CAL, FMUON, BMUON, RMUON, as well as CTD measurements are used.

An important question, which has to be discussed here, is fake muon background. The fake muon background sources can be summarised as:

- **Muons from kaon and pion decays:**
  Despite the fact that kaons and pions are long-lived particles, they have a finite probability to decay within the CTD volume before they reach the CAL or in the CAL before they interact. Many of such muons can be rejected by the muon track momentum matching between the CTD and the muon chamber measurements or the CTD track vertex reconstruction. But some fake muons can pass through the rejection.

- **Punch through of hadrons:**
  In the case of high energy hadrons there is a small, but finite probability, that one of the shower particles leaks out of the back of the CAL and then can be detected by the inner muon chambers and/or BAC. The high energy hadron, initiator of the shower, can be associated to the leakage and reconstructed as a muon.

- **Sail through of hadron:**
  Hadrons have a very small, but finite probability to behave like a MIP. In such a case, they will be identified as muons.

- **Matching ambiguities:**
  Non-muon tracks reconstructed in the CTD can be accidentally matched to hits or tracks reconstructed by the muon identification system.

5.9.1 Muon Reconstruction Algorithms

For the identification of muons in charm events, different muon reconstruction algorithms are available. Most of them (like BREMAT and MPMATCH) are using the BMUON and RMUON or FMUON chambers, some the BAC (i.e. MUBAC) or only the CAL information (MV). In the following, only the algorithms actually used in this analysis are discussed.

BREMAT Barrel and Rear Extrapolation Matching.
BREMAT [66] reconstructs muons by matching tracks extrapolated from the CTD to the BMUI and RMUI and reconstructed muon segments in the inner and/or outer muon chambers. Only muons with a momentum higher than 1 GeV can reach the inner muon chambers. This is an effective momentum threshold for BREMAT. CTD tracks are extrapolated starting from the reconstructed interaction point going outward. This ensures the best treatment for low momentum muons as they lose a significant fraction of their energy before they reach the inner muon chambers. The magnetic field in the CAL does not affect the track extrapolation strongly. The field is small in the CAL compared to the inside of the solenoid. The GEANE package [28] and a Kalman filter [68] are used to perform the extrapolation and matching. They take into account the errors of the tracking to the muon chambers as well as multiple scattering and energy loss of the muon candidates, traversing the ZEUS detector.

One important advantage of the algorithm that it is suited not only for isolated but also for non-isolated muons since no MIP signature in the CAL is required. Therefore also muons included inside hadronic flows are reconstructed. The BREMAT algorithm uses the following cuts for the preselection of the muon candidate:

- Track momentum p > 1 GeV,
- Track polar angle $\theta > 20^o$,
- Track should start from the first CTD superlayer and reach at least the third superlayer,
- Distance-of-closest-approach (DCA) of the muon track to the interaction point $|\text{DCA}| < 10$ cm,
- Z position of the DCA to the interaction point $|Z_{\text{DCA}}| < 75$ cm,
- χ^2 per number of degrees of freedom (ndf) of the track fit $\chi^2/\text{ndf} < 5$,
- Distance between a central point on a barrel/rear muon segment and the crossing point of a straight line obtained by extrapolation of the track to the muon chambers should be less than 150 cm.

The reconstructed muon track segments can contain either hits of the inner muon chambers or, if muons reached the outer muon chamber, hits from both the inner and outer muon chambers. In the first case, extrapolated CTD

tracks are matched to muon segments in position and angle in two projections (4 degrees of freedom (dof) match). In the second case, the muon momentum can be measured by the outer and inner muon chambers. This provides an additional degree of freedom in order to gain a high quality matching (5 dof match).

MPMATCH A Package to Match FMUON Tracks with CTD.
To reconstruct forward muons, the algorithm called MPMATCH [67] is used. The algorithm is similar to BREMAT. It performs matching of tracks in the forward muon chambers with tracks reconstructed in the CTD. The acceptance of the algorithm is constrained by the overlap between CTD and the forward muon chambers. Muon tracks reconstructed in the forward muon chambers are defined by five parameters in the ZEUS detector reference frame: $(x, y, dx/dz, dy/dz, Q/p)$. The match starts with an FMUON track by opening a cone in the polar angle θ and the azimuth angle ϕ around the track. The inner tracking detectors are searched for tracks inside the cone. If at least one CTD track is found, the FMUON track is extrapolated backwards to the outermost hit position of the CTD track. To extrapolate the muon track and fit both tracks, the GEANE package and the Kalman filter are used. In the case of multiple CTD tracks in the corridor, the match with best the χ^2 of the fit is used. The procedure is iterative for each track. To obtain the best match, a vertex refit is done for the FMUON track and it is extrapolated backwards to the reconstructed event vertex. Finally, a fit between the extrapolated FMUON track and the CTD track including the vertex position is performed. Like BREMAT, MPMATCH is suited for high momentum non-isolated muons in the forward region but suffers from low FMUON efficiency and a high momentum threshold.

MUBAC Reconstruction of Muon Candidates in the BAC.
The algorithm [59] provides BAC muon candidates to be further matched with a vertex fitted track reconstructed in the CTD by a simple DCA algorithm[1]. To match both tracks, the DCA should be less 120 cm, whereas for the case of high quality reconstructed muons, the cut on the DCA is tightened to 50 cm.

The BAC provides a digital (hit) and an analog (pad) readout which are used in combination to reconstruct muons, taking into account the errors on the measurement. The BAC provides a clean muon signature with a larger geometrical coverage than the muon chambers, in particular the bottom part of the detector and the gaps between the forward and barrel muon chambers. The momentum threshold on reconstructed muon is high due to the amount of material along the trajectory of the muon from the interaction point to the BAC. Therefore, the minimum transverse momentum of muons in the barrel to reach the BAC is 2 GeV. Muons in the forward region need momentum p $>$ 2.8 GeV and in the rear region p $>$ 1.6 GeV is required.

[1] GMUON performs this matching

MV Reconstruction of Muons from CAL Cell Patterns.
The MV algorithm [69] performs a match of a CAL MIP signature with a CTD reconstructed track to identify muons. It is suited for isolated muons of momentum $p > 1$ GeV. The MV algorithm evaluates the compatibility of the cluster shape and energy distribution with a MIP signature like a neural net. The MV combines the energy deposit in different CAL sections (EMC, HAC1, HAC2), the number of cells in these sections and the polar θ and azimuthal ϕ angle and compares these variables to MC samples of muons and hadrons. Based on these quantities, it provides a probability for an energy deposit to be associated with a muon.

MV can be also used in order to identify very forward muons without a track because it is able to detect clusters without a track, and it has a large geometric coverage with a low momentum threshold.

MUFO Muon Reconstruction using FMUON and BAC.
The MUFO reconstruction algorithm [70] matches a track segment from the FMUON to a track reconstructed in the CTD similar to MPMATCH. It can use MUBAC for additional background rejection and provides a momentum fit of the muon using the FMUON and CTD information. The advantages of the Mufo algorithm are similar to the MPMATCH. It represents a sophisticated algorithm including a momentum fit using also the forward muon chambers. The MUFO algorithm is also suited for non-isolated muons. The disadvantages for both algorithms are the limited geometrical coverage due to the restriction to the FMUON-CTD overlap region and a high momentum threshold.

The algorithm can provide also matching between a FMUON track and the reconstructed event vertex without CTD tracking. This is an option which can be used to reconstruct very forward muon tracks, which can not be reconstructed by the CTD due to the acceptance of the tracking chamber.

GLOMU Inclusive Muon Reconstruction at the TLT.
The muon reconstruction algorithm GLOMU [71] is a muon finder for the TLT. It is also available for offline analysis. GLOMU combines the muon track segment reconstruction in the inner chambers of BMUON and RMUON with the tracking in the CTD and a MIP signature in the CAL. In this analysis, GLOMU is only used for efficiency correction purpose.

In Table 5.4 the kinematic acceptance of detector components participating in the muon reconstruction is summarised.

5.10 GMUON

The recently developed GMUON [59] finder combines all the muon reconstruction algorithms discussed above in order to exploit the redundancy for a better signal

detector	momentum threshold	pseudorapidity η^μ range
BMUO	$p_T > 2.5$ GeV	-0.9 $< \eta^\mu <$ 1.2
BMUI	$p_T > 1.2$ GeV	-0.9 $< \eta^\mu <$ 1.2
FMUO	$p > 5$ GeV	2.0 $< \eta^\mu <$ 3.1
FMUI	$p > 2.4$ GeV	1.2 $< \eta^\mu <$ 2.7
RMUO	$p > 2.2$ GeV	-1.75 $< \eta^\mu <$ -1.0
RMUI	$p > 1.0$ GeV	-1.75 $< \eta^\mu <$ -1.0
BAC(central)	$p_T > 2.0$ GeV	continuous
BAC(forward)	$p > 2.8$ GeV	continuous
BAC(rear)	$p > 1.6$ GeV	continuous
BCAL	$p_T > 1.0$ GeV	continuous
FCAL	$p > 1.5$ GeV	continuous
RCAL	$p > 0.9$ GeV	continuous

Table 5.4: Kinematic thresholds for the detector components participating in the muon reconstruction.

.

to background ratio and good geometric coverage and to provide an overall quality variable for the muon candidate. A high quality means, that a high signal to background ratio is to be expected. For lower quality, this ratio decreases, depending on the sample used. GMUON is tuned on an inclusive beauty MC sample. For this sample the relative signal to background ratio increases by about a factor of two for each quality level. Signal means semi-leptonic muons from beauty decay, while background refers here to all other fake muon candidates in beauty events. To rely on the provided quality, the hadronic background of the events should not be much different to the hadronic activity of charm events. This was checked on the charm MC samples used in this analysis.

Examples of finder combinations and the resulting GMUON quality are given in Table 5.5 for muon quality 4 or higher.

Muons in the forward region are detected using the MPMATCH or MUFO finder. The original GMUON quality assignment does not treat some sources of background and overestimates the quality of forward muon candidates. The noise in the muon chambers is not included in the simulations but is sometimes high in data. When an arbitrary track is matched to these noisy cells the identification of muons can be faked. In addition, the forward region suffers from secondary particles produced in the magnets and in material of the beam pipe.

To take into account the background discussed above, the default quality is reduced depending on the used finders. The reduction of spurious hits in the forward muon chamber is based on the number of detector planes used by the forward muon track fit (less than five planes) and the start point of the muon track in FMUON (not the innermost plane). The quality can be recovered, when MUBAC or MV found the same muon candidate. An additional reconstruction in MUBAC increases the quality

quality	finder combination	Ctd match	match prob. or DCA	vtx ass.	MIP prob.	p^μ / η^μ
6	BREMAT 5dof	yes	pr.>0.01	yes	-	-
	MPMATCH/MUFO	yes	pr.>0.05	yes	-	-
	MPMATCH/MUFO + MV	yes	pr.>0.01/< 0.05	-	pr.>0.6	p>1 GeV
5	BREMAT 4dof + MV	yes	pr.>0.01	yes	pr.>0.6	$\|\eta\|$>0.6
	MUBAC + MV	yes	-	yes	pr.>0.6	$\|\eta\|$>0.6
	MUBAC + BREMAT 4dof + MV	yes	pr.>0.01	yes	pr.>0.6	$\|\eta\|$<0.6
	MUBAC + BREMAT 5dof + MV	yes	pr.>0.01	no	pr.>0.6	-
	MPMATCH/MUFO	yes	0.01<pr.<0.05	-	-	-
	MUFO good vtx	no	-	yes	-	-
4	BREMAT 4dof	yes	pr.>0.01	yes	-	-
	MUBAC	yes	DCA<50cm	yes	-	-
	MUBAC + MV	yes	DCA<120cm	yes	pr.>0.6	$\|\eta\|$<0.6
	MUBAC + MIP	yes	DCA<120cm	-	impl.	p_T>2GeV
	MUFO other vtx	no	-	yes	-	-
	MCTS + MV	no	-	no	pr.>0.6	-

Table 5.5: Default muon quality assignments in ORANGE for muons quality of 4 or higher.

quality modification	condition	comment modifier
0	number of Fmuon planes hit > 4	
-2	number of Fmuon planes hit = 4	
-4	number of Fmuon planes hit < 4	minimal number used: 3
-1	no hit in innermost Fmuon chamber	low matching quality
+1	(Mpmatch or Mufo) and Mubac	amplify gain of two identifications
+2	(Mpmatch or Mufo) and Mv	amplify gain of two identifications
-1	only Mubac	identification treat noise in Bac

Table 5.6: Modifications to the default quality of forward muons.

by one, in the case of MV, the quality is increased by two but only to a maximum of the initial quality. Thus the resulting quality is never higher than before the correction. The modification of the quality is given in Table 5.6.

Prompt muons should leave a MIP energy deposit in the HAC2. All muon candidates in the forward region without an energy deposit in HAC2 are thus rejected. In the barrel region the muon probability calculated by the MV finder is used in addition to take into account the passage of muons through gaps in the coverage of the CAL. Only muon candidates without an HAC2 energy deposit and a MV probability p $<$ 0.01 are discarded.

5.11 MC Muon Efficiency Correction

Since the muon reconstruction efficiency is overestimated in the MC, it needs to be corrected. The technique of determination and application of the MC efficiency

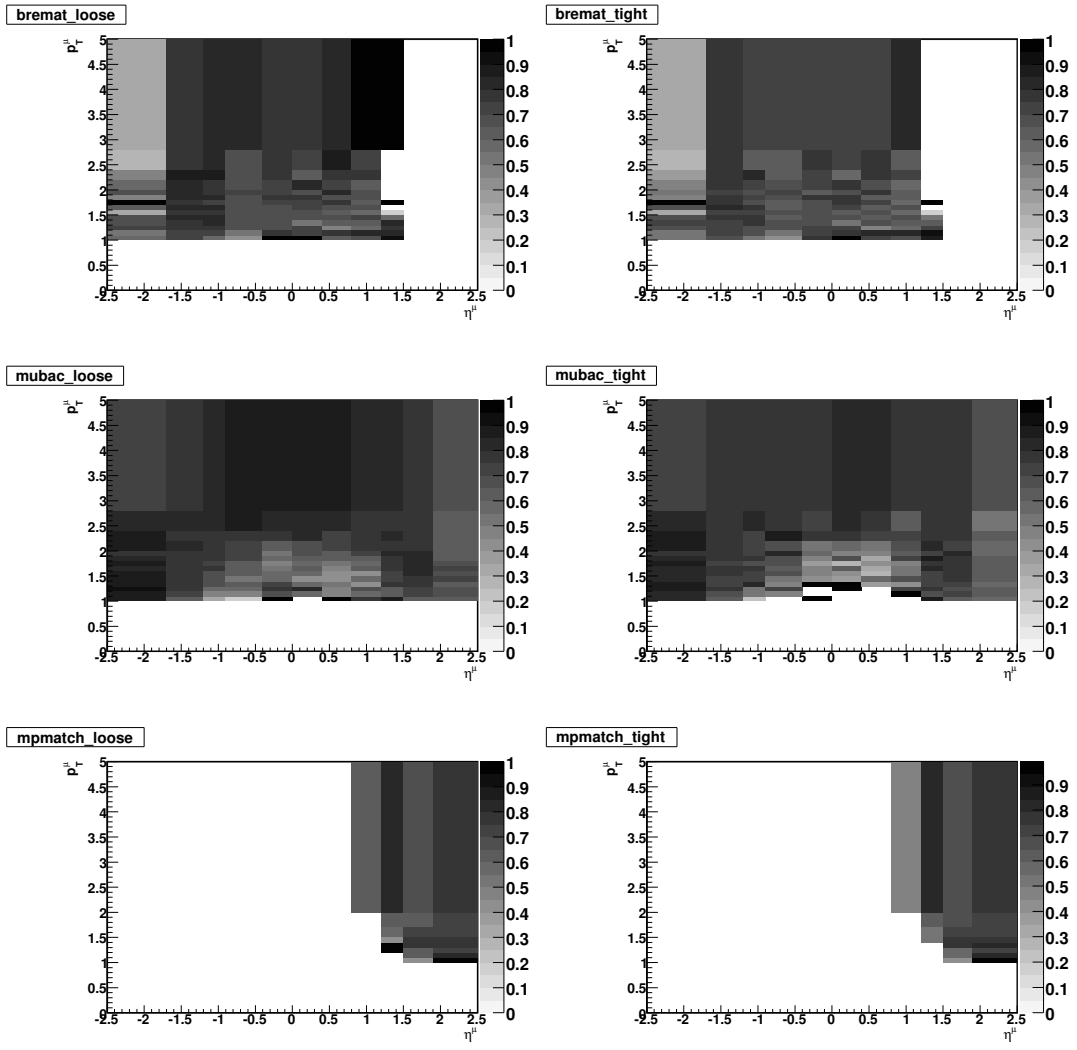

Figure 5.5: Evaluated efficiency correction factors in bins of p_T^μ and η^μ corresponding to the BREMAT (top), MUBAC (middle) and MPMATCH (bottom) finders for loose (left) and tight (right) configurations.

correction is well described in [72] and [73]. Here, only the principle of the determination and application is discussed.

- Muon efficiency determination:
  The determination of the muon efficiency correction is based on the assumption that both the tracking and calorimeter reconstruction are described correctly in the MC simulation. Since both the track reconstruction and calorimeter measurement was tested and tuned in high precision measurements at ZEUS, the assumption can be used in order to measure efficiencies for both the data and MC with respect to the muons found by the MV finder, the measurement of which is based on the energy deposition in the CAL. The efficiency was estimated for the BREMAT, MUBAC and MPMATCH finders and also includes the respective segment track matching efficiency. The influence of muon triggers was unfolded [72]. In addition, the finder efficiencies were determined for the *loose* and *tight* muon track matches, where tight and loose was defined as:

BREMAT: tight requires a track segment matching probability of P $>$ 0.01, loose for all other matches (typical efficiency values for the data and MC are are 30% and 40% respectively).

MUBAC: tight requires a DCA of the matched track to the muon segment on the BAC surface to be less than 0.5 m, loose for all other matches (typical efficiency values for the data and MC are are 60% and 80% respectively).

MPMATCH: tight requires a track segment matching probability of P $>$ 0.05, loose for all other matches with minimal matching probability of P $>$ 0.01 (typical efficiency values for the data and MC are 20% and 30% respectively).

- Muon efficiency correction application:
  The efficiency correction factor is calculated as ratio of the measured efficiencies in data and MC and can be expressed as :

$$factor_{eff.corofX-Finder}(\eta^{\mu}, p_T^{\mu}) = \frac{efficiency_{Data,X-Finder}(\eta^{\mu}, p_T^{\mu})}{efficiency_{MC,X-Finder}(\eta^{\mu}, p_T^{\mu})}, \qquad (5.7)$$

  where the factor for X-Finder (typical value is 0.75) is evaluated for either the tight or loose configuration and depends on both the muon transverse momentum p_T and pseudorapidity η^{μ}. Figure 5.5 exhibits the evaluated efficiency correction factors in bins of the p_T^{μ} and η^{μ} corresponding to the BREMAT (top), MUBAC (middle) and MPMATCH (bottom) finders for loose (left) and tight (right) configurations. These evaluated efficiencies were applied in a random number scheme, where a randomly generated value x is required to be $x < factor_{eff.corfroX-Finder}$. As a consequence, the X-Finder information is changed according to the application of the efficiency correction factor and therefore, the muon quality based on the X-Finder information should be recalculated. In Figure 5.6 a comparison between the rate of muons before (left) and after (right) application of the efficiency correction for combinations of muon finders is shown. The reconstructed MC is fitted to the data by means

of the fit procedure described in Section 6.3. In general, a good improvement can be seen.

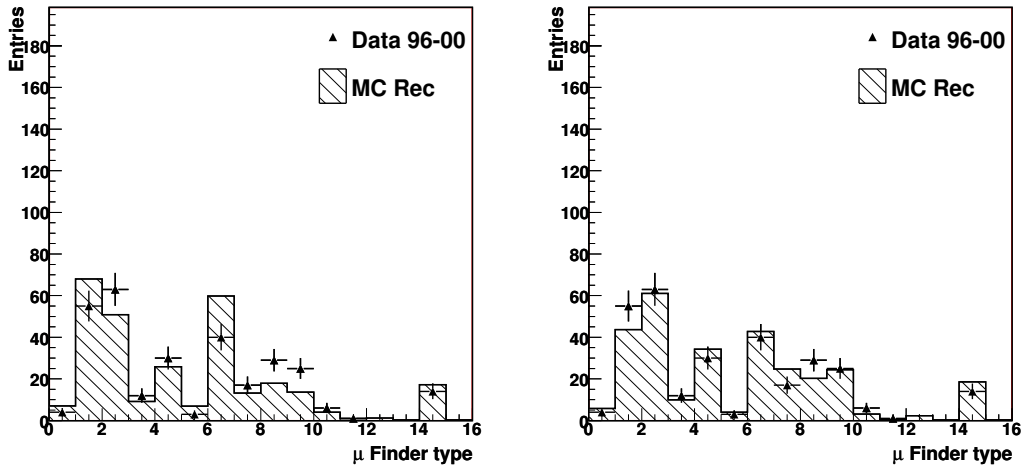

Figure 5.6: Distribution of finder combinations before (left) and after (right) applying the muon efficiency correction. The data points are shown as triangles, wheres as the reconstructed MC is depicted by the hatched histogram. The reconstructed MC is fitted to the data by means of the fit procedure described in Section 6.3.
Bin meaning of the histogram with the combination of muon finders:
0: barrel BREMAT and MUBAC and not MV 1: barrel BREMAT and MUBAC and MV 2: barrel BREMAT and not MUBAC 3: barrel not BREMAT and (MUBAC and not MV) 4: barrel not BREMAT and (MUBAC and MV) 5: rear BREMAT and (MUBAC and not MV) 6: rear BREMAT and (MUBAC and MV) 7: rear BREMAT and not MUBAC 8: rear not BREMAT and (MUBAC and not MV) 9: rear not BREMAT and (MUBAC and MV) 10: forward (MPMATCH or MUFO) and (MUBAC and not MV) 11: forward (MPMATCH or MUFO) and (MUBAC and MV) 12: forward (MPMATCH or MUFO) and not MUBAC 13: forward not (MPMATCH or MUFO) and (MUBAC and not MV) 14: forward not (MPMATCH or MUFO) and (MUBAC and MV).

5.12 D^* Meson Reconstruction

In order to perform the D^* reconstruction, the CTD track reconstruction is used. A D^* meson candidate is reconstructed in the analysis by means of the measurement of the D^* meson decay products in the following mode[2]:

$$D^{*+} \rightarrow D^0(K^- + \pi^+) + \pi_s^+. \tag{5.8}$$

The main advantage of this decay mode is the low combinatorial background and a large enough branching ratio as discussed in Section 2.5.4. The low combinatorial background is a consequence of the small number of D^* decay products required to form the D^* meson candidate and constraints on the D^0 mass (M^{D^0}) and on the

[2]The charge-conjugate state is also included

difference of D^* and D^0 mesons masses ($\Delta M = M^{D^*} - M^{D^0}$).

The kinematics of the decay is dominated by the small phase space available for the two products of the D^* meson decay. The momentum of the D^0 and π_s is only about 40 MeV in the D^* meson rest frame. As a consequence, the π_s is very *slow* and most of its momentum comes from the boost between the D^* meson rest frame and the detector reference system. The D^0 decay products have much more available phase space and their momentum spectra are therefore harder(700 MeV in the D^0 rest frame). The correlation with the D^* kinematics is therefore not as strong as for the π_s. Furthermore, the kaon and pion from the D^0 decay have almost symmetric properties.

The following requirements should be met in order to select tracks for D^* candidate formation:

- Tracks should be associated to the reconstructed vertex,
- Tracks should traverse at least three CTD superlayers,
- Tracks should lie in the pseudorapidity range $|\eta| < 1.75$,
- Tracks should have transverse momentum above 120 MeV.

The reconstruction procedure of D^* meson candidates can be described by the following steps:

- **Formation of D^0 candidates:**
  All combinations of two oppositely charged tracks with transverse momentum above 350 MeV are taken into account to form D^0 candidates. Each of the tracks is alternatively assigned to be a kaon or a pion. No particle identification is used. Only those combinations are considered for which the invariant mass is between 1.4 GeV and 2.2 GeV.

- **Formation of right sign D^* candidates:**
  The considered track pairs are combined with a third track in order to form a D^* candidate with calculated ΔM of the D^* and D^0 candidates less than 170 MeV. The third track should have a charge opposite to the kaon candidate and is assigned to be the π_s. Only those candidates are kept which fall into the D^* signal region: $\Delta M < 170$ MeV and 1.78 GeV $< M^{D^0} <$ 1.95 GeV.

- **Formation of wrong sign D^* candidates:**
  The procedure is the same as for the right sign D^* candidate, but the D^0 candidate consists of two same charged tracks and the D^* charge sign should be ± 1. Since there are no doubly charged D^0 mesons, there is no significant bias from signal reflections.

- **Preselection of D^* candidates:**
  A transverse momentum cut $p_T^{D^*} > 1.5$ GeV and a pseudorapidity cut $|\eta^{D^*}| < 1.5$ are applied to D^* candidates.

In the standard ZEUS D^* analyses it turns out that the shape of the D^* background is well simulated by taking wrong sign D^0 candidates instead. The estimation of the D^* background in the signal region of the ΔM distribution is done by scaling of the wrong sign D^* combination distribution found in the signal region with the normalisation factor evaluated in the side-band above the signal region. Thus, the number of the D^* candidates can be calculated as the difference between the D^* right sign candidates and scaled wrong sign D^* candidates under the signal peak. Both the ΔM (top) and M^{D^0} (bottom) distributions are shown in Figure 5.7 after applying all D^* selection cuts discussed in Section 6.1.4 except the ΔM and M^{D^0} cuts respectively. The dataset was preselected by requirements to have either more than one muon or the muon quality ≥ 4 or $p_T^{\mu} \geq 5$ GeV. Signal peaks can be clearly seen on both distributions in the regions which fulfil the kinematic properties of the decay mode. An additional broad peak around 1.65 GeV in the M^{D^0} distribution corresponds to semi-leptonic and hadronic D^0 decays reconstructed only partially.

5.13 D^*-Muon Kinematic Variables

Reconstructed D^* meson candidates and muons are combinatorially paired in the analysis framework to form D^*-muon pairs. There are two possible charge sign configurations of formed D^* muon pairs: either like- or unlike-sign. This is described in Section 2.6. D^*-muon pairs produced in charm events naturally populate the unlike-sign configuration region due to the unlike-sign of the parent charm quark pairs. The charm event topology reflects the charm quark pair production topology and is mainly back-to-back due to the BGF process which is dominant in the analysis. The topology can be described in spatial reconstruction variables as ΔR or $\Delta\phi$:

$$\Delta R^{D^*\mu} = \sqrt{(\Delta\phi^{D^*\mu\ 2} + \Delta\eta^{D^*\mu\ 2})}, \tag{5.9}$$

where $\Delta\phi^{D^*\mu}$ and $\Delta\eta^{D^*\mu}$ are azimuthal and pseudorapidity difference of the D^* and muon momenta.

In order to describe the D^* muon pair kinematics, a number of reconstruction variables can be introduced. One can define:

$$P^{D^*} = \{E^{D^*}, \vec{p}_T^{\,D^*}, p_z^{D^*}\} \text{ and } P^{\mu} = \{E^{\mu}, \vec{p}_T^{\,\mu}, p_z^{\mu}\}, \tag{5.10}$$

which are four-momenta of the D^* and muon respectively.

The invariant mass of the D^*-muon pair defined as:

$$M^{D^*\mu} = \sqrt{(P^{D^*} + P^{\mu})^2} \tag{5.11}$$

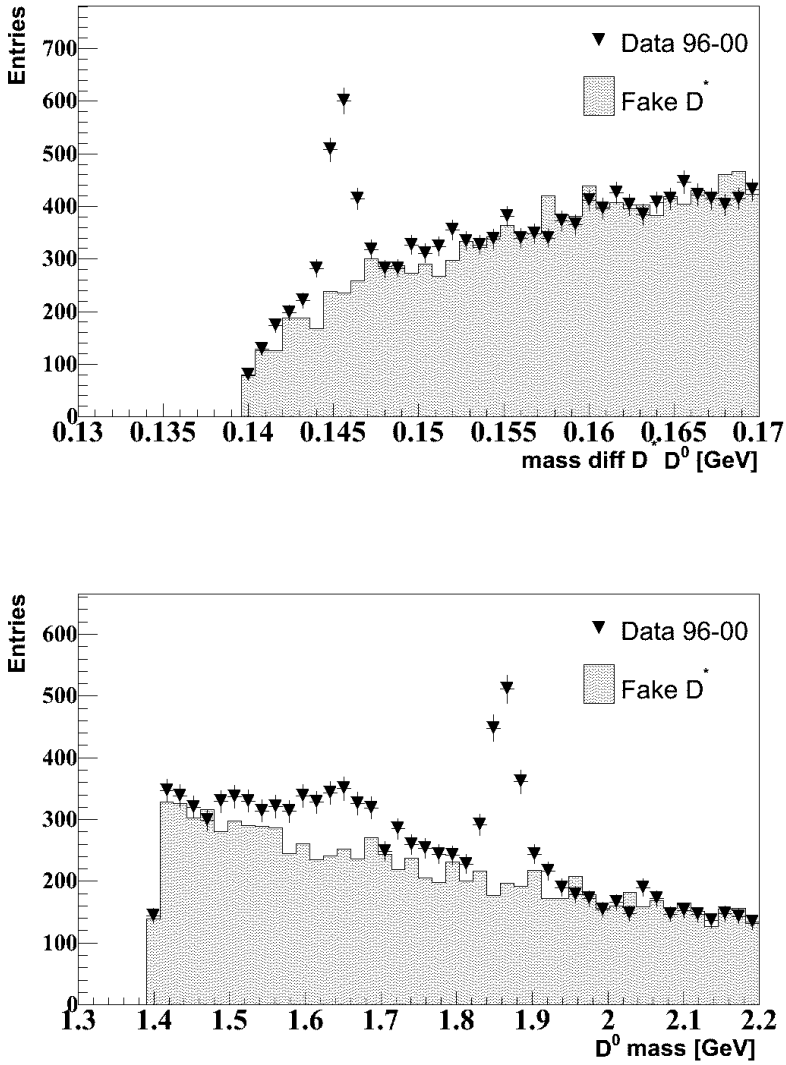

Figure 5.7: ΔM distribution of D^* candidates (top) reconstructed in the dataset (triangle) with all D^* selection cuts except the ΔM cut. Invariant mass of kaon pion pairs (bottom) reconstructed in the dataset (triangle) and participating in the formation of the D^0 candidates after applying selection cuts except the M^{D^0} cut. The estimated contribution of the D^* background (filled area) is also shown.

is proportional to the center-of-mass energy of the struck gluon and the exchanged photon.

Two variables, which are introduced here in order to describe the kinematics of the charm quark pair production, are the scalar sum of transverse momenta and the rapidity of the D-muon pair:

$$p_T^{D^*\mu} = p_T^{D^*} + p_T^{\mu}, \tag{5.12}$$

$$\hat{y}^{D^*\mu} = \frac{1}{2}\ln\left(\frac{\sum_i^{D^*\mu}(E_i + p_{z\ i})}{\sum_i^{D^*\mu}(E_i - p_{z\ i})}\right). \tag{5.13}$$

The $p_T^{D^*\mu}$ kinematic variable is related to the transverse energy of the D^*-muon pair which inherits properties of the parent charm pair system. The $\hat{y}^{D^*\mu}$ quantity is susceptible to the direct and resolved photon processes since the numerator is proportional to the momentum fraction carried by the parton in the proton, whereas the denominator depends on the momentum fraction carried by the parton in the photon. Since charm pair production in BGF is governed by the gluon distribution function, all the introduced kinematic variables are sensitive to the gluon density in the proton.

Chapter 6

Signal Extraction

This chapter is dedicated to the event selection, the signal extraction procedure used in the analysis for the charm D^*-muon pair production cross section measurement and a comparison of the data and MC. At the end of the chapter a discussion of the obtained results is presented.

6.1 Event Selection

In order to study charm quark pair correlations with a D^*-muon tag and calculate the cross section for the process

$$ep \rightarrow e' \, c\bar{c} \, X \rightarrow e' \;\; D^*(D^0(K\pi)\pi_s) \; \mu \;\; X',$$

D^* meson candidates and muons reconstructed in the data and MC samples are selected. The dataset was preselected by the trigger as discussed in Section 5.1 and therefore the trigger slots, which are appropriate for the D^* meson candidate and muon selections, are employed. This analysis covers the inclusive, PHP and DIS regimes of the D^*-muon pair production. To separate the photoproduction and deep inelastic scattering regions, a set of separation cuts is hence applied. To reject non-physics backgrounds such as proton beam-gas interactions or cosmic ray events, a cut on the reconstructed Z vertex position, $|Z_{vertex}| < 50$ cm, is used for all three regimes.

In order to minimise background and separate the charm and beauty enriched regions, the selection cuts applied to D^* candidates, muons and D^*-muon pairs are introduced in this section as well. For the evaluation of the number of charm D^*-muon pairs in the dataset, a signal extraction procedure is provided.

6.1.1 Trigger Selection

Since the HERA I dataset used in the analysis has been preselected by the ZEUS three level trigger system (see Section 3.2.8), the trigger decision is used in order to

select events with at least a D^* meson candidate or at least a muon candidate in the final state. To do this, a set of trigger slots implemented in the ZEUS third level trigger is therefore employed. These trigger slots are presented in Table 6.1, where a brief description for each slot is given as well. These slots are subdivided into three trigger groups: the hadronic, muon and DIS triggers. These trigger groups provide capabilities to select events, which may contain a D^* meson candidate or a muon. The same trigger selection is also used in the MC. Trigger efficiency studies show that the trigger efficiency is about 74%.

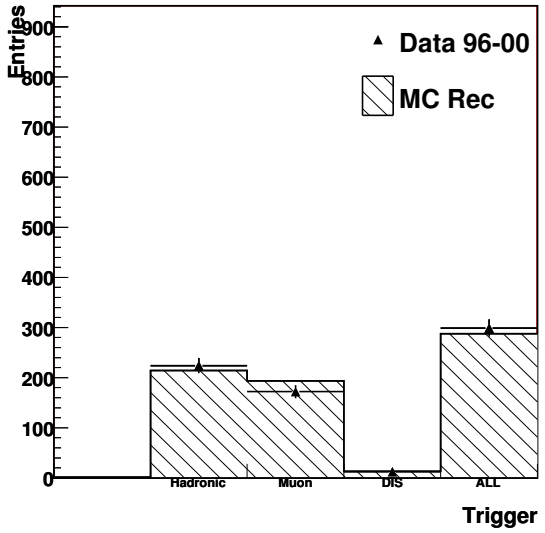

Figure 6.1: Rates in the trigger slots used in the analysis in the charm enriched region defined in Section 6.1.5. The data are presented as triangles. The reconstructed MC is indicated as the hatched histogram. The reconstructed MC is fitted to the data by means of the fitting procedure discussed in Section 6.3. Bin meaning of this histogram (see also Table 6.1):
1(Hadronic): Hadronic and any, 2(Muon): Muon and any, 3(DIS): DIS and any, 4(All): Any.

The trigger slot rate distribution is shown in Figure 6.1, where the data (triangles) and reconstructed MC (hatched histogram) are compared. The reconstructed MC is fitted to the data by means of the fit procedure discussed in Section 6.3. A good agreement between the data and MC can be seen for all bins except the bin *Muon*, where the difference is due to the overestimation of the muon reconstruction efficiency by the inclusive muon trigger in the MC. In the case of the exclusive muon trigger, where the muon efficiency correction is applied, a agreement between the data and MC in this bin is expected. The difference should thus not affect the measured cross sections.

Trigger name	Trigger property	Conditions
Hadronic trigger		
HPP14	Dijet	2 jets with E_T^{jet}>4(4.5) GeV, $\|\eta^{jet}\|$<2.5
HFL10/11	Generic charm	D^* in K$\pi\pi_s$ mode with $p_T^{D^*}$>1.8 GeV
Muon trigger		
MUO3	Barrel/Rear muon	η^{μ}<1.3
HFL1	Dijet + muon	η^{μ}<1.3, 2 jets with E_T^{jet}>3.5 GeV, $\|\eta^{jet}\|$<2.5
EXO11/12	outer Barrel/Rear Muon	outer BMUON and RMUON by GLOMU
DIS27	DIS + muon	$E^{electron}$>7 GeV, η^{μ}<1.3
DIS trigger		
DIS3	Generic DIS	$E^{electron}$>4 GeV, 30 <$E - p_Z$<100 GeV

Table 6.1: The third level trigger slots used in the event selection.

6.1.2 DIS and PHP Separation

Using the reconstructed kinematic variables Q^2 and y described in Section 5.8, the separation between the DIS and PHP regimes is performed by introducing the selection criteria which are described below.

- DIS selection:
  - $40 < E - p_Z < 65$ GeV.
    The lower cut is used in order to reject PHP events, whereas the upper cut is applied to remove residual cosmic ray background.
  - The presence of the DIS electron candidate defined as:
    - At least one electron candidate found by SINISTRA with probability P > 0.9.
    - The electron candidate is required to have an energy $E^e > 10$ GeV. The low Q^2 region is restricted by the acceptance of the RCAL.
    - $y_{el} < 0.7$.
      This cut is used to reduce the fraction of wrongly selected PHP events.
  - $Q^2_{el} > 2$ GeV^2.
  - $y_{JB} > 0.05$.
    This cut requires the presence of a minimal hadronic activity.
- The electron position in the RCAL should be outside of a box with $|X_e| < 13$ cm and $|Y_e| < 7$ cm to ensure a good resolution of the electron energy measurement.
- PHP selection:
  Samples with photoproduction events are selected by requiring the absence of the DIS electron candidate defined above and adding a requirement:

- $E - p_Z < 34$ GeV. This cut is used to reject background from residual DIS events.

6.1.3 Muon Selection

In order to select muon candidates from heavy quark semi-leptonic decays the GMUON finder information is used (see Section 5.10). Only muons with corrected quality of 4 or higher are considered in this analysis. In addition to the muon quality selection, the following cuts are applied to muon candidates:

- muon transverse momentum $p_T^\mu > 1.0$ GeV,
- muon pseudorapidity $|\eta^\mu| < 2.2$.

The cut on the transverse momentum is introduced due to the fact that prompt muons from heavy quark semi-leptonic decays have a harder p_T spectrum than fake muons which are dominant at low p_T. This cut is also correlated with the acceptance provided by the GMUON finder (see Table 5.4). In the real experiment environment the fraction of fake muons is large due to the light flavour background. In the analysis framework, where the D^*-muon tag is exploited, the muon and D^* meson are correlated. The fraction of the fake muons is thus decreased by the requirement of the presence of D^* meson candidate. Studies [76] devoted to the fake muon contamination treatment showed that the MC simulation can be used for the description of the fake muon contamination. The fake muon contamination is therefore treated by means of the MC simulation along with the D^* background discussed in Section 6.1.5. For the rejection of both the D^* and fake muon backgrounds the cut on muon p_T is therefore used. The η cut is defined by the acceptance provided by the GMUON finder and the CTD track reconstruction.

6.1.4 D^* Meson Selection

The selection of D^* meson candidates is based on the D^* reconstruction given in Section 5.12 and the detector acceptance. The following D^* selection cuts are used in the analysis.

- The transverse momentum of the kaon and pion participating in the formation of the D^0 meson candidate $p_T^{K,\pi} > 0.5$ GeV. The cut is used to provide a good ratio of the signal to the D^* background.
- The transverse momentum of the *slow* pion $p_T^{\pi_s} > 0.125$ GeV. This cut corresponds to the requirement of a reliable track measurement in the CTD.
- The pseudorapidity of the pions and kaon $|\eta^{K,\pi,\pi_s}| < 1.75$. This cut is employed due to the acceptance of the CTD.

- The invariant mass of the pion and kaon of the D^0 meson candidate is in the range 1.8 GeV $< \mathrm{M}^{D^0} <$ 1.9 GeV.
- The transverse momentum of the D^* meson candidate $p_T^{D^*} > 1.5$ GeV.
- The pseudorapidity of the D^* meson candidate $|\eta^{D^*}| < 1.5$.

The D^* combinatorial background can be reduced by cutting on the transverse momentum of the D^* meson and the D^* decay products. This is due to the fact that tracks from the decay of a real D^* meson have on average higher transverse momentum than random tracks used to form D^* candidates.

The following cut is applied in order to define a D^* signal region:

- Difference of D^* and D^0 meson candidate masses ΔM should fall in the range 0.1435 GeV $< \Delta M <$ 0.1475 GeV.

Due to the presence of the D^* combinatorial background the wrong sign D^* combination sample is used to estimate the fraction of the D^* background directly from the dataset. The same procedure is performed separately for the reconstructed charm and beauty MC samples. The concept of the D^* background estimation is given in Section 5.12. Since both the D^* meson and the muon are used in the analysis to tag the original charm quark pair, the D^* background is therefore evaluated in the framework of D^*-muon correlations. This is described in the Section 6.1.5.

6.1.5 D^*-Muon Pair Selection

After applying the muon and D^* selection cuts muons and D^* meson candidates are combinatorially coupled to form D^*-muon pairs. Due to the presence of muons coming from semi-leptonic D meson decays and the muon misidentification discussed in Section 5.9, D^*-muon pairs, where a muon corresponds to one of tree tracks participating in the formation of a D^* meson candidate, are rejected.

A D^*-muon pair produced in a charm event naturally has unlike-sign due to the corresponding configuration of the parent charm quark pair. This is discussed in Section 2.6. This unlike-sign configuration region is used as the signal region, whereas the region with the like-sign configuration of the pair can be used as a cross check of the fake muon contamination.

In the direct process the charm event topology with a D^* and a muon is mainly back-to-back. Beauty production events in the unlike-sign configuration are the mix of two sub-processes (see Section 2.6) with the one-side and back-to-back topologies. To separate these two topologies the ΔR kinematic variable defined in Section 5.13 is used. This variable is convenient to describe the kinematics of a D^*-muon pair

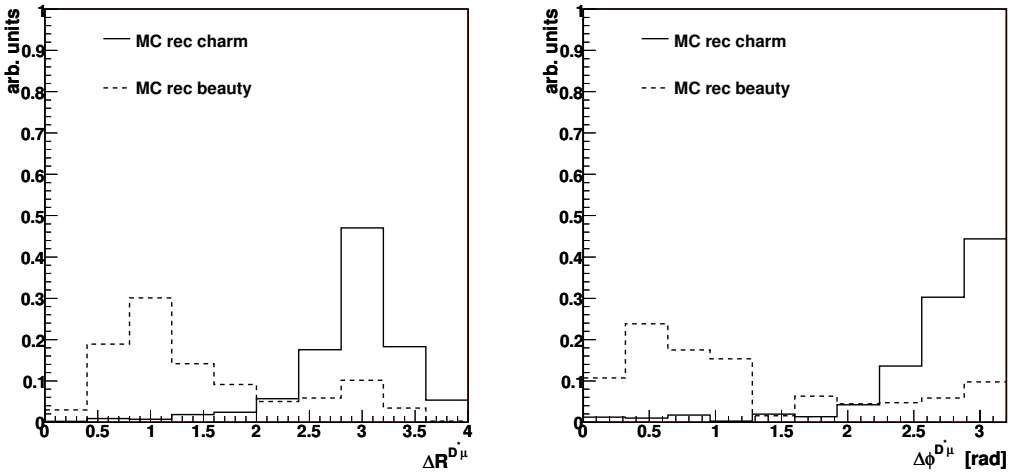

Figure 6.2: The ΔR (left) and $\Delta\phi$ (right) distributions of unlike-sign $D^*\mu$ pairs reconstructed in the charm (solid line) and beauty (dashed line) MC samples.

coming from a single b quark. In Figure 6.2 the ΔR distributions (left) of unlike-sign D^*-muon pairs reconstructed in the charm (solid line) and beauty (dashed line) MC samples are shown. The charm and beauty contributions are given in arbitrary scales. Two topologies can be distinctly separated as it can be seen in this Figure. In order to distinguish between these two topologies a cut $\Delta R < 2$ is therefore introduced. The ΔR cut thus splits the unlike-sign region into beauty ($\Delta R < 2$) and charm ($\Delta R > 2$) enriched regions.

The ΔR variable can be used for the description of the kinematics of the pair in the charm enriched region as well. But in order to avoid the effect of the longitudinal boost of the final state particles in the ep scattering process and study the pair azimuthal correlation, the $\Delta\phi$ variable is more convenient. The $\Delta\phi$ distributions are also shown in Figure 6.2 (right).

Using the ΔR cut and the charge correlation of the D^* and muon the data and reconstructed MC are split into four correlation regions (samples):

1. The unlike-sign configuration and one-side topology ($\Delta R < 2$)
   (the beauty enriched region),
2. The unlike-sign configuration and back-to-back topology ($\Delta R > 2$)
   (the charm enriched region),
3. The like-sign configuration and one-side topology,
4. The like-sign configuration and back-to-back topology.

The D^* background is estimated for these four regions separately. Tagging a muon in the D^* production event means an efficient reduction of the D^* combinatorial back-

ground which arises from the three track random combination forming a D^* meson candidate. In contrast to the previous D^* inclusive measurements, in this analysis the charge correlation of D^* meson candidates and muons affects the D^* background estimation. To avoid the charge correlation in the D^* background evaluation, a blind muon charge schema [76] is used. It turns out that the combinatorial background can be estimated from the dataset itself using the classical wrong sign D^* technique described in the Section 5.12, but with the averaged charge sign configuration of D^*-muon pairs:

$$WSC_{av}^{D^*\mu} = \frac{WSC_{us}^{D^*\mu} + WSC_{ls}^{D^*\mu}}{2}, \tag{6.1}$$

where $WSC_{av}^{D^*\mu}$ is the average of the wrong sign D^* sample, $WSC_{us}^{D^*\mu}$ and $WSC_{ls}^{D^*\mu}$ are the unlike- and like-sign samples of D^*-muon pairs, which contain wrong sign D^* candidates only. In this way the D^* combinatorial background shape is better reproduced for both the like- and unlike-sign cases.

Evaluation of the fake muon contamination is based on the MC simulation [76]. Event information from the generator level (*true level*) is therefore exploited together with the event reconstruction information. Reconstructed D^*-muon pairs are associated to corresponding true level D^*-muon pairs coming from heavy quark pairs. When a D^* meson candidate from the D^*-muon pair has been matched on the true level but the muon has not then the muon is assigned to be fake. The fake muon contamination estimated in this way can be further subtracted. The D^* background also contains fake muons. These fake muons are simultaneously eliminated along with the D^* background subtraction.

To reduce the D^* background, an additional cut $f^{D^*} > 0.15$ for the back-to-back topology sample is applied. The f^{D^*} quantity is defined according the following formula:

$$f^{D^*} = \frac{p_T^{D^*}}{\sum_i^{\text{ZUFO}} |\vec{p}_{T\ i}|}, \tag{6.2}$$

where $\vec{p}_{T\ i}$ is the transverse momentum of ZUFO i and the sum runs over all reconstructed ZUFOs. Cutting on f^{D^*} rejects the fake D^* mesons formed by the random combination of three tracks with low transverse momenta. The cut is appropriate for the back-to-back topology because the D^* meson and muon are produced from the different heavy quarks.

For the one-side topology in addition to the the D^* selection cuts, a combinatorial D^* background reduction cut $f^{D^*\mu} > 0.2$, which is similar to the f^{D^*} cut, is used. The $f^{D^*\mu}$ quantity is calculated as:

$$f^{D^*\mu} = \frac{p_T^{D^*\mu}}{\sum_i^{\text{ZUFO}} |\vec{p}_{T\ i}|}, \tag{6.3}$$

where the sum in the denominator is a scalar sum of the transverse momenta of all reconstructed ZUFOs. A D^*-muon pair produced in the beauty enriched region

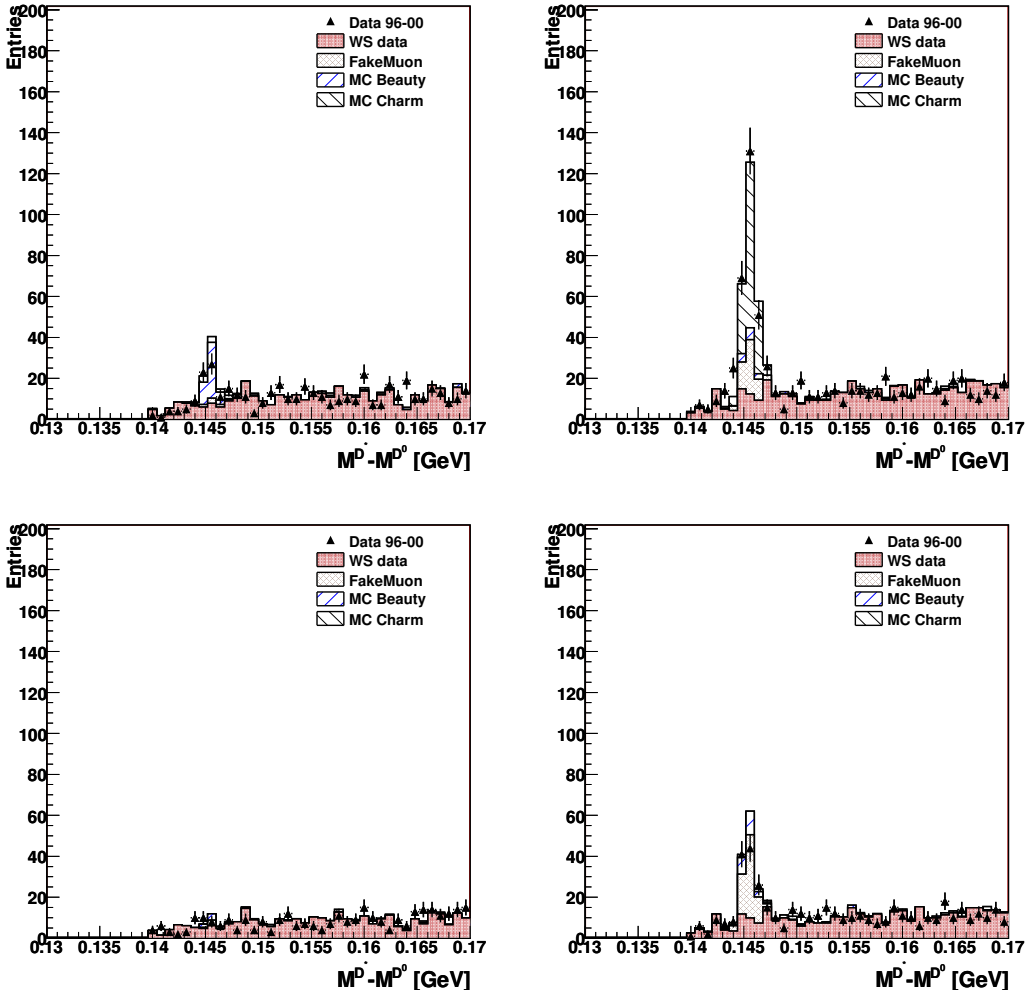

Figure 6.3: The ΔM distributions of the four different correlation regions: 1. unlike-sign configuration and one-side topology (top left), 2. unlike-sign configuration and back-to-back topology (top right), 3. like-sign configuration and one-side topology (bottom left), 4. like-sign configuration and back-to-back topology (bottom right). All cuts are applied except the ΔM cut. The ΔR cut separates the one-side ($\Delta R < 2$) and back-to-back topologies. The data are indicated as triangles. The charm and beauty contributions evaluated by the signal extraction procedure (see Section 6.3) are given as well. The estimated D^* background and the fake muon contamination are indicated according to the plot legends.

comes essentially from the semi-leptonic decay of the B meson into both a D^* and a muon. Therefore, the cut is more convenient for this topology. The effect of applying the cut is the same as in case of the charm enriched region.

The invariant mass $M^{D^*\mu}$ calculated for the beauty D^*-muon pair in the beauty enriched region is restricted by the B meson mass (5 GeV, upper limit). The lower limit of the $M^{D^*\mu}$ is dictated by the fake muon contamination rejection (3 GeV) [76].

Figure 6.3 represents the ΔM distributions with all selection cuts except the ΔM cut for the four correlation regions: unlike-sign and one-side topology (top left), unlike-sign and back-to-back topology (top right), like-sign and one-side topology (bottom left), like-sign and back-to-back topology (bottom right). The data points are shown as triangles. The charm and beauty contributions evaluated by the fit procedure (see Section 6.3) are given as well. The estimated D^* background and the fake muon contamination are indicated according to the plot legends. In this Figure signal peaks, which correspond to the different correlation regions, can be clearly seen. As it is expected, in the unlike-sign configuration and the back-to-back topology charm production is dominant, whereas the beauty enriched region exhibits the dominance of beauty production. The statistics of the charm enriched region is larger than the beauty enriched region. Furthermore, the statistic of this analysis is larger than in [76] due to the selection cuts summarised in Section 6.2 and the muon identification redundancy provided by the GMUON finder. The like-sign region shows that charm fake muons and beauty production contribute to this configuration as expected and the MC provides the good description of a fake muon contamination.

6.2 Summary of Final Cuts

The final offline cuts applied in this analysis are summarised below.

INCLUSIVE:

- $|Z_{vertex}| < 50$ cm.
- No separation between DIS and PHP is performed.

DIS:

- $|Z_{vertex}| < 50$ cm.
- 40 GeV $< E - p_Z <$ 65 GeV.
- The presence of the DIS electron candidate defined as:
  - At least one electron found by SINISTRA with probability P > 0.9.
  - $E^e > 10$ GeV.
  - $y_{el} < 0.7$.

- $Q^2_{el} > 2$ GeV^2.
- $y_{JB} > 0.05$.
- Electron position box cut $|X_e| < 13$ cm and $|Y_e| < 7$ cm.

PHP:

- $|Z_{vertex}| < 50$ cm.
- $E - p_Z < 34$ GeV.
- Absence of the DIS electron candidate defined above.

D^*:

- 1.81 GeV $<$ M$^{D^0}$ $<$ 1.92 GeV.
- 0.1435 GeV $<$ M$^{D^*}$ - M$^{D^0}$ $<$ 0.1475 GeV.
- $p_T^{D^*} > 1.5$ GeV.
- $|\eta^{D^*}| < 1.5$.
- $p_T^{K,\pi} > 0.5$ GeV.
- $p_T^{\pi_s} > 0.125$ GeV.
- $|\eta^{K,\pi,\pi_s}| < 1.75$.

μ:

- $p_T^{\mu} > 1.0$ GeV.
- $|\eta^{\mu}| < 2.2$.
- Quality ≥ 4.

$D^*\mu$:

ΔR > 2 charm enriched region
- $f^{D^*} > 0.15$.

ΔR < 2 beauty enriched region
- $f^{D^*\mu} > 0.2$.
- 3 GeV $<$ M$^{D^*\mu}$ $<$ 5 GeV.

6.3 Charm Signal Extraction Procedure

In this section the charm signal extraction procedure is described. The main aim of the extraction procedure is the evaluation of the number of D^*-muon pairs from charm production in the data. In order to do this samples with D^*-muon pairs reconstructed in the charm and beauty MCs are fitted to the data. The MC luminosities are normalised to the data luminosity before the fit. In order to consider only the signal in the reconstructed MC samples, the estimated D^* background is subtracted from these samples using the same procedure as for the data. Exploiting the angular correlation of D^*-muon pairs in the signal region the evaluation of

the scale factor f_{ch} for charm (f_{bt} for beauty) contribution in the dataset is done. To perform this evaluation, a simultaneous $\Delta\phi$ or ΔR fit for both the charm and beauty enriched regions, is performed. As previously discussed, the $\Delta\phi$ variable is more convenient for the back-to-back topology and the $\Delta\phi$ fit is therefore treated as the reference fit, whereas the ΔR fit is used as a systematic uncertainty check.

In this analysis, for evaluation of the charm f_{ch} (as well as beauty f_{bt}) scale factor, two kinds of fit procedures are used: χ^2 and likelihood technique (LH). In both cases the MINUIT minimisation package [78] in the ROOT [79] environment is used. Because of the low statistics and the implicit property of a quantity to be distributed in a bin under the Poisson law, the χ^2 fit, which implies Gaussian behaviour, is expected to systematically underestimate the scale factor. In contrast to the χ^2 fit, the LH fit treats low bin statistics correctly. However, the LH fit cannot treat bins with negative content, whereas the χ^2 fit does. With regard to what is said above, the LH fit is used in this analysis to evaluate the charm scale factor. The χ^2 fit is employed as a cross check.

LH fit:

The LH fit procedure used in the analysis is the fraction fitter included in the ROOT package. The fraction fitter contains the correct MC error treatment [80] and it provides ample opportunities to use the ROOT graphical and computational capabilities. To avoid appearance of bins with negative value, the D^* background contribution estimated from the data are included and fixed in the fit procedure.

χ^2 fit:

In case of the χ^2 fit the following minimisation function is used:

$$F(f_{ch}, f_{bt}) = \sum_{i}^{\Delta\phi\ histo\ bins} \frac{(N_i^D - (f_{ch} \cdot N_{ch\ i}^{\mathrm{Mc}} + f_{bt} \cdot N_{bt\ i}^{\mathrm{Mc}}))^2}{\sigma_{D\ i}^2 + \sigma_{\mathrm{Mc}_{ch\ i}}^2 + \sigma_{\mathrm{Mc}_{bt\ i}}^2}, \qquad (6.4)$$

where N_i^D, $N_{ch\ i}^{\mathrm{Mc}}$ and $N_{bt\ i}^{\mathrm{Mc}}$ are contents of i^{th} bin in $\Delta\phi$ histograms of the data and charm and beauty reconstructed MC samples respectively and $\sigma_{D\ i}$, $\sigma_{\mathrm{Mc}_{ch\ i}}$ and $\sigma_{\mathrm{Mc}_{bt\ i}}$ are statistical errors in the i^{th} bin of the corresponding histograms. The function $F(f_{ch}, f_{bt})$ is minimised by the MINUIT package.

Numbers of charm $N_{ch\ rec}^{D^*\mu}$ and beauty $N_{bt\ rec}^{D^*\mu}$ D^*-muon pairs extracted from the data in the charm enriched region are calculated according to the following equation:

$$N_{ch,bt\ rec}^{D^*\mu} = N_{ch,bt\ rec\ MC}^{D^*\mu} \cdot f_{ch,bt} - N_{ch,bt\ fake}^{D^*\mu},$$

where $N_{ch,bt\ rec\ MC}$ is the number of charm (or beauty) D^*-muon pairs reconstructed in the charm (or beauty) MC sample. $N^{D^*\mu}_{ch,bt\ fake}$ is the number of charm (beauty) fake muons which is calculated as

$$N^{D^*\mu}_{ch,bt\ fake} = N^{D^*\mu}_{ch,bt\ fake\ MC} \cdot f_{ch,bt},$$

where $N^{D^*\mu}_{ch,bt\ fake\ MC}$ is the number of charm (beauty) muons reconstructed in the charm (beauty) MC and found as fake by matching with true level information.

6.4 MC and Data Comparison

After the event selection and the signal extraction procedure (see Section 6.3), where the charm f_{ch} and beauty f_{bt} scale factors are evaluated for the inclusive, PHP and DIS regimes, control plots for both the charm and beauty enriched regions are presented in this section. Control plots for the like-sign configuration can be found in Appendix 10.1.

Control plots are divided into three groups, which correspond to the inclusive, PHP and DIS regimes. The plots of the first group are shown in Figures 6.4 and 6.5 for the charm and beauty enriched regions respectively. The plots of the second and third groups are given in Figures 6.6 and 6.7 as well as in Figures 6.8 and 6.9 respectively for the charm and beauty enriched regions. The data are shown as triangles. The charm and beauty contribution are hatched according to the plot legends. The fake muon contamination and the D^* background are indicated as well.

For the inclusive D^*-muon production the control plots shown in Figures 6.4 and 6.5 for the charm and beauty enriched regions respectively exhibit a comparison between the data and MC for the following kinematic variables:

- The D^* transverse momentum $p_T^{D^*}$,
- The D^* pseudorapidity η^{D^*},
- The muon transverse momentum p_T^{μ},
- The muon pseudorapidity η^{μ},
- The scalar sum of the D^* and muon transverse momenta $p_T^{D^*\mu}$,
- The vectorial sum of the D^* and muon transverse momenta $p_{T\ v}^{D^*\mu}$,
- The D^*-muon pair rapidity $\hat{y}^{D^*\mu}$,
- The D^*-muon pair invariant mass $M^{D^*\mu}$,
- The pseudorapidity difference $\Delta\eta^{D^*\mu}$ between the D^* and the muon,

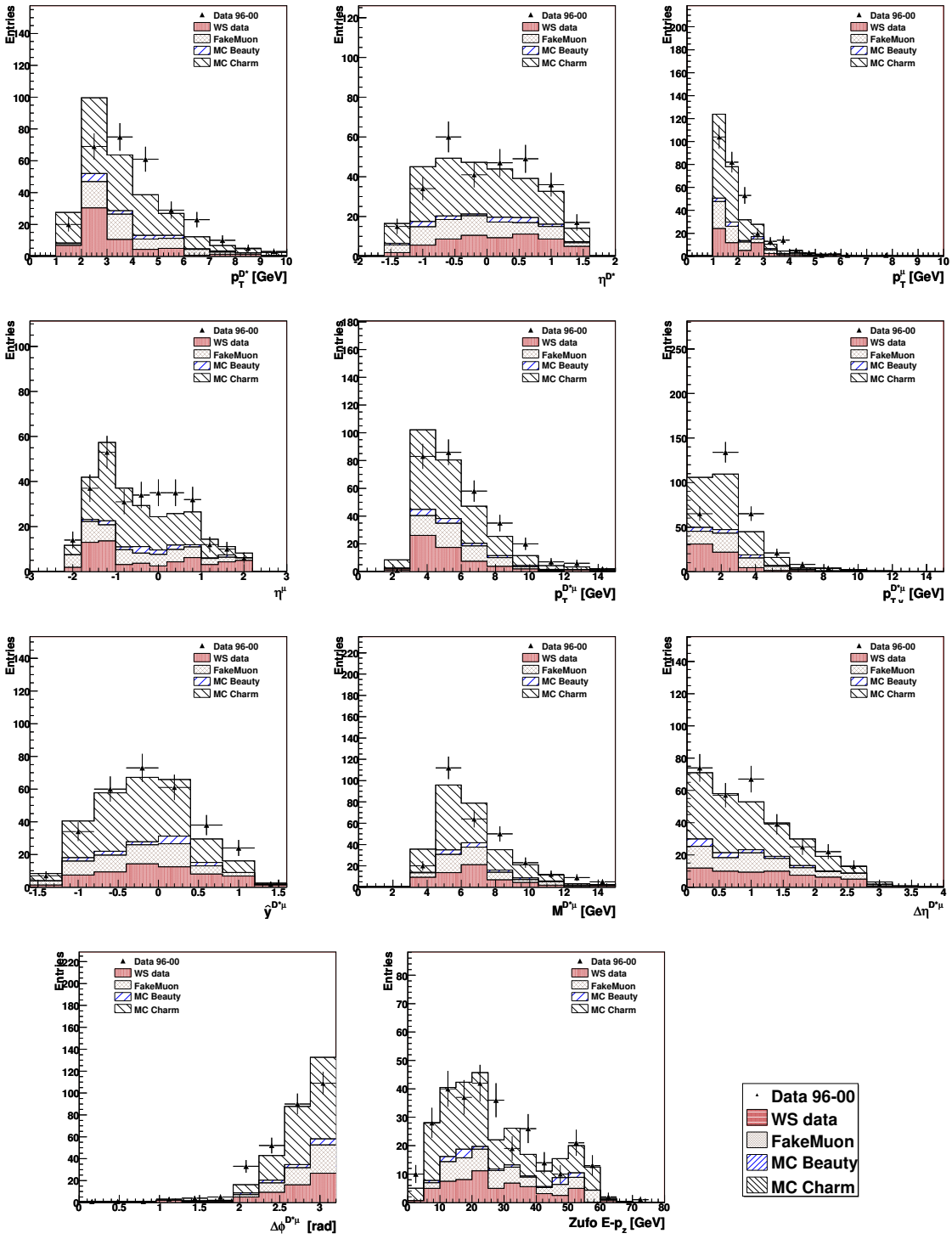

Figure 6.4: Control plots for the inclusive D^*-muon pair production in the charm enriched region. The data are shown as triangles. Contributions of charm and beauty productions as well as the D^* and fake muon background are also given.

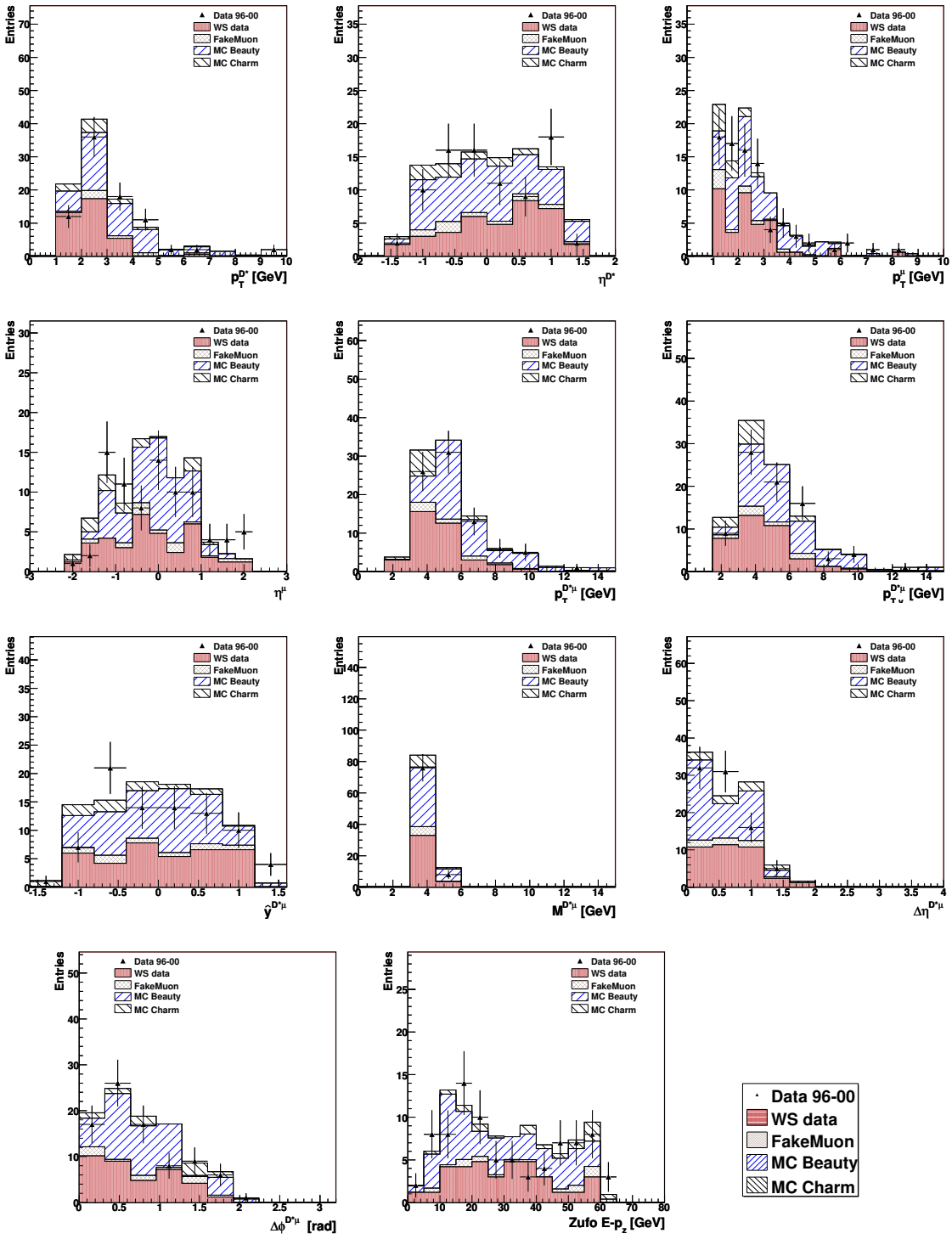

Figure 6.5: Control plots for the inclusive D^*-muon pair production in the beauty enriched region. The data are shown as triangles. Contributions of charm and beauty productions as well as the fake D^* and fake muon background are also given.

- The azimuthal angle difference $\Delta\phi^{D^*\mu}$ between the D^* and the muon,

- The ZUFO $E - p_z$ variable.

In general the comparison shows that the MC is in an agreement with the data. But some differences can be observed in the $p_T^{D^*}$ and $\Delta\phi^{D^*\mu}$ spectra for the charm enriched region. This is discussed later in Section 6.5.

The D^* transverse momentum distributions for the charm and beauty enriched regions show the rise of the fraction of the D^* background for low $p_T^{D^*}$ as expected. In the charm enriched region the MC overestimates the data at the low $p_T^{D^*}$ region and underestimates the data at the higher $p_T^{D^*}$ values, whereas in the beauty enriched region the $p_T^{D^*}$ distribution exhibits a good agreement. The η^{D^*} distributions in both the charm and beauty enriched regions reflect the CTD acceptance and demonstrate a good agreement between the data and MC.

In both the charm and beauty enriched regions the MC describes the shape of the data p_T^{μ} distribution well. At low p_T^{μ}, the net effect of the fake muon and D^* backgrounds can be clearly seen. The data muon pseudorapidity distributions are also well described by the MC. The bump near value -1.2 in the η^{μ} distribution for the charm enriched region is mainly due to the fact that the RCAL has only one section of the EMC and one section of the HAC. It reduces the muon absorption and results in a rise of the muon detection rate.

The $p_T^{D^*\mu}$, $\hat{y}^{D^*\mu}$, $M^{D^*\mu}$, $\Delta\phi^{D^*\mu}$ and $p_{T\ v}^{D^*\mu}$ distributions demonstrate the kinematic properties of the D^*-muon system. In the beauty enriched region the MC provides a good description of the data. In case of the charm enriched region the MC exhibits a good agreement with the data for the $p_T^{D^*\mu}$, $\hat{y}^{D^*\mu}$ and $M^{D^*\mu}$ spectra, whereas differences between the data and MC in the shapes of the $p_{T\ v}^{D^*\mu}$ and $\Delta\phi^{D^*\mu}$ distributions is seen. The difference found in the $p_{T\ v}^{D^*\mu}$ histogram is due to the observed difference in $p_T^{D^*}$ spectrum since the D^*-muon system inherits of the kinematic properties of the D^* and the muon. Possible sources of the divergence in the $\Delta\phi^{D^*\mu}$ distribution can be the same as in case of the $p_T^{D^*}$ and is discussed later in Section 6.5.

For the PHP regime the control plots given in Figure 6.6 and 6.7 show a comparison of the data and MC in the charm and beauty enriched regions. For the DIS regime control distributions are given in Figures 6.8 and 6.9 for the charm and beauty enriched regions. In case of PHP a y_{JB} spectrum is also presented. For DIS additional y_{Si}, Q^2_{Si} and scattered electron energy E^e distributions are given. All plots exhibit a good agreement between the data and MC. In principle, the inclusive regime contains PHP as well as DIS. Therefore, the observed differences in the inclusive production are also present in the PHP regime. As it can be seen, the statistics in the DIS region is low and only a general statement about agreement can be made.

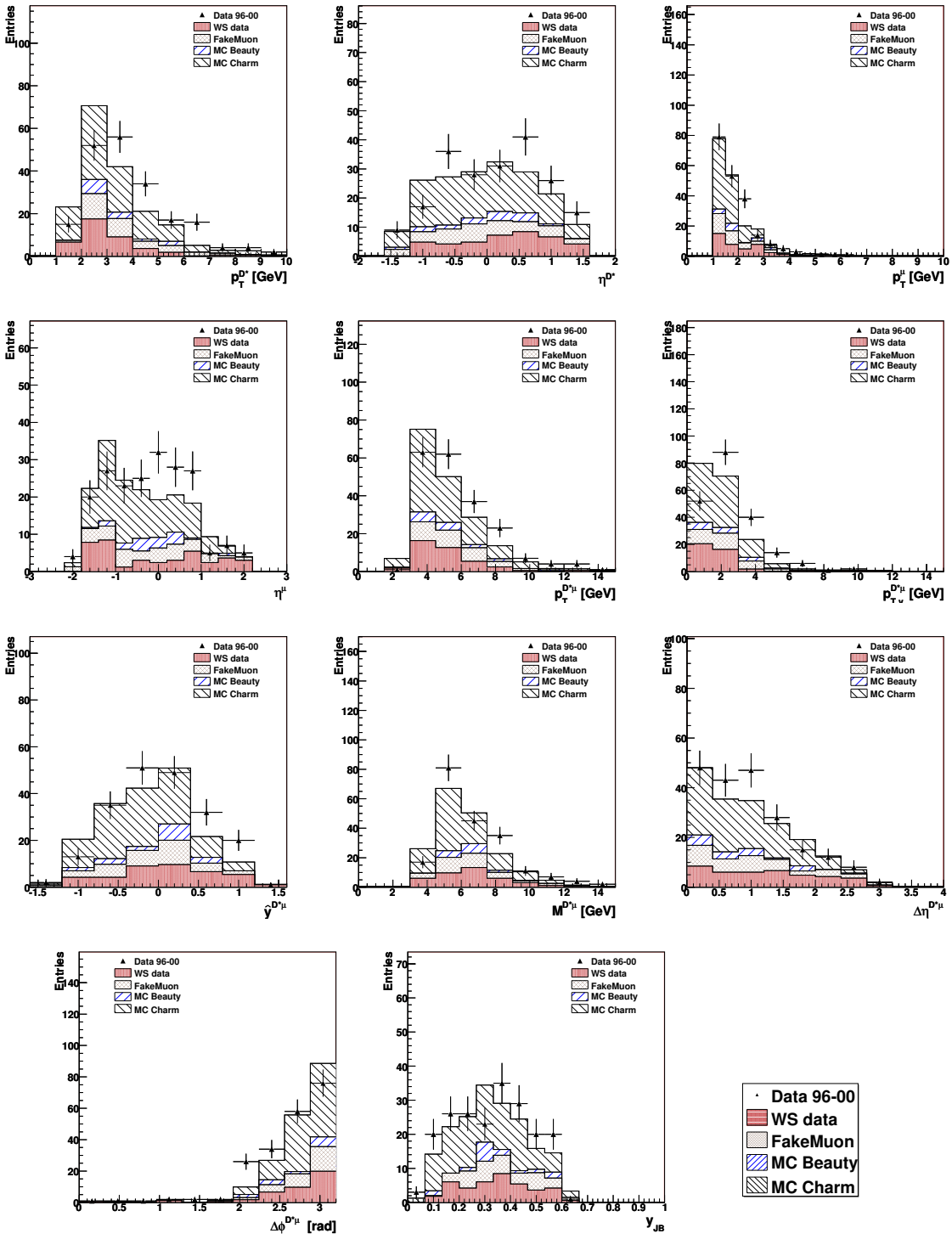

Figure 6.6: The control plots for the PHP regime in the charm enriched region. The data are shown as triangles. Contributions of charm and beauty productions as well as the D^* and fake muon background are indicated according to the plots legends.

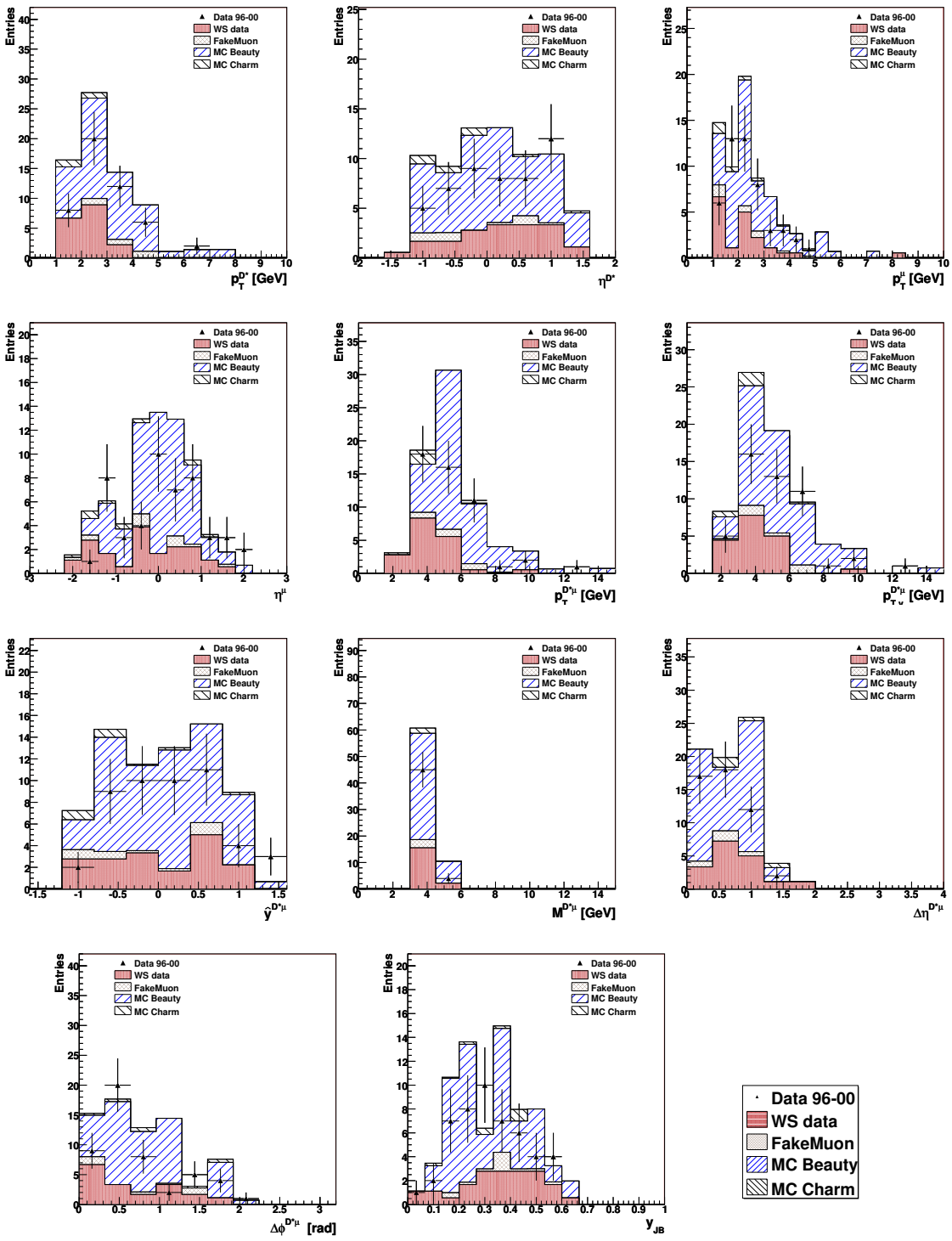

Figure 6.7: The control plots for the PHP regime in the beauty enriched region. The data are shown as triangles. Contributions of charm and beauty productions as well as the D^* and fake muon background are indicated according to the plots legends.

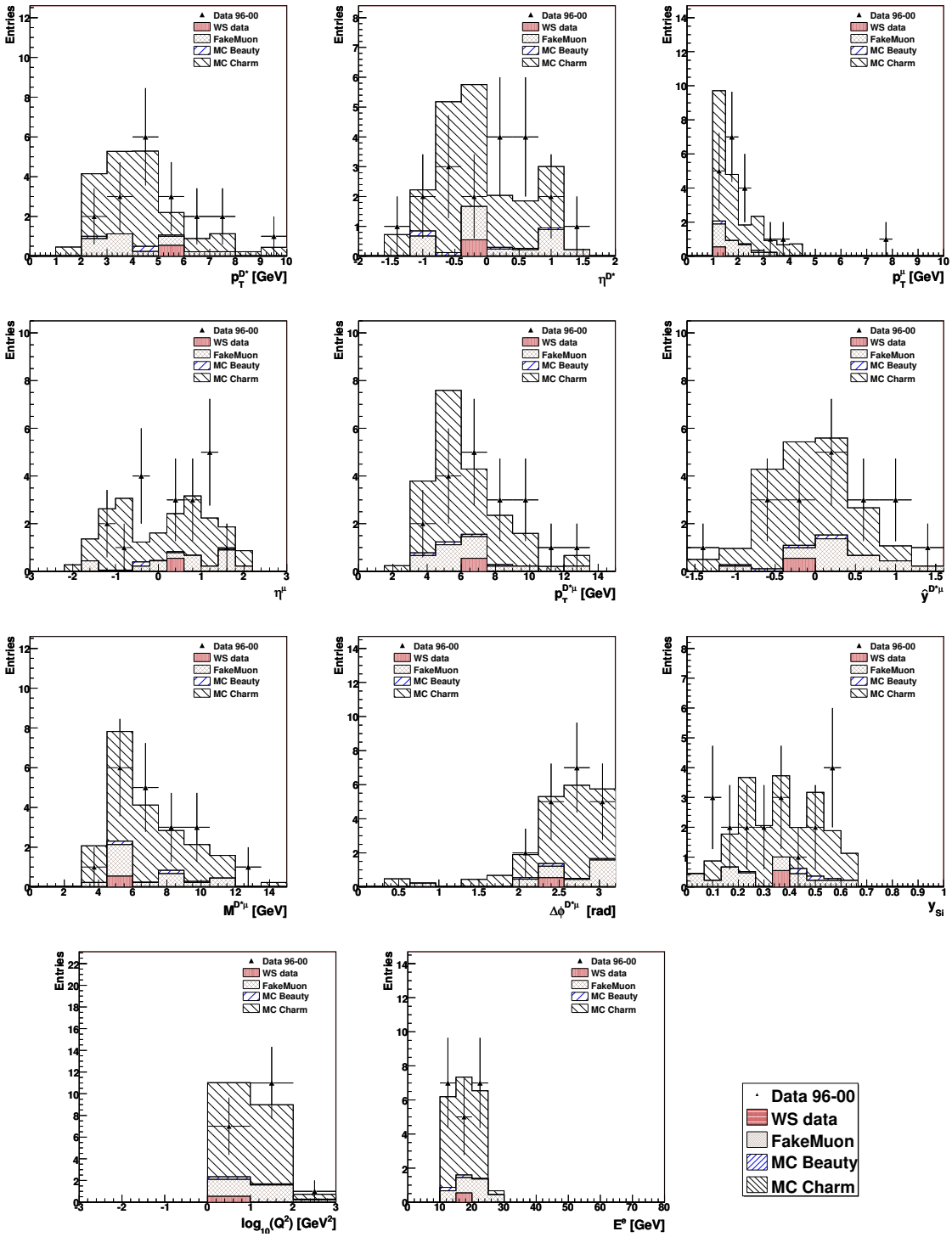

Figure 6.8: The control plots for the DIS regimes in the charm enriched region The data are shown as triangles. Contributions of charm and beauty productions as well as the D^* and fake muon background are indicated according to the plots legends.

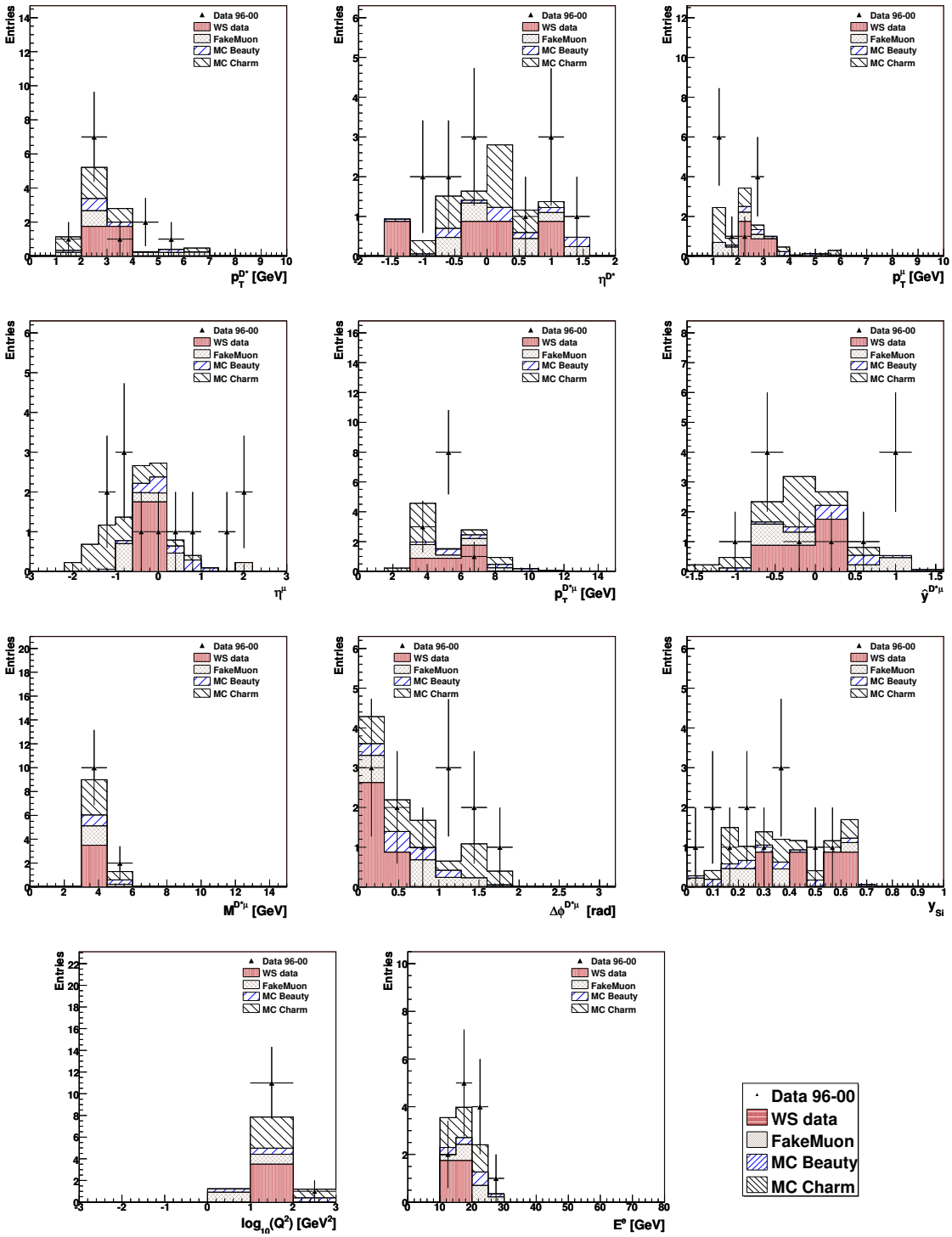

Figure 6.9: The control plots for the DIS regimes in the beauty enriched region The data are shown as triangles. Contributions of charm and beauty productions as well as the D^* and fake muon background are indicated according to the plots legends.

6.5 Discussion

In this section the differences observed for inclusive production in the MC and data in the charm enriched region are discussed.

As it is noticed above, the MC prediction shows a softer D^* transverse momentum distribution with respect to the data (see Figure 6.4). The reconstruction of the $p_T^{D^*}$ quantity has a good resolution and correlation with corresponding information from the true generator level (see Section 7.4). The origin of the problem remains still unclear. This might be due to the incomplete simulation of the hadronisation process, which is based on the parton shower approach, or higher order effects. That is the subject of further studies.

The next plot, which should be discussed, is the $\Delta\phi$ distribution (see Figure 6.4). A peak around π radians corresponding to the clear back-to-back topology is clearly seen. But in the region below 2.5 radians one can distinguish the difference between the data and the MC, which might be due to the same reasons as in case of the difference observed in the $p_T^{D^*}$ spectrum. It should be noted that the $p_T^{D^*}$ and $\Delta\phi$ kinematic variables are not independent. This can be understood from the fact that in the case of the BGF process an additional gluon radiation can spoil the original back-to-back topology of the quark pair and decrease the outgoing quark transverse momentum.

In order to study the differences discussed above and compensate their effects on the acceptance, the following procedures are performed in the analysis environment for the inclusive D^*-muon pair production in the charm enriched region:

- Reweighting of the $p_T^{D^*}$ spectrum.
  A scale factor for each bin of the $p_T^{D^*}$ histogram is calculated and applied in the MC reconstruction and the corresponding MC generator true level. Only the fraction of charm events is considered to be reweighted under an assumption that the beauty production simulation is correct. The result of the $p_T^{D^*}$ spectrum reweighting is that the data $p_T^{D^*}$ distribution is well described by the MC, but the difference in the $\Delta\phi$ distribution is not cancelled (see Figure 6.10 top).

- Reweighting of the $\Delta\phi^{D^*\mu}$ spectrum.
  The same procedure described above is performed for the $\Delta\phi$ distribution. It results in an agreement in the $\Delta\phi$ spectrum for the data and the MC, but the $p_T^{D^*}$ spectrum shows only small improvement (see Figure 6.10 second row).

- Reweighting of the direct and non-direct fractions.
  Fractions of charm direct and non-direct events in the PYTHIA prediction are reweighted. The non-direct fraction is scaled up by factor 3, whereas the direct fraction is scaled down by a factor to recover the normalisation of the sum of the two processes. The factor of three is reasonable since the fraction

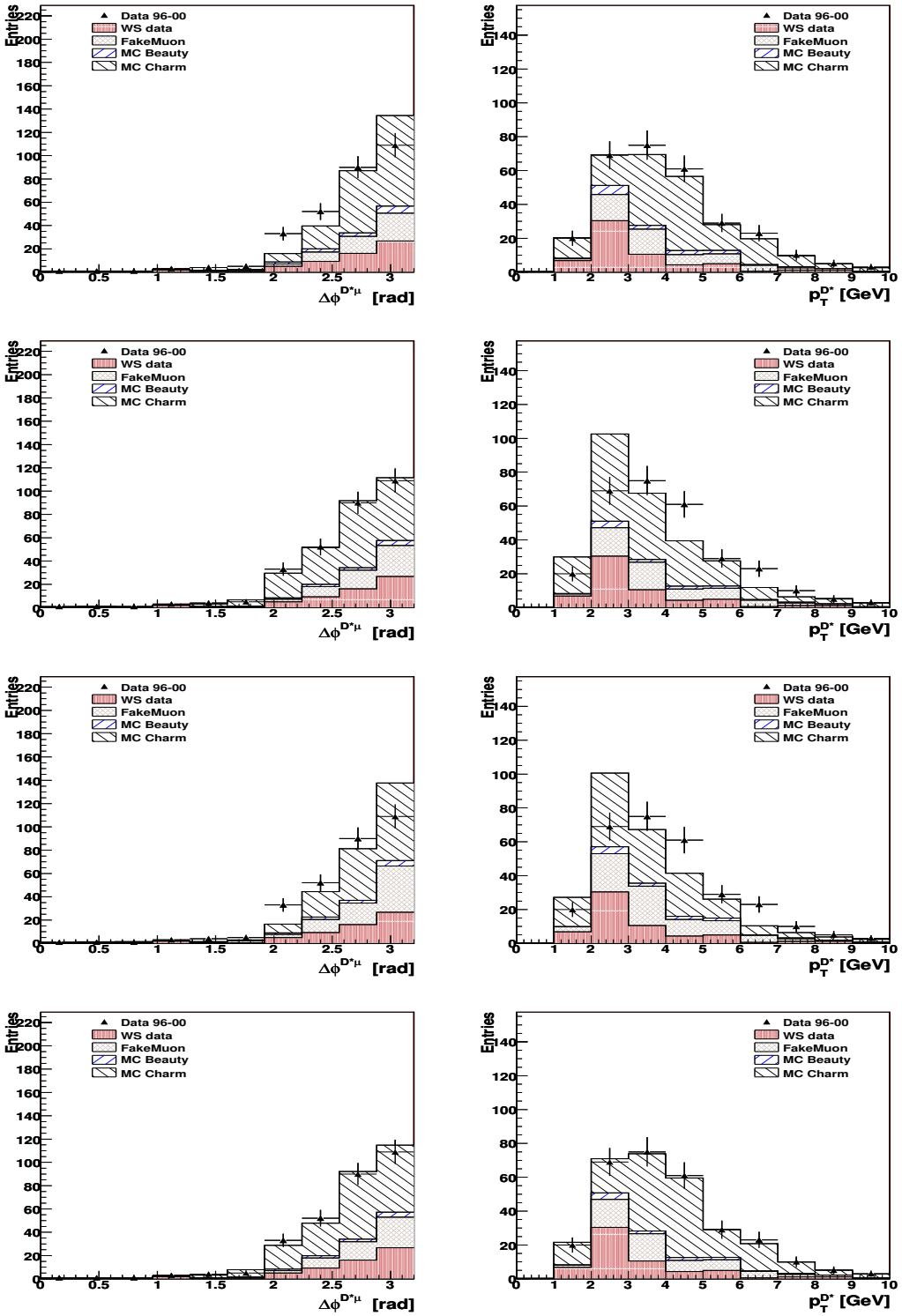

Figure 6.10: The $\Delta\phi$ and $p_T^{D^*}$ spectra after the $p_T^{D^*}$ distribution reweighting (top left and right), after the $\Delta\phi$ distribution reweighting (second row left and right), after the reweighting of the direct and non-direct fractions (third row left and right) and after the simultaneously reweighting of the $\Delta\phi^{D^*\mu}$ and $p_T^{D^*}$ spectra (bottom left and right). The data are shown as triangles. Contributions of charm and beauty productions as well as the D^* and fake muon background are indicated according to the plots legends.

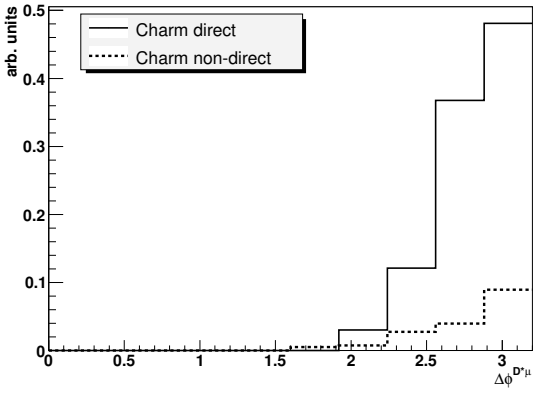

Figure 6.11: The fraction of direct and non-direct events in the charm enriched region.

of the non-direct events is roughly three times lower than the fraction of direct events in the region $\Delta\phi^{D^*\mu} < 2.5$ (see Figure 6.11), where the difference is observed. As a result, no significant improvement is observed (see Figure 6.10 third row). In contrast to direct events the $\Delta\phi^{D^*\mu}$ distribution of non-direct events is expected to be flat, but in Figure 6.11 one can see a peak around π radians. Because the non-direct processes contain the hadron-like process (gluon-gluon fusion), which is similar to the direct process, and the gluon splitting contribution (double charm quark pair production), the non-direct $\Delta\phi^{D^*\mu}$ distribution has such behaviour.

- Reweighting of the $\Delta\phi^{D^*\mu}$ and $p_T^{D^*}$ spectra simultaneously.
  Finally, the simultaneous reweighting the $\Delta\phi^{D^*\mu}$ distribution along with the $p_T^{D^*}$ spectrum is performed. This results in a good agreement between the data and MC (see Figure 6.10 bottom).

As a conclusion of the performed study, one can say, that differences observed in the $\Delta\phi^{D^*\mu}$ and the $p_T^{D^*}$ distributions seem to be almost independent on each other and the relative fraction of the direct and non-direct processes is not the source of observed differences. The simultaneously reweighted MC is used in order to extract the charm event fraction in the data and to calculate the cross sections.

After the simultaneous reweighting, the MC sample luminosities are not normalised to the data luminosity anymore. Using these simultaneously reweighted MC samples the charm f_{ch} and beauty f_{bt} scale factors are evaluated according to the fit procedures described in Section 6.3.

The results of the LH and χ^2 $\Delta\phi$ fit procedures for the inclusive (left), PHP (right) and DIS (bottom) regimes are given in Figures 6.12 and 6.13 respectively, where the data, charm and beauty contributions are shown according to the plots legend. In order to increase the statistical content of histogram bins in case of the DIS region,

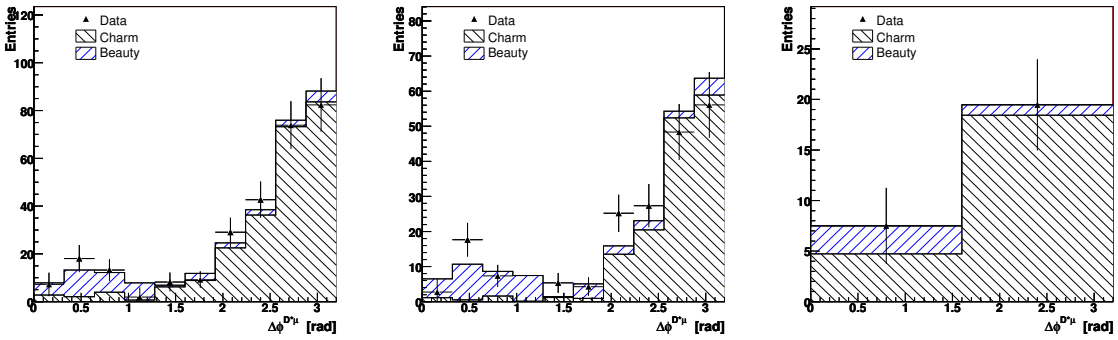

Figure 6.12: The LH $\Delta\phi$ fit results for the inclusive (left), PHP (center) and DIS (right) regimes. Data points are shown as triangles. The charm and beauty contributions are hatched according to the plots legends. The D^* background is subtracted from the distributions. The charm and beauty contributions contain the fake muon contamination (not shown).

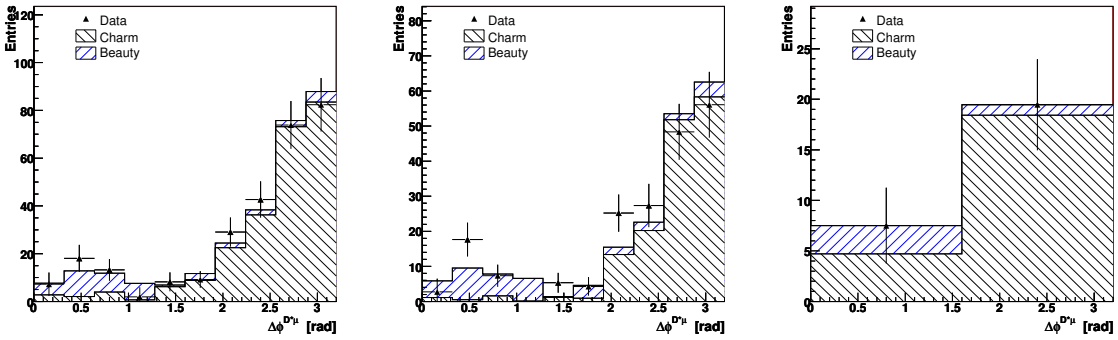

Figure 6.13: The χ^2 $\Delta\phi$ fit results for the inclusive (left), PHP (center) and DIS (right) regimes. Data points are shown as triangles. The charm and beauty contributions are hatched according to the plots legends. The D^* background is subtracted from the distributions. The charm and beauty contributions contain the fake muon contamination (not shown).

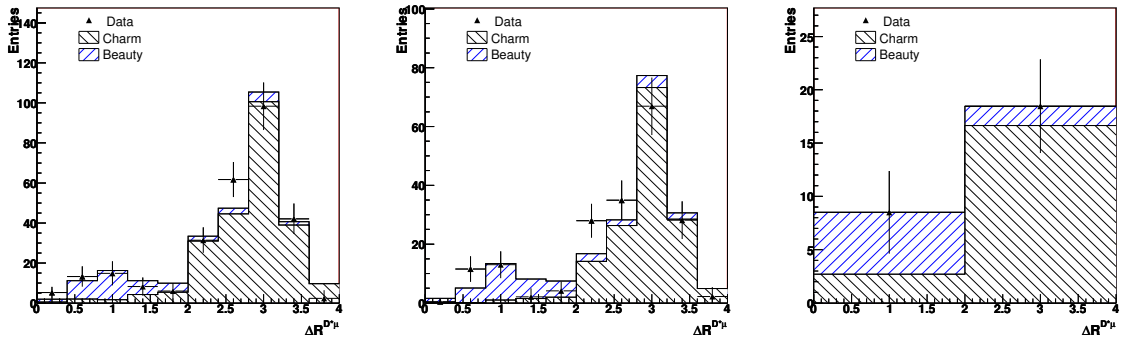

Figure 6.14: The LH ΔR fit results for the inclusive (left), PHP (center) and DIS (right) regimes. Data points are shown as triangles. The charm and beauty contributions are hatched according to the plots legends. The D^* background is subtracted from the distributions. The charm and beauty contributions contain the fake muon contamination (not shown).

the $\Delta\phi$ distributions are rebinned. The D^* background is subtracted from these distributions. The charm and beauty contributions contain also the fake muon contamination which is not shown.

Regime	$N_{ch\ rec}^{D^*\mu}$	$N_{bt\ rec}^{D^*\mu}$	$N_{fake}^{D^*\mu}$	$N_{WS}^{D^*\mu}$
Inclusive	173.4	9.6	55.0	60.8
PHP	112.2	8.9	36.4	40.5
DIS	17.9	0.9	2.0	0.54

Table 6.2: The number of D^*-muon pairs of charm and beauty events in the inclusive, PHP and DIS regimes in the charm enriched region. The number of fake muons and fake D^*s is given as well.

The obtained charm and beauty scale factors given below.

The LH $\Delta\phi$ fit results for the inclusive D^*-muon pair production, PHP and DIS regimes are:

- Inclusive D^*-muon production:
  $f_{ch} = 1.13 \pm 0.13 \quad f_{bt} = 1.3 \pm 0.5$
- PHP:
  $f_{ch} = 1.18 \pm 0.18 \quad f_{bt} = 2.2 \pm 0.9$
- DIS:
  $f_{ch} = 0.7 \pm 0.2 \quad f_{bt} = 0.7 \pm 1.2$

The χ^2 $\Delta\phi$ fit results for the inclusive D^*-muon pair production, PHP and DIS regimes and:

- Inclusive D^*-muon production:
  $f_{ch} = 1.13 \pm 0.11 \quad f_{bt} = 1.3 \pm 0.4$

- PHP:
  $f_{ch} = 1.17 \pm 0.14 \quad f_{bt} = 1.9 \pm 0.7$
- DIS:
  $f_{ch} = 0.7 \pm 0.2 \quad f_{bt} = 0.7 \pm 1.1$

The comparison of the charm and beauty scale factors obtained from both the fit procedures indicates that these results are consistent within the error. In order to estimate the systematics of the fit procedure the results of the LH and χ^2 ΔR fit procedures are given below.

The LH ΔR fit results for the inclusive D^*-muon pair production, PHP and DIS regimes (see Figure 6.14 left, center and right respectively) are:

- Inclusive D^*-muon production:
  $f_{ch} = 1.13 \pm 0.12 \quad f_{bt} = 1.4 \pm 0.5$
- PHP
  $f_{ch} = 1.21 \pm 0.17 \quad f_{bt} = 2.0 \pm 0.8$
- DIS:
  $f_{ch} = 0.6 \pm 0.2 \quad f_{bt} = 1.4 \pm 1.3$

The additional comparison of the charm and beauty scale factors obtained from the LH $\Delta\phi$ and ΔR fit procedures shows that these results are also consistent within the statistical error.

The results of the signal extraction procedure using the LH $\Delta\phi$ fit are summarised in Table 6.2, where the number of charm and beauty D^*-muon pairs extracted from the data in the charm enriched region is given along with the number of fake muons $N_{fake}^{D^*\mu}$ and the fake D^*s $N_{WS}^{D^*\mu}$ respectively.

Chapter 7

Cross Section Measurement

In this chapter the measurement of the charm D^*-muon pair production cross section is described. The systematic uncertainties affecting the cross section measurement are also discussed. Differential cross sections in bins of most relevant kinematic parameters of the D^*-muon pair are measured. A comparison between the measurements with LO+PS QCD predictions as well as with NLO calculations is also given.

7.1 Principle of Charm D^*-Muon Pair Production Cross Section Measurement

Exploiting the angular and charge correlations of the D^* meson and the muon produced from the charm quark pair (see Section 2.6), the charm and beauty contributions can be extracted. To evaluate the number of the charm and beauty D^*-muon pairs in the dataset, reconstructed charm and beauty MC D^*-muon pair samples are fitted to the data using the $\Delta\phi$ fit (see Section 6.3) and the corresponding charm and beauty scale factors are extracted. Scaling the number of the reconstructed charm (beauty) MC D^*-muon pairs (see Section 6.5) the number of charm $N^{D^*\mu}_{ch\ rec}$ (beauty $N^{D^*\mu}_{bt\ rec}$) D^* muon pairs in the dataset is thus obtained.

7.2 Total Visible Cross Section

Using the number of charm events (see Section 6.5) obtained after the signal extraction described in Section 6.3 and relying on the good description of the data by the reweighted MC, the visible cross sections for the process[1]

$$ep \ \rightarrow \ e'\ c\bar{c}\ X \ \rightarrow \ e' \ \ D^{*+}\mu^- \ \ X'$$

[1]The charge conjugate modes are also implied

are calculated. Only the $D^* \to D^0(K\pi) + \pi_s$ decay mode is considered in the MC and data. Because the charm quark pair measurements with the D^*-muon tag are evaluated in a restricted kinematic range of the final state particles, the calculated cross sections are called *visible*. The measurements performed in the analysis cover three regimes: inclusive D^*-muon pair production, PHP and DIS. Three kinematic ranges are therefore defined:

Inclusive:

D^***:**

$p_T^{D^*} > 1.5$ GeV,
$|\eta^{D^*}| < 1.5$.

μ**:**

$p_T^{\mu} > 1.0$ GeV,
$|\eta^{\mu}| < 2.2$.

PHP:

the kinematic range of the inclusive production, plus:
$Q^2 < 1$ GeV^2,
$0.05 < y < 0.8$.

DIS:

the kinematic range of the inclusive production, plus:
$Q^2 > 2$ GeV^2,
$0.05 < y < 0.65$.

The visible cross section of the process defined above is evaluated according to the following formula:

$$\sigma_{vis\ mes} = \frac{N^{D^*\mu}_{ch\ rec}}{A \cdot \mathcal{L} \cdot Br}, \tag{7.1}$$

where Br is the branching ratio of the process $D^{*+} \to D^0(K^-\pi^+)\pi_s^+$ (2.57%), $\mathcal{L}$ is the luminosity of 114 pb^{-1} for the 1996-2000 data taking period, A is the detector acceptance which is determined as:

$$A = \frac{N^{D^*\mu}_{ch\ rec\ MC}}{N^{D^*\mu}_{ch\ MC}}, \tag{7.2}$$

where $N^{D^*\mu}_{ch\ MC}$ is the number of unlike-sign charm MC D^*-muon pairs generated in the defined kinematic range. Due to the correlation between $N^{D^*\mu}_{ch\ rec}$ and $N^{D^*\mu}_{ch\ MC}$, the error on the acceptance is given by:

$$\Delta(A) = \sqrt{\frac{N^{D^*\mu}_{ch\ rec\ MC}}{N^{D^*\mu\ \ 3}_{ch\ MC}}[N^{D^*\mu}_{ch\ MC} + N^{D^*\mu}_{ch\ rec\ MC} - 2N^{D^*\mu}_{ch\ mat}]}, \tag{7.3}$$

where $N^{D^*\mu}_{ch\ mat}$ is the number of charm MC reconstructed D^*-muon pairs matched with corresponding true level D^*-muon pairs.

Regime	$N^{D^*\mu}_{ch\ rec}$	Accep. %	Kinematic range	$\sigma^{D^*\mu}_{vis\ mes}$ [nb]
Inclusive	173 ± 20	10.3 ± 0.8	$p_T^{D^*} > 1.5$ GeV $\lvert\eta^{D^*}\rvert < 1.5$ $p_T^{\mu} > 1.0$ GeV $\lvert\eta^{\mu}\rvert < 2.2$	0.57±0.06
PHP	112 ± 14	9.2 ± 0.9	$p_T^{D^*} > 1.5$ GeV $\lvert\eta^{D^*}\rvert < 1.5$ $p_T^{\mu} > 1.0$ GeV $\lvert\eta^{\mu}\rvert < 2.2$ $Q^2 < 1.0$ GeV^2 $0.05 < y < 0.8$	0.42±0.05
DIS	18 ± 5	9.1 ± 1.7	$p_T^{D^*} > 1.5$ GeV $\lvert\eta^{D^*}\rvert < 1.5$ $p_T^{\mu} > 1.0$ GeV $\lvert\eta^{\mu}\rvert < 2.2$ $Q^2 > 2.0$ GeV^2 $0.05 < y < 0.65$	0.07±0.02

Table 7.1: Visible cross sections of charm D^* muon pair production in the inclusive, PHP and DIS regimes. Numbers of reconstructed charm D^*-muon pairs (the D^* background and the fake muon contamination are subtracted) as well as acceptances for the three regimes are also given. The quoted errors are only statistical.

The results of the measured cross sections for the three regimes are given in Table 7.1 along with acceptances, kinematic ranges and numbers of reconstructed charm D^*-muon pairs (see Section 6.5). The quoted errors are only statistical.

The acceptance for the PHP and DIS regimes is smaller than in case of the inclusive regime due to the photoproduction and DIS selection cuts.

To compare the measured visible cross sections with the MC predictions (unreweighted MC samples used) provided by PYTHIA and RAPGAP, the predicted cross section is calculated according to the following equation (the MC sample luminosities are

Regime	$\sigma^{D^*\mu}_{vis\ MC}$ [nb]	$\sigma^{D^*\mu}_{vis\ mes.}$ [nb]
Inclusive	0.560±0.016	$0.57\pm0.06(stat.)^{+0.12}_{-0.09}(syst.)$
PHP	0.428±0.012	$0.42\pm0.05(stat.)^{+0.09}_{-0.07}(syst.)$
DIS	0.073±0.005	$0.07\pm0.02(stat.)^{+0.03}_{-0.014}(syst.)$

Table 7.2: Comparison of the visible cross sections of the charm D^*-muon pair production with the MC prediction in the inclusive, PHP and DIS regimes. The quoted errors are statistical and systematic (see Section 7.3).

normalised to the data luminosity):

$$\sigma^{D^*\mu}_{vis.MC} = \frac{N^{D^*\mu}_{ch\ UMC}}{\mathcal{L} \cdot Br}, \tag{7.4}$$

where $N^{D^*\mu}_{ch\ UMC}$ is the number of unlike-sign charm MC D^*-muon pairs generated in the defined kinematic range. The result of the comparison is summarised in Table 7.2. The quoted errors are statistical and systematic (see Section 7.3). The cross section measurement summary is given in Section 7.7. Here, one can say that a good agreement between the measurements and the MC predictions is seen within the errors.

7.3 Systematic Uncertainties

The systematic uncertainties treated in the analysis can be split into two groups. The first group contains systematic uncertainties induced by the selection cuts. The second group corresponds to systematic uncertainties originating from discrepancies in comparison of the data and MC expectation as discussed in Section 6.5, the muon efficiency correction (see Section 5.11) and the fake muon contamination. The systematic uncertainty values presented below are obtained for the inclusive production. The systematic uncertainty checks for the PHP and DIS regimes can be found in Appendices 10.2 and 10.3 respectively. The first group of systematic uncertainty checks consists of the following issues:

- The muon p_T cut $(^{+1.2\%}_{-0.8\%})$.
  This cut is varied for the data and MC by ± 40 MeV, which corresponds to the resolution of the muon transverse momentum reconstruction.

- The D^* selection cuts $(^{+2.9\%}_{-1.6\%})$.
  Due to the larger statistics in contrast to this measurements this systematic uncertainty is taken from the analysis [75], where the similar D^* selection cuts are used.

- The D^* energy fraction f^{D^*} selection cut $(^{+3.3\%}_{-2.2\%})$.
  The effect of applying of the f^{D^*} cut is evaluated by a variation of the cut by ± 0.05 for the data and MC.

The second group of the systematic uncertainty checks of the present analysis contains the following points:

- The uncertainty check of the fit systematics $(+2.2\%)$.
  To check systematic effects referred to the fit procedure, the $\Delta R^{D^*\mu}$ fit is used instead the $\Delta\phi^{D^*\mu}$ one. This systematic uncertainty is not included in the total systematic uncertainty in order to avoid double counting of the statistical error. The check shows that the both fit procedures are consistent with each other within the statistical error (see Section 6.5).

- The simultaneously $p_T^{D^*}$ and $\Delta\phi^{D^*\mu}$ spectra reweighting (+8.3%).
  Due to the observed discrepancy between the data and MC expectation (see Section 6.4), the MC $\Delta\phi^{D^*\mu}$ and $p_T^{D^*}$ spectra are simultaneously reweighted in both the reconstruction and true levels. It results in good agreement of the measurement and MC. The difference between two cross sections calculated using the reweighted and unreweighted MCs is used as a systematic error, taking reweighted one for the central value.

- Reweighting of the direct and non-direct process fractions (+6.0%).
  In order to check the influence of the PYTHIA MC prediction, the fractions of direct and non-direct processes are reweighted. The non-direct fraction is scaled up by a factor 3 (see Section 6.5), whereas the direct fraction is scaled down by a factor to recover the normalisation of the sum of the two processes.

- The fake muon contamination uncertainty $(^{+6.3\%}_{-5.6\%})$.
  Despite the good description of the fake muon contamination by the simulation, the fake muon fraction is varied by ±20% in order to estimate the effect of a possible underestimation or overestimation of the fake muon background by the MC simulation. D^*-muon pairs in the like-sign configuration and back-to-back topology are used to estimate this variation range (see Appendix 10.1).

- The muon efficiency correction (±13.9%).
  To estimate the effect of the application of the muon reconstruction efficiency correction, the efficiency correction is varied by ±50% (see Figure 5.6).

- The luminosity measurement uncertainty (±2%).
  The uncertainty for the 1996-2000 data taking period used in the analysis is taken from [84].

- The D^* branching ratio (±2.3%).
  The uncertainty for the D^* branching ratio is taken from [25].

The largest systematic error mainly comes the muon efficiency correction. In principle it can be reduced by a detailed systematic uncertainty study. Systematic effects of the $p_T^{D^*\mu}$ and $\Delta\phi^{D^*\mu}$ simultaneous reweighting and the fake muon background and tracking (selection cut variations) are small. The systematic uncertainty from the relative branching ratios of D^*-muon pair from the b quark and from the $b\bar{b}$ pair in the charm dominant region (see Section 2.6) is expected to be small due to the small fraction of beauty events (9%). The hadronisation systematic uncertainty (fragmentation and parton showering) is included in the systematic uncertainty of the $p_T^{D^*\mu}$ and $\Delta\phi^{D^*\mu}$ simultaneous reweighting. The trigger selection systematics is also expected to be small (see Section 6.1.1).

The systematic uncertainty checks for the visible cross section measurements of charm quark production in the PHP and DIS regimes are performed in the same way as for the inclusive production. Since the reweighting of the direct and non-direct process fractions is done only for the PYTHIA simulation, the corresponding

systematic uncertainty check for the DIS regime is not performed. The systematic uncertainty studies reveal that no excessive uncertainty variations are found and the errors correspond to the inclusive production cross section except the simultaneous $p_T^{D^*\mu}$ and $\Delta\phi^{D^*\mu}$ spectra reweighting systematics in DIS (35%). This is due to the small statistics of the DIS dataset.

The total systematic error obtained by quadratically summing the various system-

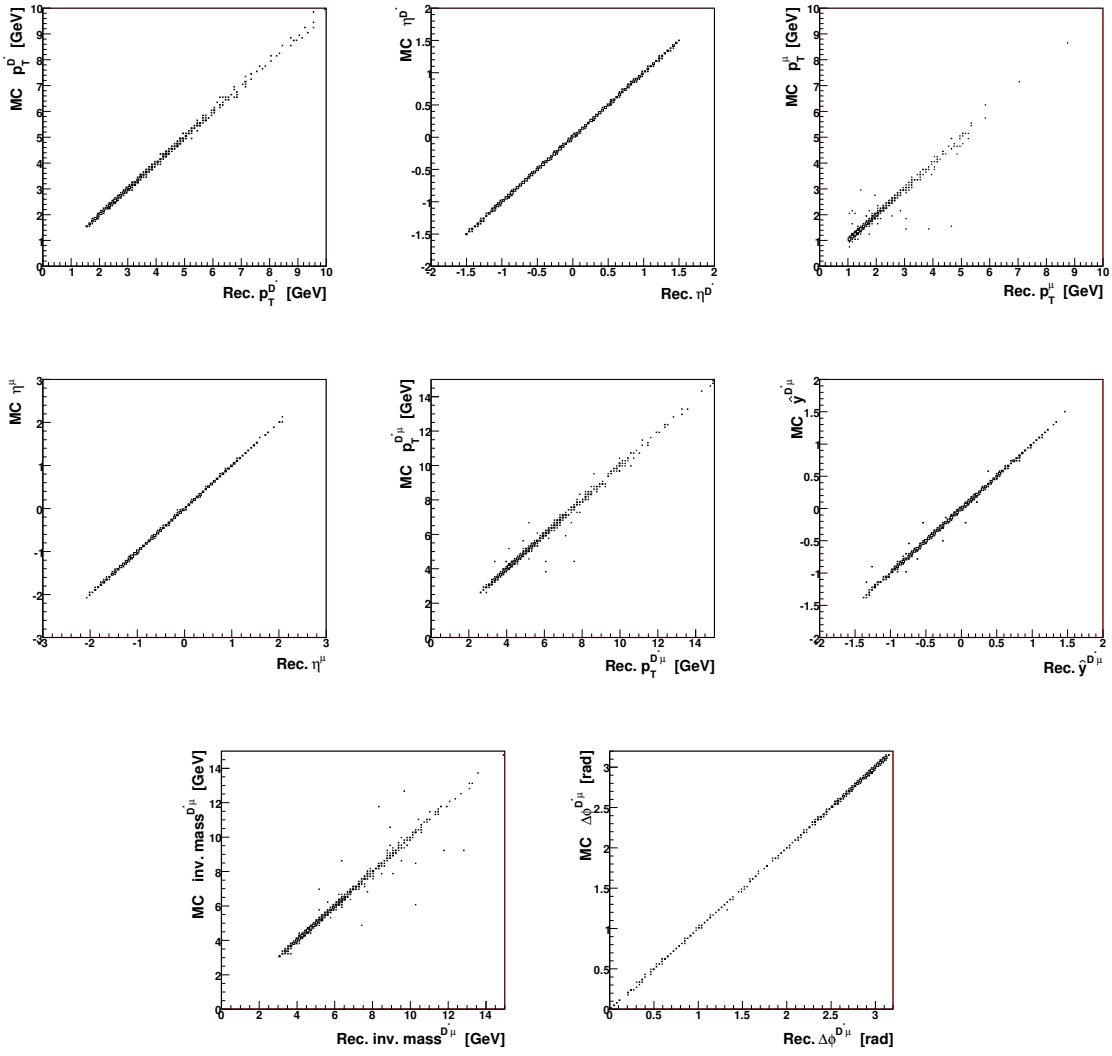

Figure 7.1: Correlations between the reconstruction and true levels for the $p_T^{D^*}$, η^{D^*}, p_T^{μ}, η^{μ}, $p_T^{D^*\mu}$, $\hat{y}^{D^*\mu}$, $M^{D^*\mu}$ and $\Delta\phi^{D^*\mu}$ variables.

atic uncertainties in the inclusive production is $^{+20.3\%}_{-16.6\%}$. The corresponding values for the PHP and DIS regions are $^{+20.6\%}_{-15.7\%}$ and $^{+39.9\%}_{-16.7\%}$ respectively. The statistical error of the cross section measurement for the inclusive charm D^*-muon pair production is $\pm 11.3\%$. The statistical errors for PHP and DIS are $\pm 15\%$ and $\pm 34\%$ respectively.

7.4 Inclusive Differential Cross Sections

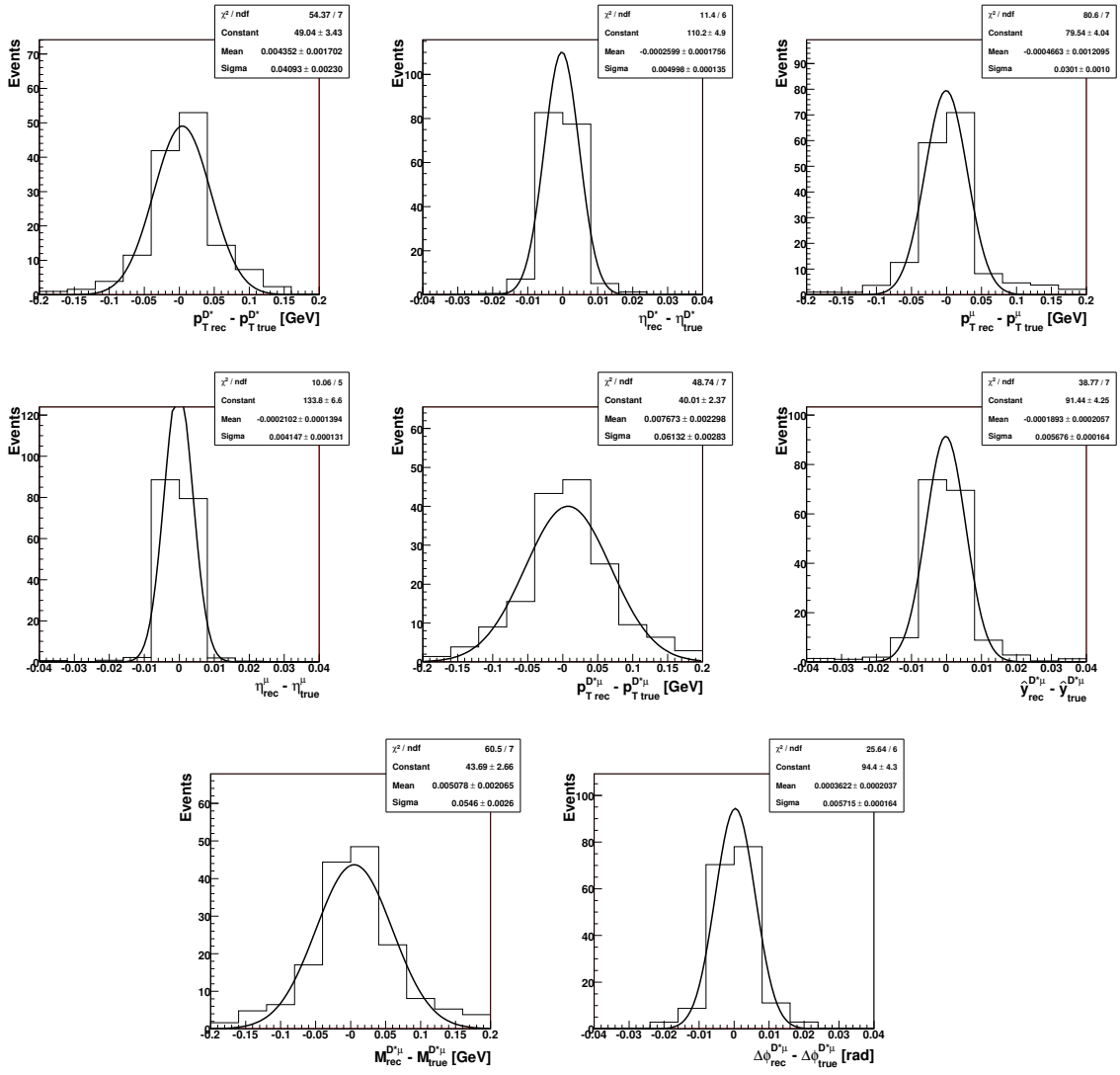

Figure 7.2: Resolutions of the reconstructed kinematic parameters: $p_T^{D^*}$, η^{D^*}, p_T^{μ}, η^{μ}, $p_T^{D^*\mu}$, $\hat{y}^{D^*\mu}$, $M^{D^*\mu}$ and $\Delta\phi^{D^*\mu}$.

The inclusive visible cross section calculated in Section 7.2 does not provide a shape description of the relevant kinematic variables. Differential cross sections are therefore a useful instrument to study the shape of the distributions. The differential cross sections discussed in this section are measured for the inclusive charm D^*-muon pair production.

Calculation of differential cross sections are similar to the total visible cross section calculation. The same steps performed for the total visible cross section measurement are repeated in each bin of a selected kinematic variable. Therefore, in addition

Kinematic variable	Bin Size	Diff. cross section
$p_T^{D^*}$	1.5 GeV $< p_T^{D^*} \leq$ 2.5 GeV	$0.20 \pm 0.06(stat.)^{+0.06}_{-0.08}(syst.)$ nb/GeV
	2.5 GeV $< p_T^{D^*} \leq$ 5.0 GeV	$0.111 \pm 0.013(stat.)^{+0.019}_{-0.019}(syst.)$ nb/GeV
	5.0 GeV $< p_T^{D^*} \leq$ 15.0 GeV	$0.0090 \pm 0.0016(stat.)^{+0.001}_{-0.002}(syst.)$ nb/GeV
η^{D^*}	-1.5 $< \eta^{D^*} \leq$ -0.5	$0.15 \pm 0.03(stat.)^{+0.03}_{-0.02}(syst.)$ nb
	-0.5 $< \eta^{D^*} \leq$ 0.5	$0.19 \pm 0.03(stat.)^{+0.05}_{-0.03}(syst.)$ nb
	0.5 $< \eta^{D^*} \leq$ 1.5	$0.26 \pm 0.05(stat.)^{+0.05}_{-0.05}(syst.)$ nb
p_T^{μ}	1.0 GeV $< \eta^{D^*} \leq$ 1.5 GeV	$0.58 \pm 0.11(stat.)^{+0.11}_{-0.10}(syst.)$ nb/GeV
	1.5 GeV $< \eta^{D^*} \leq$ 2.5 GeV	$0.19 \pm 0.02(stat.)^{+0.04}_{-0.04}(syst.)$ nb/GeV
	2.5 GeV $< \eta^{D^*} \leq$ 8.0 GeV	$0.007 \pm 0.002(stat.)^{+0.004}_{-0.0009}(syst.)$ nb/GeV
η^{μ}	-2.2 $< \eta^{\mu} \leq$ -1.1	$0.08 \pm 0.015(stat.)^{+0.016}_{-0.02}(syst.)$ nb
	-1.1 $< \eta^{D^*} \leq$ 0.0	$0.18 \pm 0.02(stat.)^{+0.06}_{-0.03}(syst.)$ nb
	0.0 $< \eta^{D^*} \leq$ 1.1	$0.21 \pm 0.03(stat.)^{+0.04}_{-0.04}(syst.)$ nb
	1.1 $< \eta^{D^*} \leq$ 2.2	$0.03 \pm 0.03(stat.)^{+0.03}_{-0.013}(syst.)$ nb
$p_T^{D^*\mu}$	3.0 GeV $< p_T^{D^*\mu} \leq$ 4.5 GeV	$0.15 \pm 0.04(stat.)^{+0.04}_{-0.06}(syst.)$ nb/GeV
	4.5 GeV $< p_T^{D^*\mu} \leq$ 7.0 GeV	$0.08 \pm 0.011(stat.)^{+0.02}_{-0.016}(syst.)$ nb/GeV
	7.0 GeV $< p_T^{D^*\mu} \leq$ 15.0 GeV	$0.013 \pm 0.002(stat.)^{+0.0014}_{-0.003}(syst.)$ nb/GeV
$\hat{y}^{D^*\mu}$	-1.5 $< \hat{y}^{D^*\mu} \leq$ -0.5	$0.13 \pm 0.02(stat.)^{+0.03}_{-0.02}(syst.)$ nb
	-0.5 $< \hat{y}^{D^*\mu} \leq$ 0.5	$0.28 \pm 0.04(stat.)^{+0.06}_{-0.05}(syst.)$ nb
	0.5 $< \hat{y}^{D^*\mu} \leq$ 1.5	$0.18 \pm 0.05(stat.)^{+0.04}_{-0.04}(syst.)$ nb
$M^{D^*\mu}$	3.0 GeV $< M^{D^*\mu} \leq$ 5.0 GeV	$0.11 \pm 0.02(stat.)^{+0.02}_{-0.04}(syst.)$ nb/GeV
	5.0 GeV $< M^{D^*\mu} \leq$ 8.0 GeV	$0.073 \pm 0.011(stat.)^{+0.016}_{-0.012}(syst.)$ nb/GeV
	8.0 GeV $< M^{D^*\mu} \leq$ 15.0 GeV	$0.009 \pm 0.002(stat.)^{+0.003}_{-0.003}(syst.)$ nb/GeV
$\Delta\phi^{D^*\mu}$	0.0 $< \Delta\phi^{D^*\mu} \leq$ 2.4	$0.115 \pm 0.019(stat.)^{+0.06}_{-0.03}(syst.)$ nb/rad
	2.4 $< \Delta\phi^{D^*\mu} \leq$ 2.8	$0.56 \pm 0.08(stat.)^{+0.2}_{-0.12}(syst.)$ nb/rad
	2.8 $< \Delta\phi^{D^*\mu} \leq$ 3.1415	$0.72 \pm 0.09(stat.)^{+0.3}_{-0.12}(syst.)$ nb/rad

Table 7.3: Cross sections in different bin of the $p_T^{D^*}$, η^{D^*}, p_T^{μ}, η^{μ}, $p_T^{D^*\mu}$, $\hat{y}^{D^*\mu}$, $M^{D^*\mu}$ and $\Delta\phi^{D^*\mu}$ kinematic variables in the inclusive charm D^*-muon pair production. The bin width corresponding to each variable is also given.

to the defined kinematic range, a bin range of a kinematic variable is introduced. The χ^2 $\Delta\phi$ fit procedure is exploited in order to extract charm and beauty scale factors in each bin, where the cross section is calculated. The reason to use the χ^2 fit instead of the likelihood one is due to the appearance of negative values in some bins of the kinematic quantities after the D^* background subtraction. The differential cross section in a bin of the kinematic variable x is given by:

$$\frac{d\sigma}{dx} \equiv \frac{\Delta\sigma}{\Delta x} = \frac{N_{ch\ bin}^{D^*\mu}}{A_{bin} \cdot \mathcal{L} \cdot Br \cdot \Delta x}, \tag{7.5}$$

where Δx is the bin width, $N_{ch\ bin}^{D^*\mu}$ is the number of charm D^*-muon pairs extracted from the data in this bin by means of the signal extraction procedure (see Section 6.3), A_{bin} is the acceptance in this bin.

Differential cross sections are measured as a function of:

- The D^* transverse momentum $p_T^{D^*}$,

- The D^* pseudorapidity η^{D^*},
- The muon transverse momentum p_T^{μ},
- The muon pseudorapidity η^{μ},
- The scalar sum of the D^* meson and muon momenta $p_T^{D^*\mu}$,
- The rapidity of the D^*-muon pair $\hat{y}^{D^*\mu}$,
- The invariant mass of the D^*-muon system $M^{D^*\mu}$,
- The azimuthal angle difference of directions of the D^* and muon $\Delta\phi^{D^*\mu}$.

In order to study the resolution of the kinematic variable reconstruction, needed to define lower limits on the bin size, the MC simulation is used. The correlations between the reconstructed variables (reconstruction level) and corresponding true level variables produced by the MC generators for $p_T^{D^*}$, η^{D^*}, p_T^{μ}, η^{μ}, $p_T^{D^*\mu}$, $\hat{y}^{D^*\mu}$, $M^{D^*\mu}$ and $\Delta\phi^{D^*\mu}$ are given in Figure 7.1. The resolution R of the kinematic variable x is calculated according to the following formula:

$$R = x_{rec} - x_{true} \tag{7.6}$$

The resolution of the kinematic parameter reconstruction is shown in Figure 7.2. Since the resolution of the reconstruction is quite good, a very fine binning could be chosen. In practice the selection of the bin width is dictated by the bin statistics in order to allow the fit procedure. In Table 7.3 the widths of the bins used for the differential cross section measurements are given.

The systematic uncertainties of the differential cross sections are checked in the same way as for case of the total visible cross section, but for each bin, and included in the Figure 7.3 as the quadratic sum of statistical and systematic error (see also Appendix 10.4). Acceptances in each bin of the differential cross sections are given in Figure 7.4. The calculated cross sections are then compared with the LO+PS MC cross section predictions from PYTHIA and RAPGAP.

The differential cross sections in bins of $p_T^{D^*}$ and η^{D^*} are shown in Figure 7.3. In general, agreement between the measurement and the expectation in the $d\sigma/dp_T^{D^*}$ distribution can be seen. It should be noted that the expectation shows a softer $p_T^{D^*}$ spectrum than the measurement. The cross section as a function η^{D^*} exhibits agreement between the measurement and the prediction within the error although the MC prediction shows a more backward η^{D^*} distribution. This behaviour was also observed in the analysis [85].

In the same Figure 7.3 one can see the differential cross sections in bins of p_T^{μ} and η^{μ}. Here, one can see good description of the measurement by the MC.

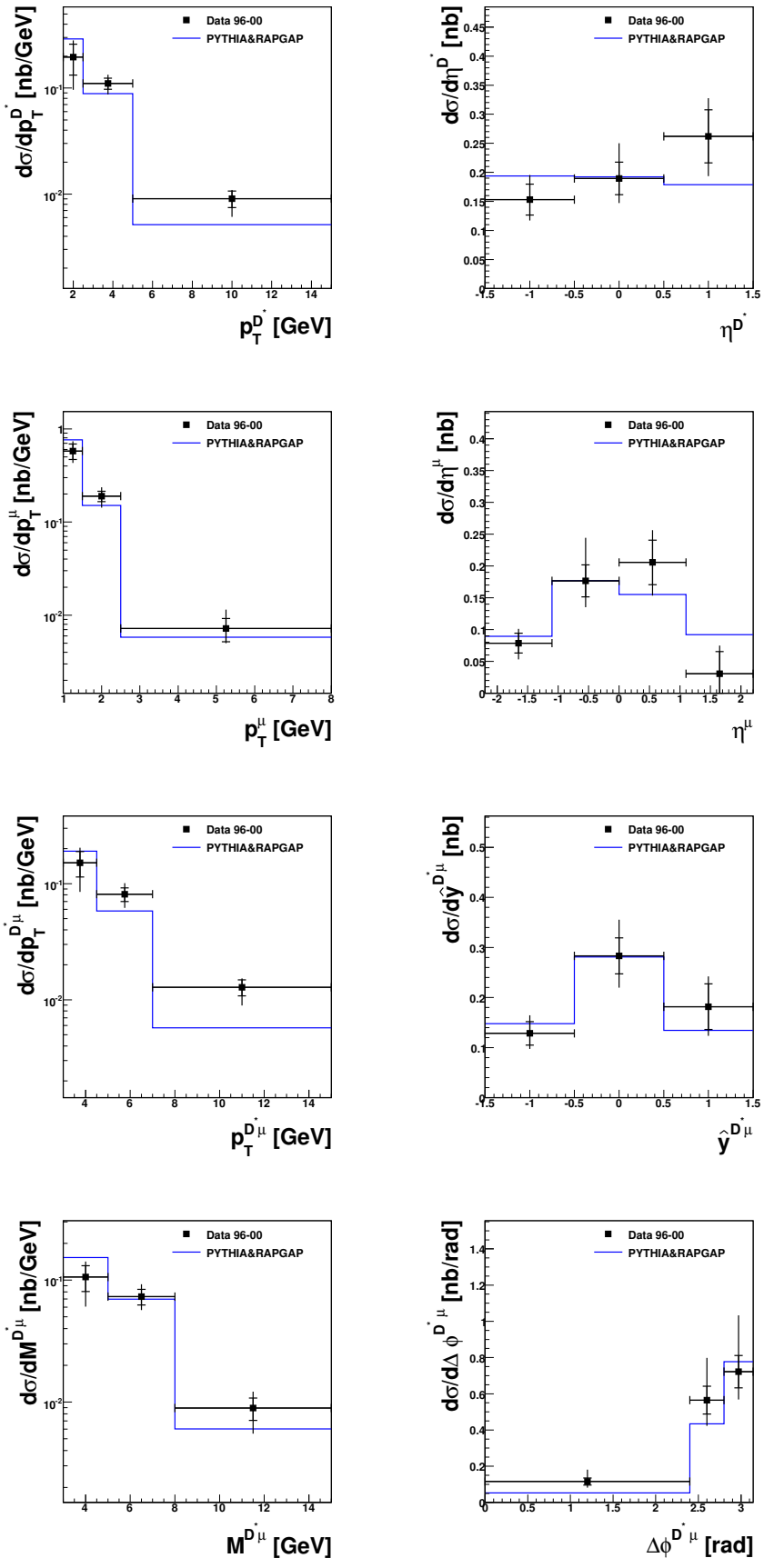

Figure 7.3: Differential cross section in bins of $p_T^{D^*}$, η^{D^*}, p_T^{μ}, η^{μ}, $p_T^{D^*\mu}$, $\hat{y}^{D^*\mu}$, $M^{D^*\mu}$ and $\Delta\phi^{D^*\mu}$ in the inclusive charm D^*-muon pair production. The measurement is shown as squares. The MC prediction is indicated as the solid line.

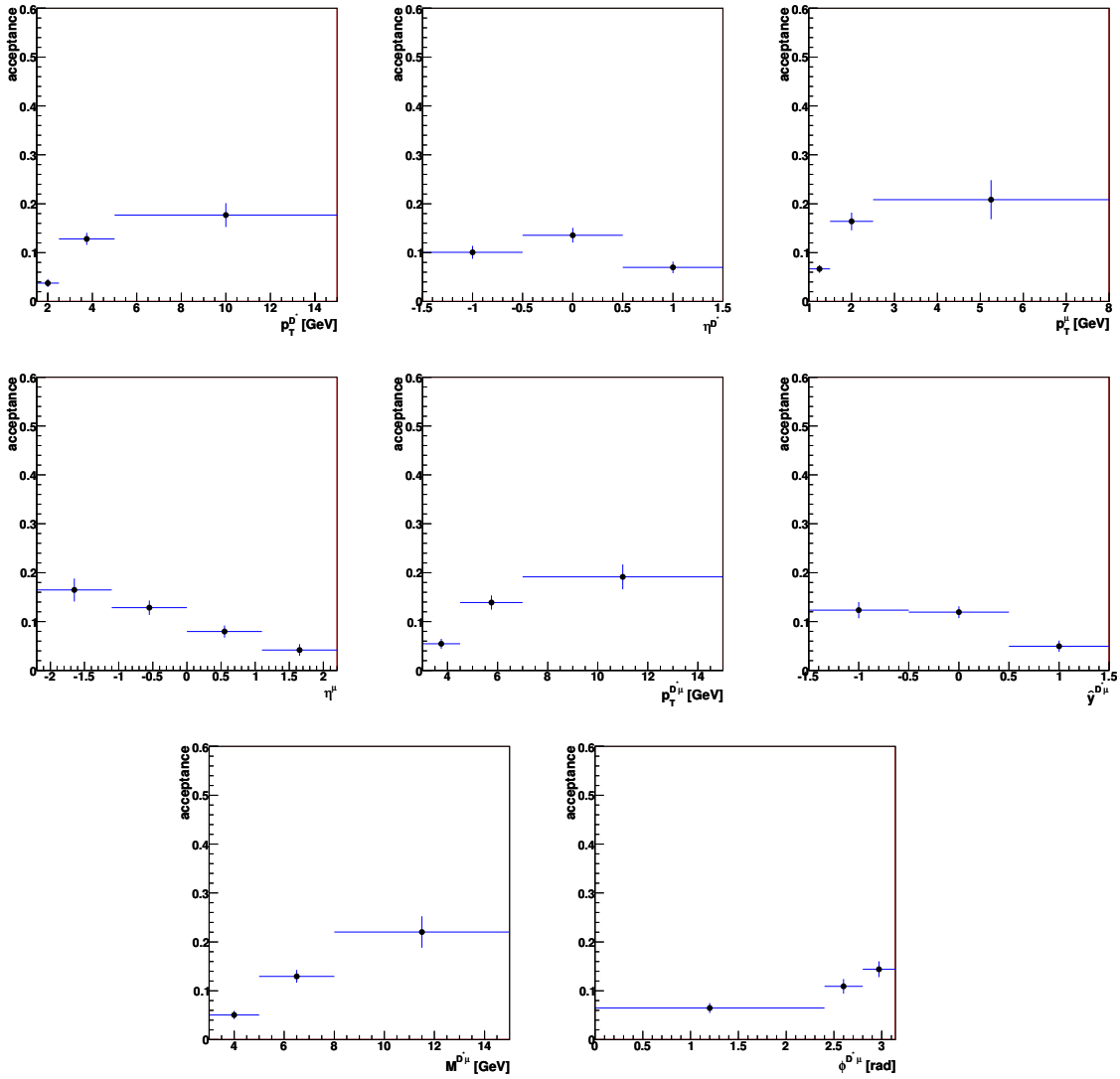

Figure 7.4: Acceptance values in bins of $p_T^{D^*}$, η^{D^*}, p_T^{μ}, η^{μ}, $p_T^{D^*\mu}$, $\hat{y}^{D^*\mu}$, $M^{D^*\mu}$ and $\Delta\phi^{D^*\mu}$ in the inclusive charm D^*-muon pair production.

The differential cross sections as a function of $p_T^{D^*\mu}$ and $\hat{y}^{D^*\mu}$ are given in Figure 7.3. Both kinematic variables are combinations of the kinematic quantities of the D^* meson and the muon. Both distributions show agreement between the measurement and the MC expectation.

The differential cross sections in bins of $M^{D^*\mu}$ and $\Delta\phi^{D^*\mu}$ are also represented in the same Figure 7.3. The comparison between the MC prediction and the data for the $d\sigma/dM^{D^*\mu}$ distribution shows good agreement, whereas the MC simulation does not reproduce the shape of the measured $d\sigma/d\Delta\phi^{D^*\mu}$ distribution. A difference can be observed in the region less than 2.5 radians which indicates that the LO+PS MC approach does not describe the measurement in this region.

7.5 Photoproduction Differential Cross Sections

The same differential cross sections as in case of the inclusive production are also measured in the PHP region. In Table 7.4 one can find the bin widthes and the cross section values in the corresponding bins. The fit procedure as well as systematic uncertainty checks of the differential cross section measurements are the same as for the inclusive production. The systematic uncertainties are included (the quadratic sum of the statistical and systematic error) in Figure 7.5 (see also Appendix 10.5). The differential cross sections in bins of the same kinematic variables as in case of the inclusive production are shown in the same Figure. Acceptances in each bin of the differential cross sections are given in Figure 7.6.

The same statement about general agreement between the MC predictions and the measurements for the PHP differential cross section can be made. The differences observed in the inclusive $d\sigma/d\Delta\phi^{D^*\mu}$ distribution can clearly be also seen in the photoproduction region, which is expected, since the two samples are strongly correlated. This also confirms that the differences are not due to biases induced by the DIS contribution.

7.6 Comparison with NLO Predictions

The NLO predictions used in this analysis are calculated by means of the FMNR program including the FMNR⊗PYTHIA interface (see Section 2.8). The FMNR program was designed to evaluate the NLO prediction in the PHP regime. The analysis is therefore switched to the photoproduction region. The systematic uncertainties of the NLO expectation are not yet estimated due to time constraints. This is the subject of a future study. For the moment a value of $\pm 40\%$ (the value taken from [74]) is used as the systematic error for the total visible cross section and all bins of the differential cross sections.

Kinematic variable	Bin Size	Diff. cross section
$p_T^{D^*}$	1.5 GeV $< p_T^{D^*} \leq$ 2.5 GeV	$0.15 \pm 0.05(stat.)^{+0.05}_{-0.04}(syst.)$ nb/GeV
	2.5 GeV $< p_T^{D^*} \leq$ 5.0 GeV	$0.079 \pm 0.012(stat.)^{+0.019}_{-0.013}(syst.)$ nb/GeV
	5.0 GeV $< p_T^{D^*} \leq$ 15.0 GeV	$0.0063 \pm 0.0014(stat.)^{+0.0007}_{-0.0015}(syst.)$ nb/GeV
η^{D^*}	-1.5 $< \eta^{D^*} \leq$ -0.5	$0.07 \pm 0.03(stat.)^{+0.06}_{-0.008}(syst.)$ nb
	-0.5 $< \eta^{D^*} \leq$ 0.5	$0.14 \pm 0.03(stat.)^{+0.06}_{-0.02}(syst.)$ nb
	0.5 $< \eta^{D^*} \leq$ 1.5	$0.20 \pm 0.04(stat.)^{+0.04}_{-0.05}(syst.)$ nb
p_T^{μ}	1.0 GeV $< \eta^{D^*} \leq$ 1.5 GeV	$0.5 \pm 0.1(stat.)^{+0.12}_{-0.1}(syst.)$ nb/GeV
	1.5 GeV $< \eta^{D^*} \leq$ 2.5 GeV	$0.11 \pm 0.02(stat.)^{+0.03}_{-0.03}(syst.)$ nb/GeV
	2.5 GeV $< \eta^{D^*} \leq$ 8.0 GeV	$0.004 \pm 0.0015(stat.)^{+0.003}_{-0.0004}(syst.)$ nb/GeV
η^{μ}	-2.2 $< \eta^{\mu} \leq$ -1.1	$0.05 \pm 0.013(stat.)^{+0.018}_{-0.009}(syst.)$ nb
	-1.1 $< \eta^{D^*} \leq$ 0.0	$0.13 \pm 0.02(stat.)^{+0.05}_{-0.03}(syst.)$ nb
	0.0 $< \eta^{D^*} \leq$ 1.1	$0.15 \pm 0.03(stat.)^{+0.03}_{-0.02}(syst.)$ nb
	1.1 $< \eta^{D^*} \leq$ 2.2	$0.02 \pm 0.03(stat.)^{+0.03}_{-0.008}(syst.)$ nb
$p_T^{D^*\mu}$	3.0 GeV $< p_T^{D^*\mu} \leq$ 4.5 GeV	$0.09 \pm 0.03(stat.)^{+0.02}_{-0.03}(syst.)$ nb/GeV
	4.5 GeV $< p_T^{D^*\mu} \leq$ 7.0 GeV	$0.06 \pm 0.01(stat.)^{+0.016}_{-0.01}(syst.)$ nb/GeV
	7.0 GeV $< p_T^{D^*\mu} \leq$ 15.0 GeV	$0.008 \pm 0.002(stat.)^{+0.001}_{-0.002}(syst.)$ nb/GeV
$\hat{y}^{D^*\mu}$	-1.5 $< \hat{y}^{D^*\mu} \leq$ -0.5	$0.07 \pm 0.02(stat.)^{+0.03}_{-0.01}(syst.)$ nb
	-0.5 $< \hat{y}^{D^*\mu} \leq$ 0.5	$0.18 \pm 0.04(stat.)^{+0.05}_{-0.03}(syst.)$ nb
	0.5 $< \hat{y}^{D^*\mu} \leq$ 1.5	$0.16 \pm 0.04(stat.)^{+0.03}_{-0.03}(syst.)$ nb
$M^{D^*\mu}$	3.0 GeV $< M^{D^*\mu} \leq$ 5.0 GeV	$0.08 \pm 0.02(stat.)^{+0.02}_{-0.03}(syst.)$ nb/GeV
	5.0 GeV $< M^{D^*\mu} \leq$ 8.0 GeV	$0.06 \pm 0.01(stat.)^{+0.012}_{-0.009}(syst.)$ nb/GeV
	8.0 GeV $< M^{D^*\mu} \leq$ 15.0 GeV	$0.0051 \pm 0.0015(stat.)^{+0.0016}_{-0.0009}(syst.)$ nb/GeV
$\Delta\phi^{D^*\mu}$	0.0 $< \Delta\phi^{D^*\mu} \leq$ 2.4	$0.11 \pm 0.02(stat.)^{+0.06}_{-0.04}(syst.)$ nb/rad
	2.4 $< \Delta\phi^{D^*\mu} \leq$ 2.8	$0.39 \pm 0.07(stat.)^{+0.14}_{-0.08}(syst.)$ nb/rad
	2.8 $< \Delta\phi^{D^*\mu} \leq$ 3.1415	$0.58 \pm 0.09(stat.)^{+0.2}_{-0.18}(syst.)$ nb/rad

Table 7.4: Differential cross sections in bins of the $p_T^{D^*}$, η^{D^*}, p_T^{μ}, η^{μ}, $p_T^{D^*\mu}$, $\hat{y}^{D^*\mu}$, $M^{D^*\mu}$ and $\Delta\phi^{D^*\mu}$ kinematic variables in the charm D^*-muon pair photoproduction. The bin width corresponding to each variable is also given.

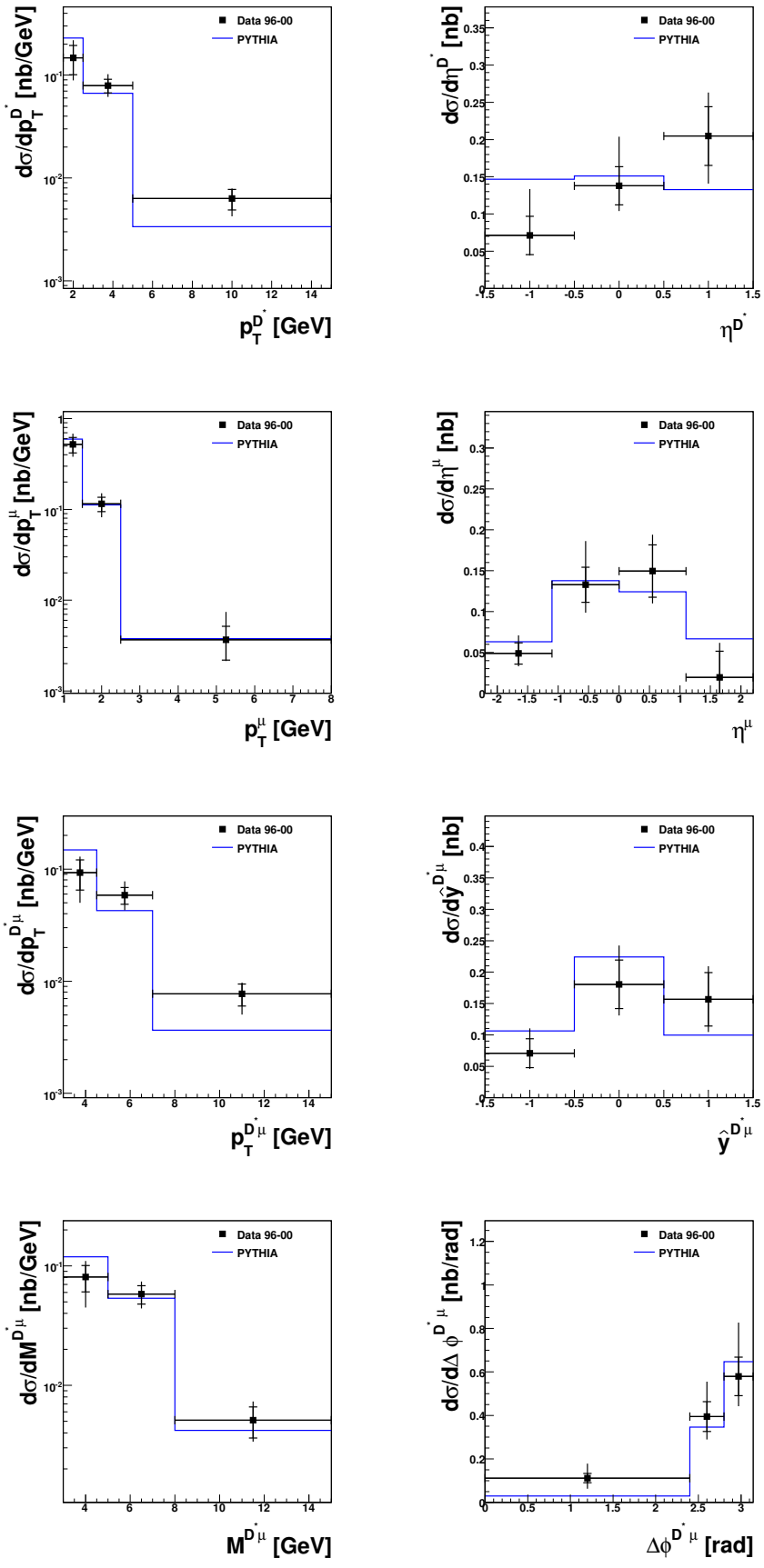

Figure 7.5: Differential cross section in bins of $p_T^{D^*}$, η^{D^*}, p_T^{μ}, η^{μ}, $p_T^{D^*\mu}$, $\hat{y}^{D^*\mu}$, $M^{D^*\mu}$ and $\Delta\phi^{D^*\mu}$ in the photoproduction region. The measurement is shown as squares. The MC prediction is indicated as the solid line.

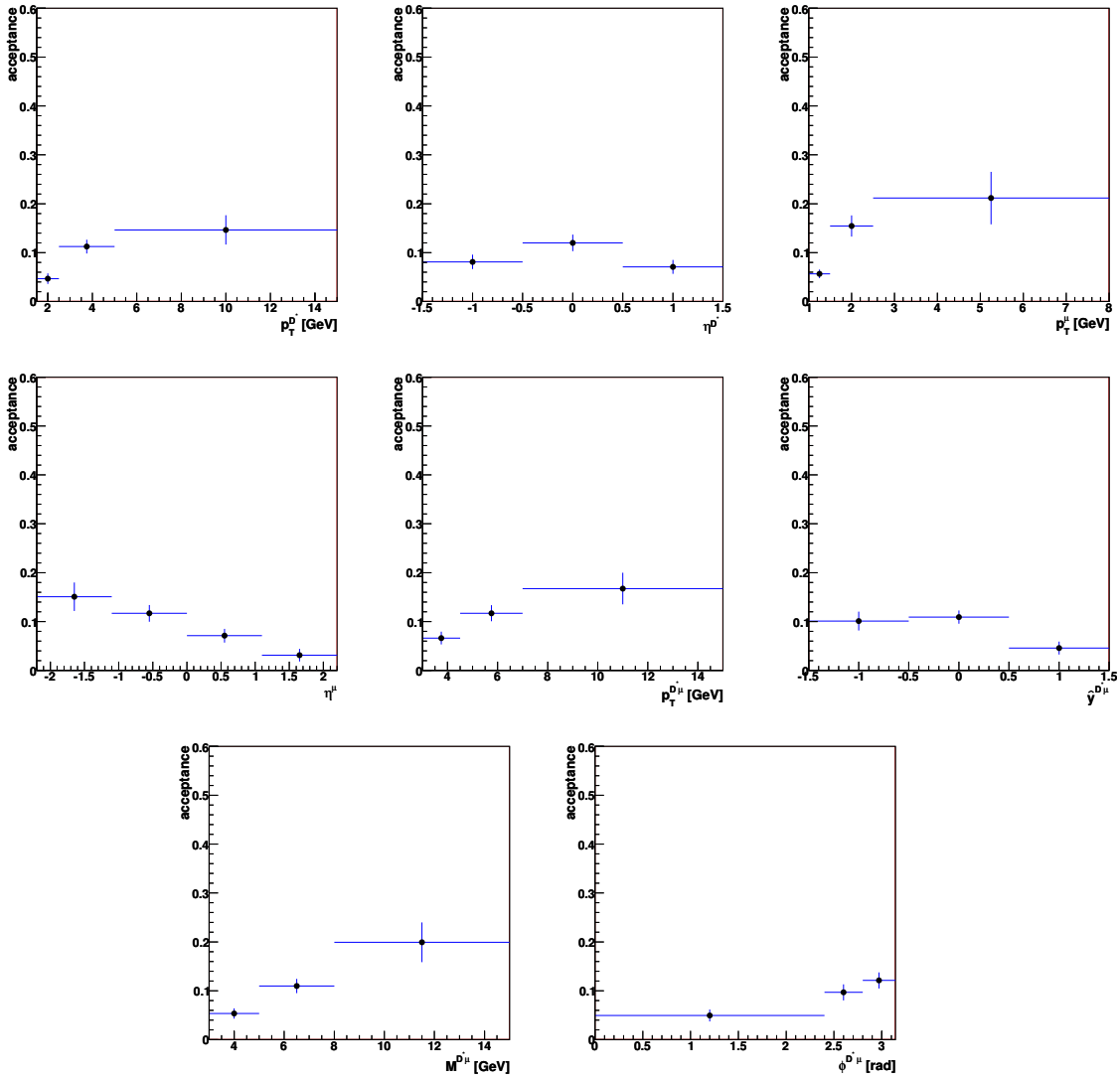

Figure 7.6: Acceptance values in bins of $p_T^{D^*}$, η^{D^*}, p_T^{μ}, η^{μ}, $p_T^{D^*\mu}$, $\hat{y}^{D^*\mu}$, $M^{D^*\mu}$ and $\Delta\phi^{D^*\mu}$ in the PHP region.

The NLO prediction of the charm D^*-muon pair production visible cross section measured in the PHP regime within the defined kinematic range:

$$\sigma^{\text{PHP}}_{vis\ \text{NLO}} = 0.537 \pm 0.214 \text{ nb}$$

shows that the charm D^*-muon pair production measurement (see Table 7.2) is in a agreement with the NLO calculation.

The differential cross sections in bins of the same kinematic variables as in case of the inclusive D^*-muon pair production are measured and shown in Figure 7.7.

In general, the shapes of the measured differential cross sections are well reproduced by the NLO expectations. The central values mainly lie above the measurements, but the predictions are consistent with the measurements within the error. The largest deviations are observed in the $d\sigma/d\Delta\phi^{D^*\mu}$ distribution. The observed stronger smearing can be due to even higher order effects. The similar behaviour was observed in the ZEUS analysis [83].

7.7 Total Visible Cross Section Summary

The visible cross sections for the process:

$$ep \ \rightarrow \ e' \ c\bar{c} \ X \ \rightarrow \ e' \ D^*\mu \ + \ X'$$

in the defined kinematic ranges (the inclusive, PHP and DIS regimes) with corresponding statistical and systematic errors are summarised here:

$$\sigma^{\text{INC}}_{vis\ mes} = 0.57 \pm 0.06(stat.)^{+0.12}_{-0.09}(syst.) \text{ nb},$$

$$\sigma^{\text{PHP}}_{vis\ mes} = 0.42 \pm 0.05(stat.)^{+0.09}_{-0.07}(syst.) \text{ nb},$$

$$\sigma^{\text{DIS}}_{vis\ mes} = 0.07 \pm 0.02(stat.)^{+0.03}_{-0.014}(syst.) \text{ nb}.$$

The corresponding cross sections obtained from the LO+PS MC predictions are:

$$\sigma^{\text{INC}}_{vis\ MC} = 0.560 \pm 0.016(stat.) \text{ nb},$$

$$\sigma^{\text{PHP}}_{vis\ MC} = 0.428 \pm 0.012(stat.) \text{ nb},$$

$$\sigma^{\text{DIS}}_{vis\ MC} = 0.073 \pm 0.005(stat.) \text{ nb}.$$

The comparison demonstrates good agreement between the measurements and the MC expectations.

The measurement of the relative fractions of the direct and non-direct processes

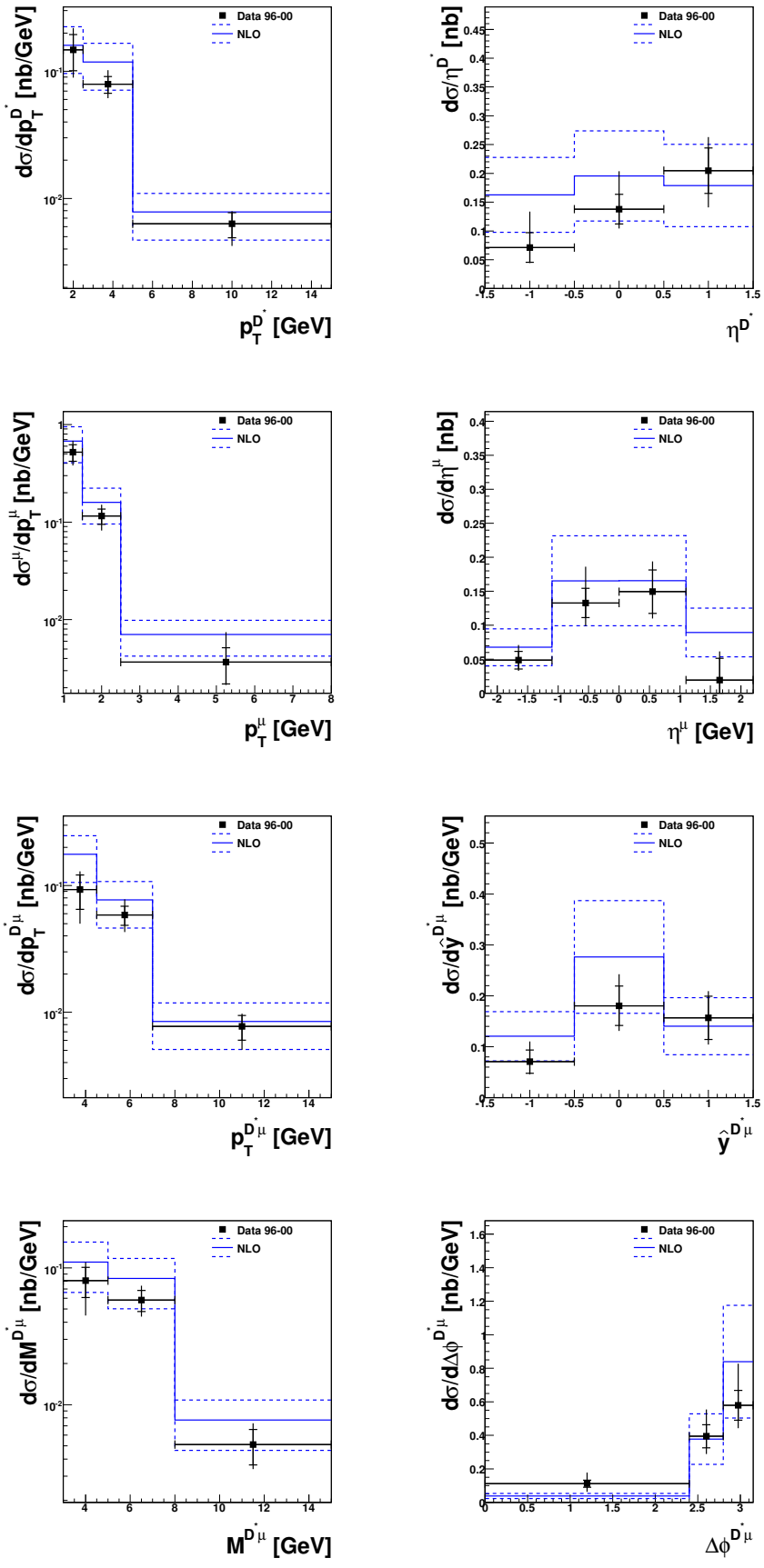

Figure 7.7: Differential cross section in bins of $p_T^{D^*}$, η^{D^*}, p_T^{μ}, η^{μ}, $p_T^{D^*\mu}$, $\hat{y}^{D^*\mu}$, $M^{D^*\mu}$ and $\Delta\phi^{D^*\mu}$ in the charm D^*-muon pair photoproduction. The measurement is shown as squares. The NLO prediction is indicated as the solid line.

can be preformed by means of PYTHIA. The non-direct process includes the resolved photon process and the charm excitation process in the proton (expected to be small). The LO+PS MC prediction in the PHP region shows that the fractions of the direct and non-direct processes are 80% and 20% respectively. In fact, the measurements performed in this analysis are not efficient for the estimation of the relative fractions of the direct and resolved photon processes in contrast to the analysis [30], where two jets, only one of which is tagged with single D^* meson tag, are used in order to measure charm production.

The NLO prediction of the charm D^*-muon pair production visible cross section measured in the PHP regime within the defined kinematic range:

$$\sigma^{\mathrm{PHP}}_{vis\ \mathrm{NLO}} = 0.537 \pm 0.214 \text{ nb}$$

shows that the charm D^*-muon pair production measurement is in a agreement with the NLO calculation. The NLO expectation of charm D^*-muon pair production shows that the hadron-like component of the resolved photon process is only about 3.6% of the NLO visible cross section. The cut selection used in the analysis makes the analysis environment insensitive to this component.

In order to make a comparison with the analysis performed by the H1 experiment [31], the charm D^*-muon pair production visible cross section is extrapolated to the kinematic range $Q^2 < 1$ GeV^2, $0.05 < y < 0.75$, $p_T^{D^*} > 1.5$ GeV, $|\eta^{D^*}| < 1.5$, $p^\mu > 2$ GeV and $|\eta^\mu| < 1.735$ used in [31]. The corresponding cross section extrapolated by means of the PYTHIA prediction ($\sigma^{\mathrm{PHP}}_{vis\ \mathrm{PYTHIA}} = 0.178 \pm 0.04$ nb) in the kinematic region defined above and with the muon preselection transverse momentum cut $p_T^\mu > 0.5$ GeV (see Section 5.2) is:

$$\sigma^{\mathrm{PHP}}_{vis\ mes} = 0.174 \pm 0.021(stat.)^{+0.037}_{-0.029}(syst.) \text{ nb},$$

whereas the measured visible cross section in [31] is:

$$\sigma = 0.250 \pm 0.057(stat.) \pm 0.040(syst.) \text{ nb},$$

which is consistent within the error with the result shown above. The central value of the measured cross section in this analysis for the kinematic range of the H1 analysis is lower due to the mentioned preselection transverse momentum cut on the muon (see Section 5.2).

7.8 Beauty Production Cross Check

The inclusive beauty D^*-muon pair production cross section is also measured. The beauty D^*-muon pair production contributes to the like- and unlike- charge sign

configurations and to all topologies (see Section 2.6). Therefore, all the charge sign configurations and all the topologies are considered and the beauty D^*-muon pair production cross section is calculated. The result of this measurement in the same kinematic range as the inclusive charm production is given below (statistical error quoted only).

$$\sigma^{\text{INC}}_{vis\ mes} = 0.273 \pm 0.095(stat.) \text{ nb.}$$

The corresponding cross section obtained from the LO+PS MC predictions are:

$$\sigma^{\text{INC}}_{vis\ \text{MC}} = 0.208 \pm 0.008(stat.) \text{ nb.}$$

In order to perform a cross check with beauty production measured in a previous analysis by the ZEUS experiment [82] in the kinematic range $p_T^{D^*} > 1.9$ GeV, $|\eta^{D^*}| < 1.5$, $p_T^{\mu} > 1.4$ GeV and -1.75 $< \eta^{\mu} <$ 1.3 using an integrated luminosity of 114 pb^{-1} (the same dataset is used in this thesis), the visible cross section of beauty D^*-muon pair production is extrapolated by means of the MC prediction ($\sigma^{\text{INC}}_{vis\ \text{MC}} = 0.087 \pm 0.004$ nb, statistical error quoted only) in this kinematic range and is:

$$\sigma^{\text{INC}}_{vis\ mes} = 0.114 \pm 0.039(stat.) \text{ nb.}$$

This value is in agreement with the inclusive beauty production cross section:

$$\sigma^{\text{INC}}_{vis\ mes} = 0.160 \pm 0.037(stat)^{+0.030}_{-0.057}(syst.) \text{ nb}$$

measured in [82].

Chapter 8

Measurement of x_g in Proton

Heavy quark production provides an opportunity to measure the momentum fraction x_g carried by the gluon in the incoming proton. The measurement of the gluon momentum fraction in the proton is an interesting question now because the measured x_g can be directly used in an extraction of the gluon density in the proton. The gluon distribution function can be thus extracted and used further in other experiments. This is of particular interest for the future LHC collider, where the gluon density is a important ingredient in Higgs production.

The main heavy flavour production mechanism at HERA is the BGF process, where a pair of heavy quarks are produced dynamically. The gluon density is one of the most important inputs and the charm quark pair kinematics can be approximated by kinematic variables of the D^*-muon pair reconstructed in the final state. Thus, to measure the momentum fraction carried by the gluon the kinematics of the D^*-muon pair is exploited. All D^*-muon pairs with the unlike-sign configuration and the back-to-back topology are therefore considered. A cut $\Delta\phi > 2.5$ radians is applied in order to decrease the influence of the non-direct processes (mainly resolved photon process). To avoid spoiling the back-to-back topology by the scattered electron in DIS, the PHP regime is selected.

The outgoing charm quarks produced in the hard process pass through the hadronisation stage due to the confinement. Hadrons produced during the hadronisation stage approximately follow the original quark direction. The D^* meson carries a large fraction of the momentum ($\sim$60%, see Section 2.5.2) of its parent charm quark and the D^* meson information can be used as an approximation of the parent quark kinematics. To restore the full parent quark energy, a summation of the energy flow around the D^* meson momentum is introduced. In case of the muon, the correlation between the muon and its parent quark momentum is poor due to the kinematics of the semi-leptonic decay and the hadronisation. Nevertheless, the parent quark kinematics can be approximated by the muon due to the fact that muons are inside the hadronic flows produced by the charm quark hadronisation and charm meson decays. In order to estimate the energy of the original charm quark, the same sum-

mation procedure is used. A schematic view of the summation technique is presented in Figure 8.1.

A technique of the gluon momentum measurement is based on the method which is

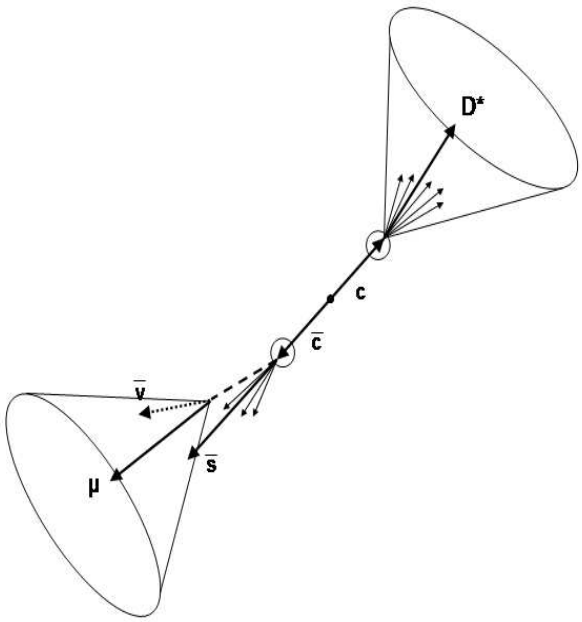

Figure 8.1: Schematic view of the approximation approach of the charm pair kinematics. The summing of the energy flows around the D^* meson and muon are shown as well.

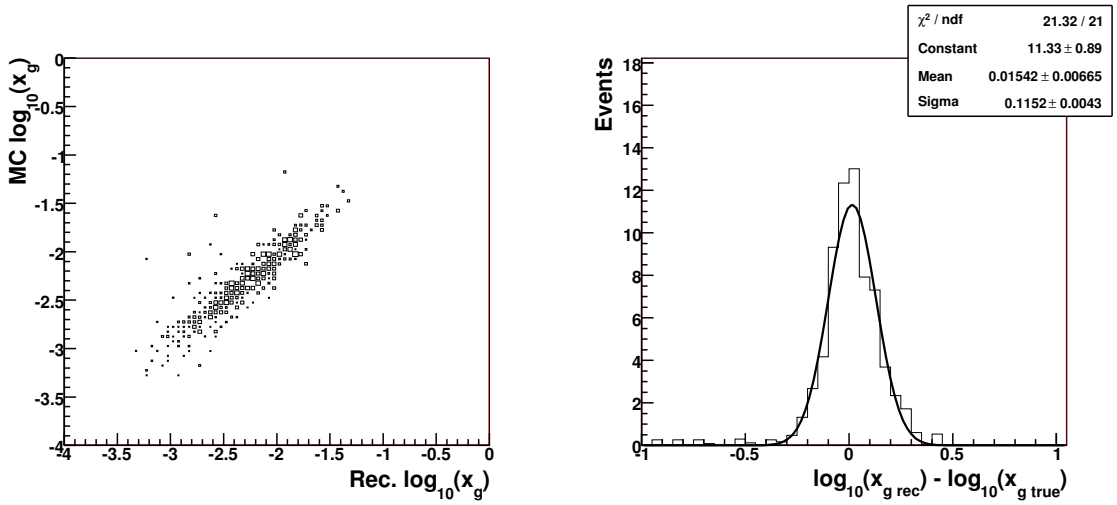

Figure 8.2: Correlation between the reconstructed and true level x_g (left). Resolution provided by the x_g reconstruction technique (right).

used in the analysis [87] and adopted for the present analysis. The concept of the technique can be expressed as the following equation:

$$x_g = \frac{E_{T\ iso}^{D^*} e^{\eta^{D^*}} + E_{T\ iso}^{\mu} e^{\eta^{\mu}}}{2E_p}, \tag{8.1}$$

where E_p is a energy of the incoming proton, $E_{T\ iso}^{D^*}$ and $E_{T\ iso}^{\mu}$ is a scalar sum of transverse momenta of ZUFOs around the D^* and muon directions respectively. Both sums are calculated for all ZUFOs in the cone $\Delta R < 1.0$. The $E_{T\ iso}^{D^*}$ and $E_{T\ iso}^{\mu}$ kinematic variables constructed in this way describe the energy flow distributed around the D^* meson and muon track respectively.

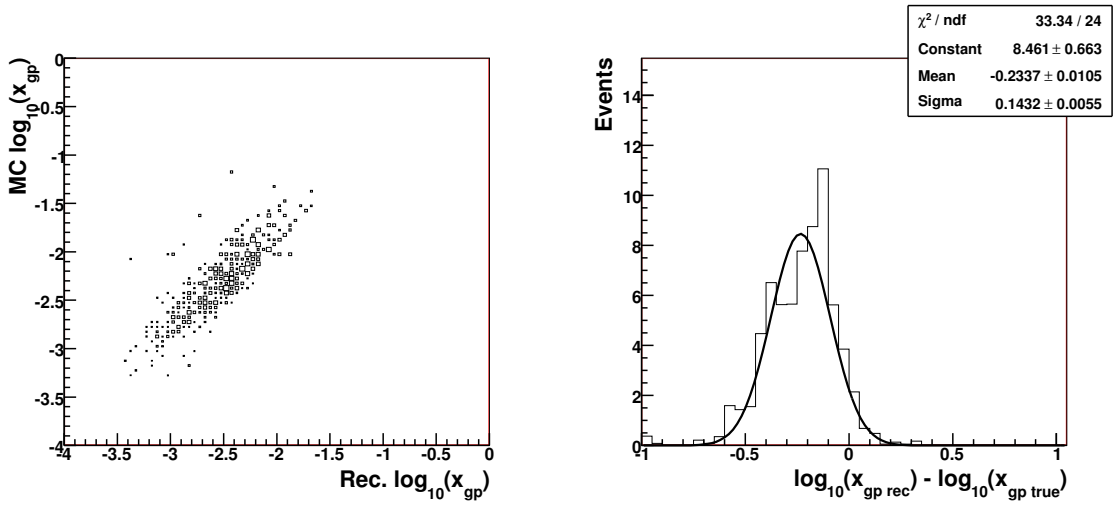

Figure 8.3: Correlation between the reconstructed and true level x_{gp} (left). Resolution of the x_{gp} reconstruction technique (right) when only D^* and muon information is used.

The reconstructed $x_{g\ rec}$ in the MC is compared to the same quantity $x_{g\ true}$ obtained from the MC generator level. The correlation plot is presented in Figure 8.2 (left). The resolution of the x_g reconstruction is evaluated according to the following formula:

$$R = log_{10}(x_{g\ rec}) - log_{10}(x_{g\ true}). \tag{8.2}$$

The resolution of the x_g reconstruction is shown in Figure 8.2 (right). The x_g reconstruction yields a good result ($\sigma \approx 0.11$) as it is clearly seen. It is useful to compare the obtained correlation and resolution with corresponding values in the case of the reconstruction of x_{gp} by means of D^* and muon kinematic quantities only as it is expressed by the following equation:

$$x_{gp} = \frac{p_T^{D^*} e^{\eta^{D^*}} + p_T^{\mu} e^{\eta^{\mu}}}{2E_p}. \tag{8.3}$$

This comparison is shown in Figure 8.3. In this case, resolution of the reconstructed x_{gp} shows a systematic shift due to the poor charm quark pair kinematics approximation provided by the D^* and muon information alone.

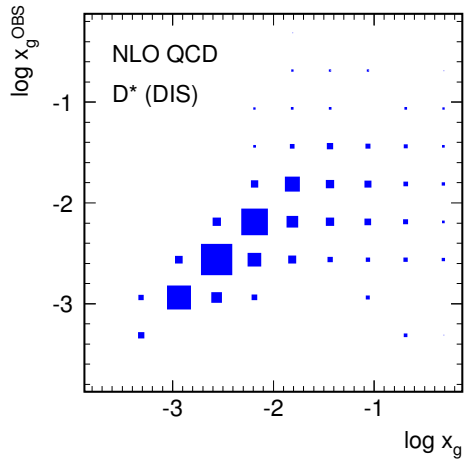

Figure 8.4: Correlation between the true level and reconstructed x_g measured in the analysis [89].

The momentum fraction x_g carried by the gluon in the proton was measured in the analysis [89] (also in [86]), where D^* meson was used to tag charm events. Using the kinematic information of the D^* meson as an approximation of the parent charm quark the measurement of x_g was performed. The correlation plot is presented in Figure 8.4. The correlation is distorted due to the effects of the gluon radiation and the fragmentation. The resolution of the x_g measurement method in [89] is about 0.2. A correction factor to the D^* momentum was used to recover the original quark momentum due to the fragmentation. In contrast to [89], the technique discussed in this chapter allows measurement of the momentum fraction carried by the gluon in the proton without such momentum correction and with almost two times better resolution.

The x_g distribution evaluated by using the equation 8.1 is presented in Figure 8.5. The charm and beauty production contributions are estimated by means of the fit procedure discussed in Section 6.3 and indicated according to the plot legend. The D^* background and fake muon contamination are shown as well. The distribution starts from the value around $10^{-3.5}$, which corresponds to the kinematic limit for charm quark pair production in the measured kinematic range.

The measured x_g distribution can be used to extract the gluon density distribution function $x_g G(x_g)$ in the proton. To do this, the NLO calculation is needed due

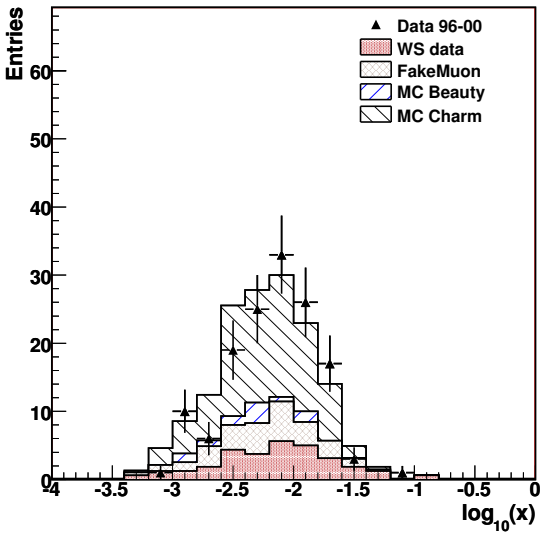

Figure 8.5: The measured x_g in charm and beauty D^*-muon pair production. The charm and beauty contributions are shown as the hatched histograms. The fake muon contamination and D^* background are indicated as the shadowed histograms.

to the systematic uncertainties coming from the variation of the renormalisation and factorisation scales. Suppose that the NLO of perturbative QCD are well described by the factorisation approach, where $x_g G(x_g)$ is a key component of the convolution. The gluon density distribution in the proton is related to the measured charm production cross section in bins of x_g:

$$x_g G(x_g, \mu^2) \;=\; \frac{\frac{d\sigma_{mes}}{dx_g}}{\frac{d\sigma_{\rm Mc}}{dx_g}} [x_g G(x_g, \mu^2)]_{\rm PDF}, \tag{8.4}$$

where $[x_g G(x_g, \mu^2)]_{\rm PDF}$ is the gluon density distribution function provided by the PDF. For every x_g the gluon density is probed at a different hard scale μ^2. Therefore, the average value of μ^2 is needed for each bin of x_g. This can be calculated from the true level information by using the $\{x_g, \mu\}$ dependence. In the case of the absence of true level information, the hard scale can be approximated by the $E^{\mu}_{T\ iso}$ and $E^{D^*}_{T\ iso}$ kinematic variables.

The gluon density extraction is not yet performed in this thesis due to the time constraints. This is the subject of a future study.

Chapter 9

Summary

This thesis presents the measurement of double-tagged charm production via the process:

$$ep \;\rightarrow\; e'\; c\bar{c}\; X \;\rightarrow\; e'\;\; D^{*\pm}\mu^{\mp}\;\; X'$$

in lepton-proton collisions at HERA, using a dataset with an integrated luminosity of 114 pb^{-1} gated by the ZEUS detector.

Using the angular and charge correlations between the D^* meson and the muon, the fraction of charm events is extracted from the data. Cross sections of charm D^*-muon pair ($D^{*+}\mu^-$ and $D^{*-}\mu^+$) production in the visible range of:

$p_T^{D^*} > 1.5$ GeV, $|\eta^{D^*}| < 1.5$,

$p_T^{\mu} > 1.0$ GeV, $|\eta^{\mu}| < 2.2$

are measured for the inclusive, photoproduction (inelasticity $0.05 < y < 0.8$ at $Q^2 < 1$ GeV^2) and deep inelastic scattering ($y < 0.65$ at $Q^2 > 2$ GeV^2) regimes. The results are:

$$\sigma^{\text{INC}}_{vis\ mes} = 0.57 \pm 0.06(stat.)^{+0.12}_{-0.09}(syst.) \text{ nb},$$

$$\sigma^{\text{PHP}}_{vis\ mes} = 0.42 \pm 0.05(stat.)^{+0.09}_{-0.07}(syst.) \text{ nb},$$

$$\sigma^{\text{DIS}}_{vis\ mes} = 0.07 \pm 0.02(stat.)^{+0.03}_{-0.014}(syst.) \text{ nb}.$$

These values can be compared with corresponding cross sections predicted by the leading order (LO) plus parton shower (PS) MC approach:

$$\sigma^{\text{INC}}_{vis\ MC} = 0.560 \pm 0.016 \text{ nb},$$

$$\sigma^{\text{PHP}}_{vis\ MC} = 0.428 \pm 0.012 \text{ nb},$$

$$\sigma^{\text{DIS}}_{vis\ MC} = 0.073 \pm 0.005 \text{ nb}.$$

The comparison shows good agreement between measurements and MC predictions.

The charm D^*-muon production next-to leading order (NLO) calculation provided by the FMNR⊗PYTHIA interface is performed for the photoproduction region and gives the result:

$$\sigma^{\text{PHP}}_{vis\ \text{NLO}} = 0.537 \pm 0.214 \text{ nb}.$$

A comparison with the measurement shows a good agreement within the error.

For the inclusive and photoproduction regimes differential cross sections in various kinematic variables of the D^*-muon pair are also measured. The differential cross sections for the inclusive regime are compared with the LO+PS MC, while the differential cross sections for the photoproduction regime are compared with the LO+PS MC and the NLO calculations.

In the case of the comparison with the LO+PS MC simulation a general agreement can be seen, although some differences in the $d\sigma/d\Delta\phi^{D^*\mu}$ spectrum is observed. The sources of this difference might be in the higher order effects.

The comparison of the measurement with the NLO calculation in principle also exhibits good agreement, although the central values of the NLO calculations are above the measurement but within the error. The massive approach used NLO calculation demonstrate good results. Differences in shape are also observed in the $d\sigma/d\Delta\phi^{D^*\mu}$ distribution. This can be an indication of the need of next-to-NLO calculations or the PS implementation at NLO.

Since the boson gluon fusion process is dominant at HERA, the momentum fraction x_g carried by the gluon in the proton can be measured. Using the developed technique, which exploits kinematic information of the D^*-muon pair to approximate the parent charm quark pair, this measurement is performed. The resolution of this method yields good results. In contrast to the analysis [89], where the D^* meson was used to tag the charm quark and to measure gluon momentum fraction x_g in the proton, the x_g measurement performed in this thesis obtains a better resolution. The extraction of the gluon density is not yet preformed in this thesis.

The possibility of extending the Global Track Trigger (GTT) of the ZEUS DAQ/trigger system with a forward trigger algorithm is also studied in this thesis. The Forward GTT algorithm has been written, which finds the event vertex position using STT and FMVD detector data. As a conclusion of this study on can say that the performance of the FGTT algorithm satisfies easily the time latency requirements and vertex finding efficiency and resolution, but its use online is prevented by the large data transfer latencies measured in the STT frontend readout.

Acknowledgements

I should say that the presented results of this thesis would be not possible without the constant efforts of the members of the ZEUS Collaboration.

First of all, I would like to express my gratitude to Prof. Dr. Peter Schleper for giving me the opportunity to work on my PhD in the ZEUS Collaboration and for his valuable suggestions and corrections of this thesis.

I would like to express my gratitude to my supervisor Dr. Achim Geiser for his considerable assistance at all stages of my analysis. All his new ideas, enthusiastic discussions, strong physics background and big experimental experience made this analysis very exiting for me.

I would like to thank my technical supervisor Dr. Christopher Youngman for his support and providing the working environment for developing the Forward GTT algorithm.

I also thank my friends and colleagues Nicolai Vlasov and Gayane Aghuzumtsyan for their help, support and useful discussions during my PhD. Additionally my thank goes to Julia Grebenyuk for her help in correction of English of the thesis. Thanks to John Loizides and James Ferrando, who kindly agreed to proofread the thesis. During my PhD I worked in collaboration with the members of the Beauty team: Achim Geiser, Oliver Gutsche, Ingo Bloch, Benjamin Kahle and A. Elizabeth Nuncio Quiroz. I would like to thank the team for the perfect working environment and help.

During my staying in Hamburg it was great luck to meet Family Borgwardt and Family Protzen. These wonderful people were always around me and helped me a lot! Liebe Frau Birgit Borgwardt, Herr Werner Borgwardt, Frau Jutta Protzen und Herr Peter Protzen, ich möchte ihnen für ihre Hilfe DANKE sagen!

I also would like to thank my parents for their assistance and wise advices. Last but not least I thank my friend and my wife Tatiana for enormous help, encouragement and believe in my hopes and plans that made the completion of my PhD possible.

Chapter 10

Appendix

10.1 Control Plots for Like-Sign Configuration

The charm and beauty contributions shown in control plots in this Section are evaluated by means of the fit procedure (see Section 6.3).

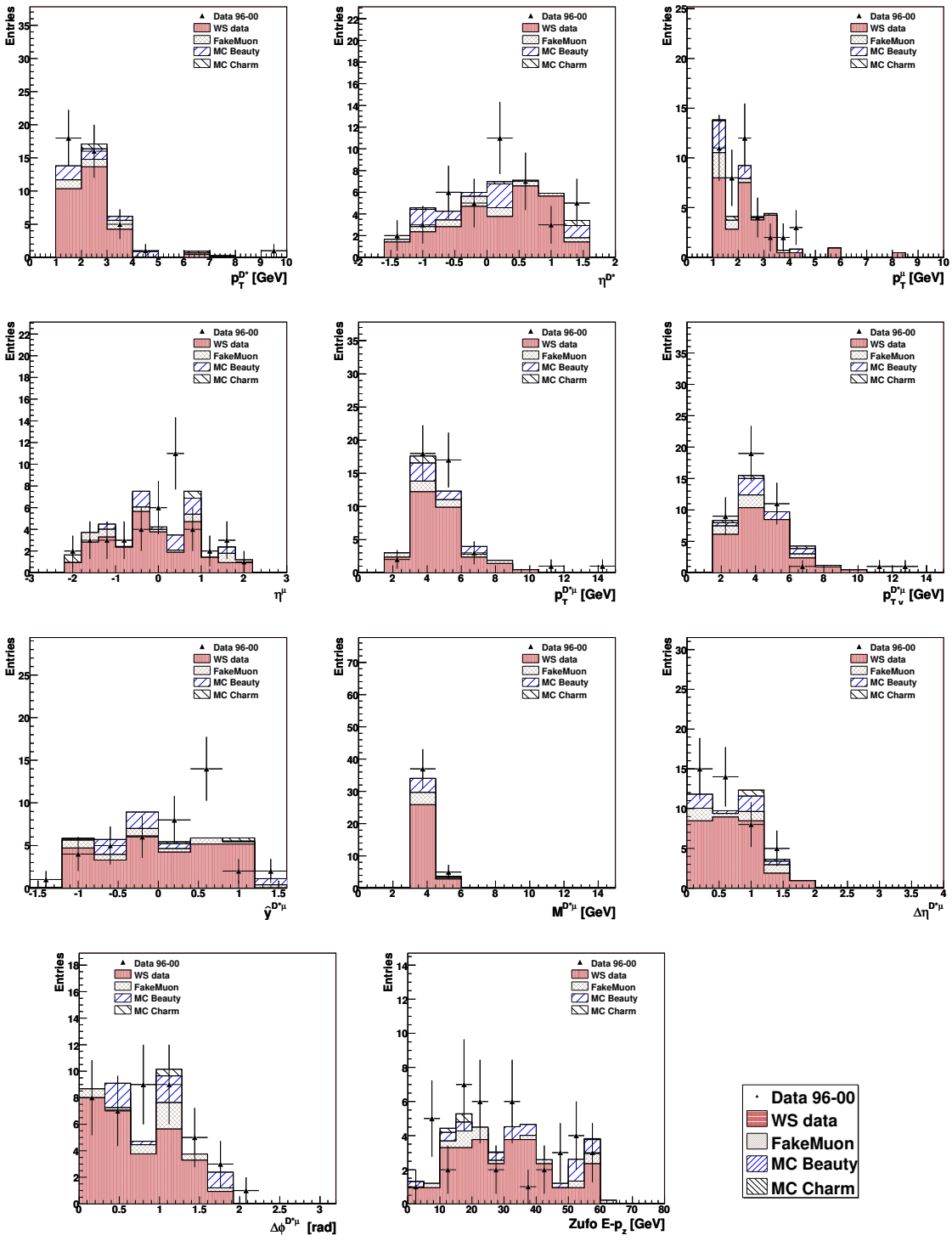

Figure 10.1: The control plots for the inclusive production and the like-sign configuration in the region $\Delta R < 2$. The data is shown as triangles. Contributions of charm and beauty productions as well as the D^* and fake muon backgrounds are indicated according to the plots legends.

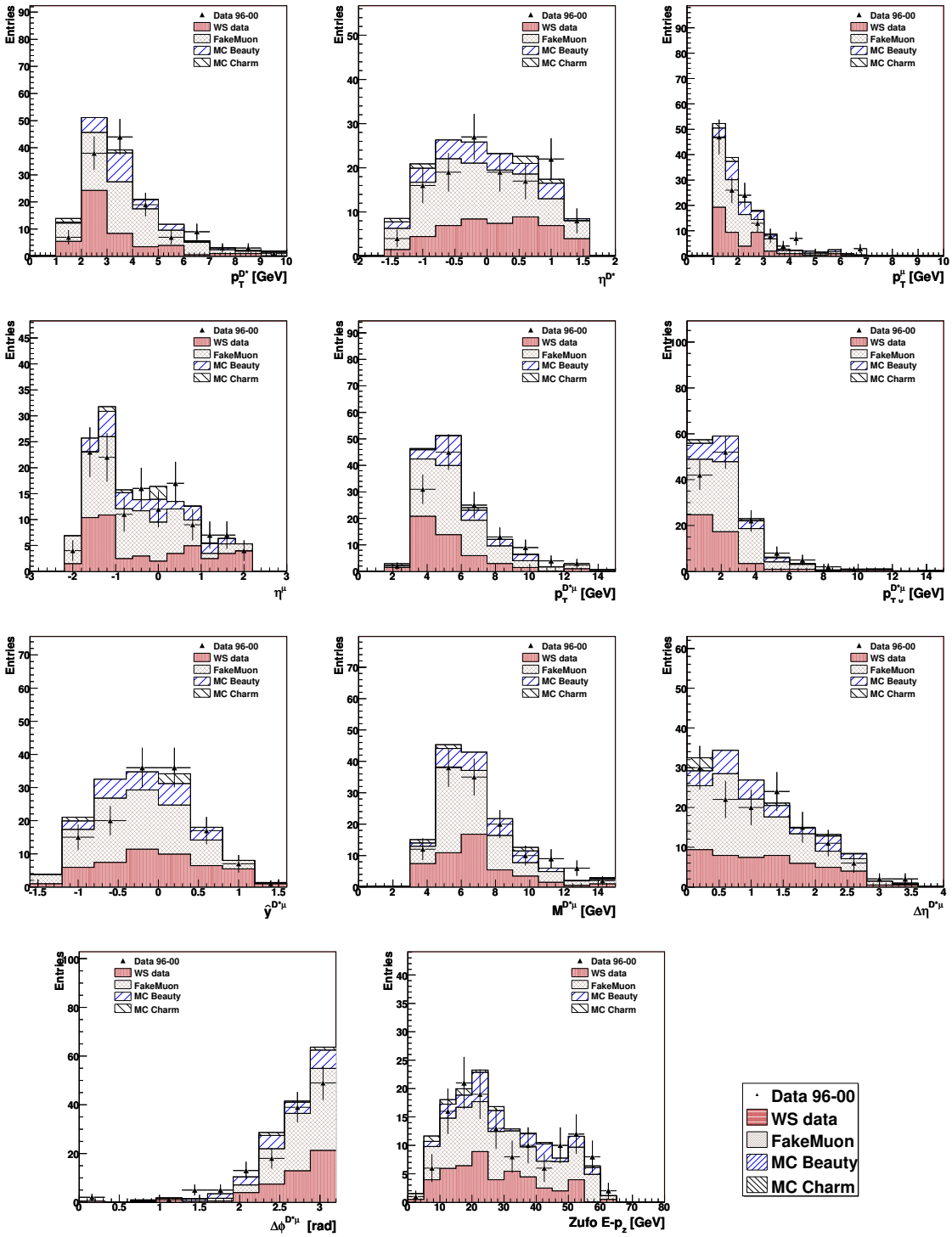

Figure 10.2: The control plots for the inclusive production and the like-sign configuration in the region $\Delta R \geq 2$. The data is shown as triangles. Contributions of charm and beauty productions as well as the D^* and fake muon backgrounds are indicated according to the plots legends.

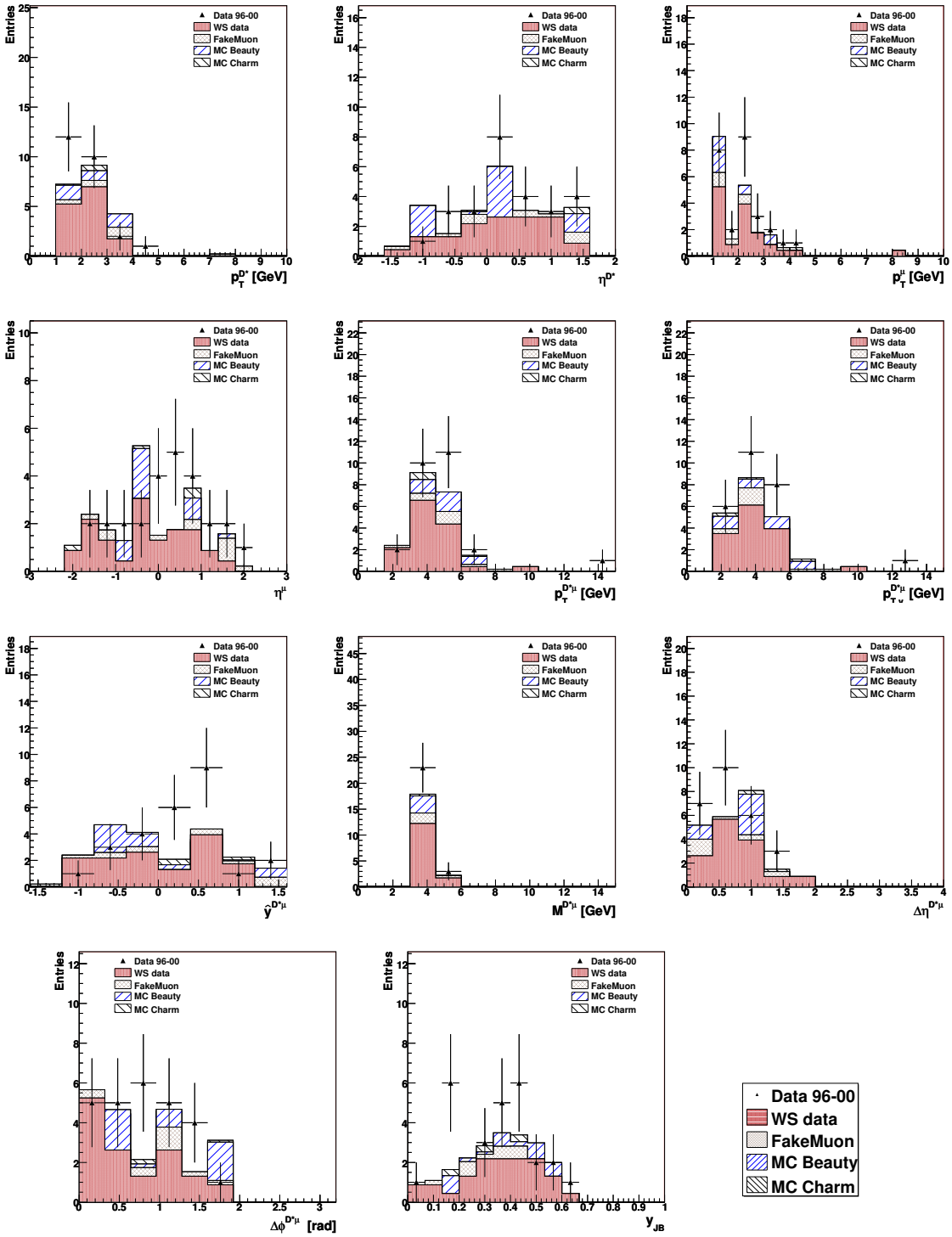

Figure 10.3: The control plots for the PHP regime and the like-sign configuration in the region $\Delta R < 2$. The data is shown as triangles. Contributions of charm and beauty productions as well as the D^* and fake muon backgrounds are indicated according to the plots legends.

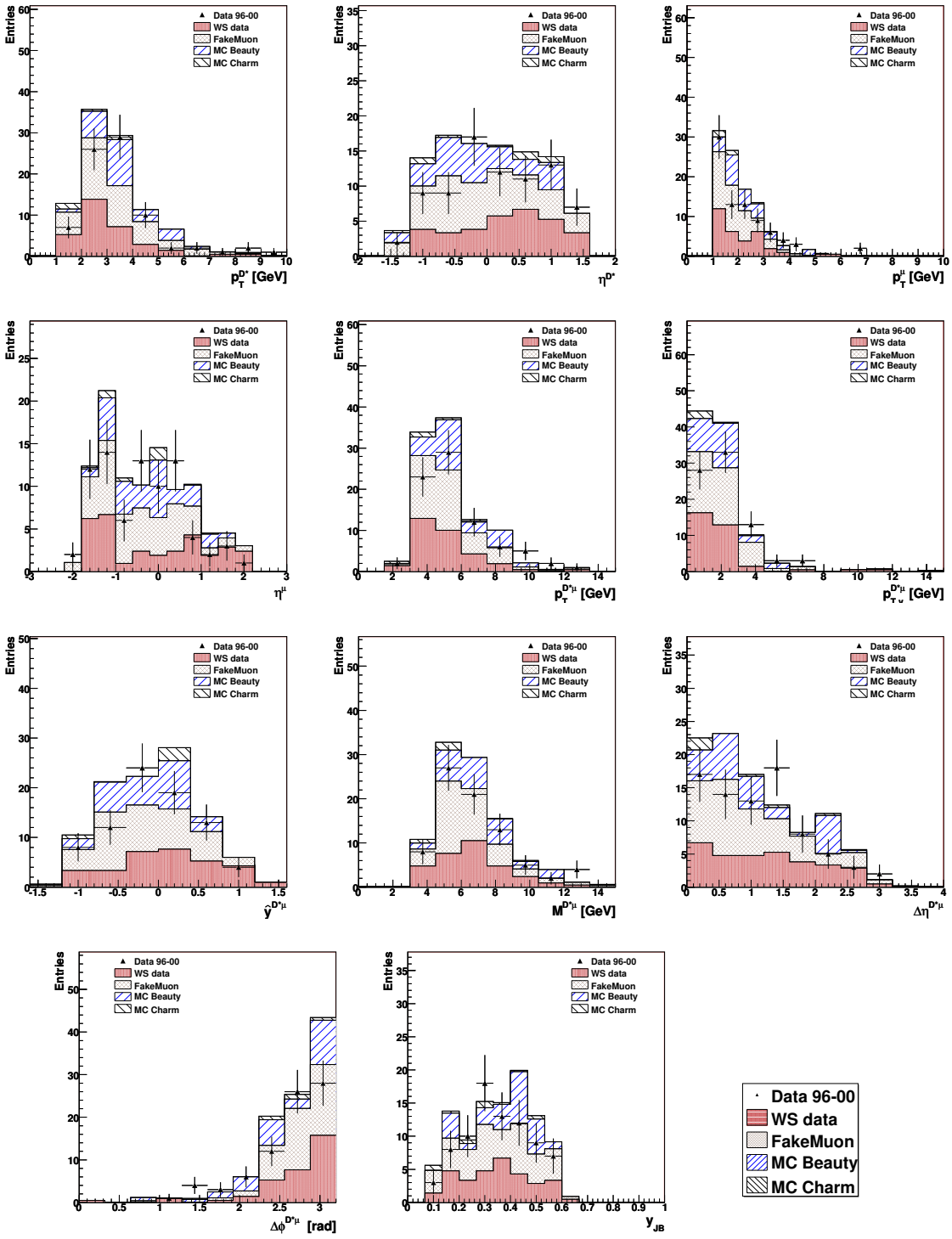

Figure 10.4: The control plots for the PHP regime and the like-sign configuration in the region $\Delta R \geq 2$. The data is shown as triangles. Contributions of charm and beauty productions as well as the D^* and fake muon backgrounds are indicated according to the plots legends.

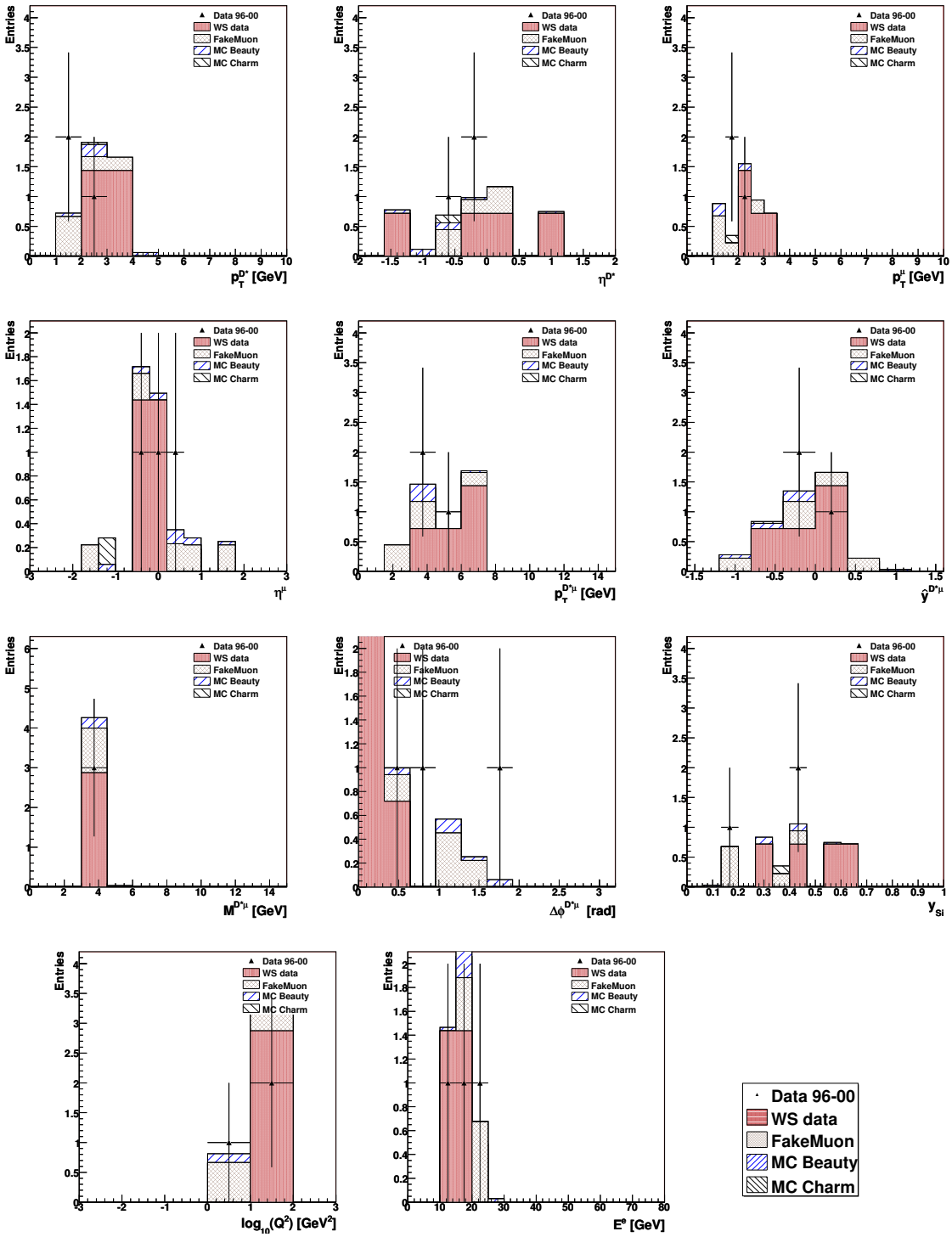

Figure 10.5: The control plots for the DIS regimes and the like-sign configuration in the region $\Delta R < 2$. The data is shown as triangles. Contributions of charm and beauty productions as well as the D^* and fake muon backgrounds are indicated according to the plots legends.

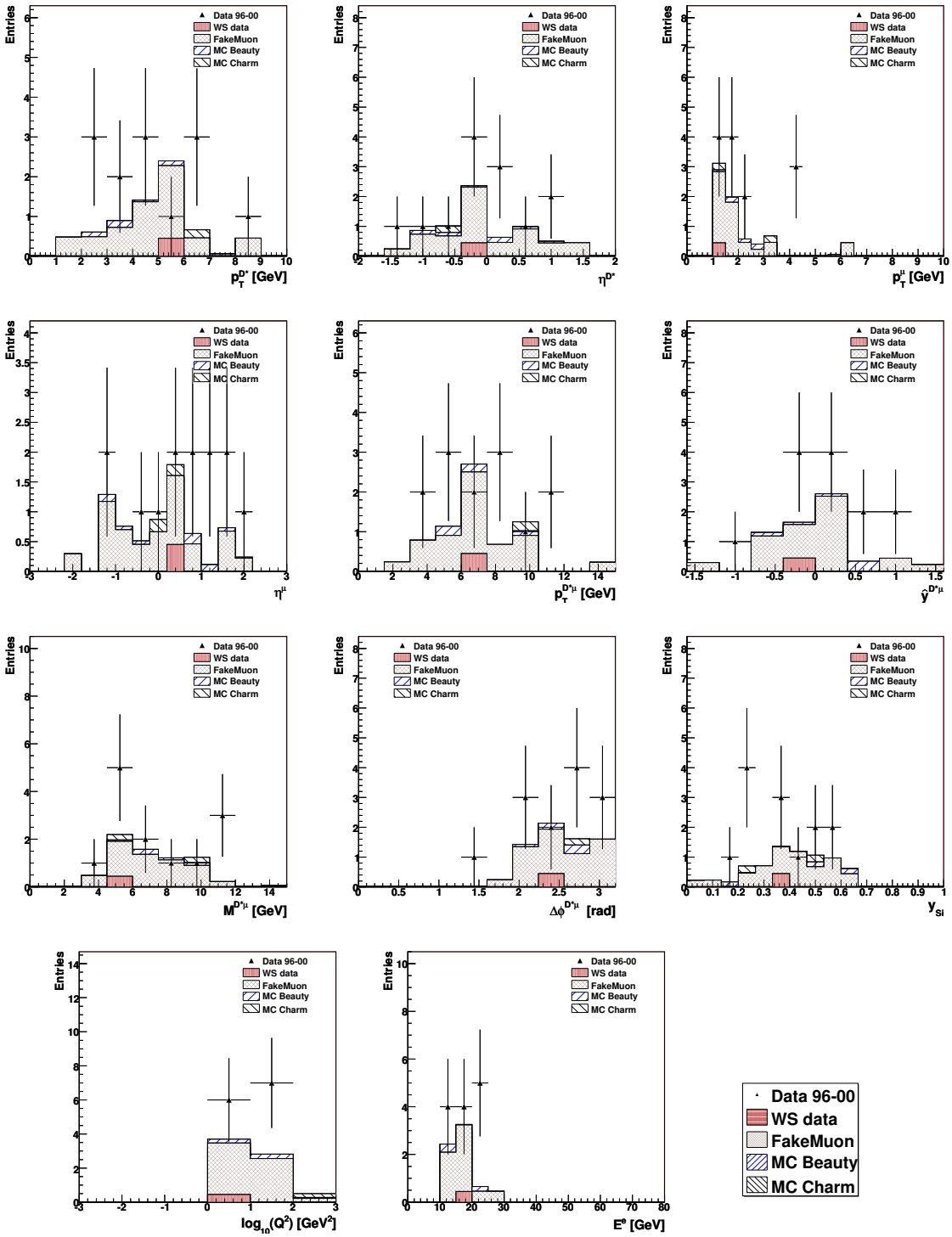

Figure 10.6: The control plots for the DIS regimes and the like-sign configuration in the region $\Delta R \geq 2$. The data is shown as triangles. Contributions of charm and beauty productions as well as the D^* and fake muon backgrounds are indicated according to the plots legends.

10.2 Systematic Uncertainties for PHP

- muon p_T cut (-1.5%);
- D^* selection cuts ($^{+2.9\%}_{-1.6\%}$);
- The D^* energy fraction f^{D^*} selection cut ($^{+11.0\%}_{-4.0\%}$);
- Simultaneous $p_T^{D^*}$ and $\Delta\phi^{D^*\mu}$ spectra reweighting ($+1.4\%$);
- Reweighting of the direct and non-direct process fractions ($+7.9\%$);
- The fake muon contamination uncertainty ($^{+5.6\%}_{-5.0\%}$);
- The muon efficiency correction ($\pm 14.2\%$);

10.3 Systematic Uncertainties for DIS

- muon p_T cut ($^{+5.8\%}_{-4.3\%}$);
- D^* selection cuts ($^{+2.9\%}_{-1.6\%}$);
- The D^* energy fraction f^{D^*} selection cut ($^{+6.8\%}_{-0.8\%}$);
- Simultaneous $p_T^{D^*}$ and $\Delta\phi^{D^*\mu}$ spectra reweighting ($+35\%$);
- The fake muon contamination uncertainty ($^{+5.3\%}_{-4.7\%}$);
- The muon efficiency correction ($\pm 10.8\%$);

10.4 Systematic Uncertainties for Inclusive Differential Cross Sections

Systematic check for $\Delta\phi^{D^*\mu}$	Error (%) in bin $0.0 < \Delta\phi^{D^*\mu} \leq 2.4$	$2.4 < \Delta\phi^{D^*\mu} \leq 2.8$	$2.8 < \Delta\phi^{D^*\mu} \leq 3.1415$
Muon eff. corr.	±14.4	±15.0	±12.8
Fake muon cont. -20%	-2.5	-1.1	-1.1
Fake muon cont. +20%	2.6	1.1	1.1
f^{D^*} -0.5	-0.9	2.0	10.6
f^{D^*} +0.5	-11.1	-8.4	-1.4
p_T^μ -40 MeV	0.8	3.6	1.4
p_T^μ +40 MeV	-6.0	1.8	2.1
dir./non-dir frac. rew.	26.8	16.3	13.3
simul. spect. rew.	34.9	26.4	31.2

Systematic check for $p_T^{D^*\mu}$	Error (%) in bin 3.0 GeV $< p_T^{D^*\mu} \leq$ 4.5 GeV	4.5 GeV $< p_T^{D^*\mu} \leq$ 7.0 GeV	7.0 GeV $< p_T^{D^*\mu} \leq$ 15.0 GeV
Muon eff. corr.	±19.9	±13.5	±11.7
Fake muon cont. -20%	-4.4	-5.5	-5.1
Fake muon cont. +20%	5.1	6.2	5.7
f^{D^*} -0.5	-9.6	15.2	0.3
f^{D^*} +0.5	-26.7	2.3	-0.7
p_T^μ -40 MeV	-0.2	0.05	-0.9
p_T^μ +40 MeV	4.1	1.2	0.6
dir./non-dir frac. rew.	17.7	-6.9	-8.4
simul. spect. rew.	-14.3	-12.9	-22.7

Systematic check for $M^{D^*\mu}$	Error (%) in bin 3.0 GeV $< M^{D^*\mu} \leq$ 5.0 GeV	5.0 GeV $< M^{D^*\mu} \leq$ 8.0 GeV	8.0 GeV $< M^{D^*\mu} \leq$ 15.0 GeV
Muon eff. corr.	±16.9	±15.8	±12.8
Fake muon cont. -20%	-4.8	-5.2	-4.8
Fake muon cont. +20%	5.5	5.8	5.3
f^{D^*} -0.5	-18.8	1.4	26.
f^{D^*} +0.5	-23.9	13.7	-26.6
p_T^μ -40 MeV	7.1	-2.3	-0.4
p_T^μ +40 MeV	4.4	-0.5	0.2
dir./non-dir frac. rew.	12.6	-1.9	-3.7
simul. spect. rew.	0.9	-4.3	-12.7

Systematic check for $\hat{y}^{D^*\mu}$	Error (%) in bin -1.5 $< \hat{y}^{D^*\mu} \leq$ -0.5	-0.5 $< \hat{y}^{D^*\mu} \leq$ 0.5	0.5 $< \hat{y}^{D^*\mu} \leq$ 1.5
Muon eff. corr.	±13.1	±13.2	±16.6
Fake muon cont. -20%	-5.2	-5.1	-5.2
Fake muon cont. +20%	5.8	5.8	5.8
f^{D^*} -0.5	3.6	6.2	-3.1
f^{D^*} +0.5	4.2	-9.4	10.5
p_T^μ -40 MeV	3.6	-3.4	-0.4
p_T^μ +40 MeV	0.1	2.3	-0.5
dir./non-dir frac. rew.	6.2	11.9	-5.9
simul. spect. rew.	9.6	5.7	4.5

Systematic check for $p_T^{D^*}$	Error (%) in bin 1.5 GeV $< p_T^{D^*} \leq$ 2.5 GeV	2.5 GeV $< p_T^{D^*} \leq$ 5.0 GeV	5.0 GeV $< p_T^{D^*} \leq$ 15.0 GeV
Muon eff. corr.	±18.7	±13.1	±11.8
Fake muon cont. -20%	-4.7	-4.9	-6.1
Fake muon cont. +20%	5.2	5.5	6.8
f^{D^*} -0.5	1.6	8.2	0.1
f^{D^*} +0.5	-31.6	0.1	-2.9
p_T^μ -40 MeV	0.6	0.1	-3.4
p_T^μ +40 MeV	-2.3	3.1	-0.8
dir./non-dir frac. rew.	29.5	-10.3	-6.4
simul. spect. rew.	-16.3	-2.2	-24.5

Systematic check for η^{D^*}	Error (%) in bin $-1.5 < \eta^{D^*} \leq -0.5$	$-0.5 < \eta^{D^*} \leq 0.5$	$0.5 < \eta^{D^*} \leq 1.5$
Muon eff. corr.	±13.6	±13.0	±-15.5
Fake muon cont. -20%	-5.5	-5.1	-5.2
Fake muon cont. +20%	6.1	5.7	-5.9
f^{D^*} -0.5	11.8	1.4	-4.7
f^{D^*} +0.5	0.5	-2.4	-8.1
p_T^μ -40 MeV	3.1	-0.7	-4.1
p_T^μ +40 MeV	-2.2	4.7	-0.5
dir./non-dir frac. rew.	6.9	14.8	-2.5
simul. spect. rew.	3.1	14.3	0.7

Systematic check for p_T^μ	Error (%) in bin 1.0 GeV $< p_T^\mu \leq$ 1.5 GeV	1.5 GeV $< p_T^\mu \leq$ 2.5 GeV	2.5 GeV $< p_T^\mu \leq$ 8.0 GeV
Muon eff. corr.	±13.5	±15.7	±8.6
Fake muon cont. -20%	-4.9	-5.2	-4.9
Fake muon cont. +20%	5.9	5.8	5.6
f^{D^*} -0.5	6.4	-9.0	49.5
f^{D^*} +0.5	-5.6	-6.7	11.1
dir./non-dir frac. rew.	3.4	5.3	8.1
simul. spect. rew.	7.0	7.9	-6.5

Systematic check for η^μ	Error (%) in bin $-2.2 < \eta^\mu \leq -1.1$	$-1.1 < \eta^\mu \leq 0.0$	$0.0 < \eta^\mu \leq 1.1$	$1.1 < \eta^\mu \leq 2.2$
Muon eff. corr.	±9.2	±14.7	±15.7	±16.1
Fake muon cont. -20%	-5.9	4.4	-4.7	-9.0
Fake muon cont. +20%	6.7	4.9	5.3	8.9
f^{D^*} -0.5	-0.8	12.3	-0.4	-15.3
f^{D^*} +0.5	-22.5	7.2	-8.7	80.5
p_T^μ -40 MeV	1.5	-0.1	0.1	-4.1
p_T^μ +40 MeV	-0.9	1.7	0.3	-9.9
dir./non-dir frac. rew.	13.1	16.3	5.2	-22.2
simul. spect. rew.	7.0	18.2	-0.4	32.0

10.5 Systematic Uncertainties for PHP Differential Cross Sections

Systematic check for $\Delta\phi^{D^*\mu}$	Error (%) in bin $0.0 < \Delta\phi^{D^*\mu} \leq 2.4$	$2.4 < \Delta\phi^{D^*\mu} \leq 2.8$	$2.8 < \Delta\phi^{D^*\mu} \leq 3.1415$
Muon eff. corr.	±15.3	±16.0	±14.1
Fake muon cont. -20%	-3.2	-1.3	-0.9
Fake muon cont. +20%	3.4	1.4	0.9
f^{D^*} -0.5	2.6	16.5	16.4
f^{D^*} +0.5	-32.3	-7.0	2.1
p_T^μ -40 MeV	-2.4	5.6	0.7
p_T^μ +40 MeV	-15.6	1.7	0.6
dir./non-dir frac. rew.	53.6	17.4	16.5
simul. spect. rew.	0.4	16.0	23.9

Systematic check for $p_T^{D^*\mu}$	Error (%) in bin 3.0 GeV $< p_T^{D^*\mu} \leq$ 4.5 GeV	4.5 GeV $< p_T^{D^*\mu} \leq$ 7.0 GeV	7.0 GeV $< p_T^{D^*\mu} \leq$ 15.0 GeV
Muon eff. corr.	±20.1	±13.8	±10.7
Fake muon cont. -20%	-3.6	-4.9	-4.8
Fake muon cont. +20%	4.5	5.5	5.4
f^{D^*} -0.5	5.1	24.7	7.4
f^{D^*} +0.5	-27.1	-0.5	4.8
p_T^μ -40 MeV	4.8	0.9	-0.5
p_T^μ +40 MeV	-0.9	-0.1	-0.2
dir./non-dir frac. rew.	17.3	-3.0	-17.7
simul. spect. rew.	-12.0	-15.9	-20.4

Systematic check for $M^{D^*\mu}$	Error (%) in bin		
	3.0 GeV $< M^{D^*\mu} \leq$ 5.0 GeV	5.0 GeV $< M^{D^*\mu} \leq$ 8.0 GeV	8.0 GeV $< M^{D^*\mu} \leq$ 15.0 GeV
Muon eff. corr.	$\pm$17.6	$\pm$15.4	$\pm$11.2
Fake muon cont. -20%	-4.6	-4.6	-4.3
Fake muon cont. +20%	5.2	5.1	4.7
f^{D^*} -0.5	-11.2	12.3	29.5
f^{D^*} +0.5	-29.0	5.2	-11.2
p_T^μ -40 MeV	6.3	-1.5	0.3
p_T^μ +40 MeV	-6.2	-0.4	0.3
dir./non-dir frac. rew.	19.6	-1.1	-4.6
simul. spect. rew.	-7.2	-5.0	-0.8

Systematic check for $\hat{y}^{D^*\mu}$	Error (%) in bin		
	-1.5 $< \hat{y}^{D^*\mu} \leq$ -0.5	-0.5 $< \hat{y}^{D^*\mu} \leq$ 0.5	0.5 $< \hat{y}^{D^*\mu} \leq$ 1.5
Muon eff. corr.	$\pm$7.4	$\pm$11.6	$\pm$17.8
Fake muon cont. -20%	-5.1	-4.3	-5.6
Fake muon cont. +20%	6.0	4.7	6.3
f^{D^*} -0.5	38.7	14.1	0.6
f^{D^*} +0.5	18.9	-9.7	3.4
p_T^μ -40 MeV	7.5	-1.0	-0.7
p_T^μ +40 MeV	-8.4	1.0	-1.7
dir./non-dir frac. rew.	6.4	12.2	-3.0
simul. spect. rew.	-6.1	11.0	0.2

Systematic check for $p_T^{D^*}$	Error (%) in bin		
	1.5 GeV $< p_T^{D^*} \leq$ 2.5 GeV	2.5 GeV $< p_T^{D^*} \leq$ 5.0 GeV	5.0 GeV $< p_T^{D^*} \leq$ 15.0 GeV
Muon eff. corr.	$\pm$18.3	$\pm$14.4	$\pm$11.7
Fake muon cont. -20%	-4.8	-4.3	-5.5
Fake muon cont. +20%	05.5	4.8	6.1
f^{D^*} -0.5	12.4	19.7	0.7
f^{D^*} +0.5	-13.7	-2.7	-6.5
p_T^μ -40 MeV	1.4	0.1	-1.2
p_T^μ +40 MeV	-2.1	-0.1	-2.3
dir./non-dir frac. rew.	31.4	-3.3	-12.2
simul. spect. rew.	-7.9	-6.7	-17.2

Systematic check for η^{D^*}	Error (%) in bin		
	-1.5 $< \eta^{D^*} \leq$ -0.5	-0.5 $< \eta^{D^*} \leq$ 0.5	0.5 $< \eta^{D^*} \leq$ 1.5
Muon eff. corr.	$\pm$3.3	$\pm$12.5	$\pm$16.9
Fake muon cont. -20%	-5.3	-3.9	-5.3
Fake muon cont. +20%	6.2	4.4	6.0
f^{D^*} -0.5	74.6	4.1	10.4
f^{D^*} +0.5	26.3	6.0	-15.8
p_T^μ -40 MeV	2.6	-0.3	-3.3
p_T^μ +40 MeV	-7.5	4.0	-1.4
dir./non-dir frac. rew.	4.7	30.5	-4.2
simul. spect. rew.	-4.1	17.5	-1.5

Systematic check for p_T^μ	Error (%) in bin		
	1.0 GeV $< p_T^\mu \leq$ 1.5 GeV	1.5 GeV $< p_T^\mu \leq$ 2.5 GeV	2.5 GeV $< p_T^\mu \leq$ 8.0 GeV
Muon eff. corr.	$\pm$15.4	$\pm$19.2	$\pm$8.9
Fake muon cont. -20%	-4.6	-4.2	-4.9
Fake muon cont. +20%	5.1	4.8	5.2
f^{D^*} -0.5	14.4	-3.7	89.8
f^{D^*} +0.5	-7.1	-6.8	23.5
dir./non-dir frac. rew.	7.4	10.7	7.0
simul. spect. rew.	3.5	5.5	5.5

Systematic check for η^μ	Error (%) in bin			
	-2.2 $< \eta^\mu \leq$ -1.1	-1.1 $< \eta^\mu \leq$ 0.0	0.0 $< \eta^\mu \leq$ 1.1	1.1 $< \eta^\mu \leq$ 2.2
Muon eff. corr.	$\pm$11.9	$\pm$14.9	$\pm$4.8	$\pm$7.4
Fake muon cont. -20%	-4.9	-4.9	-4.3	-7.1
Fake muon cont. +20%	5.1	4.8	5.7	8.8
f^{D^*} -0.5	29.2	10.0	9.2	-25.4
f^{D^*} +0.5	12.1	-7.1	-1.0	38.1
p_T^μ -40 MeV	2.4	-0.2	0.5	-1.2
p_T^μ +40 MeV	-11.6	1.2	0.4	-2.6
dir./non-dir frac. rew.	9.2	21.4	9.2	-24.4
simul. spect. rew.	7.5	16.2	-3.5	29.6

Bibliography

[1] F. Halzen,. A. Martin, Quarks and Leptons: An introduction course in modern particle physics. John Wiley & Sons, 1984.

[2] D.Perkins, Introduction to high energy physics. Addision-Wesley Publishing Company 1987.

[3] R. Feynmann, Very high-energy collisions of hadrons, Phys. Rev. Lett. 23, 1969

[4] A. Cooper-Sarkar, R. Devenish, Structure function of the nucleon and their interpretation, DESY-97-226

[5] J. Collins, D. Soper and G. Sterman, Nucl. Phys. B 308, 833 (1988).

[6] Altarelli, Guido and Parisi, G., Nucl. Phys. B126, 298 (1977).

[7] E. Kuraev, L. Lipatov and V. Fadin, The Pomeranchuk Singularity in Non-Abelian Gauge Theories, Sov. Phys. JETP 45 (1977) 199-204.
I. Balitsky and L. N. Lipatov, The Pomeranchuk Singularity in Quantum Chromo-Dynamics, Sov. J. Nucl. Phys. 28 (1978) 822-829.

[8] M. Ciafaloni, Coherence in Initial Jets at Small Q^2/s, Nucl. Phys. B296 (1988) 49.
S. Catani, F. Fiorani and G. Marchesini, QCD Coherence in Initial State Radiation, Phys. Lett. B234 (1990) 339.

[9] ZEUS Structure Function and Electroweak Physics working group, Combined H1 and ZEUS proton PDFs (unpublished), 2004

[10] C. Weizsäcker, Z. Phys. 88 (1934) 612.
E. Williams, Phys. Rev. 45 (1934) 729

[11] L. Jones and H. Wyld, Charmed-particle production by photon-gluon fusion, Phys. Rev. D17(1978)

[12] J. Smith, W.L. van Neerven, QCD Corrections to Heavy Flavour Photoproduction and Electroproduction

[13] C. Peterson, D. Schlatter, I. Schmitt, P.M. Zerwas, Phys. Rev. D27(1983).

[14] P. Nason, C. Oleari, A phenomenological study of heavy-quark fragmentation functions in e^+e^- annihilation, hep-ph/9903541

[15] Sjostrand, Torbjorn et al. , Comput. Phys. Commun. 135, 238 (2001).

[16] S. Frixione, et al., Phys.Lett. B348, 633 (1995).

[17] A. Geiser, A.E. Nuncio Quiroz, FMNR⊗PYTHIA interface, ZEUS Note-06-012

[18] L. Gladilin, Charm hadron production fractions, 1999, hep-ex/9912064.

[19] B. Andersson, et. al., Parton fragmentation and string dynamics, Phys. Rept. 97 (1983) 31.

[20] M. Cacciari, S. Frixione and P. Nason, JHEP 0103, 006 (2001).

[21] B.W. Harris, J. Smith, Phys. Rev. D57(1998)

[22] OPAL Col., Measurement of $f(c \to D^*X)$, $f(b \to D^*X)$ and $\Gamma_{c\bar{c}}/\Gamma_{had}$ using D^*-mesons, Eur. Phys. J. C1 (1998), hep-ex/9708021.

[23] K. Hagiwara et al. (Particle Data Group), Review of particle physics, Phys. Rev. D66 (2002).

[24] H. Jung, Comp. Phys. Comm. 86, 147 (1995).
H. Jung, The RAPGAP Monte Carlo for deep inelastic scattering. DESY Hamburg, 2005.
available on http://www.desy.de/ jung/rapgap/

[25] W-M. Yao et al., J. Phys. G33 (2006).

[26] D. Groom et. al., The Eur. Phys. J. C15 (2000).
L. Gladilin, private communication.

[27] B. Kniehl, et. al., 1997 Z. Phys. C 76 689.

[28] V. Innocente, and M. Maire, and E. Nagy, *In Amsterdam 1991, Proceedings, MC91: Detector and event simulation in high energy physics* 58-78.
(see HIGH ENERGY PHYSICS INDEX 30 (1992)No. 3237).

[29] ZEUS Coll., Measurement of D^* production in deep inelastic $e\pm p$ Scattering at HERA, DESY Report DESY-03-115

[30] ZEUS Coll., Dijet angular distributions in photoproduction of charm at HERA, DESY Report DESY-03-015

[31] H1 Coll., Measurement of charm and beauty photoproduction at HERA using $DS\mu$ correlations, DESY Report DESY-05-040.

[32] CTEQ Coll., Global QCD analysis of parton structure of the nucleon: CTEQ5 parton distributions, hep-ph/9903282

[33] M Glück, E. Reya, A. Vogt, Phys. Rev. D46(1992)

[34] P. Nason, S. Dawson, R. Ellis, Nucl. Phys. B327(1989)

[35] S. Dhawan, Proceedings of the Conference Real Time 2003, Montreal. (2003).
M. Sutton, Proceedings of the Conference Real Time 2003, Montreal. (2003).
C. Youngman, Proceedings of the Conference Real Time 2003, Montreal. (2003).
A. Polini, ECONF C0303241, MOGT005 (2003).

[36] P. Allfrey, et al., The Design and Performance of the ZEUS Global Tracking Trigger. ZEUS Note-07-001.

[37] A. Antonov, et al., STRECON - Track finding in STT (unpublished), ZEUS Note.

[38] R. Mankel, Pattern Recognition and Event Reconstruction in Particle Physics Experiments, Rep. Prog. Phys. 67 (2004) 553-622

[39] HERA : A Proposal for a Large Electron Proton Colliding Beam Facility at DESY, DESY-HERA81/10 , Hamburg (1981).

[40] U. Schneekloth, (ed.). DESY-HERA-98-05.

[41] G. Wolf et.al., (ZEUS collaboration), The ZEUS Detector; Technical Proposal DESY internal report, (March 1986).

[42] ZEUS Coll.,U. Holm (ed.), The ZEUS Detector, Status Report (unpublished), DESY (1993), available on
http://www-zeus.desy.de/bluebook/bluebook.html.

[43] The ZEUS Coll., A Microvertex Detector for ZEUS (unpublished).
Tech. Report DESY-PRC 97/01, 1997.

[44] V. Chiochia, Nucl. Instrum. Meth. A501, 60 (2003).
E. Koffeman, Nucl. Instrum. Meth. A473, 26 (2001).
M. Petrucci, Int. J. Mod. Phys. A16S1C, 1078 (2001).
U. Koetz, Nucl. Instrum. Meth. A461, 210 (2001).
E. Koffeman, Nucl. Instrum. Meth. A453, 89 (2000).
C. Coldewey, Nucl. Instrum. Meth. A453, 149 (2000).
C. Coldewey, Nucl. Instrum. Meth. A447, 44 (2000).

[45] ZEUS Coll., B. Foster, et al., Nucl. Instr. and Meth. A338 254 (1994).
N. Harnew, et al., Nucl. Instr. and Meth. A279 290 (1989).

[46] R. Hall-Wilton et al., The CTD tracking resolution (unpublished). ZEUS Note-99-024, 1999.

[47] S. Goers, The Straw-Tube Tracker of the ZEUS-Detector at HERA.
IEEE Instrumentation and Measurement Technology Conference, Lake Como, Italy, May 18-20, 2004

[48] M. Derrick, et al., Nucl. Instrum. Meth. A309, 77 (1991).
A. Andresen, et al., Nucl. Instrum. Meth. A309, 101 (1991).
A. Caldwell, et al., Nucl. Instrum. Meth. A321, 356 (1992).
A. Bernstein, et al., Nucl. Instrum. Meth. A336, 23 (1993).

[49] ZEUS Coll., A Presampler for the Forward and Rear Calorimeter in ZEUS detector. DESY Report DESY-96-139.

[50] ZEUS Coll., The Small Angle Rear Tracking Detector of ZEUS. DESY Report DESY-97-157.

[51] T. Jezynski et al. , Proc. SPIE 5484, 180 (2004).
K. Pozniak et al. , Proc. SPIE 5484, 186 (2004).

[52] G. Abbiendi, et al., Nucl. Instrum. Meth. A333, 342 (1993).

[53] j. Andruszkow, et al., Acta Phys. Polon. B32, 2025 (2001).

[54] W. Smith, K. Tokushuku and L. Wiggers. Proc. Computing in High-Energy Physics (CHEP).
Annecy, France, 1992, C. Verkerk and W. Wojcik (eds.), p.222. CERN, Geneva, Switzerland (1992).
Also in pre print DESY-92-150B.

[55] ZEUS Coll., available on http://www-zeus.desy.de/physics/lumi/

[56] S. Fisher and P. Palazzi, ADAMO reference manual for version 3.3. CERN ECP.
available on http://adamo.web.cern.ch/Adamo/refmanual/Document.html .

[57] TLT Simulation CZAR,
available on http://giroz.desy.de/components/funnel/MONTE_CARLO/CZAR.html

[58] G. Hartner, (1997). ZEUS Note-97-064.
G. Hartner, (1998). ZEUS Note-98-058.

[59] A. Geiser, GMUON - a general ZEUS muon finder. ZEUS Note-06-016.

[60] J. Repond. Jet Energy Corrections. ZEUS Note-96-133.

[61] Briskin, Gennady M. DESY-THESIS-1998-036.
Tuning, N., ZUFOs: Hadronic final state reconstruction with calorimeter, tracking and backsplash correction (unpublished). ZEUS-Note 01-021, 2001.

[62] J. Repond, Jet Energy Corrections, ZEUS Note-96-113.
M. Turcato, Measurement of beauty photoproduction at HERA. DESY-THESIS-2003-039.
V. Chiochia, Measurement of beauty quark production in deep inelastic scattering at HERA. DESY-THESIS-2003-031.

[63] A. Caldwell, H. Abramowicz and R. Sinkus. Neural network based electron identification in the ZEUS calorimeter.
Nucl. Inst. and Meth., A, 365:508 (1995).

[64] M. Klein, Physics at HERA, ed. W. Buchmüller and G. Ingelman vol. 1, p.71, Hamburg (1991), DESY.

[65] F. Jacquat and A. Blondel, Proceedings of the study for an ep facility for Europe. 79-48, p.391 (1979), DESY.

[66] G. Abbiendi, Global tracking of muons in the Barrel and Rear region.
ZEUS Note-99-063.

[67] L. Bellagamba, MVMATCH: A package to match FMUON tracks with Central Detectors.
ZEUS Note 96-051, 1996.

[68] Kalman, Rudolph, Emil, Transactions of the ASME-Journal of Basic Engineering 82, 35 (1960);
Fruhwirth, R., Nucl. Instrum. Meth. A262, 444 (1987).

[69] V. Kuzmin, Identification of leptons by ZEUS calorimeter.
Nucl. Inst. and Meth., A, Volume 453.

[70] G. Bruni. MUFO algorithm.
available on http://www-zeus.desy.de/$\tilde{}$bruni/ZEUS_ONLY/muons.html

[71] G. Abbiendi et al., Observation of $J/\psi \to \mu^+ + \mu^-$ in the first 273 nb$^-$1 of 1993 run.
ZEUS Note-93-120.

[72] O. Gutsche. Measurement of beauty quark cross sections in photoproduction with the ZEUS experiment at the electron-proton collider HERA, Ph.D. thesis. Hamburg, 2005.

[73] I. Bloch. Measurement of beauty production from dimuon events at HERA/ZEUS.
Ph.D. thesis. Hamburg, 2005.

[74] J. Wagner. Charm and Beauty production at HERA with D^*-muon events.
Ph.D. thesis. Hamburg, 2004.

[75] ZEUS Coll., Measurement of D^* production in deep inelastic e+p scattering at HERA.
DESY report DESY-03-115, Physical Review D 69 0120004 (2004)

[76] A. Longhin, Measurement of the beauty production at HEAR with $D^* + \mu$ tag. Ph.D. thesis.

[77] A. Longhin, Fake muon probabilities studies. ZEUS Note-05-001

[78] MINUIT (physics analysis tool for function minimization)
available on http://seal.cern.ch/documents/minuit/mntutorial.pdf

[79] ROOT (the interactive data analysis systems)
available on http://root.cern.ch/

[80] R. Barlow and C. Beeston, Comp. Phys. Comm. 77 (1993) 219-228

[81] ZeVis Event Display, available on http://www-zeus.desy.de/ zevis/

[82] ZEUS Coll., Measurement of open beauty production at HERA in the D^* muon final state.
DESY Report DESY-06-166, 2006. hep-ex/0609050.

[83] ZEUS Coll., Inclusive jet cross sections and dijet correlations in DSS photoproduction at HERA, DESY Report DESY-05-132

[84] L. Adamczyk et al., Luminosity measurement in the ZEUS experiment, ZEUS Note-01-004.

[85] L. Gladilin, private communication.
ZEUS Coll., Measurement of D^* photoproduction at HERA, XXXIst International Conference on High Energy Physics 24-31 July 2002, Amsterdam, The Netherlands

[86] L. Gladilin, I. Korzhavina,
Measurement of the gluon density inside the proton from ZEUS D^* tagged photoproduction events, ZEUS Note-96-129.

[87] ZEUS Coll., Dijet angular distributions in direct and resolved photoproduction at HERA, 1996, DESY Report DESY-96-094

[88] ZEUS Coll., Measurement of inclusive D^* and associated dijet cross sections in photoproduction at HERA, DESY Report DESY-98-085

[89] H1 Coll., Measurement of D^* meson cross sections at HERA and determination of the gluon density in the proton, DESY-98-204.

List of Figures

List of Tables